Estimation of field-scale soil moisture content and its uncertainties using Sentinel-1 satellite imagery

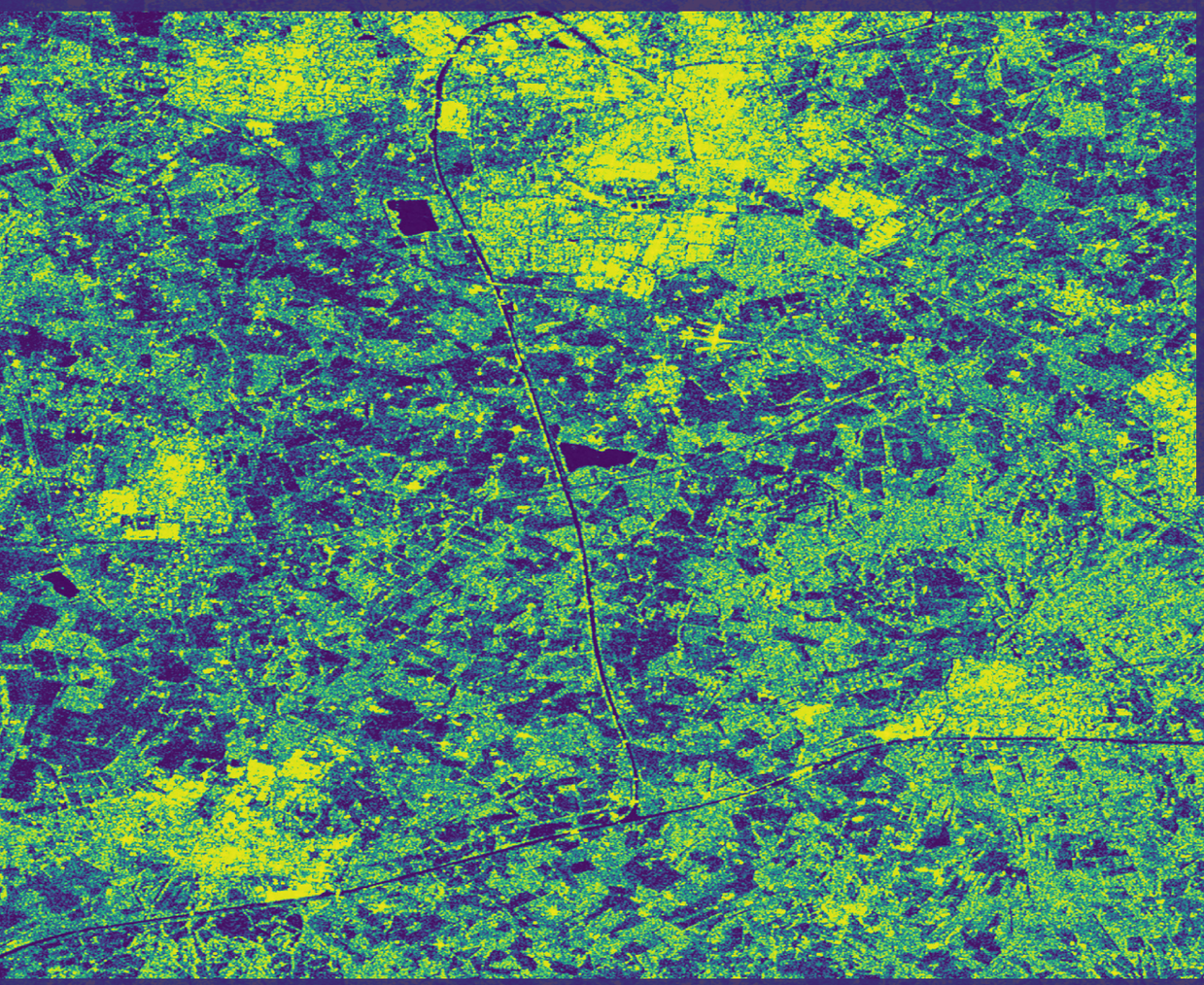

Estimation of field-scale soil moisture content and its uncertainties using Sentinel-1 satellite imagery

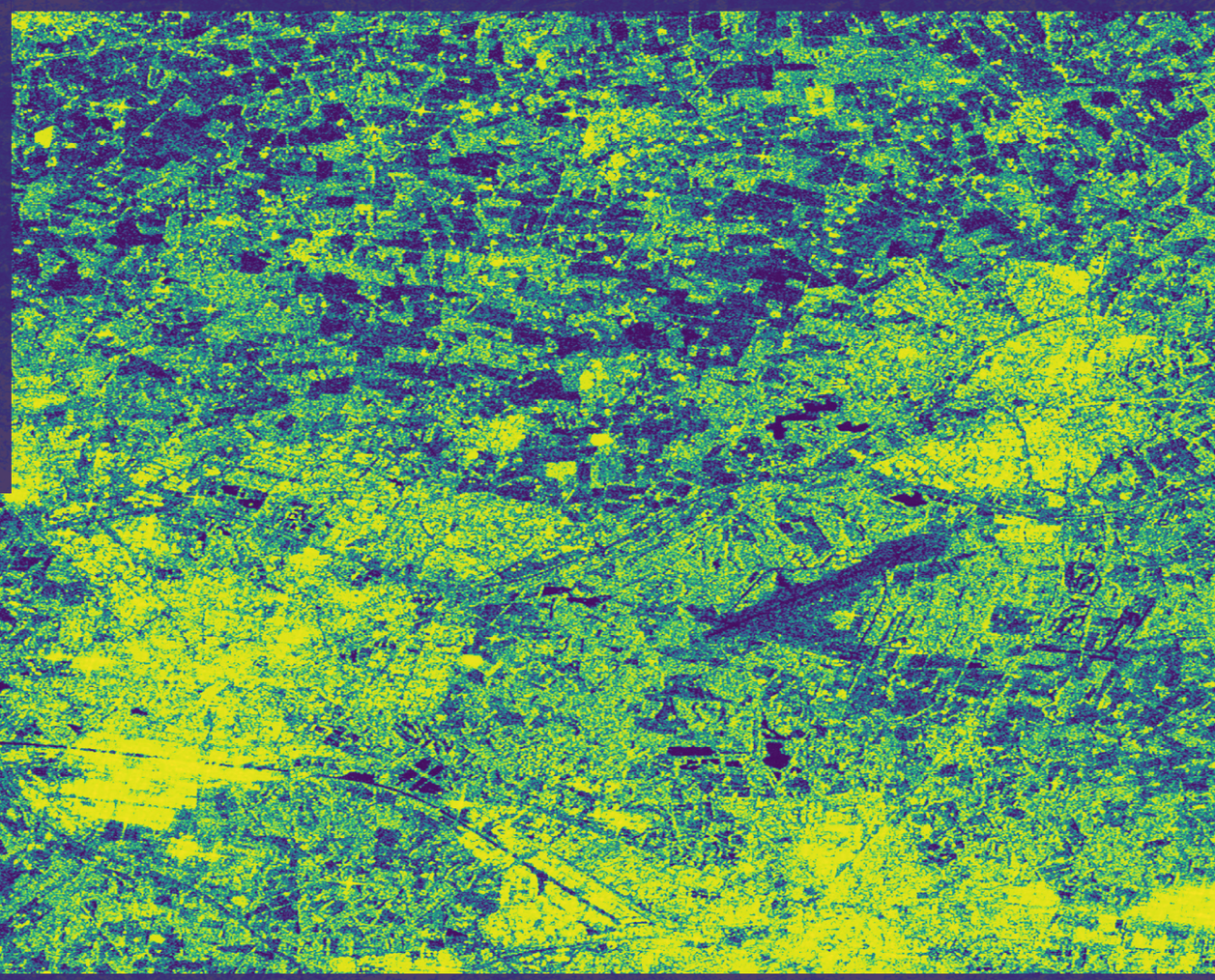

UNIVERSITY OF TWENTE. | ITC

ISBN: 978-90-365-5338-4

DOI: 10.3990/1.9789036553384

ITC dissertation nr: 412

Harm-Jan Benninga

Harm-Jan Benninga

ESTIMATION OF FIELD-SCALE SOIL MOISTURE CONTENT AND ITS UNCERTAINTIES USING SENTINEL-1 SATELLITE IMAGERY

Harm-Jan Frederik Benninga

ESTIMATION OF FIELD-SCALE SOIL MOISTURE CONTENT AND ITS UNCERTAINTIES USING SENTINEL-1 SATELLITE IMAGERY

D I S S E R T A T I O N

to obtain
the degree of doctor at the University of Twente,
on the authority of the rector magnificus,
prof. dr. ir. A. Veldkamp,
on account of the decision of the Doctorate Board,
to be publicly defended
on Thursday the 24th of March 2022 at 14.45 hours

by

Harm-Jan Frederik Benninga
born on the 15th of February 1992
in Aalsmeer, The Netherlands

This dissertation has been approved by:

Supervisor:
prof. dr. Z. Su

Co-supervisor:
dr. ir. R. van der Velde

This publication is part of the project OWAS1S (Optimizing Water Availability with Sentinel-1 Satellites) with project number 13871 of the research programme Water2014 which is partly financed by the Dutch Research Council (NWO). All OWAS1S project partners are thanked for their contributions.

© Cover design: Job Duim and Harm-Jan Benninga,
contains modified Copernicus Sentinel data [2015]
Printed by: CTRL-P, Hengelo, The Netherlands
Lay-out: UT-ITC PhD thesis LaTeX template
ISBN: 978-90-365-5338-4
DOI: 10.3990/1.9789036553384

UNIVERSITY OF TWENTE.

FACULTY OF GEO-INFORMATION SCIENCE AND EARTH OBSERVATION

GRADUATION COMMITTEE

Chair/secretary		
	prof. dr. F. D. van der Meer	University of Twente
Supervisor		
	prof. dr. Z. Su	University of Twente
Co-supervisor		
	dr. ir. R. van der Velde	University of Twente
Members		
	prof. dr. D. van der Wal	University of Twente
	prof. dr. A. D. Nelson	University of Twente
	prof. dr. M. Zribi	Centre d'Etudes Spatiales de la Biosphère
	prof. dr. N. Pierdicca	Sapienza University of Rome
	dr. C. Notarnicola	Eurac Research - Institute for Earth Observation

Acknowledgements

These pages may be the first you read in this thesis, they are the last ones I add. After more than six years of work, it is now time for a little retrospective and, especially, to thank a number of people both within the university and outside.

In het najaar van 2015, vlak na mijn afstuderen, kreeg ik de mogelijkheid om promotieonderzoek te doen aan de faculteit Geo-Informatie Wetenschappen en Aardobservatie (ITC). Daarmee kon ik mij helemaal gaan verdiepen in bodemvocht, satellietdata en het doen van metingen. Tijdens de eerste vier jaar van mijn promotieonderzoek kon ik mij volledig op het onderzoek richten, samen met alle betrokkenen van het OWAS1S-project en binnen het ITC. Hierna mocht ik doorgaan met mijn onderzoek terwijl ik werkzaam was als docent. Ik heb me met veel plezier verdiept in de verschillende vakken en projecten, lessen verzorgd en studenten begeleid. Gedurende deze laatste periode moesten we echter ook veel thuiswerken en miste ik het sociale contact en het laagdrempelige inhoudelijke overleg op het ITC. Tenslotte prijs ik me gelukkig dat ik Gemma leerde kennen. Het geheel is een mooie tijd geweest.

De eersten die ik wil bedanken zijn mijn promotor Bob en copromotor Rogier. Met zijn drieën hebben we goede discussies gehad over de grote lijnen en wetenschappelijke richting van het onderzoek. Rogier, jij was van begin tot eind zeer betrokken en had waardevolle commentaren op manuscripten. Je was altijd bereid om even mee te denken, bijvoorbeeld over een lastig commentaar van een reviewer. We hadden het niet alleen maar over wetenschappelijke onderwerpen. Bij het koffieapparaat hebben we heel wat afgepraat over wielrennen, voetbal, politiek, economie, de faculteit, enzovoort; momenten die ik zeer gewaardeerd heb. Je hebt je op meerdere momenten ingezet om een vorm voor mij te vinden om bij de afdeling werkzaam te blijven toen mijn proefschrift nog niet helemaal af was. Bob, je organiseerde workshops en had motiverende woorden voor alle promovendi van de afdeling. Dankjewel voor de betrokkenheid die je toonde als we elkaar tegenkwamen en het vertrouwen dat je in mij hebt gesteld.

Binnen het OWAS1S-project kon ik veel samenwerken met twee andere promovendi – Coleen Carranza en Michiel Pezij – en hun begeleiders – Martine van der Ploeg en Denie Augustijn. Ik wil jullie allemaal hartelijk bedanken voor de leuke samenwerking. Coleen, we hebben samen heel

wat bezoeken door het land afgelegd en hebben op de EGU-conferentie in Wenen gestaan. Michiel, het was heel leuk om na onze studie bij elkaars promotieonderzoek betrokken te zijn. We blijven zeker af en toe lunchwandelen, mountainbiken of poolen. Alle projectpartners van het OWAS1S-project – Deltares, HKV, HydroLogic, provincie Overijssel, Rijkswaterstaat, STOWA, ZLTO, en waterschappen Aa en Maas, Drents Overijsselse Delta en Vechtstromen – wil ik bedanken voor de steun en inspiratie. We werden altijd gastvrij ontvangen bij jullie. De projectvergaderingen en de bezoeken gaven veel inzicht in de Nederlandse waterwereld en in mogelijke toepassingen van mijn onderzoek. Aan het einde van het project hebben we samen met jullie interviews gemaakt over het project en toepassingen van bodemvochtinformatie, waarvan de filmpjes, heel toepasselijk, online kwamen in de eerste coronamaanden.

My time at the ITC faculty was made by the people there. I would like to thank all the PhD candidates and colleagues of Water Resources (WRS) throughout the years. In particular, I would like to thank Bagher, César, Chandra, Egor, Hong, Jan, Moiteela, Mostafa, Peiqi, Sammy and Tebogo Larry Soxapapantriaos. We had a great time in ITC, and with participating in the football competition at the ITC sports day, visiting the stadium and the city centre, and the lunch walks. Chris, you helped me a lot during the last two and a half years and have given me many opportunities. You always showed interest in my ideas and in my personal life. We are practically neighbours, so we will probably meet in Hengelo. Gabriel, we were a good team in finding out how to organize the education online. I enjoyed your funny stories, for example about your experiences in the Netherlands, openness and creativity. Anke, Ceciel, Lindy and Tina, thank you for the nice atmosphere you created at the department and the kind support. Benno and Job, thank you for the assistance with digital designs and fieldwork equipment, Carla, Grietha, Katinka and Marga for the assistance with data management and open access journals, Caroline for the lab assistance, and Annelies for the help with the organization towards the defence. Students of ITC, thank you for your international perspectives and ambition. It was very nice to work with you on several topics. Lastly, the assistance in collecting field measurements by students and colleagues from the WRS department was obviously very much appreciated.

Natuurlijk mama, papa en Wouter, Anita en Kees, mijn hele familie, Dennis en Kevin, Hemco, BWO Zaterdag 3, Integralis en het tennisgroepje. Bedankt voor de afleiding en gezellige momenten. Tenslotte Gemma, je bent super belangrijk voor mij (en voor de afronding van dit proefschrift). Wat ben ik blij dat we elkaar hebben leren kennen toen je in Deventer woonde en contact hebben gehouden toen je een paar maanden niet in Nederland was. Door jou was de coronatijd ook heel mooi, met heel veel tijd samen en waarin we elkaar heel goed hebben leren kennen. Nu gaan we samen op weg naar een mooie en spannende toekomst.

Harm-Jan
Hengelo, February 2022

Summary

The soil moisture content (SMC) expresses the amount of water in the unsaturated zone. The variable is essential for vegetation growth and hydrological processes. SMC can be estimated from satellite microwave observations across spatial domains. This thesis focuses on the field-scale, at which more direct relations between the ground conditions (SMC, surface roughness and vegetation) and satellite microwave observations are expected. The uncertainties in the field-scale SMC retrievals were studied and decomposed in uncertainties originating from in situ references (U_{sp} and $U_{s,S1}$), satellite observations (U_{S1}) and model parameters (U_p).

Two regional networks were employed for the in situ monitoring of SMC, namely the Twente network in the east and the Raam network in the south of the Netherlands. Both networks have stations with sensors at depths of 5 cm, 10 cm, 20 cm, 40 cm and 80 cm. From soil-specific calibrations follow station probe measurement uncertainties (U_{sp}) of $0.018\,m^3\,m^{-3}$ to $0.023\,m^3\,m^{-3}$ for the Raam network and $0.028\,m^3\,m^{-3}$ for the Twente network. The sensor's influence zone, determined in Raam soil, is 3 cm–4 cm. A vertical mismatch and a horizontal mismatch between SMC retrievals from satellites and the station measurements cause a spatial mismatch uncertainty ($U_{s,S1}$). Using measurements inside four agricultural fields, the $U_{s,S1}$ estimate is $0.051\,m^3\,m^{-3}$.

The Sentinel-1 satellites provide microwave backscatter (σ^0) observations, which can be used for field-scale SMC retrieval. The σ^0 observations are found to be disturbed by frozen conditions below an air temperature of 1 °C, snow during Sentinel-1's morning overpasses on meadows and cultivated fields, and interception after more than 1.8 mm of rain in the 12 h preceding a Sentinel-1 overpass. Dew was not found to be of influence. After masking based on these rules, the Sentinel-1 σ^0 observations still contain radiometric uncertainty (s_{S1}) originating from calibration uncertainties, sensor instabilities and speckle. σ^0 over forests is assumed time-invariant; the observed deviations were used to estimate the s_{S1}. The s_{S1} improves from 0.85 dB (for a surface area of 0.25 ha) to 0.30 dB (10 ha) for the VV polarization and from 0.89 dB (0.25 ha) to 0.36 dB (10 ha) for the VH polarization, following approximately an inverse square root dependency on the surface area over which the σ^0 observations are averaged. The retrieval uncertainty due to

s_{S1} (U_{S1}) is low ($-0.01\,\mathrm{m^3\,m^{-3}}$ to $+0.01\,\mathrm{m^3\,m^{-3}}$) for dry soils and large surface areas and high ($-0.10\,\mathrm{m^3\,m^{-3}}$ to $+0.17\,\mathrm{m^3\,m^{-3}}$) for wet soils and small surface areas.

The uncertainties involved in surface scattering simulations and SMC retrievals were investigated. The surface roughness parameters that are input to the integral equation method (IEM) surface scattering model were calibrated for two sparsely vegetated meadows and two fallow maize fields. A Bayesian framework was used for the calibration as well as for deriving the model parameter uncertainty (U_p) and total uncertainty ($U_{total\text{-}B}$). The resulting $U_{total\text{-}B}$ successfully reproduces the uncertainty estimated empirically against the in situ references. The combination of the derived U_p with U_{sp}, $U_{s,S1}$ and U_{S1} also constitute the total SMC retrieval uncertainty. The main uncertainty originates from the in situ references (U_{sp} and $U_{s,S1}$) and the Sentinel-1 observations (U_{S1}), whereas the contribution from the surface roughness parameters (U_p) is small.

For the two meadows the surface roughness parameter distributions are similar, time-invariant and independent of Sentinel-1's ascending/descending orbits. These are promising results for the operational retrieval of SMC over meadows across a larger region because they suggest that using a single set of surface roughness parameters is permitted. The IEM surface scattering model and the Tor Vergata (TV) vegetation scattering and absorption model were parameterised for grass-covered soil surfaces. A Sentinel-2 leaf area index (LAI) product provides field-scale vegetation information, as was demonstrated by validation against in situ measurements on two meadows and four maize fields. However, uncertainty propagation shows that the Sentinel-2 LAI uncertainty of $0.71\,\mathrm{m^2\,m^{-2}}$ has a large impact on SMC retrievals. The SMC retrievals for 21 meadows in the Twente region, validated against adjacent in situ station references, have mean Pearson correlation coefficients of 0.55 for IEM and 0.64 for TV-IEM, root mean square deviations ($RMSD$) of $0.14\,\mathrm{m^3\,m^{-3}}$ for IEM and $0.13\,\mathrm{m^3\,m^{-3}}$ for TV-IEM, and $RMSD$s relative to the range of the SMC references ($RRMSD$) of 24 % for both IEM and TV-IEM. The performance metrics for IEM and TV-IEM, i.e. without and with a vegetation correction, are similar if the same retrieval-reference pairs are considered.

In conclusion, the quantification of uncertainty contributions helps to comprehend SMC retrieval accuracy. A large part of the uncertainty originates from the in situ references and the Sentinel-1 σ^0 observations. The uncertainty in the Sentinel-2 LAI estimates also has a large impact. The thesis' methods and findings lead to several directions for future research. Future research could focus on the uncertainty sources with the largest contributions to effectively improve the SMC retrievals, assessing the general applicability and improvement of the SMC retrieval scheme, functionally evaluating the SMC retrievals in potential applications, and representing field-scale SMC as an ensemble of SMC products.

Samenvatting

Het bodemvochtgehalte (*soil moisture content* of SMC) drukt de hoeveelheid vocht in de onverzadigde zone uit. Deze variabele is essentieel voor vegetatiegroei en hydrologische processen. SMC kan over grote gebieden bepaald worden met microgolfobservaties vanuit satellieten. Dit proefschrift richt zich op de veldschaal, waarop directere relaties tussen grondomstandigheden (SMC, oppervlakteruwheid en vegetatie) en de microgolfobservaties worden verwacht. De onzekerheden in de SMC-bepalingen zijn onderzocht en onderverdeeld in onzekerheden afkomstig van in situ referenties (U_{sp} en $U_{s,S1}$), satellietobservaties (U_{S1}) en modelparameters (U_p).

Voor de in situ monitoring van SMC zijn twee regionale netwerken gebruikt, namelijk het Twente netwerk in het oosten en het Raam netwerk in het zuiden van Nederland. Beide netwerken bestaan uit stations met sensoren op 5 cm, 10 cm, 20 cm, 40 cm en 80 cm diepte. Vanuit grondspecifieke calibraties volgen onzekerheden van de sensoren (U_{sp}) van 0,018 $m^3\,m^{-3}$ tot 0,023 $m^3\,m^{-3}$ voor het Raam netwerk en 0,028 $m^3\,m^{-3}$ voor het Twente netwerk. De zone die van invloed is op de sensormetingen, zoals bepaald met grond uit de Raam, is 3 cm-4 cm. Een verticale ongelijkheid en een horizontale ongelijkheid tussen de SMC-satellietbepalingen en de stationsmetingen zorgen voor een onzekerheid ($U_{s,S1}$). Met behulp van metingen binnen vier agrarische velden, is de $U_{s,S1}$ geschat op 0,051 $m^3\,m^{-3}$.

De Sentinel-1-satellieten leveren observaties van microgolfterugkaatsing (σ^0), die gebruikt kunnen worden voor SMC-bepaling op veldschaal. De σ^0-observaties worden verstoord door bevroren omstandigheden onder een luchttemperatuur van 1 °C, sneeuw tijdens ochtendobservaties op grasland en akkers, en interceptie na meer dan 1,8 mm regen in de 12 uur voorafgaand aan een Sentinel-1-observatie. Dauw heeft geen verstorend effect. Met maskering op basis van deze regels, bevatten de Sentinel-1-observaties nog steeds radiometrische onzekerheid (s_{S1}) als gevolg van calibratie-onzekerheden, sensorinstabiliteiten en *speckle*. Aangenomen is dat σ^0 over bos constant is over tijd; de geobserveerde afwijkingen zijn gebruikt om de s_{S1} te schatten. De s_{S1} verbetert van 0,85 dB (voor een oppervlakte van 0,25 ha) naar 0,30 dB (10 ha) voor de VV-polarisatie en van 0,89 dB (0,25 ha) naar 0,36 dB (10 ha) voor de VH-polarisatie, waarbij s_{S1} bij benadering een omgekeerd wortelverband heeft

met het oppervlakte waarover de σ^0-observaties zijn gemiddeld. De SMC-bepalingsonzekerheid als gevolg van s_{S1} (U_{S1}) is laag ($-0{,}01\,\mathrm{m^3\,m^{-3}}$ tot $+0{,}01\,\mathrm{m^3\,m^{-3}}$) voor droge gronden en grote oppervlaktes en hoog ($-0{,}10\,\mathrm{m^3\,m^{-3}}$ tot $+0{,}17\,\mathrm{m^3\,m^{-3}}$) voor natte gronden en kleine oppervlaktes.

De onzekerheden in oppervlakteverstrooiingssimulaties en SMC-bepalingen zijn onderzocht. De oppervlakteruwheidsparameters in het *integral equation method* (IEM) oppervlakteverstrooiingsmodel zijn gekalibreerd voor twee dun begroeide graspercelen en twee braakliggende maïspercelen. Een Bayesiaanse methode is gebruikt voor zowel de kalibratie als voor het afleiden van de modelparameteronzekerheid (U_p) en de totale onzekerheid ($U_{total\text{-}B}$). De $U_{total\text{-}B}$ reproduceert met succes de empirische onzekerheid die is geschat ten opzichte van de in situ referenties. Ook de combinatie van de U_p met U_{sp}, $U_{s,S1}$ en U_{S1} vormt de totale onzekerheid van de SMC-bepalingen. De grootste onzekerheid is afkomstig van de in situ referenties (U_{sp} en $U_{s,S1}$) en de Sentinel-1-observaties (U_{S1}), terwijl de bijdrage van de oppervlakteruwheidsparameters (U_p) klein is.

Voor de twee graspercelen zijn de oppervlakteruwheidsparameterverdelingen vergelijkbaar, constant over tijd en onafhankelijk van de Sentinel-1-observatierichting. Dit zijn veelbelovende resultaten voor de operationele bepaling van SMC op graspercelen over een groter gebied, omdat ze suggereren dat één set van oppervlakteruwheidsparameters gebruikt kan worden. Het IEM oppervlakteverstrooiingsmodel en het *Tor Vergata* (TV) vegetatie verstrooiings- en absorptiemodel zijn geparametriseerd voor bodemoppervlaktes met gras. Een Sentinel-2-product van bladoppervlakte-index (*leaf area index* of LAI) geeft vegetatie-informatie op veldschaal, hetgeen is aangetoond door validatie ten opzichte van in situ metingen op twee graspercelen en vier maïspercelen. Uit een propagatie van de Sentinel-2 LAI-onzekerheid van $0{,}71\,\mathrm{m^2\,m^{-2}}$ blijkt echter dat deze onzekerheid een grote invloed op de SMC-bepalingen heeft. De SMC-bepalingen voor 21 graspercelen in de regio Twente, gevalideerd ten opzichte van in situ stationsreferenties, hebben gemiddelde Pearsons correlatiecoëffiënten van 0,55 voor IEM en 0,64 voor TV-IEM, kwadratische gemiddeldes van de afwijkingen (*root mean square deviations* of *RMSD*) van $0{,}14\,\mathrm{m^3\,m^{-3}}$ voor IEM en $0{,}13\,\mathrm{m^3\,m^{-3}}$ voor TV-IEM en *RMSD*s relatief aan het bereik van de SMC-referenties (*RRMSD*) van 24 % voor zowel IEM als TV-IEM. De prestatiestatistieken voor IEM en TV-IEM, oftewel zonder en met een vegetatiecorrectie, zijn vergelijkbaar als dezelfde paren van SMC-bepalingen en -referenties worden gebruikt.

Concluderend kan worden gesteld dat de kwantificering van onzekerheidsbijdragen helpt om de nauwkeurigheid van SMC-bepalingen te interpreteren. Een groot deel van de onzekerheid is afkomstig van de in situ referenties en de Sentinel-1-observaties. Ook de onzekerheid van de Sentinel-2 LAI-bepalingen heeft een grote invloed. Uit de methodes en bevindingen van dit proefschrift volgen verscheidene mogelijkheden voor toekomstig onderzoek. Toekomstig onderzoek zou zich kunnen richten op de onzekerheidsbronnen met de grootste bijdragen om de

SMC-bepalingen op een effectieve manier te verbeteren, het beoordelen van de algemene toepasbaarheid en het verbeteren van de SMC-bepalingsmethode, het functioneel evalueren van de SMC-bepalingen in potentiële toepassingen, en het weergeven van SMC op veldschaal als een ensemble van SMC-producten.

Contents

List of Figures

List of Tables

Lists of abbreviations and symbols

Abbreviations

AHN	Digital terrain model for the Netherlands ('Actueel Hoogtebestand Nederland' in Dutch)
AHN2	AHN version 2
AHN3	AHN version 3
AMSR2	Advanced Microwave Scanning Radiometer 2
AR(1)	First-order autoregressive model
AR(2)	Second-order autoregressive model
ASCAT	Advanced Scatterometer
BOFEK	Soil physical units map of the Netherlands ('bodemfysische eenhedenkaart' in Dutch)
CDF	Cumulative distribution function
DINOloket	Data and Information on the Dutch Subsurface ('Data en Informatie van de Nederlandse Ondergrond' in Dutch)
DREAM	DiffeRential Evolution Adaptive Metropolis
DTM	Digital terrain model
ESA CCI SM	European Space Agency's Climate Change Initiative for Soil Moisture
ERS SAR	European Remote Sensing Synthetic Aperture Radar
ESA	European Space Agency
FV2000	LAI-2000 File Viewer
GCOS	Global Climate Observing System
GDN	Geological Survey of the Netherlands ('Geologische Dienst Nederland' in Dutch)
GHG	Mean highest groundwater depth ('gemiddeld hoogste grondwaterstand' in Dutch) [m]
GRD	Ground Range Detected
GVSMC	Gravimetrically determined volumetric soil moisture content [$m^3\ m^{-3}$]
HR	High Resolution
Hydros	Hydrosphere State
IEM	Integral equation method
ITC	Faculty of Geo-Information Science and Earth Observation
IW	Interferometric Wide Swath
KNMI	Royal Netherlands Meteorological Institute ('Koninklijk Nederlands Meteorologisch Instituut' in Dutch)
LAI	Leaf area index [$m^2\ m^{-2}$]

LHM	National Hydrological Model ('Landelijk Hydrologisch Model' in Dutch)
LSM	Land surface model
MAP	Maximum a posteriori
NDVI	Normalized difference vegetation index [−]
NHI	Netherlands Hydrological Instrument
NWO	Dutch Research Council ('Nederlandse Organisatie voor Wetenschappelijk Onderzoek' in Dutch)
OWAS1S	Optimizing Water Availability with Sentinel-1 Satellites
PDF	Probability density function
$RMSD$	Root mean square deviation [unit of data]
$RRMSD$	Root mean square deviation relative to the range of references [% or −]
RWA	Regional water authority
SAR	Synthetic aperture radar
SMAP	Soil Moisture Active Passive
SMC	Soil moisture content [$m^3\,m^{-3}$]
SMC^+	Effect of an upward perturbed leaf area index value on soil moisture content retrievals [$m^3\,m^{-3}$]
SMC^-	Effect of a downward perturbed leaf area index value on soil moisture content retrievals [$m^3\,m^{-3}$]
SMOS	Soil Moisture and Ocean Salinity
SNAP	Sentinel Application Platform
TDR	Time-domain reflectometry
TV	Tor Vergata
TV-IEM	Coupled integral equation method and Tor Vergata model
$uRMSD$	Unbiased root mean square deviation [unit of data]
VITO	Flemish Institute for Technological Research ('Vlaamse Instelling voor Technologisch Onderzoek' in Dutch)
VWC	Vegetation water content [$kg\,kg^{-1}$]
WCM	Water cloud model
WMO	World Meteorological Organization

Symbols

$5TM_{reading}$	Raw output 5TM probe [mV]
A	Surface area [ha]
a, b	Intercept [$m^3\,m^{-3}$] and slope [−] of linear regression functions between native and calibrated soil moisture content measurements
c_1, c_2, c_3	Power function coefficients between surface area and Sentinel-1's radiometric uncertainty
c_A, c_B, c_C	Power function coefficients between measured relative permittivity and soil moisture content
c_l	Autocorrelation length of the surface height [cm]
Cov	Covariance terms [units of data]
D_{leaf}	Leaves' disc thickness [cm]
D_s	Snow depth [cm]

E_{ref}	Reference crop evapotranspiration [mm]
h	Pressure head [cm]
M	Number of independent samples [−]
N	Number of pairs or observations [−]
N_W	Number of observations in moving average window [−]
n_G	Pore size distribution parameter Van Genuchten equation [−]
P	Rainfall [mm]
R^2	Coefficient of determination [−]
RC_p	Relative contribution of model parameter uncertainty [% or −]
RC_{S1}	Relative contribution of Sentinel-1's radiometric uncertainty [% or −]
RC_{sp}	Relative contribution of station probe measurement uncertainty [% or −]
$RC_{s,S1}$	Relative contribution of stations' spatial mismatch uncertainty [% or −]
R_{leaf}	Leaves' disc radius [cm]
r	Snow's ice-crystal radius [mm]
r_P	Pearson correlation coefficient [−]
r_S	Spearman's rank correlation coefficient [−]
s	Root mean square surface height [cm]
s_{S1}	Sentinel-1's radiometric uncertainty [dB]
T	Time of a Sentinel-1 observation [timestamp]
T_{air}	Air temperature [°C]
t	Observation number [−]
U_{fp}	Measurement uncertainty of the soil moisture content field probe [$m^3\,m^{-3}$]
U_p	Soil moisture content retrieval uncertainty from model parameter uncertainty [$m^3\,m^{-3}$]
U_{S1}	Soil moisture content retrieval uncertainty due to Sentinel-1's radiometric uncertainty [$m^3\,m^{-3}$]
$U_{s,\overline{F}}$	Total uncertainty between soil moisture content station measurements and the spatial mean of field measurements [$m^3\,m^{-3}$]
$U_{s,f}$	Spatial mismatch uncertainty between soil moisture content at station and field [$m^3\,m^{-3}$]
U_{sp}	Measurement uncertainty of soil moisture content station probes [$m^3\,m^{-3}$]
$U_{s,S1}$	Spatial mismatch uncertainty in the soil moisture content station measurements as references for satellite (Sentinel-1) observed field-scale soil moisture content [$m^3\,m^{-3}$]
$U_{total\text{-}B}$	Total soil moisture content retrieval uncertainty derived with Bayesian calibration [$m^3\,m^{-3}$]
$U_{total\text{-}C}$	Total soil moisture content retrieval uncertainty from the combination of its constituents [$m^3\,m^{-3}$]
V_t	Total soil volume [m^3]
V_w	Volume of water in a soil volume [m^3]
W	Moving average window [days]
Y_e	Estimates [unit of data]
$\overline{Y_e}$	Mean of estimates [unit of data]
Y_r	References [unit of data]
$\overline{Y_r}$	Mean of references [unit of data]
z	Reference data [unit of data]

α_G	Scale parameter Van Genuchten equation [cm^{-1}]
γ	Vegetation transmissivity [−]
$\Delta\theta^+$	Upper boundary of soil moisture content retrieval uncertainty [$m^3\,m^{-3}$]
$\Delta\theta^-$	Lower boundary of soil moisture content retrieval uncertainty [$m^3\,m^{-3}$]
$\Delta\sigma^0$	Deviation in backscatter [dB]
ε_a	Relative permittivity 5TM reading [−]
ε_r	Relative permittivity [−]
ε_r'	Real part of the relative permittivity [−]
ε_r''	Imaginary part of the relative permittivity [−]
θ	Soil moisture content [$m^3\,m^{-3}$]
θ_{cp}	Calibrated soil moisture content probe reading [$m^3\,m^{-3}$]
θ_p	Native soil moisture content probe reading [$m^3\,m^{-3}$]
θ_r	Residual soil moisture content [$m^3\,m^{-3}$]
θ_s	Saturated soil moisture content [$m^3\,m^{-3}$]
$p(\vartheta\|z)$	Probability density function of parameters (ϑ) given reference data (z) [−]
ϑ	Parameters
λ	Wavelength [mm]
μ	Mean [unit of data]
$d\sigma^0$	Backscatter anomaly with moving average [dB]
$\overline{d\sigma^0}$	Mean of backscatter anomalies [dB]
σ	Standard deviation [unit of data]
σ_0	Standard deviation of backscatter residuals [dB]
σ^0	Backscatter coefficient [dB or $m^2\,m^{-2}$]
σ_s^0	Backscatter from the soil surface [dB or $m^2\,m^{-2}$]
σ_{sv}^0	Backscatter from soil-vegetation pathways [dB or $m^2\,m^{-2}$]
σ_v^0	Direct vegetation backscatter [dB or $m^2\,m^{-2}$]
σ_{VV}^0	Backscatter in VV polarization [dB]
σ_{VH}^0	Backscatter in VH polarization [dB]

Introduction

1

This section outlines what soil moisture content (SMC) is, how it can be measured, its role in understanding and coping with hydrological conditions, as well as the lack of SMC information up to the desired scale and with the associated uncertainties.

1.1 Background

1.1.1 Soil moisture content and its variability

Soil can be considered a three-phase system consisting of a matrix of mineral and organic solid grains between which are pores that can contain air or water. This is schematised in Figure 1.1a. SMC expresses the amount of water in the unsaturated zone of the soil, often defined as the ratio of the volume of water (V_w, in m^3, see Figure 1.1a) to the total soil volume (V_t, in m^3, see Figure 1.1a):

$$SMC = \frac{V_w}{V_t}. \tag{1.1}$$

Figure 1.1b shows characteristic SMC levels. Under saturated conditions all the soil pores are filled by water, i.e. the maximum SMC is equal to a soil's porosity (Dingman, 2015; Seneviratne et al., 2010). The porosity ranges from approximately $0.35\,m^3\,m^{-3}$, associated with coarse-grained sandy soils, to $0.55\,m^3\,m^{-3}$ for fine-grained clayey soils and even up to $0.80\,m^3\,m^{-3}$ for highly organic soils (Dingman, 2015). The capacity of a soil to store additional (rain or snowmelt) water is the difference between current SMC and the saturated SMC. In the first days after a soil has been saturated, for example after an intense rain or snowmelt event, the water drains by gravity. At 'field capacity' the soil matric potential is in equilibrium with gravity. The SMC at field capacity relates to soil properties. Below field capacity, the water can be further removed from a soil by surface evaporation and plant transpiration. The 'wilting point', which depends on soil properties and vegetation type, refers to the SMC below which the water is held so tightly by the soil matrix that the vegetation cannot extract any more water and wilts (Dingman, 2015; Seneviratne et al., 2010). Dingman (2015) and Seneviratne et al. (2010) define a soil's plant available water capacity as the field capacity minus

the wilting point. The *actual* plant available water is the difference of current SMC with the wilting point SMC.

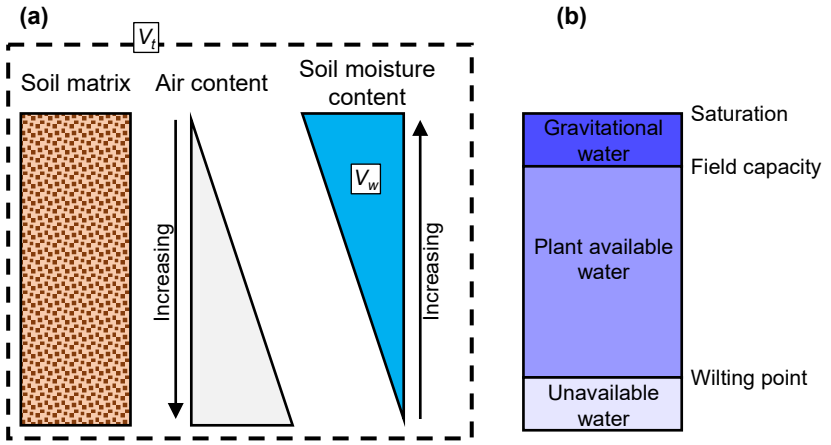

Figure 1.1 **(a)** Schematisation of soil as a three-phase system. The pores in the soil matrix can contain variable volumes of air and water. The volume of water (V_w, in m^3) and total soil volume (V_t, in m^3) are used to calculate the SMC with Equation 1.1. **(b)** SMC levels characteristic for drainage, evaporation and transpiration processes.

SMC varies over space and time due to hydrometeorological factors, such as rainfall, evapotranspiration and interactions with the groundwater. The typical temporal scale of SMC in response to wetting and drying events is in the order of days to weeks (Brutsaert, 2005); in a climate with distinct seasons this is on top of seasonal SMC dynamics. Spatial SMC variability is also controlled by landscape factors, such as soil type, topography, vegetation and groundwater table depth, which can be very local (Karthikeyan et al., 2017b; Montzka et al., 2020; Famiglietti et al., 2008; Vereecken et al., 2014).

1.1.2 Measuring soil moisture content

1.1.2.1 Direct estimation

SMC can be estimated in a direct manner by (i) collecting a soil sample (ring) of known volume, (ii) weighing the wet sample, (iii) oven-drying the sample, and (iv) weighing the dried sample. The volumetric SMC (in $m^3\ m^{-3}$) can then be calculated from the definition of SMC in Equation 1.1, whereby the difference between the wet mass and the dry mass can be used to calculate V_w and the volume of the ring is V_t. This method is known as the gravimetric method.

The gravimetric method is considered relatively accurate (Topp and Ferré, 2002b; Dobriyal et al., 2012) and often used as the reference for other measurement methods (e.g. Vaz et al., 2013; Cosh et al., 2005).

However, this method is also time-consuming, local and destructive, which disables repetition at the exact same location.

1.1.2.2 Indirect estimation through the relative permittivity

To fulfil the need for repeated SMC measurements over time and space, several alternative, indirect measurement methods have been developed. These methods are based on measuring a soil property that relates to SMC, such as the relative permittivity, electrical conductivity, heat capacity or soil water pressure. Estimating SMC from the relation with relative permittivity is most conventional, both in situ (Robinson et al., 2008) and from satellites (Petropoulos et al., 2015).

'Relative permittivity' (ε_r) is also known as 'dielectric constant'. The term 'dielectric constant' has been deprecated because ε_r is frequency-dependent and thus is not a constant (Thiel, 2010; IEEE Standards Board, 2018, 1997). Moreover, in the context of this study, a soil's bulk ε_r varies as a function of the SMC. This originates from the large contrast between the ε_r of water ($\varepsilon_r \approx 80$ for frequencies below 1 GHz), versus soil minerals ($\varepsilon_r \approx 3$ to $\varepsilon_r \approx 7$), air ($\varepsilon_r = 1$) and organic material ($\varepsilon_r \approx 2$ to $\varepsilon_r \approx 5$) (Topp and Ferré, 2002c; Robinson et al., 2008). Accordingly, the soil's bulk ε_r increases with increasing SMC.

The ε_r of water depends on the frequency of the incident electromagnetic waves, temperature and salinity (Ulaby and Long, 2014; Dobson et al., 1985; Mironov et al., 2009). Furthermore, with regard to Figure 1.1, 'free water' and 'bound water' should be distinguished. The water molecules close to soil particles are bound to the soil matrix, disabling the interaction with the electromagnetic waves that yields the high ε_r of free water (Dobson et al., 1985; Mironov et al., 2009; Jackson and Schmugge, 1989; Wang and Schmugge, 1980). The amount of bound water is controlled by soil properties. As such, the relation between the bulk ε_r and SMC is affected by soil texture, mineralogy, bulk density, organic matter content and salinity (Starr and Paltineanu, 2002; Ulaby and Long, 2014). Topp et al. (1980) determined a general relation between ε_r and SMC, which gives reasonable SMC measurement accuracy for a wide range of soils (Vaz et al., 2013; Ferré and Topp, 2002). Figure 1.2 shows the Topp function, illustrating that ε_r increases with increasing SMC.

The estimation of SMC from satellites imagery, based on the relation with ε_r, operate in the microwave spectrum. For microwaves with frequencies less than about 10 GHz, the impact of the atmosphere, i.a. clouds, is considered negligible (Woodhouse, 2006). This includes the most common microwave bands; L-band (0.39 GHz–1.55 GHz), C-band (3.9 GHz–5.75 GHz) and X-band (5.75 GHz–10.9 GHz), making them well suited for observing the Earth's surface (Kornelsen and Coulibaly, 2013). However, in the L- to X-band, the water's dielectric loss, represented by the imaginary part of ε_r (ε_r''), cannot be neglected and the ε_r is frequency-dependent (Topp and Ferré, 2002c; Ulaby and Long, 2014; Robinson et al., 2008). For a frequency of 5.405 GHz (Sentinel-1), for example, water's $\varepsilon_r' \approx 73$ and $\varepsilon_r'' \approx 22$ (Ulaby and Long, 2014). This is in contrast with

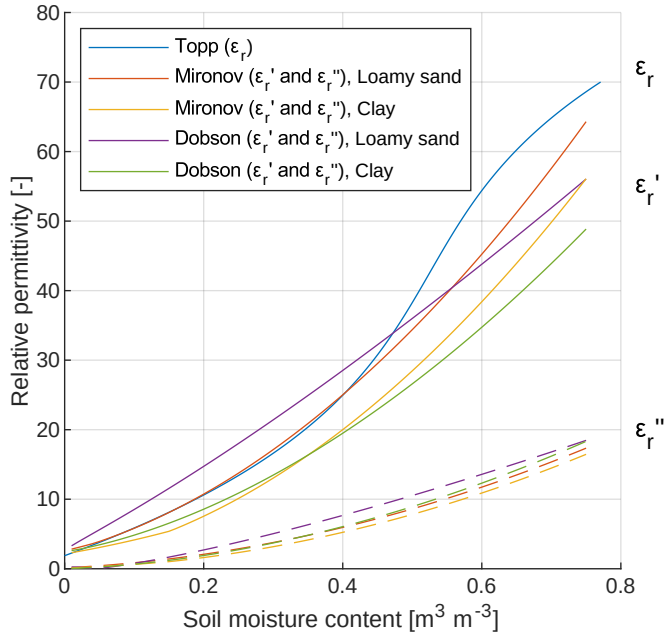

Figure 1.2 Relative permittivity - with the real (ε_r') and imaginary (ε_r'') part - as a function of SMC, using three different dielectric mixing models. The Mironov et al. (2009) model was run for a frequency of 5.405 GHz (Sentinel-1). The Dobson et al. (1985) model was run for a temperature of 10 °C and also for a frequency of 5.405 GHz.

the frequencies at which in situ devices operate, and the Topp equation is not suited for the microwave frequencies. Figure 1.2 shows ε_r as a function of SMC for two models commonly used at microwave frequencies, namely the Dobson et al. (1985) model and the Mironov et al. (2009) model.

1.2 Development of SMC products

Monitoring SMC is crucial for agricultural productivity, forestry and ecosystem health, and for climate change mitigation and adaptation measures (Global Climate Observing System (GCOS), 2016). GCOS (1995) recognized SMC as a key variable already in its first reports, but at that time no method for monitoring SMC at the required time and space scales existed. SMC products are now available at coarse scale (e.g. 3 km–50 km resolutions) and fine scale (e.g. 0.1 km–1 km resolutions). Section 1.2.1 discusses the available products. A field-scale product is not yet available. Section 1.2.2 outlines the importance of field-scale information for hydrological and agricultural applications.

1.2.1 Available products

1.2.1.1 Coarse scale products

After the first papers that were published on mapping SMC from passive (e.g. Schmugge et al., 1974; Poe, 1972) and active microwave observations (e.g. Macdonald and Waite, 1971; Ulaby, 1974) in the 1970s, algorithms for retrieving SMC globally were reported around the 2000s (e.g. Wagner et al., 1999; Owe et al., 2001). Furthermore, the dedicated satellite missions Soil Moisture and Ocean Salinity (SMOS; Kerr et al., 2001) and Hydrosphere State (Hydros; Entekhabi et al., 2004) were planned. GCOS (2004) then formulated the following challenge:

> **Action T37**
> Develop an experimental soil-moisture product from existing networks and satellite observations. (p. 106)

The development of an experimental product was foreseen for 2009 and a quasi-operational global product was expected in 2011 (GCOS, 2004). Hydros was cancelled in 2005, but the Soil Moisture Active Passive (SMAP) mission builds on its early work (Entekhabi et al., 2014). The most publicly visible SMC products available nowadays are derived from the microwave observations of the Advanced Scatterometer (ASCAT) at 25 km and 50 km (Wagner et al., 2013; Bartalis et al., 2007), Advanced Microwave Scanning Radiometer 2 (AMSR2) at 0.1° and 0.25° (Zhang et al., 2017; Kim et al., 2015), SMOS at on average 43 km (Kerr et al., 2010, 2016) and SMAP products at 3 km, 9 km and 36 km resolution (Chan et al., 2016, 2018; Das et al., 2019). The European Space Agency's Climate Change Initiative for Soil Moisture (ESA CCI SM) harmonizes and merges SMC retrievals from various satellites, which have finite lifetimes and different instrument algorithms, resulting in a consistent global SMC time series from 1978 (Gruber et al., 2019). Regarding the currently available products, GCOS (2016) emphasizes as main tasks to ensure their sustainability and improve them step-by-step.

1.2.1.2 Fine scale products

A new challenge GCOS (2016) proposed is:

> **Action T18: Regional high-resolution soil-moisture data record**
> Develop high-resolution soil-moisture data records for climate change adaptation and mitigation by exploiting microwave and thermal remote-sensing data. (p. 186)

GCOS (2016) foresaw Action T18 for 2017–2020. Indeed, in 2019 the 1 km resolution Surface Soil Moisture product became operationally available over Europe (Copernicus Global Land Service, 2021). This product utilizes Sentinel-1 observations and applies a change detection algorithm to retrieve SMC (Bauer-Marschallinger et al., 2019). Three other operational SMC products downscale coarse SMC products or microwave observations, namely the ASCAT/Sentinel-1 product available at 1 km

resolution over Europe (Bauer-Marschallinger et al., 2018), the 100 m resolution - commercially available - product of VanderSat (VanderSat, 2021) and the 1 km resolution SMAP/Sentinel-1 product that is available with a research status (Das et al., 2019).

1.2.2 Relevance of field-scale information

Throughout the years GCOS has expanded the challenges for the monitoring of SMC, based on technological developments and feasibility. This resulted in at least four coarse scale and four fine scale products. Within the grids of the available products, however, SMC conditions can vary because of the high spatial variability (see Section 1.1.1). In the case of agricultural fields, this is enhanced by differences in e.g. soil management, groundwater tables and vegetation between fields. Although no specific challenge has yet been formulated, several applications would benefit from distributed information on SMC states at finer resolutions than yet available. The paragraphs below illustrate operational applications in water management and agricultural management.

SMC information can improve predictions of catchment discharges and river water levels (Cenci et al., 2017; Pauwels et al., 2001; Mahanama et al., 2008; Crow et al., 2017), which is important in mitigating the consequences of events by reliable warnings. Recently, this has been relevant during the river floods that hit Limburg (the Netherlands), Belgium and Germany in July 2021. Developing models with spatial resolutions of 1 km at global scale and 100 m at continental scale has been considered the 'grand challenge for hydrology' by Wood et al. (2011). Pezij et al. (2019b) expect that fine resolution surface SMC products will improve the SMC simulations at field scales. Besides predicting river levels, water managers can operate on wet and dry conditions by controlling weirs and pumps. Optimal management requires fine resolution information about current water system conditions, including SMC conditions (Pezij, 2020; Pezij et al., 2019a). Developments in local and operable controlling systems are small weirs (e.g. Bloemberg-Van der Hulst, 2021) and (pressure) drainage (e.g. Jansen et al., 2017; Hoving et al., 2018).

Agriculture depends on sufficient root zone soil water availability for crop growth, while excess of soil water also leads to a reduction in root water uptake (Feddes et al., 1976). During 2018 a summer drought impacted large parts of Europe (Bakke et al., 2020). The 2019 and 2020 summers were also drier than normal. Figures 1.3a–b illustrate the severe water stress that agricultural crops experienced during these summers. SMC information could improve irrigation management in terms of crop yield, water use efficiency and net income (Vereecken et al., 2014; Srivastava, 2017; Lei et al., 2020). An example is the 'irrigation signal' tool ('Beregeningssignaal' in Dutch), developed by ZLTO (ZLTO, n.d.; Nieuwe Oogst, 2015), which gives farmers advice on when and how much to irrigate at field scale. Wet soil conditions, besides limiting plant growth, are unfavourable for the trafficability of farmlands (Figures 1.3c–d). This may jeopardize the timely execution of essential agricultural practices

a A meadow experiencing water stress (photo was taken by Rogier van der Velde on 17 July 2019).

b A maize field experiencing water stress (photo was taken by the author on 22 August 2018). At the end of August 2016 the maize was 285 cm, here it is about chest height and the development of cobs is limited.

c Standing water on a meadow (photo was taken by the author on 5 April 2018).

d Issue of field trafficability, part of the maize was not harvested (photo was taken by the author on 16 October 2017).

Figure 1.3 Dry (**a** and **b**) and wet (**c** and **d**) conditions on agricultural fields in the Netherlands.

and cause structural damage of land (Batey, 2009; Hamza and Anderson, 2005). Carranza et al. (2019) developed a framework for monitoring field trafficability, using SMC information from satellite imagery.

The examples in the two paragraphs above illustrate that several applications in water management and agricultural management would benefit from SMC information, both in wet and in dry conditions. Furthermore, there is a trend towards field-scale solutions. Especially over heterogeneous landscapes with relative small agricultural fields, such as in western Europe, new applications may be anticipated with the SMC information at field scale because of larger spatial variability within the grids of the currently available products.

1.3 Estimating soil moisture content at field scale

SMC can be estimated at field scale with synthetic aperture radar (SAR) observations. This section explains the retrieval of SMC from SAR observations (Section 1.3.1.1), such as acquired by the Sentinel-1 satellites (Section 1.3.1.2), and compares its characteristics against those of in situ measurements (Section 1.3.2).

1.3.1 Satellite SAR retrieval

1.3.1.1 Theory and models

SARs are 'active' instruments, meaning that a satellite's SAR instrument sends microwaves to the Earth and measures the scattering that returns ('backscatter'). The measured backscatter intensity, expressed in terms of the area of an isotropic scatterer that would give the same level of reflection and normalised per unit area on the ground surface is termed the backscatter coefficient (σ^0, in $m^2\,m^{-2}$ or dB; Woodhouse, 2006). The σ^0 from natural surfaces constitutes of three contributions, which are visualized in Figure 1.4 and sum up as follows:

$$\sigma^0 = \gamma^2\sigma_s^0 + \sigma_v^0 + \sigma_{sv}^0, \tag{1.2}$$

where γ^2 is the two-way transmissivity of the vegetation, σ_s^0 is the σ^0 from the soil surface, σ_v^0 is the direct vegetation σ^0 and σ_{sv}^0 is the σ^0 from soil-vegetation pathways.

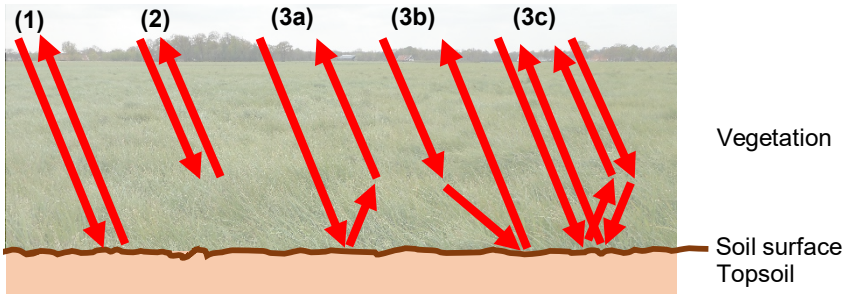

Figure 1.4 Backscattering (σ^0) contributions from a vegetated soil surface. **(1)** σ^0 from the soil, thereby considering two-way transmission through the vegetation ($\gamma^2\sigma_s^0$), **(2)** direct σ^0 from the vegetation (σ_v^0), and **(3a)** σ^0 from soil-vegetation, **(3b)** vegetation-soil and **(3c)** soil-vegetation-soil and vegetation-soil-vegetation pathways, together σ_{sv}^0. The figure is adapted from Ulaby and Long (2014) and Van der Velde (2010).

The relation between a soil's ε_r and SMC, explained in Section 1.1.2.2, governs the ability to estimate SMC in the topsoil with SAR instruments via σ_s^0. A soil medium reflects, for increasing ε_r, more of the incident microwaves' energy. Consequently, wet soils (high ε_r) produce a higher σ_s^0 than dry soils (low ε_r). Next to ε_r, the roughness of the soil surface

plays an essential role: a smooth surface produces specular reflection, i.e. away from the instrument, whereas a rougher surface produces more diffuse scattering (Woodhouse, 2006; Ulaby and Long, 2014). This diffuse scattering includes the direction of the satellite, which links soil properties to intensity received by the SAR instrument (Ulaby et al., 1996). Previous studies (Vereecken et al., 2014; Satalino et al., 2002; Altese et al., 1996) suggested that σ_s^0 is more sensitive to roughness than to SMC and that information on the surface roughness is, thus, indispensable for SMC retrieval from σ^0. The σ_s^0 as a function of the ε_r and surface roughness can be simulated with surface scattering models, such as the 'integral equation method' (IEM; Fung et al., 1992), Oh model (Oh et al., 1992, 2002) and Dubois model (Dubois et al., 1995).

Interactions of the microwaves with vegetation result in attenuation (transmission loss) of the σ_s^0, which reduces the sensitivity of σ^0 to SMC variations. Furthermore, the vegetation produces σ_v^0 and σ_{sv}^0 (Ulaby and Long, 2014). Because the σ_v^0 and σ_{sv}^0 are part of the total σ^0, for the accuracy of SMC retrievals it is important to account for these terms as well. The σ_{sv}^0 may contribute to σ^0 to SMC sensitivity under dense vegetation conditions (Joseph et al., 2010; Stiles et al., 2000; Chiu and Sarabandi, 2000). As the vegetation structure and water content typically develop throughout a year, for example on agricultural fields, vegetation effects on the σ^0 would be confused with changes in SMC if they are not incorporated in a SMC retrieval algorithm.

The estimation of SMC from σ^0 observations is an ill-posed problem because several combinations of SMC, surface roughness and vegetation would produce the same σ^0 (Vereecken et al., 2014; Satalino et al., 2002; Verhoest et al., 2008). Information on the surface roughness and vegetation status is, thus, indispensable. Data-driven, semi-empirical or physically based models can be used for incorporating the effects of surface roughness and vegetation on the relation between σ^0 and SMC. A wide range of applications with these three types of models have been studied and described in a number of review papers, such as Barrett et al. (2009), Kornelsen and Coulibaly (2013), Ali et al. (2015), Petropoulos et al. (2015), Das and Paul (2015) and Karthikeyan et al. (2017a).

1.3.1.2 Sentinel-1 SAR mission

Satellite missions since 1978 that were equipped with a SAR instrument are listed in Table 1 in Kornelsen and Coulibaly (2013). The Sentinel-1 SAR satellite constellation (Sentinel-1A and Sentinel-1B) provides images of σ^0 with fine spatial and temporal resolutions and a high radiometric accuracy. Furthermore, the images become systematically and freely available within 24 h after acquisition, and Sentinel-1C and Sentinel-1D, planned for launches in 2022 and 2023, ensure continuation of the Sentinel-1 programme until 2030 (World Meteorological Organization, 2021).

The technical details of the satellites and the operation modes are extensively described in Torres et al. (2012) and Bourbigot et al. (2016).

Sentinel-1A and Sentinel-1B provide images since October 2014 and September 2016. The technical characteristics and operational configurations have drawn already much interest for scientific and operational purposes, and many studies recognized the potential of the Sentinel-1 imagery for studying microwave scattering processes and fine-scale SMC monitoring (e.g. Baghdadi et al., 2017; Bai et al., 2017; Bousbih et al., 2017; Van Doninck et al., 2012; Attema et al., 2007; Doubková et al., 2012; Gao et al., 2017; El Hajj et al., 2017; Hornacek et al., 2012; Kornelsen and Coulibaly, 2013; Liu et al., 2017; Petropoulos et al., 2015; Wagner et al., 2009; Bauer-Marschallinger et al., 2019; Amazirh et al., 2018; Pulvirenti et al., 2018; Paloscia et al., 2013; Nguyen et al., 2021; Pandit et al., 2020; Lee and Walker, 2020; Balenzano et al., 2012, 2021).

1.3.2 SAR retrievals and in situ measurements

Next to SMC retrieved from satellite observations, it can be measured with in situ SMC sensors. SMC monitoring stations are usually a collection of sensors installed at various depths.

Table 1.1 lists the characteristics of in situ measurements and satellite retrievals. Dobriyal et al. (2012) explain that in situ measurements can be accurately calibrated, may be used at various depths and can take measurements at any time. However, the in situ measurements are only point measurements and this makes spatial application complicated (Dobriyal et al., 2012; Western et al., 2002). SMC estimates from satellite imagery provide an integral value for an entire footprint (Vereecken et al., 2014) and a large spatial coverage. It can be concluded, as is also argued by Western et al. (2002), that in situ measurements and satellite retrievals are complementary to each other.

Table 1.1 Characteristics of SMC information obtained from in situ sensors and from satellite retrievals.

In situ measurements	Satellite retrievals
Relatively accurate	Unknown accuracy
Possible at selected depths	Soil surface
High temporal resolution	Low temporal resolution
Small spatial coverage	Large spatial coverage

Figure 1.5 illustrates the spatial scales of SMC estimates by in situ stations and two fine scale products. Agricultural fields are represented by outlines from a crop parcel registry (Ministry of Economic Affairs and Climate Policy, 2020). The regular grids of the existing SMC products do not match the fields of varying sizes and orientations. Figure 1.5 also shows a Sentinel-1 image on a 10 m grid, which allows to distinguish individual fields. This thesis utilizes Sentinel-1 SAR imagery and in situ measurements to address the desired field scale as well as to investigate the uncertainties involved in the SMC retrievals.

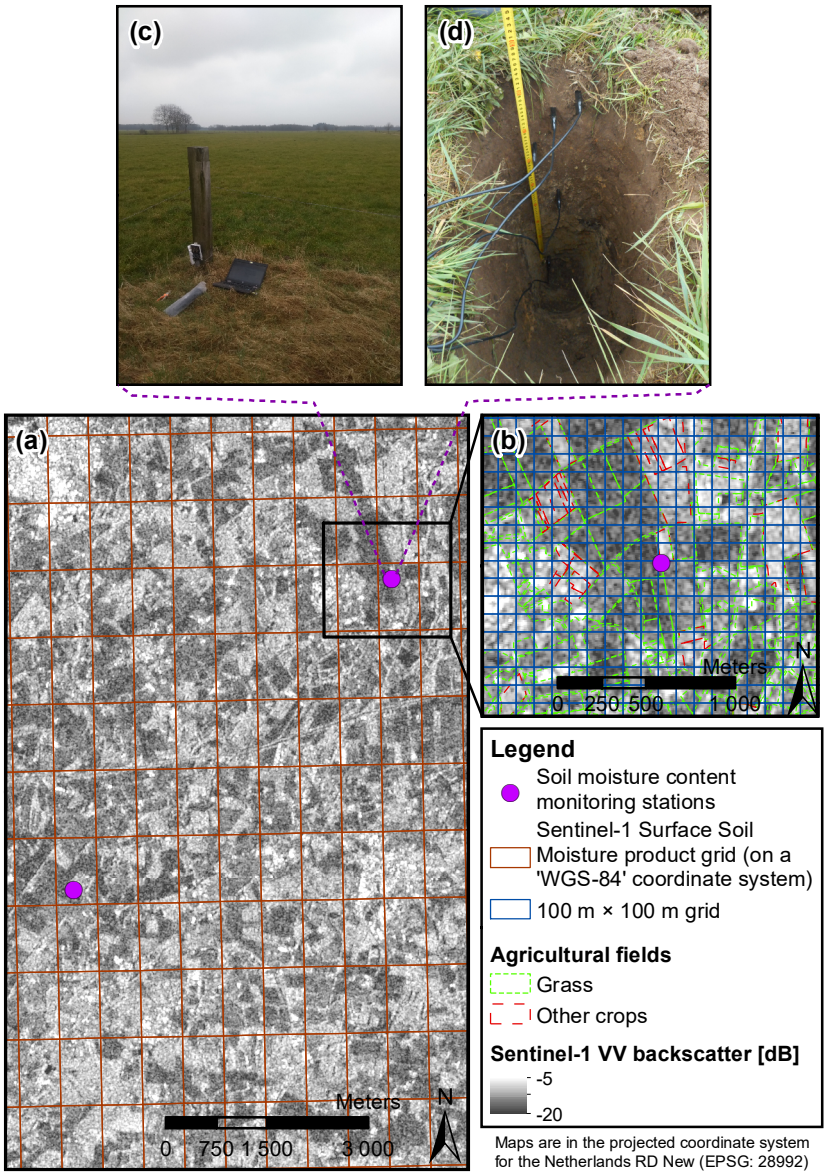

Figure 1.5 Spatial scales of SMC estimates. **(a)** Example of Sentinel-1 backscatter image (from 5 July 2016), with two SMC monitoring stations in this region and the grid of the Sentinel-1 Surface Soil Moisture product. **(b)** Zoom-in on one SMC monitoring station, which is surrounded by agricultural fields. The outlines of the agricultural fields originate from the crop parcel registry 2016 ('Basisregistratie Gewaspercelen 2016'; Ministry of Economic Affairs and Climate Policy, 2020). Also a $100\,\mathrm{m} \times 100\,\mathrm{m}$ grid is shown, which is adopted in the VanderSat SMC product. **(c)** A typical SMC monitoring station, at the border of an agricultural field (photo was taken by Rogier van der Velde on 16 March 2018). **(d)** An installation pit with SMC sensors installed at five depths (photo was taken by the author on 2 May 2017).

1.4 Scientific challenges

The step to field-scale SMC information, using SAR satellite imagery, is necessary for agricultural and water management applications. Furthermore, Kornelsen and Coulibaly (2013) consider the field scale as optimal for SMC retrieval. This is coarse enough to reduce the radiometric uncertainty in SAR σ^0 observations and, in the context of comparison against in situ references, fine enough to not introduce uncertainty in the references due to structural (heavy-tailed and multimodal) effects on SMC distributions that play a role on catchment scales, such as topography, vegetation, precipitation and soil characteristics. In the relation between σ^0 and SMC, the agricultural field is the more natural scale because SMC, surface roughness and vegetation conditions are field-dependent. For example, the change detection algorithm underlying the Copernicus Surface Soil Moisture product assumes static surface roughness and vegetation conditions. Bauer-Marschallinger et al. (2019) and Wagner et al. (2009) noted that at the field scale this assumption is unlikely to hold because the effects of temporally varying surface roughness and vegetation on the σ^0 are not averaged out spatially. As a result, the variability of the surface roughness and vegetation conditions becomes more pronounced (Wagner et al., 2009) and more direct relations between the ground conditions (SMC, surface roughness and vegetation) and σ^0 are expected. SAR σ^0 observations can be used to retrieve SMC information up to agricultural field scale (e.g. Amazirh et al., 2018; El Hajj et al., 2017; Lievens and Verhoest, 2012; Su et al., 1997; Vereecken et al., 2014). As more direct relations between the field conditions and the σ^0 observations are expected, **this scale supports the investigation of σ^0-SMC relations and the uncertainties involved in these**.

Due to uncertainty contributions, SMC retrievals from σ^0 observations will not exactly match the references. Information on the uncertainty of SMC retrievals is essential to assess their reliability and for their applicability. Firstly, this helps valuing and understanding the information content of SMC retrievals. Potential users, such as water managers and farmers, are not always aware of the complexities involved in the SMC retrieval from σ^0 observations and may think of SMC retrievals as 'SMC observations'. As such, uncertainty information is important to communicate to potential users. Secondly, combining SMC products can only be done properly when their uncertainties have been characterized (Su et al., 2014; Yilmaz et al., 2012). The assimilation of SMC retrievals into land surface models requires an estimate of the SMC retrievals' uncertainty (Pierdicca et al., 2014; Quets et al., 2019). Verhoest et al. (2007) explain that SMC retrievals with a high uncertainty will be given a low weight in changing model states, whereas SMC retrievals with a low uncertainty may be given a high weight. A specific uncertainty estimate for each SMC retrieval is preferred above a general uncertainty estimate (Pierdicca et al., 2014; Quets et al., 2019). Lei et al. (2020) found that the assimilation of Sentinel-1 SMC can be improved via the application

of a realistic time-varying uncertainty. However, data assimilation studies often rely on user-defined uncertainty assumptions (Yilmaz et al., 2012). Thirdly, uncertainty contribution from references may be misunderstood as SMC retrieval uncertainty (Crow et al., 2012), and, fourthly, information on the relative contributions of uncertainty sources directs towards the potentially (most) contributing improvements of SMC retrievals (Karthikeyan et al., 2017a). Several authors (e.g. Karthikeyan et al., 2017a; Lievens et al., 2011; Kornelsen and Coulibaly, 2013), therefore, noted that **further research is required on identifying the sources and impacts of uncertainties.** Uncertainties between SMC retrievals and references result from the in situ references (Cosh et al., 2005, 2006; Western et al., 2002), the σ^0 observations (Pathe et al., 2009; Karthikeyan et al., 2017a) and the retrieval algorithm and parameters (De Lannoy et al., 2014; Pathe et al., 2009; Karthikeyan et al., 2017a). No studies are known that identify these uncertainty contributions and their effects on SMC retrievals.

1.5 Research objective

The main objective of this study is to develop a method for retrieving SMC at field scale from Sentinel-1 satellite imagery and to obtain a better understanding of the uncertainties involved in such retrievals.

1.6 Research questions

To meet the research objective, four research questions and approaches were formulated:

Research question 1: What is the uncertainty of in situ SMC measurements as reference for field-scale SMC retrievals?
SMC monitoring networks, consisting of several stations, provide the references that are used to calibrate and validate the SMC retrievals from satellite imagery on a range of surface and hydrometeorological conditions. SMC differences occur naturally as a result of a region's topography, vegetation, soil type and groundwater depth distributions. This is illustrated for two regional SMC networks: the Twente network in the east and the Raam network in the south of the Netherlands. The SMC sensors are calibrated on the regions' soils and their influence zone is measured.

The sensors' measurement uncertainty affects the in situ measurements. Furthermore, in the context of this study, station's SMC measurements are to be compared with field-scale SMC retrievals from satellite observations. The spatial mismatch uncertainty between the two is estimated by comparison of station measurements against measurements inside four study fields with a handheld device.

Research question 2: What is the impact of Sentinel-1 σ^0 uncertainty and weather-related surface conditions on SMC retrievals?

The SAR σ^0 observations contain calibration uncertainties, sensor instabilities and speckle effects. Together these are referred to as radiometric uncertainty. The radiometric uncertainty is estimated by analysing the temporal deviations in long time series of σ^0 observations from targets which are assumed time-invariant. Besides the radiometric uncertainty, several weather-related surface conditions, such as frozen conditions, snow, intercepted rain and dew, may disturb σ^0 observations. In order to develop a masking procedure for Sentinel-1 σ^0 observations, meteorological measurements are used to investigate the effect of these weather-related surface conditions on σ^0 observations. Then, the impacts on SMC retrievals of the radiometric uncertainty and of not masking for weather-related surface conditions are quantified. This is achieved by applying a physically based surface scattering model for various surface roughness and soil wetness scenarios.

Research question 3: What are the relative uncertainty contributions to SMC retrievals under sparsely vegetated conditions?

The total SMC retrieval uncertainty constitute of the measurement uncertainty of the station sensors that provide the references, the spatial mismatch uncertainty of the references with Sentinel-1 observed SMC, Sentinel-1's radiometric uncertainty, and the retrieval algorithm and parameter uncertainty. From Section 1.3.1.1, it can be inferred that the roughness of a soil surface essentially governs the sensitivity of σ^0 to SMC. Studying sparsely vegetated conditions, namely on two sparsely vegetated meadows and two fallow maize fields, enables to focus on the surface roughness parameters. A Bayesian framework is used for calibrating the surface roughness parameters that are input to a physically based surface scattering model, and for deriving the model parameter uncertainty and total uncertainty. Subsequently, the quantifications of the references' uncertainties from research question 1 and Sentinel-1's radiometric uncertainty from research question 2 are applied to decompose the total uncertainty in its four constituents.

Research question 4: Can Sentinel-1 SMC retrievals be improved by accounting for vegetation in an operationally applicable scheme for SMC retrieval over meadows?

Based on the microwave scattering theory that is described in Section 1.3.1.1, it is expected that correcting Sentinel-1 σ^0 observations for vegetation effects contributes to more accurate SMC retrievals. However, deficiencies in the vegetation scattering model, its parameterisation, and uncertainty in the input variables influence the accuracy. A field-scale leaf area index (LAI) product, derived from Sentinel-2 optical imagery, is used as input to a physically based vegetation and surface σ^0 model that is parameterised for grass-covered soil surfaces. First, the Sentinel-2 LAI estimates were validated at field scale against in situ LAI measurements

collected on six study fields. Then, the operationally applicable retrieval scheme is demonstrated with and without applying the vegetation correction, by retrieving the SMC for 21 meadows and validating them against the measurements from adjacent in situ monitoring stations.

1.7 Thesis outline

Figure 1.6 schematizes the different parts of this thesis. Chapter 2 and 3 each describe a SMC monitoring network, the regions they were imbedded in, and SMC sensor attributes. Chapter 4 quantifies the uncertainty of SMC monitoring station measurements as a reference for the field-scale SMC which can be observed by Sentinel-1. Chapter 5 focuses on Sentinel-1, and presents masking rules for weather-related surface conditions and the radiometric uncertainty of its observations. Chapter 6 decomposes the uncertainty of SMC retrievals over sparsely vegetated fields, with a specific focus on the uncertainty of the soil surface roughness, and applies the quantifications of the references' uncertainty and the radiometric uncertainty from Chapters 2–5. Chapter 7 presents an operationally applicable scheme for SMC retrieval over meadows and evaluates whether a vegetation correction improves the retrievals. Chapter 8 summarizes the answers to the research questions and presents recommendations for future research.

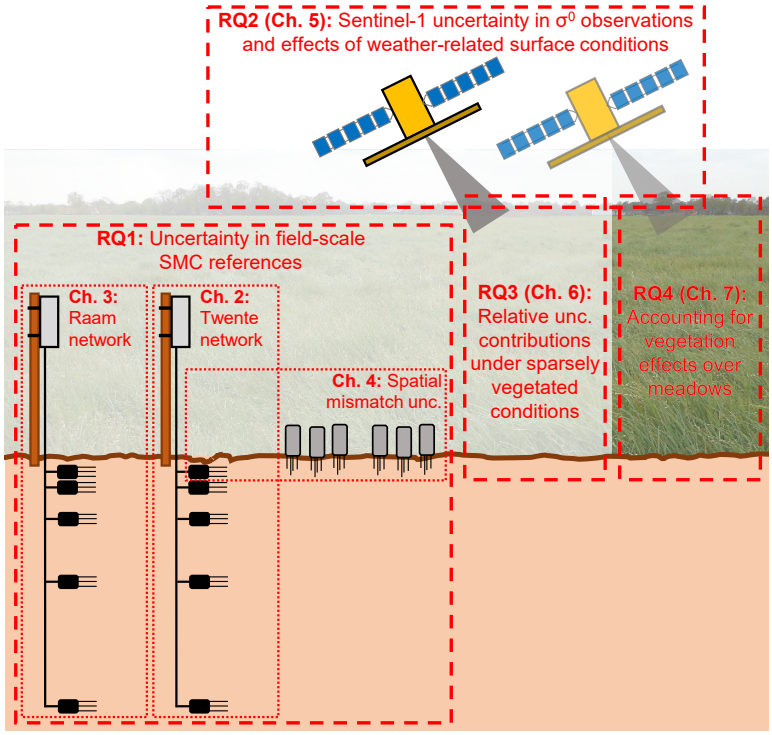

Figure 1.6 The structure of this thesis.

2

Twelve years profile soil moisture content and temperature measurements in Twente, the Netherlands

This chapter is based on:

Van der Velde, R. and Benninga, H. F.: Twelve years profile soil moisture and temperature measurements in Twente, the Netherlands, in preparation.

Abstract

Spread across the Twente region and neighbouring regions in the east of the Netherlands, a network of 20 profile soil moisture content (SMC) and temperature monitoring stations has been operational since 2009. In addition, field campaigns have been conducted covering the growing seasons of 2009, 2015, 2016 and 2017 during which soil sampling rings and handheld probes were used to measure the SMC of in total 28 fields near 12 different monitoring stations. In this chapter, we describe the design of the monitoring network and the field campaigns, adopted instrumentation, experimental setup, field sampling strategies, and the development of sensor calibration functions. The maintenance and quality control procedures, known issues specific to the Twente network, and time series of profile SMC (5 cm, 10 cm, 20 cm, 40 cm and 80 cm) and groundwater level for three stations are discussed. Further, an overview is provided of open third-party datasets (i.e. land cover/use, soil information, elevation, groundwater and meteorological observations) that can support the use and analysis of the Twente SMC and soil temperature datasets beyond the scope of this contribution.

Keywords: Soil moisture content, monitoring network, long-term measurements, measurement accuracy

2.1 Introduction

In almost every hydrology textbook (e.g. Maidment, 1993; Dingman, 2015; Brutsaert, 2005) one can read that water in the unsaturated soil, hereafter soil moisture, is needed for plants to grow, for groundwater to recharge, and for determining whether rain infiltrates or runs off laterally and contributes to the production of streamflow. Moreover, the conversion of water into vapour via evapotranspiration at the expense of solar radiation links soil moisture to the atmosphere impacting weather and climate (Seneviratne et al., 2010). Since its foundation in 1992, the Global Climate Observing System (GCOS) acknowledges the crucial role soil moisture content (SMC) plays in the Earth's climate system, supports the development of long term global monitoring programmes (GCOS, 2004) and has recognized SMC as an essential climate variable (GCOS, 2010). Considerable developments have taken place in global SMC monitoring with the launch of dedicated microwave satellites, e.g. Soil Moisture and Ocean Salinity (SMOS; Mecklenburg et al., 2016), Soil Moisture Active Passive (SMAP; Entekhabi et al., 2010a) and long-term satellite based data products have become available (Gruber et al., 2019). In addition, an International Soil Moisture Network has been established that host in situ SMC measurements from across the globe (Dorigo et al., 2011, 2021).

The number of in situ SMC monitoring programmes, dating back to the 1930s, have been small and often relied on gravimetric soil sampling (Robock et al., 2000). Gravimetrically determined SMC measurements are, however, labour intensive and have become unfeasible for long-term monitoring as the cost of labour increased. Therefore, indirect estimation of the soil water content has been widely investigated (e.g. Vereecken et al., 2008), of which the devices that measure the soil's relative permittivity have become the more commonly used instruments to base regional-scale SMC monitoring networks on (e.g. Martínez-Fernández and Ceballos, 2005; Calvet et al., 2007; Su et al., 2011; Bircher et al., 2012; Smith et al., 2012; Benninga et al., 2018c; Bogena et al., 2018; Caldwell et al., 2019; Tetlock et al., 2019). Despite that technological advances have facilitated a substantial increase in the in situ SMC monitoring infrastructure, in situ monitoring networks providing long-term and consistent SMC data records are still very scarce across the globe (GCOS, 2016).

In this chapter, we report on in situ profile SMC and soil temperature datasets collected by a regional-scale monitoring network composed of 20 measurement locations that has been operational in the Twente region situated in the east of the Netherlands. Development of the Twente network began in the fall of 2008 and was completed by the summer of 2009, and has been operational ever since. Dente et al. (2011) described the early development, and the first scientific use of the data was the validation of SMOS SMC products (Dente et al., 2012). Other studies performed with the datasets have focused on field-scale SMC retrieval (Van der Velde et al., 2015; Benninga et al., 2020b), upscaling of

point measurements to coarse satellite footprints (Van der Velde et al., 2021), agricultural and hydrological applications (Carranza et al., 2018, 2019; Pezij et al., 2019b; Buitink et al., 2020) and the Twente network has been used as one of the core international validation sites for the SMAP surface SMC products (Colliander et al., 2017; Chan et al., 2018; Chaubell et al., 2020).

Over the years the design of the monitoring network has been impacted by gradual changes, which have not been reported in a consistent manner before. In this chapter we provide a complete description of how the network developed by including the calibrated measurements, the native data records, metadata on location and land cover, field photos and field notes. In addition to the measurements collected in an automated and continuous manner, the dataset discloses the SMC records characterized with handheld probes and through gravimetric soil sampling during field campaigns conducted in 2009, 2015, 2016 and 2017. Further, we describe open third-party datasets that can support the use of the SMC data, which include maps of land cover and use, maps of soil type, texture and physical properties, high resolution (0.5 m and 5.0 m) digital terrain models (DTM), groundwater level measurements, and meteorological observations.

2.2 Study area and open datasets

2.2.1 Regional characteristics and water governance

Twente is a region in the Netherlands, about 1500 km^2, directly bordering Germany towards the east and bound in the west by a glacial ridge known as the Sallandse Heuvelrug. The majority of the network is situated in Twente, other parts are located in the neighbouring regions Salland and Achterhoek with similar characteristics. Glacial ridges formed in the second last glaciation period (Saalien) define the landscape. They have maximum elevations of around 80 m a.s.l. and consist mostly of fluvial sand deposits with glacial boulder clay sheets. This geomorphological feature in combination with a temperate oceanic climate (*Cfb* Köppen-Geiger climate classification; Beck et al., 2018) facilitated the development of a drainage system composed of brooks and small unnavigable rivers flowing via larger rivers into the IJssel lake. Although deeper groundwater levels of 6 m up to 10 m below the surface can be found on the glacial ridges, they are generally shallow and fluctuate from within the top 1 m of soil layer during winters up to maximum depths of 2 m–3 m in summers.

In the Netherlands, Twente and surroundings are considered rural areas with a few mid-sized and small cities, and a number of villages, and are known for their characteristic bocage landscape with small agricultural fields (1.63 ha on average) separated by tree lines and bushes amidst gently rolling topography. The majority of the agriculture has

a focus on animal husbandry, whereby the available land is used to produce food for livestock via grass meadows and the growing of maize.

Three types of public institutions are mandated with the regional governance of water in the study area as described in the Water Act 2009 ('Waterwet' in Dutch) and the Regional Water Authorities Act 1991 ('Waterschapswet' in Dutch). They are provinces, regional water authorities (RWAs, 'waterschap' in Dutch) and municipalities. The provinces hold responsibility over the regional groundwater systems. The RWAs are accountable for the water quality and quantity in regional surface water systems, and the municipalities are charged with the urban rainwater collection and groundwater. Readers are referred to Havekes et al. (2017) for more details. Twente is part of the province Overijssel and falls under the RWA Vechtstromen. Figure 2.1 shows, however, that the network also covers the northern part of the province Gelderland, and extends towards the west to RWA Drents Overijsselse Delta and towards the south to RWA Rijn and IJssel.

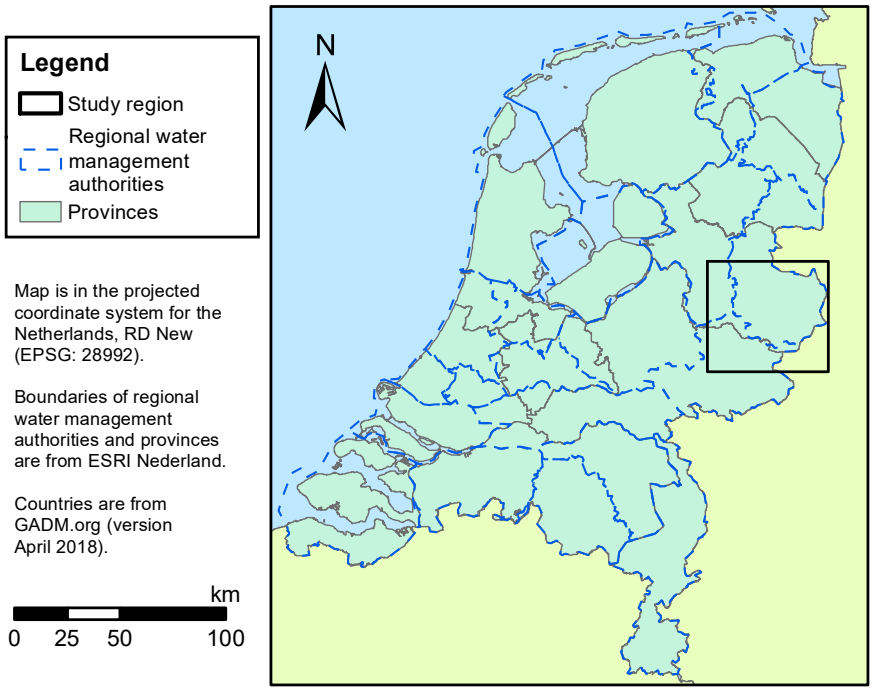

Figure 2.1 Coverage of the monitoring network (study area) within the Netherlands and the boundaries of the RWAs and provinces.

A large number of basic datasets are freely available for the Netherlands through various initiatives. In the following sections, we describe datasets on topography, soil, groundwater, land cover and weather that can support the use of the Twente SMC and soil temperature dataset. Section 2.6 lists where these datasets can be accessed.

2.2.2 Topography, soils and groundwater

Detailed spatial elevation data is available from the AHN ('Actueel Hoogtebestand Nederland' in Dutch). AHN (2019) supplies accurate (maximum 0.05 m deviation for systematic errors and 0.05 m standard deviation for random errors) and high-resolution DTMs obtained via airborne laser altimetry. In 2019, the third version (AHN3) has been completed and made available with spatial resolutions of 0.5 m and 5.0 m. The DTM for the area covered by the monitoring stations is shown in Figure 2.2 along with the various locations of the monitoring stations throughout the observation period.

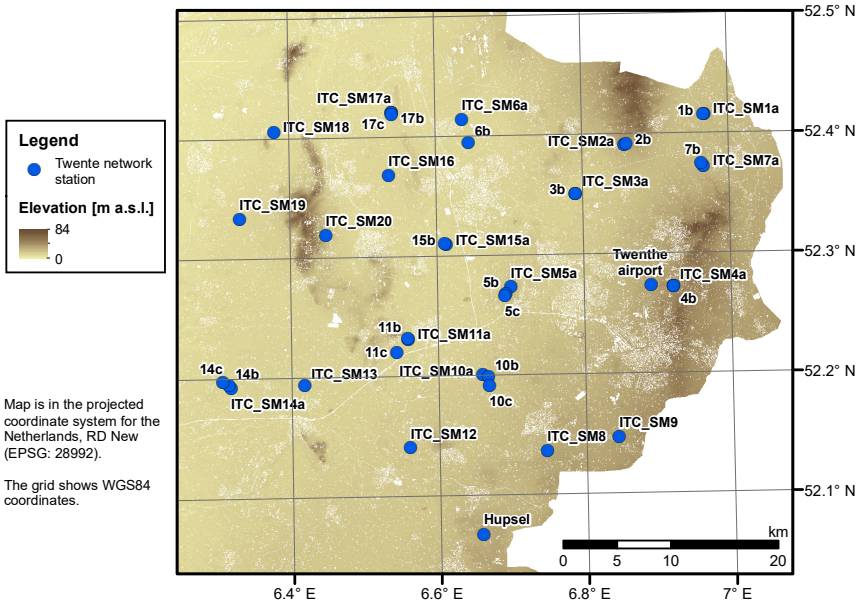

Figure 2.2 The topography of the study area (source: 5 m spatial resolution AHN3; AHN, 2019) and the locations of the Twente SMC and soil temperature monitoring stations, whereby the number refers to the station ID and the letter to the specific location within the entire observation period.

Soil information up to a depth of 1.2 m can be obtained from the soil physical units map of the Netherlands named BOFEK ('bodemfysische eenhedenkaart' in Dutch). BOFEK combines the soil map of the Netherlands with the Dutch class pedotransfer function (Heinen et al., 2021). A subset of the soil map for the study area is shown in Figure 2.3.

The Netherlands have a comprehensive network of groundwater monitoring wells supported by various public organisations all contributing to a central database that is disseminated via DINOloket (Data and Information on the Dutch Subsurface, or 'Data en Informatie van de Nederlandse Ondergrond' in Dutch). The database is managed by the Geological Survey of the Netherlands ('Geologische Dienst Nederland' in Dutch, or GDN; GDN, 2021). Not all monitoring wells in the database

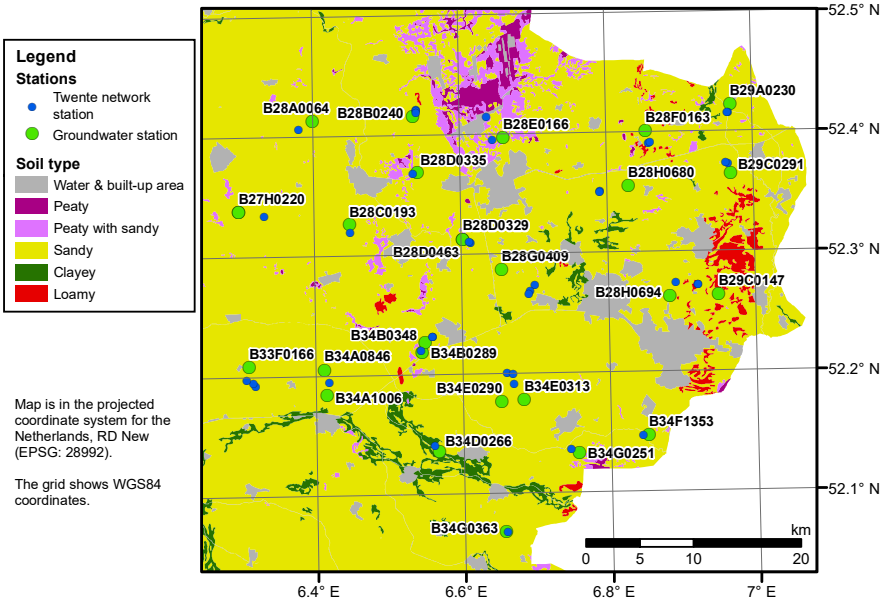

Figure 2.3 The major soil types of the study area (source: BOFEK2020; Heinen et al., 2021) and the groundwater monitoring wells near the Twente monitoring stations (source: DINOloket; GDN, 2021).

have records that cover the observation period of the Twente network. We have, therefore, selected wells nearest to our monitoring stations with matching data coverage and shown them as points in Figure 2.3. The well ID, coordinates, and distance to the associated SMC stations are listed in Supplement Table S1 (see Chapter 9).

The DTM of Figure 2.2 shows that the study area has little relief sloping gently from about 5 m a.s.l. in the west to 30 m a.s.l. in the east, with some glacial ridges up to 80 m a.s.l. The soil map in Figure 2.3 shows that sand is the major soil type in the region. On the eastern glacial ridge also wind-blown loamy deposits can be found near the surface. Organic and peaty soils are present in the parts where water naturally stagnates, which has been the case for a major area in the north and along streams where also clayey soils exist.

2.2.3 Land cover

Land use information is publicly available from Statistics Netherlands ('Centraal Bureau voor de Statistiek' in Dutch, or CBS; Statistics Netherlands, 2015) and from the Ministry of Economic Affairs and Climate Policy (2020). Statistics Netherlands provides the main land use classes based on an interpretation of a 1:10 000 topographic map of the Netherlands and is published every two to four years since 1989. The Ministry of Economic Affairs and Climate Policy is responsible for the crop parcel registry ('Basisregistratie Gewaspercelen' in Dutch). Since 2009, every

land owner in the Netherlands has to report each year the crop on each parcel in their possession.

Figure 2.4 shows the 2015 land use file from Statistics Netherlands (2015) for the study area, from which can be deduced that 70.2% of the land is used for agricultural activities, 13% is woodland, 11.3% is built-up and the remaining 5.5% is classified as water, recreational, dry and wet nature. The map illustrates that the larger forested areas are mainly found on the elevated glacial ridges and the agricultural activities take mostly place on the post-glacial soils covering the glacial pelvis. From the crop parcel registry in 2015 (Ministry of Economic Affairs and Climate Policy, 2020), we can find that the agricultural land is covered for 70.8% by grass meadows, 22.4% by maize and the remaining 6.8% is used for potato, cereals, other crops and forest and heath. The grass growing season is generally from March till November during which the meadows are either being grazed by cattle or cut four to six times per year (Benninga et al., submitted, in Chapter 7). Maize is planted approximately in the month May and harvested in October depending on the trafficability and growing conditions.

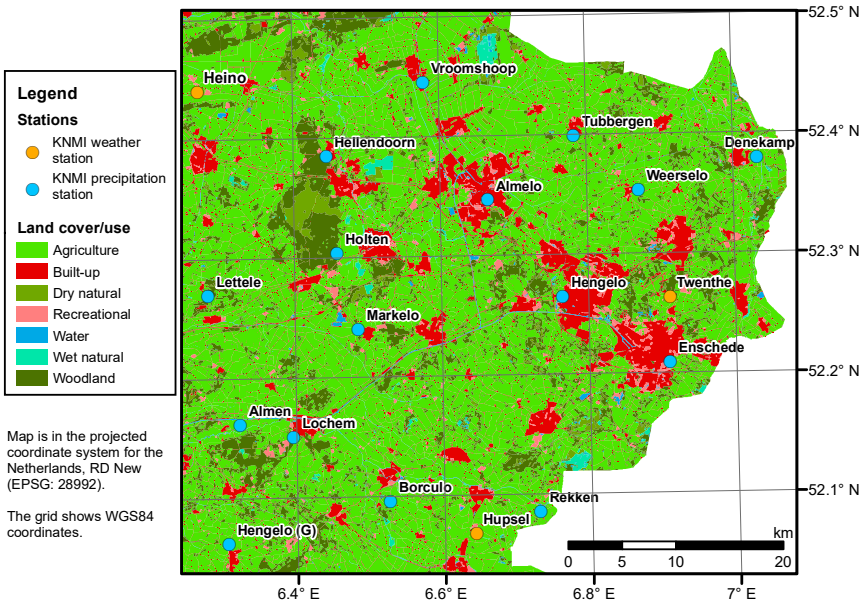

Figure 2.4 The major land use types and the meteorological measurement stations in the study area. Source of the land cover is the land use file 2015 (Statistics Netherlands, 2015).

2.2.4 Climate and weather

In Figure 2.4 the locations of the 3 automated weather and 29 precipitation stations operated by the Royal Netherlands Meteorological Institute ('Koninklijk Nederlands Meteorologisch Instituut' in Dutch, or KNMI;

KNMI, 2021) in the study area are shown. The precipitation stations are part of a network of more than 300 voluntary observers in the Netherlands. The observers record manually with a 0.1 mm resolution the rainfall collected with a World Meteorological Organization (WMO) standard gauge around 9:00 CET in the morning and measure the snow depth with ruler when applicable. The data sent to the KNMI are validated in 10 day blocks and made available as daily. The three automated weather stations are situated near the villages Heino and Hupsel, and at Twenthe airport nearby Enschede. They measure wind speed and direction, air temperature at 1.5 m and 0.1 m above ground, sunshine duration, shortwave incoming radiation, precipitation, air pressure, humidity, and cloud cover. The adopted instrumentation and measurement protocols are according to international standards, and the quality-controlled data are available as hourly and daily values. The daily set also holds the reference crop evapotranspiration (E_{ref}) calculated through application of the modified Makkink method described in De Bruin (1987).

Figure 2.5 shows for the period 2008–2020 the monthly average of daily mean 1.5 m air temperature as well as monthly precipitation and E_{ref} sums, derived as mean values for the three automated weather stations. The data in this figure confirms that the SMC monitoring network is located in a temperate oceanic climate zone (*Cfb*). The coldest and warmest months have been January and July with mean monthly temperatures of 2.9 °C and 18.3 °C, respectively. Precipitation has been evenly distributed throughout the year according to the Köppen-Geiger classification, even though a difference of 53.3 mm exists in precipitation sums between the driest (April, 33.5 mm) and wettest (August, 86.8 mm) month.

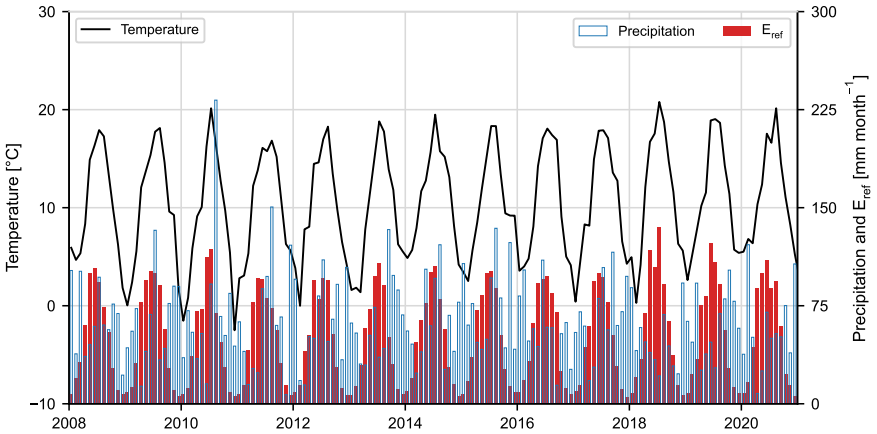

Figure 2.5 Monthly mean 1.5 m air temperature, and monthly precipitation and E_{ref} sums derived from the measurements collected at KNMI automated weather stations Heino, Hupsel and Twenthe.

Between 2008 and 2020, the annual precipitation and E_{ref} sums available for the three weather stations are 757.1 mm and 611.3 mm, respect-

ively, resulting in an annual precipitation surplus of 145.8 mm. In the years 2018, 2019 and 2020 north-western Europe has been struck by droughts (e.g. Buitink et al., 2020; Bakke et al., 2020; Buras et al., 2020) with less than normal precipitation volumes and higher evaporative demands. The most extreme precipitation day occurred on 26 August 2010, with 49.6 mm, 142.3 mm and 106.4 mm collected at KNMI stations Heino, Hupsel and Twenthe. The second and third heaviest precipitation days took place on 10 September 2013 with 22.3 mm, 74.5 mm and 57.8 mm and 3 August 2011 with 55.6 mm, 24.9 mm and 20.6 mm at Heino, Hupsel and Twenthe stations, respectively, while on all the other days less than 50 mm was recorded.

2.3 Monitoring network

2.3.1 Sites

The development of the SMC and soil temperature monitoring network started in November 2008 and was completed in November 2009, but 19 out of the 20 stations were installed already before July 2009. The prime objective for the development of the measurement infrastructure was to serve as reference for the validation and calibration of coarse resolution SMC products derived from active and passive microwave satellite observations (Dente et al., 2011). The measurement sites are spread over approximately a 45 km $\times$ 40 km area and the individual stations are typically 5 km to 13 km apart, see also Figure 2.2.

In the site selection, care was taken to evenly distribute across the land covers and soil types. The majority of stations are found on sandy soils, two stations have been installed in sandy soils with a higher organic matter content, one in a loamy soil and one in a clayey soil according to the BOFEK soil map. The land on which the monitoring took place is in all cases privately owned and actively used for farming. The instrumentation is, therefore, typically placed at the border of fields and preferably several tens of metres away from disturbing features (i.e. trees, roads or watercourses), as shown in Figure 2.6, to minimize nuisance for recurring farming practices and optimize its representativeness for the adjacent fields.

Since the completion of its development, the monitoring network has been constantly subject to modifications, such as land cover changes as a result of crop rotation, and re-installations due to changes in land ownership or equipment failures. Table 2.1 lists for each station the main soil type as indicated in the soil map, the land cover per year of the adjacent fields and the maintenance operations carried out.

2.3.2 Instrumentation and measurement setup

The Twente SMC and soil temperature monitoring network is built around instrumentation manufactured by METER Group (formerly: Decagon

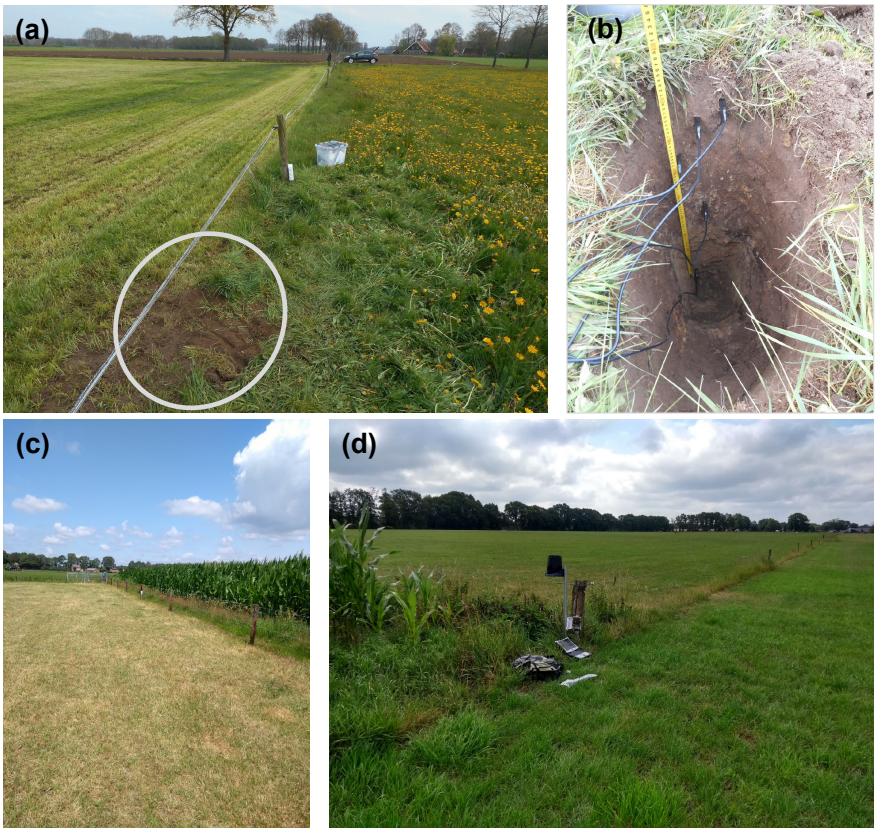

Figure 2.6 Photos taken of (**a** and **b**) the reinstallation of a SMC and soil temperature monitoring station (ITC_SM03) on 2 May 2017, **(c)** ITC_SM18 on 17 July 2019 and **(d)** ITC_SM02 on 17 July 2019.

Devices). The standard and remote versions of Em50 data logger series have been deployed to perform measurements every minute with ECH_2O EC-TM and 5TM probes, and were set to record readings at 15 min intervals. Equipment of METER Group devices has previously been used for the development of many monitoring networks, such as HOBE in Denmark (Bircher et al., 2012), TERENO in Germany (Bogena et al., 2018) and the Raam in the Netherlands (Benninga et al., 2018c, in Chapter 3), and been evaluated in several intercomparison studies (e.g. Jackisch et al., 2020; Vaz et al., 2013; Robinson et al., 2008).

The ECH_2O TM probes have a total length of 10.9 cm, a width of 3.4 cm and consist of a coated circuit board with an oscillator that applies a 70 MHz electromagnetic wave to three 5 cm long fiberglass enclosed prongs. The prongs are 5 mm wide and 1 mm thick and are placed 5 mm apart. A thermistor near one of the prongs measures the temperature with an expected ± 1 °C accuracy and 0.1 °C resolution. Probes estimate the volumetric SMC by characterizing the apparent relative permittivity

Table 2.1 Soil, land use and maintenance characteristics of the stations. The soil descriptions are from BOFEK2020 (Heinen et al., 2021). The land uses for 2009–2020 apply to adjacent fields and are from the crop parcel registry (Ministry of Economic Affairs and Climate Policy, 2020). Table classification: green stands for grass, orange stands for maize, red stands for potato, yellow stands for cereal, purple stands for other crops, brown stands for forest. Relocations of stations are noted by letters, which correspond to the locations in Figure 2.2. Other maintenance practices are noted by asterisks and are specified in Supplement Table S2 (see Chapter 9).

Station	Soil type class	Soil description translated from Dutch (BOFEK2020 classification code)	2009	2010	2011	2012	2013	2014	2015	2016	2017	2018	2019	2020
01	Sandy	Highly loamy sandy soil with clay cover (3002)	a					*	b					
02	Sandy	Highly loamy soil with man-made thick earth (3005)	a				b		*	*	* *			
03	Sandy	Highly loamy sand with clay cover (3002)	a					*			b			
04	Loamy	Tertiary clay (5003)	a							b*			*	
05	Sandy	Highly loamy soil with man-made thick earth (3005)	a							*	b	c		
06	Partly organic	Sandy cover on partly organic soil (2001)	a			*	*		*	b				
07	Sandy	Highly loamy sand with clay cover (3002)	a					*	b					
08	Sandy	Weakly loamy sand (3015)	*							*				
09	Sandy	Weakly loamy soil with man-made thick earth (3012)					* *		*			*		
10	Sandy	a & b: Highly loamy sand (3004) c: Highly loamy sand (3021)	a				*	b		c*				

Station	Soil type class	Soil description translated from Dutch (BOFEK2020 classification code)	2009	2010	2011	2012	2013	2014	2015	2016	2017	2018	2019	2020
11	Sandy	a & b: Weakly loamy soil with man-made thick earth (3012) c: Highly loamy sand (3004)	a			*			b*	* c				
12	Clayey	Clay on sand (4022)					*		*	*				
13	Sandy	Weakly loamy sand (3015)						*		*	*			
14	Sandy	Highly loamy sand (3021)	a	*	b		*	*		c	*			
15	Sandy	Highly loamy sand with clay cover (3002)	a							b*			*	
16	Partly organic	Sandy cover on partly organic soil (2001)			*	*		*			*	*		
17	Sandy	Weakly loamy sand (3015)	a		b				*	c				
18	Sandy	Highly loamy sand (3021)						*	*					*
19	Sandy	Highly loamy sand (3004)						*						
20	Sandy	Coarse sandy sand (3003)						*						
Hupsel	Sandy	Highly loamy sand (3004)												
Twenthe airport	Sandy	Weakly loamy sand (3014)										*	*	

via measurements of the capacitance, quantified as the charge needed to polarise the dielectric (soil) surrounding the prongs (Decagon Devices, 2008; METER Group, 2019). Benninga et al. (2018c, in Chapter 3) found under laboratory circumstances that the influence zone of a 5TM probe in a sandy soil is around 3 cm–4 cm.

Figure 2.6 illustrates typical measurement setups used for the Twente network with probes installed at nominal depths of 5 cm, 10 cm, 20 cm, 40 cm and 80 cm. However, due to budget constraints several stations are limited to the upper two, three or four measurements depths. At sites with a permanent grass cover, excavation of the installation pit started with cutting the grass sod of an area of approximately 40 cm by 40 cm after which the top 10 cm to 15 cm (soil layer including grass) was carefully removed and the pit was dug further until the required depth. The probes were installed in a lateral direction with the narrow side of the prongs pointing upward to avoid water ponding on the prongs, and with the printed text on the prongs in the upright direction to ensure consistency in the depth of the thermistor. After installation the pit was back filled while compacting the soil several times during the filling process, the grass sod was placed back and a trench was dug to guide the cables to a pole on which the Em50 logger was mounted. The excess cables were buried near the pole. Typically a few months after installation the plot would have returned to its original land cover. A similar installation procedure was adopted for cultivated land.

2.3.3 Capacitance probe calibration

Estimation of the SMC using the capacitance technique relies on the contrast between the relative permittivities (ε_r) of air (1), soil (2–7) and water (80). Soil-specific calibrations are needed for two main reasons: (i) to account for losses (imaginary component of ε_r) due to the molecular relaxation and electric conductivity that alter the ε_r as it appears to a capacitance sensor (Robinson et al., 2008) and (ii) the soil-dependent dielectric response to SMC. Hence, soil-specific calibration functions have been developed for both EC-TM and 5TM probes in the laboratory following the guidelines recommended by the manufacturer (Cobos and Chambers, 2010). With this approach we assume that the sensor-to-sensor variability is accounted for by the in house calibration performed at the manufacturer against reference. This can be justified based on the small variability (0.01 $m^3\,m^{-3}$) among sensors evaluated by Kizito et al. (2008) and Rosenbaum et al. (2010).

In Dente et al. (2011) the development of the calibration function for the EC-TM probe is described. They performed the calibration on soil collected from 10 sites and could identify 3 relations, but at the same time could not attribute this to a specific soil feature. Therefore, the recommendation was to use a generalized calibration function, expressed by

$$\theta_{cp} = a + b\theta_p, \tag{2.1}$$

where θ stands for the SMC ($m^3\,m^{-3}$), a and b are the intercept ($m^3\,m^{-3}$) and slope (−) of the linear regression function, and subscripts p and cp indicate the native probe reading and calibrated probe value. The native probe reading is a direct sensor output obtained by applying the mineral soil calibration to the raw signal (Decagon Devices, 2008). Dente et al. (2011) report an a of $0.0706\,m^3\,m^{-3}$ and b of 0.7751, yielding a root mean square deviation ($RMSD$, Equation A.1) of $0.023\,m^3\,m^{-3}$.

The calibration for the 5TM probe was performed in 2015 for soil taken from three sites each belonging to one of three groups earlier identified in Dente et al. (2011). The selected sites are ITC_SM03, ITC_SM07 and ITC_SM08. Similar as for the calibration of the EC-TM probe, soil was taken from the field in an ordinary 12 L bucket and was air-dried. The air-dried soil was gradually wetted by adding 50 mL–75 mL water at a time and after careful mixing a 5TM reading and $100\,cm^3$ soil sample was taken. The soil sample was used to determine the SMC from the difference in wet weight and dry weight of the sample after 24 h in the oven at 105 °C, which is referred to as gravimetrically determined volumetric SMC (GVSMC). The entire process was done twice and resulted in 38 match-ups for ITC_SM03, 32 for ITC_SM07 and 29 for ITC_SM08.

Figure 2.7a shows the GVSMC against the 5TM SMC. Linear equations of the same form as Equation 2.1 were fitted through the match-ups for each soil individually and all together. Because of the small sample size, the linear fits have been carried out for each combination of entire collections minus one ($N-1$). The match-up left out of the regression is then used for validation and the calculation of the performance metrics.

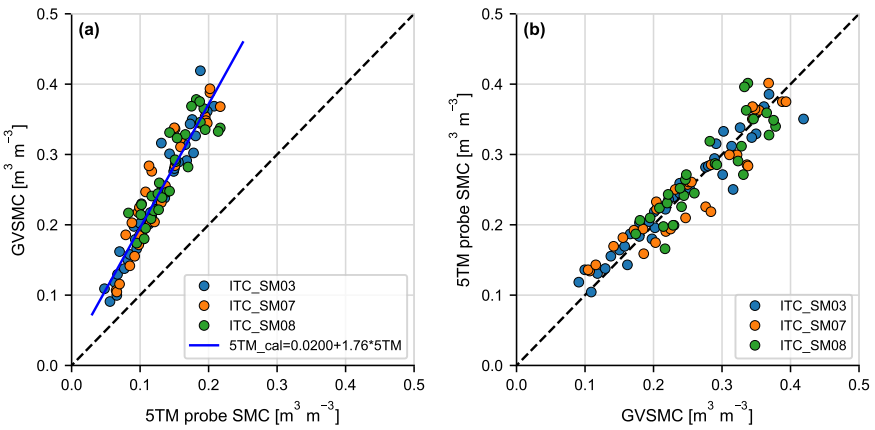

Figure 2.7 **(a)** Measurements of GVSMC against 5TM SMC on soil collected at sites ITC_SM03, ITC_SM07 and ITC_SM08, and **(b)** 5TM SMC with application of the 'all soils' calibration function against GVSMC measurements.

Table 2.2 lists the linear regression coefficients (a and b) obtained for the four sets of match-ups along with the standard deviation (σ) computed from the collection of regression coefficients for each individual set. The $RMSD$ and bias (Equation A.4) calculated from the match-ups

left for validation and the coefficient of determination (R^2) obtained with the mean regression coefficients are provided as well. The listed metrics demonstrate that the performance of the 5TM sensor is in line with that of the EC-TM given the negligible biases, $RMSD$s varying from $0.024\,m^3\,m^{-3}$ to $0.031\,m^3\,m^{-3}$ and R^2s in the 0.79–0.93 range. Even though the regression coefficients differ among the analysed soils, their point clouds in Figure 2.7a have quite some overlap, which does not justify using different calibration functions. This is further supported by the fact that the σ is only a fraction of the magnitude of the regression coefficients when including all match-ups. Notably, the obtained σs are 4.8% of the intercept and less than 0.5% of slope relative to the magnitude, while it goes up to a respective 44% and 2.4% when using data from a single site. This suggests that the reliability of the function fitted through all match-ups is higher. Therefore, we have chosen to apply the 'all soils' calibration function to every site of the Twente network, which is expected to provide an accuracy ($RMSD$) of $0.028\,m^3\,m^{-3}$. Figure 2.7b present the validation with the GVSMC plotted against the 5TM SMC using the 'all soils' mean regression coefficients.

Table 2.2 Mean (μ) regression coefficients and their standard deviations (σ) fitted through pairs of GVSMC and 5TM SMC measured in the laboratory on soil collected at sites ITC_SM03, ITC_SM07 and ITC_SM08. Performance metrics — $RMSD$, bias and R^2 — follow from the validation. N stands for the number of GVSMC-5TM SMC pairs.

Set	N	a [$m^3\,m^{-3}$]		b [−]		$RMSD$	Bias	R^2
		μ	σ	μ	σ	[$m^3\,m^{-3}$]	[$m^3\,m^{-3}$]	[−]
ITC_SM03	38	0.00423	0.00186	1.87	0.0165	0.0237	0.000	0.927
ITC_SM07	32	0.0214	0.00307	1.77	0.0208	0.0303	0.000	0.883
ITC_SM08	29	0.0546	0.00510	1.52	0.0369	0.0315	0.000	0.786
All soils	99	0.0200	0.000958	1.76	0.00737	0.0277	0.000	0.884

2.4 Field campaigns

Field campaigns were conducted in 2009, 2015, 2016 and 2017, during which SMC was measured in fields with handheld impedance probes and via soil samples taken for GVSMC determination. The sampling took place at a maximum of three fields owned by the same farmer adjacent to or near the monitoring station. This resulted in a total of 28 sampled fields near 12 monitoring stations.

The general concept of each field campaign was similar, yet the execution differed annually. For instance, sampling days in 2009 and 2015 took place weekly from the end of summer in September until the beginning of November. In 2016 and 2017, the sampling days were held weekly or biweekly depending on weather and staff availability, and covered the entire growing season from April/May till the end of fall in November (Benninga et al., 2020b, in Chapter 4). An overview of the

field campaigns is provided in Table 2.3, which includes the time period, the number of sampling days and the sampled stations. The following sections describe the sampling strategy, the instrumentation and the calibration of the probe readings.

Table 2.3 Overview of the SMC field campaigns conducted at fields adjacent to monitoring stations. In the far right column, the number in parenthesis stands for the number of sampled fields and the letter represents the land cover at the start of the campaign (g = grassland, m = maize, f = forest, fw = fallow winter wheat, w = winter wheat, p = potato).

Year	Period	Days	Probe	Stations (fields)
2009	22 Sept–28 Oct	5	ThetaProbe	ITC_SM03 (1g), 05 (2g/1m), 07 (3m), 08 (1g/1m/1f), 11 (2g/1f), 12 (3g), 17 (3g), 18 (3g)
2015	11 Sept–3 Nov	11	ThetaProbe	ITC_SM03 (1g), 04 (2g), 05 (3g), 07 (3m), 08 (1m/1g), 09 (fw2)
2016	25 May–11 Nov	15	HydraProbe & ThetaProbe	ITC_SM02 (1g/1m), 07 (2m), 10 (1m/1p)
2017/2018*	7 April–16 Nov	14	HydraProbe	ITC_SM02 (1g/1m), 03 (1g), 07 (2m), 10 (2m)

* In 2018 a limited number of fields were sampled on 2 February and 10 April.

2.4.1 Sampling strategy

The sampling strategy during campaigns aimed at characterizing the top 5 cm SMC of fields. Three to six locations within a field, about 50 m to 100 m apart, were selected to perform the measurements, depending on the size of parcels. As an example, Figure 2.8 shows the scheme applied for the fieldwork carried out in 2016 and 2017 around ITC_SM02.

Figure 2.9 illustrates the sampling strategy at sampling points. The number of handheld impedance probe readings per sampling point varied from nine in the 2009 field campaign to five readings in 2015 and four in 2016/2017. At grass-covered fields, SMC was measured with the impedance probe at four to nine points within a 1 m^2 plot and next to one of the probe readings a soil sample was taken for GVSMC determination. In maize fields, probe readings were taken along the transect perpendicular to the crop rows, approximately 0.75 m apart, with the soil sample taken in the centre of two rows. The collection of soil samples for GVSMC determination was done to calibrate the probe readings and stopped when the covered dynamic range and number of match-ups were suitable to establish a calibration function. We have noted in the provided data sheet which probe reading corresponds to the GVSMC.

2.4.2 ThetaProbe and HydraProbe

The Delta-T ThetaProbe (Type ML2; Delta-T Devices, 1998) and Stevens HydraProbe (analog version; Stevens Water Monitoring Systems, 2020) are the two handheld probes that were used for rapid SMC data collection

Figure 2.8 Example (site: ITC_SM02) of the sampling strategy followed for the fields adjacent to permanent monitoring locations during field campaigns. Background is a 2 m resolution SuperView true colour composite of 25 April 2019 made available by Netherlands Space Office satellietdataportaal. Map is in the RD New (EPSG: 28992) projected coordinate system.

during the field campaigns. Both instruments exploit the impedance mismatch between a coaxial transmission and a stainless steel pin inserted in the soil that acts as a waveguide and is electrically shielded by three other similar pins (60 mm and 57 mm in length, respectively) placed in an equilateral triangle with sides of 26.5 mm and 22 mm, respectively (Seyfried and Murdock, 2004). The ThetaProbe measures the amplitude difference of a standing sinusoidal wave between the start of a transmission line and the junction where the pins enter the soil as a result of the applied 100 MHz signal. The amplitude difference is used to determine the impedance from which the apparent relative permittivity is derived (Gaskin and Miller, 1996). The HydraProbe measures the complex ratio of the reflected and incident voltage of an applied 50 MHz signal to characterize the impedance of the soil used to determine the complex relative permittivity (Campbell, 1990; Kraft, 1987). Both the ThetaProbe and HydraProbe data loggers have built-in software to convert the voltage output to a SMC. In addition to SMC, the HydraProbe also provides bulk electric conductivity and temperature. Because the relation between ε_r and SMC is affected by the soil type, calibration of impedance probe measurements is generally needed. In case of the ThetaProbe, the calibration accounts also for conductive and molecular losses, which is less of an issue with the HydraProbe as it measures the real and imaginary components of the relative permittivity.

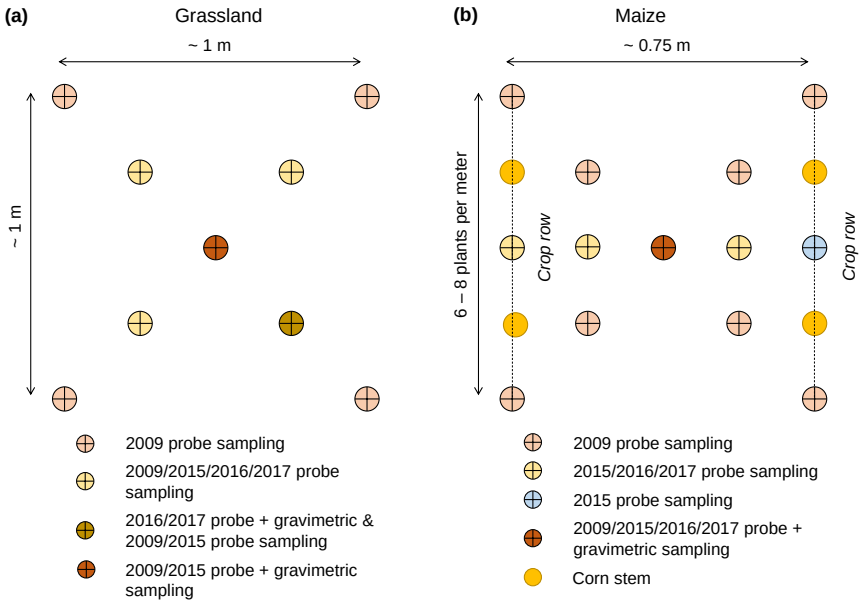

Figure 2.9 Schematisation of the impedance probe and GVSMC sampling strategy carried out at sampling points during the 2009, 2015, 2016 and 2017 field campaigns on grassland **(a)** and maize fields **(b)**.

2.4.3 Impedance probe calibration

The measurements of the 2009 and 2015 field campaigns were collected with the ThetaProbe, during which a total of 93 and 166 match-ups with GVSMC were collected at fields near eight and six different stations, respectively. Figure 2.10 presents plots of GVSMC against the ThetaProbe SMC, with in the upper panels (Figures 2.10a and 2.10b) the 2009 data and in the lower panels (Figures 2.10c and 2.10d) the 2015 data. The GVSMC against the matching ThetaProbe reading is shown in Figures 2.10a and 2.10c, and the GVSMC against the mean of the readings at a sampling point is shown in Figures 2.10b and 2.10d.

In general, it can be noted that all plots show positive relations and that the scatter among the data points is clearly less in 2015 in comparison to 2009. This is particularly the case for the matching ThetaProbe readings. Explanation for this difference in performance between the years is a combination of the larger number of stations sampled in 2009, the lower number of match-ups available for 2009, and also the operator's skills could have played a role. Regardless of the scatter noted in the data points of 2009, it is difficult to identify distinct relations for individual stations. Among the 2015 data points clusters belonging to a single station are observed, but this is primarily due to the persistent SMC levels at specific stations. The attribution of a GVSMC-ThetaProbe relation to a specific soil type or station remains unclear. Therefore, we have chosen to develop the calibration functions for the

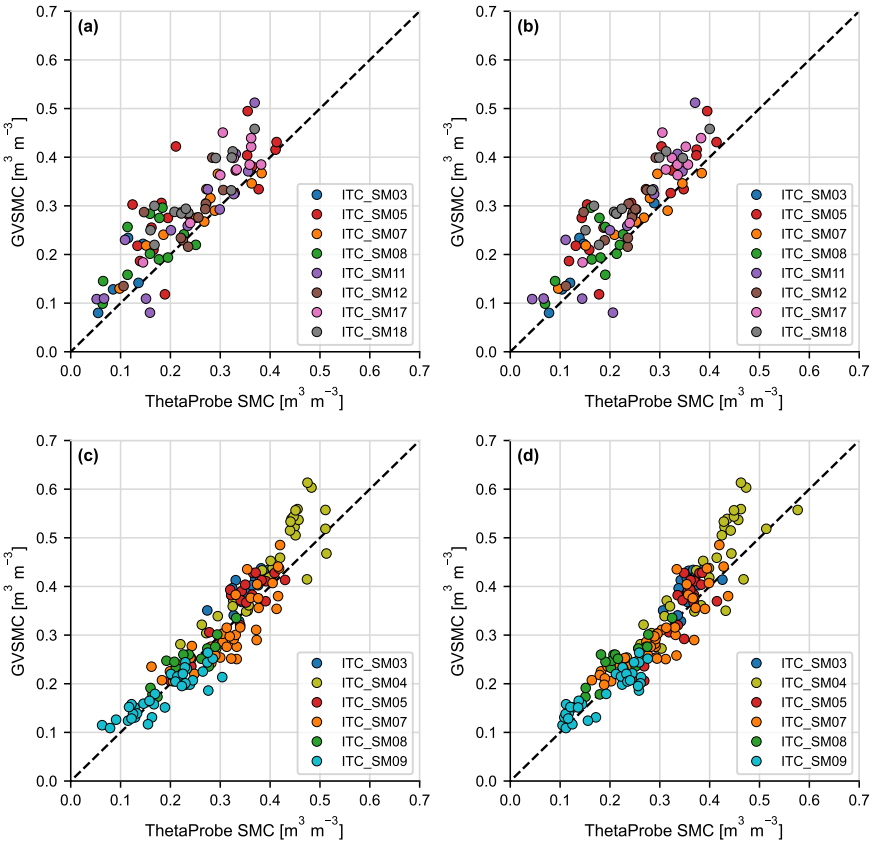

Figure 2.10 Scatter plots of the ThetaProbe SMC against GVSMC collected during the 2009 (**a** and **b**) and 2015 (**c** and **d**) field campaigns. (**a** and **c**) The ThetaProbe SMC reading taken next to a GVSMC measurement. (**b** and **d**) The mean of the ThetaProbe SMC readings taken at a sampling point.

ThetaProbe on a field campaign basis and not to make a distinction between individual stations. This also ensures a sufficient number of match-ups and a larger SMC range.

The data collection of the 2016 and 2017 field campaigns was performed with the HydraProbe and took place near three stations (ITC_SM02, ITC_SM07, and ITC_SM10) in 2016, to which ITC_SM03 was added in 2017. A total of 285 pairs of GVSMC and HydraProbe readings were acquired, with > 86 match-ups for each station at which the measurements started in 2016 and 12 match-ups for ITC_SM03. Figure 2.11 shows the GVSMC in (a) against the matching HydraProbe reading and in (b) against the mean of the four readings collected at a sampling location.

From a comparison of Figure 2.11 with Figure 2.10, it is evident that the agreement between the HydraProbe readings and GVSMC is equal or better than the results obtained for the 2009 and 2015 ThetaProbe data. Also noticeable in Figures 2.10–2.11 are the little differences among

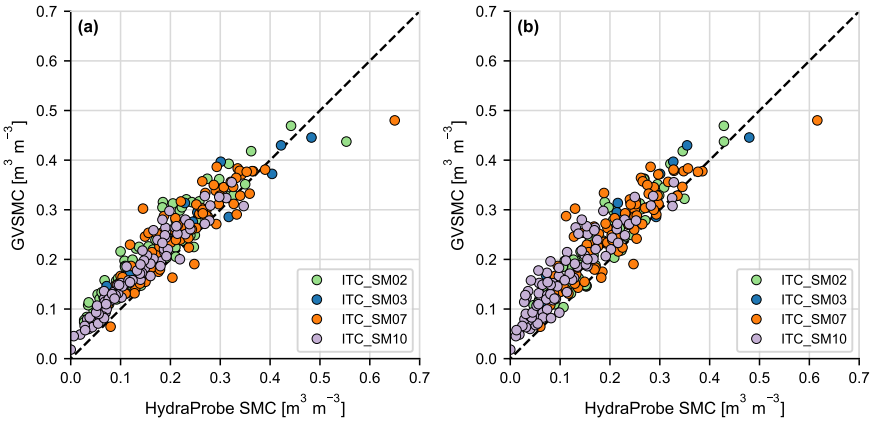

Figure 2.11 Scatter plots with the HydraProbe SMC against the GVSMC collected during the 2016 and 2017 field campaigns. **(a)** The HydraProbe SMC reading taken next to a soil sample. **(b)** The mean of the HydraProbe SMC readings taken at a sampling point.

the distributions of the data points belonging to individual stations, which again may question the added value of station-specific calibration functions. Because of the larger number of GVSMC-HydraProbe pairs (> 86) and larger SMC range for individual stations, we decided to develop for the HydraProbe measurements station-specific calibration functions. The users of the dataset have the choice to apply the calibration function that suits their application best.

The development of calibration functions for the ThetaProbe and HydraProbe measurements consists of fitting linear regression coefficients (a and b), following the same procedure as described in Section 2.3.3 for the 5TM measurements. Table 2.4 provides the μ and σ of the coefficients for the ThetaProbe functions along with performance metrics. Table 2.5 lists the same information for the HydraProbe and in Figure 2.12 the probe measurements calibrated with the field campaign-specific function are plotted against the GVSMC.

The performance metrics presented in Tables 2.4 and 2.5 show that the matching probe ('site') and GVSMC measurements generally led to better performance except for the 2009 field campaign, for which possible explanations have been given in the text above. Of the field campaign calibrations, the calibration developed for the HydraProbe (2016–2017) led to the best results in terms of $RMSD$ of $0.032\,\mathrm{m^3\,m^{-3}}$ versus $0.041\,\mathrm{m^3\,m^{-3}}$ for 2015 and $0.048\,\mathrm{m^3\,m^{-3}}$ for 2009. A very good match of the HydraProbe with the GVSMC is obtained for ITC_SM10 with a $RMSD$ of $0.022\,\mathrm{m^3\,m^{-3}}$. The explanation could be a combination of sandy soil and yearly cultivated land, which reduces disturbances due to soil clod and plant root, and is favourable for reliable soil sampling. Under more difficult circumstances, such as the loamier soil with clods at ITC_SM07, the metrics are closer to but still better than the ones obtained

Table 2.4 Mean (μ) and standard deviation (σ) of regression coefficients obtained for pairs of GVSMC and ThetaProbe SMC and associated performance metrics ($RMSD$, bias, R^2) for measurements taken during the 2009 and 2015 field campaigns. Two matching ThetaProbe values are used: (i) a reading next to the soil sample (in the table: site), (ii) the mean of all readings taken at the sampling point (in the table: mean). N stands for the number of GVSMC-ThetaProbe SMC pairs.

Set	N	Match-up	a [$m^3\,m^{-3}$]		b [−]		$RMSD$	Bias	R^2
			μ	σ	μ	σ	[$m^3\,m^{-3}$]	[$m^3\,m^{-3}$]	[−]
2009	93	site	0.0686	0.00139	0.920	0.00532	0.0522	−0.001	0.732
		mean	0.0498	0.00130	0.992	0.00484	0.0477	−0.001	0.780
2015	166	site	−0.0128	0.000735	1.09	0.00267	0.0411	0.000	0.875
		mean	−0.00899	0.000733	1.09	0.00277	0.0417	0.000	0.871

Table 2.5 Similar to Table 2.4, but for calibrations of 2016–2017 HydraProbe measurements. In this case, calibration functions were also developed for individual stations.

Set	N	Match-up	a [$m^3\,m^{-3}$]		b [−]		$RMSD$	Bias	R^2
			μ	σ	μ	σ	[$m^3\,m^{-3}$]	[$m^3\,m^{-3}$]	[−]
ITC_SM02	92	site	0.0738	0.000980	0.849	0.00670	0.0324	0.000	0.877
		mean	0.0550	0.000546	0.947	0.00352	0.0289	0.000	0.897
ITC_SM03	12	site	0.0875	0.00527	0.780	0.0196	0.0378	0.002	0.903
		mean	0.0923	0.00833	0.836	0.0405	0.0425	0.003	0.903
ITC_SM07	86	site	0.0797	0.00214	0.788	0.00988	0.0384	0.000	0.805
		mean	0.0865	0.00203	0.801	0.00956	0.0421	0.000	0.759
ITC_SM10	92	site	0.0420	0.000427	0.961	0.00388	0.0217	0.000	0.929
		mean	0.0621	0.000620	0.927	0.00453	0.0329	0.000	0.833
2016–2017*	285	site	0.0637	0.000319	0.860	0.00196	0.0323	0.000	0.881
		mean	0.0669	0.000311	0.890	0.00187	0.0351	0.000	0.858

* Three pairs collected on fields adjacent to ITC_SM05 were included in the regional calibration (2016–2017).

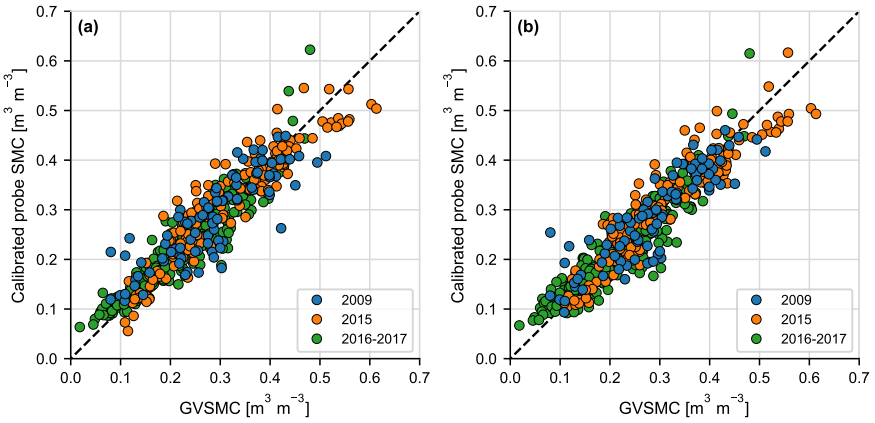

Figure 2.12 Probe SMC with application of field campaign-specific calibration functions plotted against GVSMC. **(a)** The calibrated probe SMC derived from the reading taken next a soil sample. **(b)** The calibrated probe SMC derived from the mean of the readings taken at a sampling point.

for the 2009 and 2015 field campaigns conducted with the ThetaProbe.

2.5 Data assessment

2.5.1 Maintenance and quality control

The monitoring stations were visited for maintenance operations and retrieving the recorded data twice a year from the inception of the network till 2011. This reduced to yearly visits up to 2014 and returned back to visits at least twice a year from 2015 till now. Visits are planned at the start (April/May) and at the end (October/November) of the growing season. The standard Em50 loggers are not connected to a telecommunication network and recorded data is retrieved on-site. The internal memory of the Em50 loggers is sufficient for 12.8 months of operations in the default setup with five probes recording every 15 min, before the oldest data starts to be overwritten.

Each site visit included the following standard activities: (i) retrieving the recorded data, (ii) making a preliminary check of the data quality, (iii) taking photographs of the measurement setup and its surroundings, (iv) replacing silica gel bags as desiccant (in recent years) and (v) taking notes of the undertaken maintenance operations and any specifics related to either the data quality or the measurement setup. Other typical maintenance operations consist of replacing batteries, sensors and loggers, reconnecting probes, remounting loggers, and drying and cleaning loggers. The notes, photographs and retrieved recordings are included in the published dataset.

Even though the memory of the Em50 would allow for yearly field visit, we deem a visit to each station every six months necessary to perform small maintenance, to regularly document the local conditions and to

assure continuity of operations. For instance, measurement setups may become compromised by grazing animals or through accidents during farming practices. In other situations, the stations needed to be moved because of changes in land ownership or land use, but also instruments may fail. Empty batteries, malfunctioning loggers and disconnected probes result in data gaps, but are generally of no concern for the data consistency. On the other hand, replacements of sensors or of the location of a station may cause inconsistencies in the time series and a complete overview of such interventions is given in Table 2.1 and detailed in Supplement Table S2.

Over the course of operations, errors can enter in the data series due to human failure, and malfunctioning loggers and probes. Human failure may include, for example, incorrectly reconnecting probes, applying incorrect calibration coefficients, or mistakes in the combination of raw data files. Malfunctioning loggers and probes may cause erroneous recordings. We have performed five automated checks on the consistency of the SMC and soil temperature time series (in processed files organized per station and per year), namely: (i) the first and last line of a data file should be 1 January 00:00 and 31 December 23:45, (ii) the occurrence of duplicate time stamps, (iii) the SMC and soil temperature recorded on 31 December 23:45 of year X and of 1 January 00:00 of year $X + 1$ should be the same within $\pm 0.005\,\mathrm{m^3\,m^{-3}}$ and $\pm 0.2\,^{\circ}\mathrm{C}$, (iv) the SMC should fall within the $0.00\,\mathrm{m^3\,m^{-3}}$–$1.00\,\mathrm{m^3\,m^{-3}}$ range, and (v) soil temperature should fall within the $-15.0\,^{\circ}\mathrm{C}$–$40.0\,^{\circ}\mathrm{C}$ range. Each anomaly detected by this procedure is checked manually and corrected.

2.5.2 Known issues

Long-term operation of in situ monitoring networks goes hand in hand with measurement uncertainties. In this section, we would like to make data users aware of issues specific for the Twente dataset, which can be separated into items related to the instrumentation and to the measurement setup.

EC-TM and 5TM probes have been used in the monitoring network, and other than the points earlier described in Benninga et al. (2018c, in Chapter 3), these probes are calibrated at the factory using standards among which one with an ε_r of 40 as the highest. This implicates that native EC-TM and 5TM probe readings of $0.587\,\mathrm{m^3\,m^{-3}}$ and $0.510\,\mathrm{m^3\,m^{-3}}$, respectively, reach beyond the calibration domain of the sensors based on the conversion equations supplied by the manufacturer. Another issue that has come to our attention are inconsistencies in the internal probe calibrations between the firmware of probes produced in 2013 and the latest version 4.0 as well as the earlier ones. In 2013 the manufacturer modified their calibration process to include two dielectric standards that turned out to overestimate the ε_r between 10 and 20, which theoretically leads to maximum $0.05\,\mathrm{m^3\,m^{-3}}$ SMC underestimation in the $0.12\,\mathrm{m^3\,m^{-3}}$–$0.25\,\mathrm{m^3\,m^{-3}}$ range (Chambers and Crawford, 2014).

We have investigated the practical implications for our dataset by comparing the SMC produced by 5TM probes with the 2013 firmware and with firmware v4.0. Monitoring stations with nearly complete SMC time series at depths of at least 5 cm and 40 cm for the years 2018, 2019 and 2020, and exclusively equipped with one version of the 5TM probe were selected for this analysis. The time series collected at ITC_SM01, ITC_SM07, ITC_SM12, ITC_SM14 and ITC_SM18 were used to represent the 2013 firmware, and the ones from ITC_SM05, ITC_SM08, ITC_SM10, Twenthe airport and Hupsel to represent firmware v4.0. Figure 2.13 presents the time series of the mean SMC measured at 5 cm and 40 cm depth derived from the 2013 and firmware v4.0 calibrated probes. Whereas an underestimation of the 2013 firmware is expected, these measurements are higher than the firmware v4.0 measurements. As such, we suspect that the reported inconsistency in the internal probe calibration will have limited effect on the reported dataset and that other factors will have larger impact on the magnitude of the SMC measurements. A complete overview of the types of capacitance probes installed at each station and depth is provided in Supplement Table S3 (see Chapter 9).

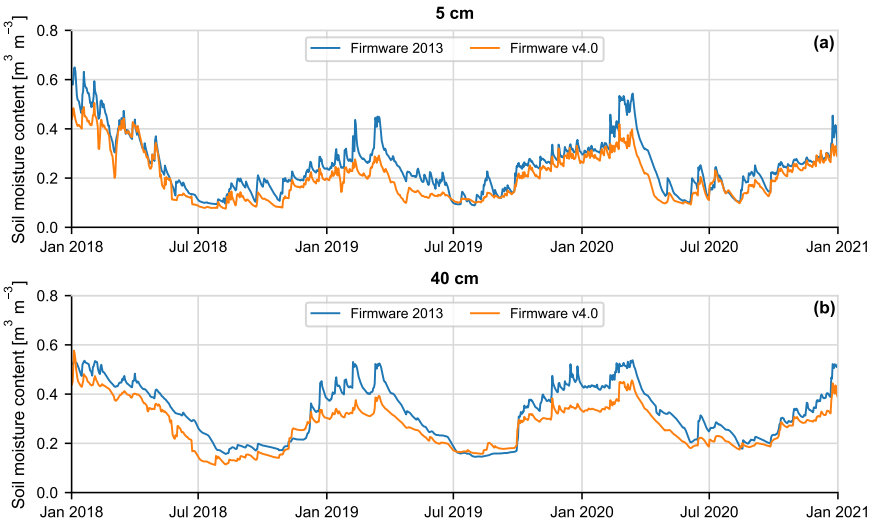

Figure 2.13 Time series of mean SMC measured at 5 cm **(a)** and 40 cm **(b)** by 5TM probes with the 2013 firmware (stations: ITC_SM01, ITC_SM07, ITC_SM12, ITC_SM14, ITC_SM18) and firmware v4.0 (stations: ITC_SM05, ITC_SM08, ITC_SM10, Twenthe airport, Hupsel).

Specific for the measurement setup of the Twente monitoring network is the placement of the instrumentation at the border of fields, which inevitably has consequences for the representativeness for the field. Large differences in the meteorological inputs, e.g. precipitation and incoming solar radiation, are not expected, but small-scale topography, spatially variable soil texture, differences in land cover and the local drainage infrastructure may cause discrepancies between the SMC at

the border and inside of the field. The field campaigns described in Section 2.4 have been conducted to address this issue. Benninga et al. (2020b, in Chapter 4) show that comparisons of 2016 and 2017 field campaign data against the measurements collected at stations yield $RMSD$s varying from 0.037 $m^3\,m^{-3}$ to 0.068 $m^3\,m^{-3}$ and R^2s values of 0.56 up to 0.81. These levels of uncertainty are larger but yet of a similar magnitude as the performance metrics reported for the probe calibrations in Section 2.3.3 and Section 2.4.3.

2.5.3 Time series

Figure 2.14 shows the SMC measured at depths of 5 cm, 10 cm, 20 cm, 40 cm and 80 cm over the period from January 2016 till June 2020 for monitoring stations ITC_SM10 (Figure 2.14b), ITC_SM14 (Figure 2.14c) and ITC_SM17 (Figure 2.14d). The groundwater level measured at the DINOloket well closest to the respective SMC monitoring station (see Supplement Table S1) is shown in the same plots and the upper panel presents daily precipitation and daily air temperature as averages of the measurements collected at the three KNMI automated weather stations in the region.

Overall the time series confirm the seasonal dynamics of wet soils and high groundwater levels in winters, and dry circumstances with low groundwater levels during summers. Also expected is the stronger response to precipitation of the SMC measured closest to the surface, whereas at 80 cm mainly seasonal variations are noted. Specifically in the 80 cm SMC the effect of the 2018, 2019 and 2020 droughts is visible, while the top soil (5 cm and 10 cm) dries out during the summer period virtually every year.

At the same time, substantial spatial differences can be noted between the three monitoring stations, which are situated 25 km–30 km apart at elevations of 10 m to 15 m a.s.l. For instance, in Figure 2.14c (ITC_SM14) the 80 cm SMC remained at a high level even during the peak of the 2018 drought, whereas deep drops are observed in Figures 2.14b (ITC_SM10) and 2.14d (ITC_SM17). These measurements demonstrate that the position within a catchment is an important factor for the impact drought has locally, even though drought may be seen as a regional-scale process.

Somewhat surprising in the plots is the response of the groundwater level to precipitation. In all three groundwater measurement series increments can be identified after precipitation events, whereas the SMC at 80 cm primarily displays seasonal variations and individual events are hardly noticeable. To take this a step further and explore the relationship with SMC, Table 2.6 presents the R^2 values computed between the SMC measurements at specific depths and groundwater levels. Indeed, the R^2 values support the above observation. The shallower 40 cm SMC yields the highest R^2 and not the deeper 80 cm measurements. This is in spite of the fact that the highest groundwater levels remain substantially below the surface with −112 cm, −83 cm and −71 cm recorded as the

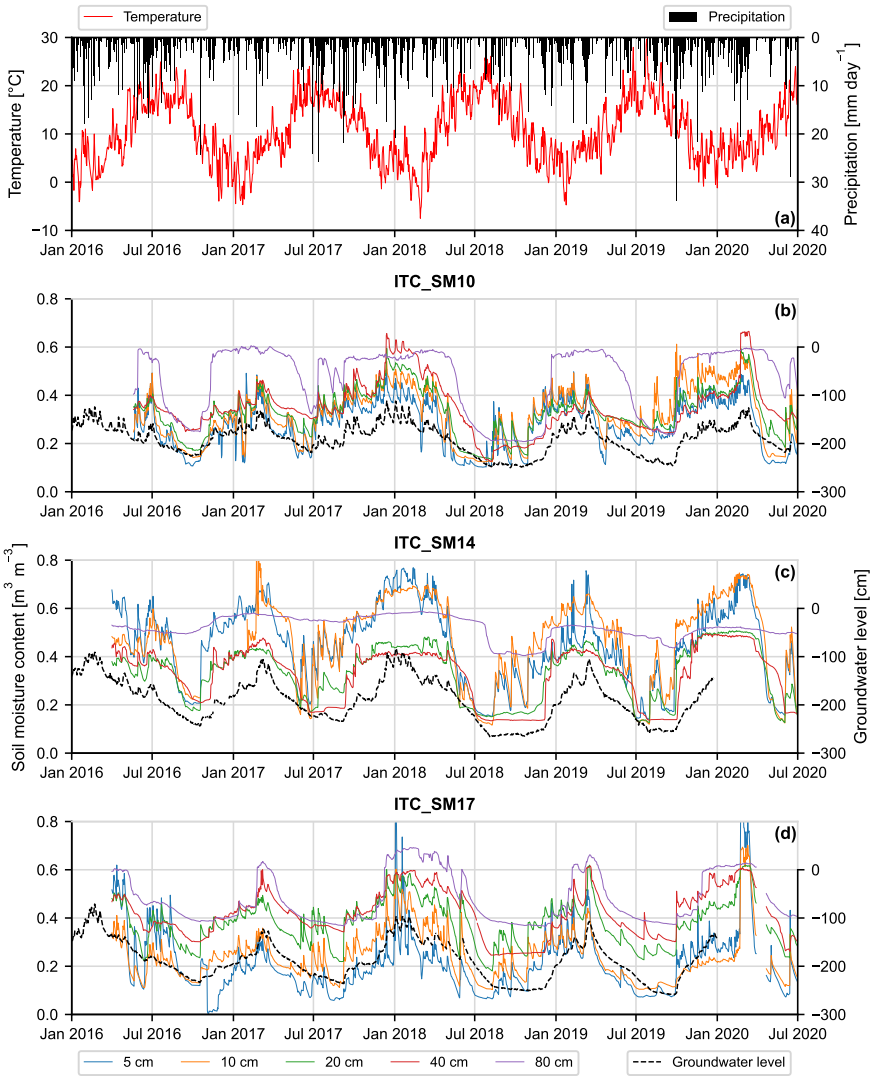

Figure 2.14 **(a)** Daily precipitation sum and mean daily air temperature as averages of the three KNMI automated weather stations. **(b–d)** Profile SMC measured at ITC_SM10, ITC_SM14 and ITC_SM17, and groundwater level measured at the nearest well available in DINOloket (see Supplement Table S1).

highest levels near ITC_SM10 (Figure 2.14b), ITC_SM14 (Figure 2.14c) and ITC_SM17 (Figure 2.14d), respectively.

Another interesting feature is that the SMC at 5 cm and 10 cm are still reasonably correlated with the groundwater level. Hence, there is a research opportunity to further investigate the potential of the near-surface SMC, observable from space, for supplying information on the groundwater level. Similar work has previously been conducted by Sutanudjaja et al. (2013), who estimated groundwater level across the

Table 2.6 R^2 computed between SMC measured at specific depths and groundwater level at the well nearest to the SMC monitoring station available in DINOloket (see Supplement Table S1). The time series are shown in Figure 2.14.

Station	Number of pairs	Depth				
		5 cm	10 cm	20 cm	40 cm	80 cm
ITC_SM10	1490	0.515	0.499	0.714	**0.779**	0.758
ITC_SM14	1338	0.722	0.575*	0.709	**0.782**	0.527
ITC_SM17	1332	0.405	0.509	0.628	**0.853**	0.851

* Obtained for 1251 pairs.

Rhine-Meuse river basin using time series of soil water index retrieved from coarse resolution scatterometer data. The present dataset allows for more detailed investigations of the relationship between phreatic groundwater and profile SMC. Moreover, the spatial measurement density of the Twente network, the access to the other relevant data documented in this chapter and the availability of higher resolution SMC products (e.g. Bauer-Marschallinger et al., 2018, 2019; Das et al., 2019) makes it possible to extend to sub-catchment scale applications.

2.6 Data availability

Chapter 9 describes the availability of the SMC and soil temperature network data and the field campaign measurements. An updated version of the dataset is expected. Table 2.7 lists the third-party datasets that are available for the study region, which may support use of the published SMC and soil temperature datasets.

2.7 Summary

Soil moisture content (SMC) and temperature profile measurements from 2008 till 2020 have been automatically collected at 15 min intervals by a network of 20 monitoring stations spread across the Twente region and neighbouring regions in the east of the Netherlands. The monitoring stations are mostly placed at the border of privately owned parcels used for agriculture with, in order of occurrence, grass, maize, cereals, potato and natural vegetation as land covers. The experimental setup includes METER Group (formerly: Decagon Devices) EC-TM and its successor 5TM capacitance probes installed at soil depths of 5 cm, 10 cm, 20 cm, 40 cm and 80 cm. Soil-specific calibration functions have been developed under controlled laboratory conditions for both probe types, suggesting accuracies of 0.023 $m^3\,m^{-3}$ and 0.028 $m^3\,m^{-3}$ for the EC-TM and 5TM respectively. Quality-controlled and calibrated datasets as well as field photos, notes and the native data records are made available.

Table 2.7 Open third-party datasets available for the study region, which are described in Section 2.2.

Name	Responsible institute(s)	Data address and instructions	Available formats
AHN (2019)	RWAs, provinces, Directorate-General for Public Works and Water Management	https://www.pdok.nl/introductie/-/article/actueel-hoogtebestand-nederland-ahn3-; under the tab 'Downloads' individual tiles can be obtained and under 'Geo Services' links to the entire dataset are provided.	GeoTIFF WMS WFS WMTS WCS
BOFEK (Heinen et al., 2021)	Wageningen Environmental Research	https://www.wur.nl/nl/show/Bodemfysische-Eenhedenkaart-BOFEK2020.htm; the map and report can be found under downloads both for BOFEK2020 and BOFEK2012.	.gdb .shp
Land use (Bestand Bodemgebruik)	Statistics Netherlands (2015)	https://www.pdok.nl/introductie/-/article/cbs-bestand-bodemgebruik; for the years 2010 and 2015 downloads as well as Geo Services are available.	.shp WMS WFS
Crop parcel registry (Basisregistratie Gewaspercelen)	Ministry of Economic Affairs and Climate Policy (2020)	https://data.overheid.nl/dataset/10674-basisregistratie-gewaspercelen--brp-; for the years 2009–2020 downloads are available at the tab 'Databronnen' and under 'INSPIRE Atom' and from 2016 also view services are available.	.gdb WMS WFS WMTS
DINOloket	Geological Survey of the Netherlands (GDN) (2021)	https://www.dinoloket.nl/en; go to 'Subsurface data', apply a filter in the menu on the left and select one of the shapes in the menu on the right to order data for measurement locations.	.csv
Precipitation and weather data	Royal Netherlands Meteorological Institute (KNMI) (2021)	https://www.knmi.nl/nederland-nu/klimatologie-metingen-en-waarnemingen; for daily precipitation measurements select 'Dagwaarden neerslagstations' and for hourly weather data select 'Dagwaarden van weerstations'.	.txt

In addition, field campaign data covering the growing seasons of 2009, 2015, 2016 and 2017, during which the SMC was measured with hand-held probes (Delta-T ThetaProbe, Type ML2, and Stevens HydraProbe) and a gravimetric method on a total of 28 fields near 12 different monitoring stations, are described and disclosed. Pairs of gravimetrically determined SMC and probe readings were used to establish calibration functions for both the ThetaProbe and HydraProbe. The accuracies obtained for the probe calibrations varied from $0.048\,m^3\,m^{-3}$ for the ThetaProbe measurements in 2009 up to $0.032\,m^3\,m^{-3}$ for the HydraProbe measurements collected in 2016–2017.

Further, descriptions of open thirty-party datasets are provided to support the use of the Twente SMC and soil temperature measurements beyond the scope for which the network was originally established: the validation of coarse resolution satellite data products. Scientists and

professionals worldwide are invited to make free use of the datasets disclosed with this contribution. We welcome any comments or suggestions that can help improve the quality and usability of the datasets. The data collection with the Twente network continues, but plans are underway to update the design of the network to the contemporary societal and scientific needs. This may include flood and drought analyses, and high-resolution satellite product validation.

The Raam regional soil moisture content monitoring network in the Netherlands

3

This chapter is based on:

Benninga, H. F., Carranza, C. D. U., Pezij, M., Van Santen, P., Van der Ploeg, M. J., Augustijn, D. C. M., and Van der Velde, R.: The Raam regional soil moisture monitoring network in the Netherlands, Earth Syst. Sci. Data, 10, 61–79, doi:10.5194/essd-10-61-2018, 2018.

Abstract

A soil moisture content (SMC) profile monitoring network was established in the Raam region in the Netherlands. This region faces water shortages during summers and excess of water during winters and after extreme precipitation events. Water management can benefit from reliable information on the soil water availability and water storing capacity in the unsaturated zone. In situ measurements provide a direct source of information on which water managers can base their decisions. Moreover, these measurements are commonly used as a reference for the calibration and validation of SMC products derived from earth observations or obtained by model simulations. Distributed over the Raam region, we have equipped 14 agricultural fields and 1 natural grass field with SMC and soil temperature monitoring instrumentation, consisting of 5TM sensors installed at depths of 5 cm, 10 cm, 20 cm, 40 cm and 80 cm. In total, 12 stations are located within the Raam catchment (catchment area of 223 km^2), and 5 of these stations are located within the closed sub-catchment Hooge Raam (catchment area of 41 km^2). Soil-specific calibration functions that have been developed for the 5TM sensors under laboratory conditions lead to an accuracy of 0.02 $m^3\,m^{-3}$. The first set of measurements has been retrieved for the period 5 April 2016–4 April 2017. In this chapter, we describe the Raam monitoring network and instrumentation, the soil-specific calibration of the sensors, the first year of measurements, and additional measurements (soil temperature, phreatic groundwater levels and meteorological data) and information (elevation, soil physical characteristics, land cover and a geohydrological model) available for performing scientific research.

Keywords: Soil moisture content, monitoring network, measurement accuracy, sensor's influence zone.

3.1 Introduction

Soil moisture content (SMC) is a hydrological state variable that affects various processes on global, regional and local scales. On the global to regional scales, the control of SMC on the exchanges of water and heat at the land surface plays an important role in the development of weather and climate systems (Global Climate Observing System (GCOS), 2010; Seneviratne et al., 2010). GCOS (2010) has identified SMC as an essential climate variable. However, SMC products from state-of-the-art land surface models (LSMs) show large biases compared to in situ observations (Xia et al., 2014; Zheng et al., 2015) and large variation among different models (Dirmeyer et al., 2006; Xia et al., 2014). Xia et al. (2014) pointed out that, in particular, the SMC outcomes from LSMs need improvement. In situ observations help to identify the shortcomings of LSMs and to improve model descriptions of related processes.

SMC also affects numerous hydrological and ecological processes that are essential for a wide spectrum of applications on the regional to local scales. Regional water management can benefit from timely and reliable information about SMC: it can improve quantifications of flood risks by its effect on rainfall estimations and streamflow predictions (Beck et al., 2009; Massari et al., 2014; Wanders et al., 2014) and negative anomalies to current plant water demands are an indicator of (the onset of) droughts (Carrão et al., 2016; Wilhite and Glantz, 1985). The agricultural sector depends on sufficient root zone soil water availability for crop growth, while excess of soil water leads to severe losses (Feddes et al., 1978). In addition, wet soil conditions are unfavourable for the trafficability of farmlands, which can jeopardize the timely execution of essential agricultural practices and cause structural damage of land (Batey, 2009; Hamza and Anderson, 2005; Schwilch et al., 2016). Lastly, information about SMC is relevant to assess the effects of groundwater extractions (Ahmad et al., 2002), drainage systems and irrigation systems.

SMC conditions can be quantified using in situ instruments (Topp and Ferré, 2002a; Vereecken et al., 2014), earth observations (Kornelsen and Coulibaly, 2013; Petropoulos et al., 2015) and land process models subject to atmospheric forcing terms (Albergel et al., 2012; De Lange et al., 2014; Srivastava et al., 2015; Vereecken et al., 2008). Of these methods, in situ instruments are the most accurate and can have a high temporal resolution when automated, but they lack spatial support. In contrast, earth observations and process models provide areal estimates and enable the quantification of SMC across large spatial domains, but uncertainties regarding their SMC estimates are still the subject of investigation. The success of SMC estimation from earth observations depends on the specifications of the sensor, the assumptions and parameter values adopted for the retrieval algorithms, and the soil and vegetation cover conditions (e.g. Burgin et al., 2017; Chan et al., 2016; Das et al., 2014; Kerr et al., 2016; Pathe et al., 2009). Earth observations in the microwave spectrum, which are most often used for the estimation of

SMC by earth observations (Kornelsen and Coulibaly, 2013; Petropoulos et al., 2015), originate from the soil surface to generally 0.01 m–0.05 m depth (Escorihuela et al., 2010; Kornelsen and Coulibaly, 2013; Nolan and Fatland, 2003; Rondinelli et al., 2015; Ulaby et al., 1996). Sampling depth is controlled by the microwave wavelength and moisture conditions (Escorihuela et al., 2010; Nolan and Fatland, 2003; Rondinelli et al., 2015; Ulaby et al., 1996; Woodhouse, 2006). However, the relation between surface SMC and SMC at deeper layers is complicated. To relate surface SMC to SMC at greater depths, the correct specification of hydraulic parameters and modelling of the hydrological processes are required (Chen et al., 2011; Das and Mohanty, 2006; Vereecken et al., 2008). Yet, several studies have reported that surface SMC may provide information about SMC at greater depths (Das and Mohanty, 2006; Ford et al., 2014; Vereecken et al., 2008). Estimations of vegetation characteristics by microwave and optical sensors also have the potential to provide estimates of root zone SMC (Van Emmerik et al., 2015; Petropoulos et al., 2015; Steele-Dunne et al., 2012; Wang et al., 2010). Regarding land process models, the implemented model physics, model structure, the quality of parameterizations, and the imposed initial and boundary conditions (including atmospheric forcing terms) determine the reliability of model results (Xia et al., 2014). Combining observations of earth variables with process models by data assimilation techniques is interesting in estimating initial model states, model state updating and parameter calibration, thereby improving the model accuracy (Houser et al., 2012; Reichle, 2008; Vereecken et al., 2008).

In situ SMC measurements provide a reference for validating earth observation retrievals and land process models. The combination of in situ measurements at various depths, earth observation products and land process models is essential to obtaining reliable SMC information at the temporal, horizontal and vertical resolutions required for the above-mentioned applications. Several regional-scale SMC monitoring networks have been established to fulfil (part of) this aim. The International Soil Moisture Network (Dorigo et al., 2011) and the Soil Moisture Active Passive (SMAP) Cal/Val Partner Sites (Colliander et al., 2017) are two initiatives that bring together the data collected by a number of networks. The Natural Resources Conservation Service - Soil Climate Analysis Network, consisting of 218 stations in agricultural areas across the United States of America, is operationally used for monitoring drought development, developing mitigation policies, predicting the long-term sustainability of cropping systems and watershed health, predicting regional shifts in irrigation water requirements, and predicting changes in runoff (U.S. Department of Agriculture, 2016). Examples of regional-scale networks in a temperate climate are the Little Washita (Cosh et al., 2006) and Little River (Bosch et al., 2007) networks in North America, REMEDHUS in Spain (Martínez-Fernández and Ceballos, 2005), Twente in the Netherlands (Dente et al., 2011, 2012; Van der Velde et al., 2015), HOBE's network in Denmark (Bircher et al., 2012), SMOSMANIA in France (Albergel et al., 2008; Calvet et al., 2007), TERENO in Germany (Zacharias et al., 2011),

and Kyeamba (Smith et al., 2012) in Australia. This chapter presents the SMC and soil temperature profile monitoring network in the Raam region, in the southeast of the Netherlands, established in April 2016. By Dutch standards and in comparison to the only existing long-term SMC monitoring network in the Netherlands, in the Twente region (Dente et al., 2011, 2012; Van der Velde et al., 2015), the Raam region faces substantial water shortages during summers. Extreme precipitation events cause an excess of water and inundation of fields. These extreme situations present a challenge for the intensive agriculture in the region: the agricultural yield largely depends on the applied water management. The Raam monitoring network is established jointly with the regional water authority (RWA, 'waterschap' in Dutch), Waterschap Aa en Maas. With the network, we aim to collect data for the calibration and validation of earth observation SMC products, the assessment of land process model performance and the understanding of processes affected by SMC (e.g. field trafficability, crop water availability). In addition, cooperation with the RWA enables the exploration of the potential of SMC information for optimizing operational regional water management. In this chapter, we describe the characteristics of the Raam catchment (Section 3.2), the network design and instrumentation (Section 3.3), the sensor's propagation distance (Section 3.4.1), the sensor calibration results (Section 3.4.2) and the verification of the first year of measurements (Section 3.4.3).

3.2 Study area

The Raam River is situated in the southeast of the Netherlands (Figure 3.1a), has a catchment area of 223 km^2 and is a tributary of the Meuse River. The catchment has a temperate oceanic climate. For the period 2000–2016, on average, the coldest month is January (3.3 °C) and the warmest month is July (18.3 °C), based on measurements at Volkel weather station (Royal Netherlands Meteorological Institute (KNMI), 2017). Annual precipitation statistics are listed in Table 3.1. Figure 3.2a shows the monthly precipitation measured at the Volkel weather station averaged for the period 2000–2015 and for the hydrological year 2016. Figure 3.2b shows the cumulative precipitation deficit for the hydrological year 2016 and the average for the period 2000–2015. The cumulative precipitation deficit is calculated by subtracting daily reference evapotranspiration rates from the daily precipitation measured at the Volkel weather station and summing the daily deficits. A number of heavy precipitation events characterized May 2016 to August 2016, which caused the 2016 summer in the Raam area to be wetter than normal. In dry years, the cumulative precipitation deficit can reach up to 100 mm in summer. During these dry periods, farmers irrigate from deep groundwater reservoirs. The RWA operates a system of weirs and pumping stations to minimize situations of excess water and droughts. In addition, the RWA continuously discharges surface water into the southern part of

the catchment to increase groundwater recharge. The average discharge into the catchment for the summer of 2016 was 900 $m^3 h^{-1}$.

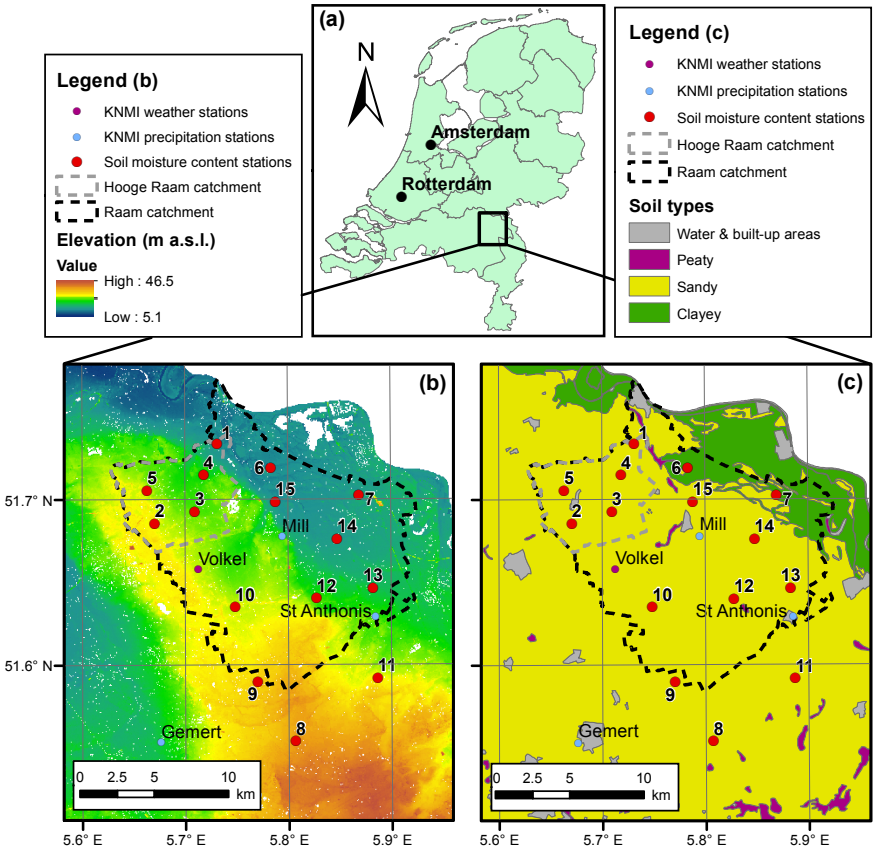

Figure 3.1 **(a)** Location of the Raam study area (black box) in the Netherlands. **(b)** Digital terrain model (Actueel Hoogtebestand Nederland, 2012a). **(c)** Major soil types classes (BOFEK2012; Wösten et al., 2013).

Table 3.1 Precipitation statistics of the KNMI weather and precipitation stations for the period 2000–2016 (KNMI, 2017).

Station	Average annual precipitation [mm]	Minimum annual precipitation [mm]	Maximum annual precipitation [mm]
Volkel (hourly measurements)	767	681	862
Mill (daily measurements)	850	692	949
St. Anthonis (daily measurements)	830	689	954
Gemert (daily measurements)	826	688	940

The subsurface of the Raam catchment consists of unconsolidated Pleistocene sandy and fluvial gravel sediments in two river terraces. The higher terrace slopes gently from 21 m a.s.l. to 17 m a.s.l., and the lower terrace slopes from 13 m a.s.l. to 8 m a.s.l., with the terrace edge lying in

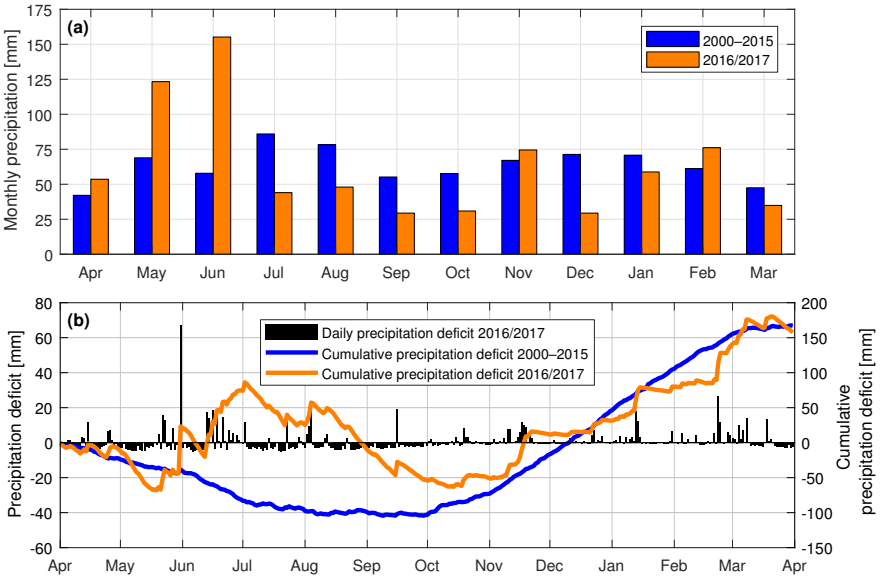

Figure 3.2 **(a)** Average monthly precipitation for the period 2000–2015 and the monthly precipitation in the hydrological year 2016 measured at Volkel weather station. **(b)** Daily and cumulative precipitation deficits for the period 2000–2015 and for the hydrological year 2016, based on precipitation measurements and reference evapotranspiration calculations at Volkel weather station.

a northwest–southeast direction (Figure 3.1b). Remnants of peat and fine sands, deposited by aeolian processes, are found on the higher terrace. In parts of the study area, anthropogenic activities — the continuous addition of straw-mixed cattle droppings — have elevated fields, resulting in an approximately 1 m thick layer of brown earth with high organic matter contents, called plaggen soils (Blume and Leinweber, 2004). The soil map in Figure 3.1c shows that the soils in the catchment are mostly sandy, with loam contents varying from 0 % to about 20 % (Wösten et al., 2013). In the eastern part, loamy and clayey soils are present. The main land cover types are grassland (30 %) and maize fields (20 %), another 14 % is used for other crops, built-up and paved areas occupy 14 %, forests cover about 10 %, and open water covers 3 %.

Several northwest–southeast-orientated dip-slip faults are present in the subsurface, as shown in Figure 3.3. Movements along these faults have caused the formation of sharp lateral transitions between highly permeable and impermeable layers, as shown in Figure 3.4. On the eastern part of the higher terrace (D–E in Figures 3.3 and 3.4) this has resulted in the existence of a phreatic aquifer only 10 m thick, whereas for the rest of the study area the phreatic aquifer is generally around 25 m to 50 m thick. The sharp transition in aquifer thickness leads to obstruction of the northeast-directed groundwater flow and high groundwater levels on the western part of the higher terrace (C–D), as shown in Figure 3.3.

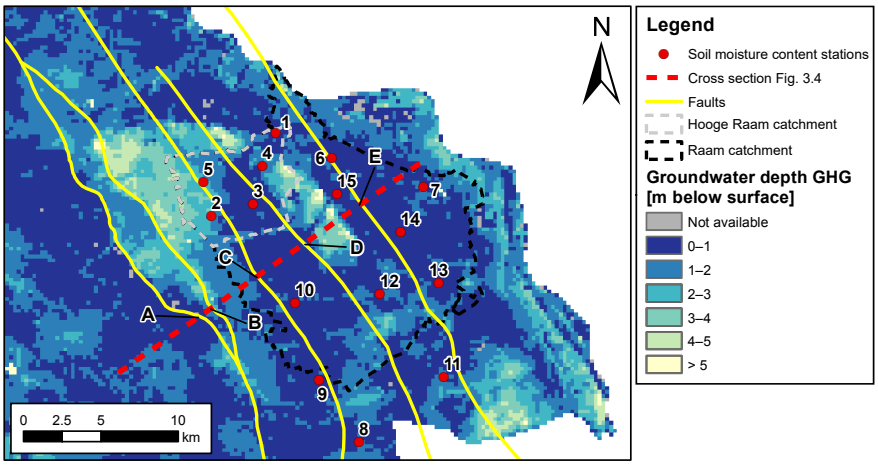

Figure 3.3 Mean highest groundwater depth ('gemiddeld hoogste grondwaterstand' in Dutch, or GHG) in the Raam catchment. The GHG is a long-term average of highest groundwater depths, defined as the average of the three highest groundwater depths per year over a period of 8 years. The groundwater data originate from the national implementation of the Netherlands Hydrological Instrument, NHI LHM (De Lange et al., 2014). The map also shows the location of faults in the area. The dashed red line represents the cross section that is shown in Figure 3.4.

3.3 Network design

3.3.1 Station locations

In April 2016, 15 stations were installed in the Raam region (Figure 3.1). The locations capture the range of physical characteristics influencing the area's hydrological dynamics. The physical characteristics considered are soil texture (Section 3.3.1.1), land cover (Section 3.3.1.2) and elevation (Section 3.3.1.3). Stations 1 to 7, 10 and 12 to 15 are located within the Raam catchment. Stations 1 to 5 are located in a closed sub-catchment of the Raam catchment, called the Hooge Raam catchment ('The High Raam'). With 15 stations distributed over a 495 km^2 area, the network's density is approximately 33 km^2 per station. The density is 18.6 km^2 per station within the Raam catchment and 8.2 km^2 per station within the Hooge Raam catchment. The number of stations and the density of the Raam network are comparable to SMC monitoring networks that are comparable in areal extent, such as the Little Washita network (20 stations, 30 km^2 average spacing), the Fort Cobb network (15 stations, 23 km^2 average spacing), the Reynolds Creek network (15 stations, 16 km^2 average spacing), the Little River network (33 stations, 10 km^2 average spacing), the Kyeamba network (14 stations, 43 km^2 average spacing) and the Adelong Creek network (5 stations, 29 km^2 average spacing) (Crow et al., 2012). Crow et al. (2012) stated that these regional-scale networks

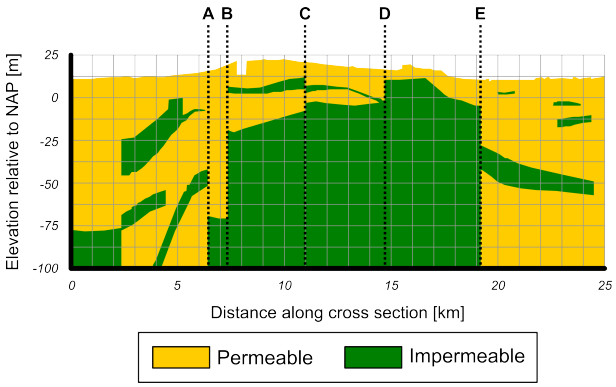

Figure 3.4 West–east cross section of the Raam catchment showing the permeable and impermeable layers of the subsoil, based on the geohydrological model REGIS II (Vernes and Van Doorn, 2005). The locations indicated by A, B, C, D and E refer to the position of the faults and correspond to the letters in Figure 3.3.

provide information over a range of land covers and on a scale that allows the validation of operational SMC products from earth observations, such as from the Advanced Scatterometer (ASCAT) at 25 km and 50 km (Wagner et al., 2013), the Advanced Microwave Scanning Radiometer 2 (AMSR2) at 0.1° and 0.25° (Zhang et al., 2017), the Soil Moisture and Ocean Salinity (SMOS) satellite at 43 km (Kerr et al., 2016) and the SMAP satellite at 40 km resolution (Chan et al., 2016). Basin-scale aggregates are expected to have root mean square deviation (*RMSD*, Equation A.1) values of 0.01 $m^3\,m^{-3}$ (Crow et al., 2012), which is small compared to the *RMSD* goal of 0.04 $m^3\,m^{-3}$ defined for the SMOS mission (Kerr et al., 2010) and SMAP mission (Chan et al., 2016). Besides, in hydrological research there is a trend towards hyperresolution land surface modelling (Beven et al., 2015; Wood et al., 2011). Wood et al. (2011) proposed developing LSMs on continental scales with a grid resolution of 100 m by 100 m. An example of a high-resolution model is the National Hydrological Model ('Landelijk Hydrologisch Model' in Dutch, or LHM) application of the Netherlands Hydrological Instrument (NHI), which is currently operating at a spatial resolution of 250 m by 250 m (De Lange et al., 2014). To facilitate the development of such high-resolution models, networks with a high density are required.

3.3.1.1 Soil texture

The Raam catchment mainly holds sandy soils. Therefore, 13 stations were positioned in coarse sandy soils. Two stations (stations 6 and 7) were positioned in clayey sands and loamy sands respectively, at the northeastern part of the study area. Table 3.2 lists the soil type descriptions adopted from BOFEK2012 ('bodemfysische eenhedenkaart 2012' in Dutch). BOFEK2012 provides the soil physical characteristics (e.g. soil

Table 3.2 Characteristics of the SMC monitoring stations.

Station	Soil description[a]	Soil order[b]	Sand fraction (> 50 µm) [%]	Silt fraction (50–2 µm) [%]	Clay fraction (< 2 µm) [%]	Organic matter fraction [%]
1	Weakly loamy sandy soil on subsoil of coarse sand (305)	Podzols	91.3	1.9	3.5	3.3
2	Weakly loamy sandy soil on subsoil of coarse sand (305)	Podzols	90.4	3.7	2.1	3.8
3	Weakly loamy Podzol soil (304)	Podzols	93.3	2.4	1.9	2.4
4	Weakly loamy sandy soil on subsoil of coarse sand (305)	Podzols	90.0	2.0	2.9	5.2
5	Weakly loamy sandy soil with thick man-made earth soil (311)	Anthrosols	93.1	2.3	1.1	3.5
6	Clayey sand on sand (fluvial) (409)	Anthrosols/ Vague soils	83.7	4.8	9.9	1.6
7	Loamy sandy soil with thick man-made earth soil (317)	Anthrosols	82.1	10.5	5.2	2.2
8	Weakly loamy Podzol soil (304)	Podzols	92.8	1.6	1.4	4.1
9	Weakly loamy Podzol soil (304)	Podzols	95.4	1.1	0.8	2.6
10	Weakly loamy Podzol soil (304)	Podzols	96.3	0.8	0.7	2.2
11	Weakly loamy Podzol soil (304)	Podzols	94.8	1.7	1.6	1.9
12	Weakly loamy Podzol soil (304)	Podzols	92.0	2.5	1.7	3.9
13	Weakly loamy soil partly on subsoil of coarse sand (309)	Podzols	96.7	1.1	0.8	1.4
14	Loamy Podzol soil (312)	Podzols	90.0	4.7	2.3	3.0
15	Weakly loamy sandy soil with thick man-made earth soil (311)	Anthrosols	88.6	5.5	2.8	3.1

[a] Soil description and classification code from BOFEK2012 (Wösten et al., 2013).
[b] Approximate Soil Order Equivalent in the World Reference base (Hartemink and De Bakker, 2006).

texture, water retention curve and hydraulic conductivity curve) for the soil units in the Netherlands, based on the Dutch class pedotransfer functions known as the Staring series (Wösten et al., 2001, 2013). Table 3.2 also lists the corresponding World Reference base soil order (Hartemink and De Bakker, 2006).

Complementing the available soil texture information, we performed particle size analyses in a laboratory, following the pipette method described by Van Reeuwijk (2002), on samples representing the upper 40 cm of the soil profile at each monitoring station. Organic matter content was determined by the loss of ignition method (Davies, 1974; Hoogsteen et al., 2015) at 500 °C. The results reveal very high sand contents for most stations, and as expected, stations 6 and 7 have higher volume fractions of silt and clay. The results are consistent with the BOFEK2012 class descriptions.

3.3.1.2 Land cover

For practical reasons, the monitoring stations were installed at the border of fields. Table 3.3 lists the land cover of the adjacent fields in 2016 as well as the land cover at the exact location of the monitoring stations in 2016. Positioning of stations on agricultural areas was preferred over forest and natural areas. Microwave remote-sensing instruments are typically unable to observe the soil under dense forest canopies, so measurements at agricultural areas are the most valuable for validating SMC retrievals from earth observations. Furthermore, agricultural areas in particular are manageable regarding water-related processes. Station 6 was positioned in natural grassland.

Table 3.3 Land cover of adjacent fields and at the locations of the SMC monitoring stations.

Station	Land cover of the adjacent field(s) in 2016	Land cover at the location of the station in 2016
1	Grass	Grass
2	Sugar beets	Grass
3	Grass	Grass
4	Grass	Grass
5	Onions	Grass fallow
6	Natural grass	Natural grass
7	Maize and Cichorium	Grass fallow
8	Sugar beets	Grass
9	Sugar beets	Grass fallow
10	Grass	Grass
11	Maize and grass	Grass
12	Grass	Grass
13	Maize	Grass
14	Grass	Grass
15	Grass	Grass

3.3.1.3 Elevation

The stations were distributed in such a way that they cover the elevation gradient of the catchment. This will be valuable for observing the influence of groundwater level and water-limited evapotranspiration conditions on SMC.

3.3.2 Instrumentation

Common instruments to measure volumetric SMC are based on time-domain reflectometry (TDR) or capacitance techniques. Capacitance sensors are the most attractive choice for networks consisting of multiple SMC monitoring stations because of their relatively low costs, ease of operation and applicability to a wide range of soil types (Bogena et al., 2007; Kizito et al., 2008; Vereecken et al., 2014). We deploy the METER Group (formerly: Decagon Devices) 5TM capacitance sensor in the Raam network. The 5TM and other METER Group sensors that use the same technique and frequency have been widely used for in situ SMC networks and have proved to fulfil the performance requirements (Bircher et al., 2012; Bogena et al., 2010; Dente et al., 2009, 2011; Kizito et al., 2008; Matula et al., 2016; Varble and Chávez, 2011; Vaz et al., 2013).

5TM sensors use an oscillator operating at 70 MHz to measure the capacitance of the soil, which is affected by the soil's relative permittivity. The sensor prongs charge the surrounding soil, and the time needed to fully charge the soil defines the capacitance and consequently the relative permittivity of the soil. The relative permittivity of the soil varies as a function of the volumetric SMC. METER Group (2019) reports the following specifications for the 5TM: the resolution of the SMC measurements is $0.0008\,m^3\,m^{-3}$, and the accuracy is $\pm 0.03\,m^3\,m^{-3}$ for mineral soils by applying the function established by Topp et al. (1980) to convert relative permittivity to volumetric SMC. A thermistor on the same probe measures soil temperature. The resolution of the temperature measurements is 0.1 °C, and the accuracy is ±1 °C.

The sensors are installed horizontally, with the prongs in vertical orientation to avoid ponding on the sensors due to water infiltration or condensation of vapour (Figure 3.5). SMC and soil temperature are logged every 15 min with METER Group Em50 data loggers. At each location we installed 5TM sensors at depths of 5 cm, 10 cm, 20 cm, 40 cm and 80 cm (Figure 3.5). Next to all monitoring stations, phreatic groundwater levels are monitored by Waterschap Aa en Maas at an hourly time interval or by the Province of Noord-Brabant at a daily time interval with a MiniDiver DI501 (Van Essen Instruments, 2016).

3.3.3 Zone of influence of 5TM sensors

For practical reasons, the shallowest in situ sensors are typically installed at 5 cm depth (Rondinelli et al., 2015; Shellito et al., 2016). In air,

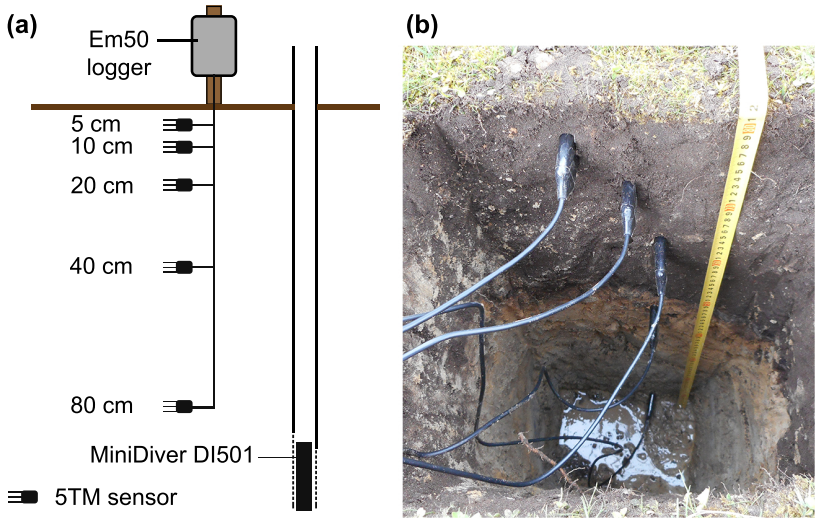

Figure 3.5 **(a)** Schematic cross section of the SMC monitoring stations and nearby phreatic groundwater level monitoring well. **(b)** Photo of an installation pit with the SMC sensors installed at the five depths.

5TM sensors integrate a volume of 715 mL around the prongs, with a maximum distance of 6 cm from the centre of the sensor (Cobos, 2015). This means that open air above the soil surface would affect the sensor readings at 5 cm. In soil, which has a higher relative permittivity, the outer edge will be closer to the sensor (Cobos, 2015). Sakaki et al. (2008) and Cobos (2015) investigated the measurement volume in air and Vaz et al. (2013) in deionized water by moving the sensor towards/from a front of water and air. We conducted the same kind of experiment with a soil sample from station 1. A steel knife was inserted into a soil-filled container with a 5TM sensor buried in the middle. The steel knife was brought towards the 5TM sensor from the direction similar to where the soil surface would be in the field. With this experiment we were able to leave the 5TM sensor in the same position to eliminate effects other than the steel knife. This procedure was performed five times for a range of SMC conditions.

3.3.4 Calibration

To convert sensor readings to volumetric SMC we use a two-step calibration procedure (Bogena et al., 2007; Rosenbaum et al., 2010). The first step is the conversion of the sensor reading to relative permittivity. Kizito et al. (2008) concluded that there is no significant probe-to-probe variability among METER Group ECH_2O-TE sensors, and Rosenbaum et al. (2010) found a *RMSD* of approximately 0.01 $m^3\,m^{-3}$ as a result of METER Group 5TE probe-to-probe variability. METER Group calibrates each 5TM sensor to account for probe-to-probe variability and to provide

a linear relation between the sensor's response and the real part of the relative permittivity (Rosenbaum et al., 2010):

$$\varepsilon_a = \frac{5\mathrm{TM}_{\mathrm{reading}}}{50}, \tag{3.1}$$

where $5\mathrm{TM}_{\mathrm{reading}}$ (mV) is the raw output of the 5TM and ε_a (−) is the relative permittivity.

The second step is converting relative permittivity to volumetric SMC. The relation between relative permittivity and SMC is affected by soil composition, bulk density, organic matter content and soil salinity (Starr and Paltineanu, 2002). Relative permittivity can be converted to SMC using a general calibration function or using a soil-specific calibration function. By default the ECH_2O Utility software applies the Topp function (Topp et al., 1980). However, Vaz et al. (2013) stated that soil-specific calibration is often recommended to address the various soil property effects. According to METER Group (2019) the accuracy can be improved from $\pm 0.03\,\mathrm{m^3\,m^{-3}}$ to $\pm 0.02\,\mathrm{m^3\,m^{-3}}$ by using a soil-specific calibration function. Indeed, several studies concluded that soil-specific calibration can significantly improve the accuracy (Section 3.4.2, Table 3.6).

We developed soil-specific calibration functions for the main soil types present in the study area, by analysing soil samples taken from stations 1, 7 and 10. The soil texture at these stations is considered representative of the soils at other stations; see Table 3.4. The measurements to establish the calibration function were collected following the procedure described by Starr and Paltineanu (2002), as recommended by Cobos and Chambers (2010). The procedure employs pairs of gravimetrically determined volumetric SMC (GVSMC) and sensor readings of relative permittivity. The GVSMCs and 5TM measurements were obtained under laboratory conditions in disturbed soil samples, while gradually wetting the soil from air-dried conditions to saturated conditions by adding 75 mL to 100 mL of water. In every session typically 15 to 18 pairs of measurements were collected. The described procedure has been performed three times for each of the three soil samples.

The capability of the calibration functions to reproduce GVSMC with 5TM measurements is evaluated with Spearman's rank correlation coefficient (r_S), the $RMSD$ (Equation A.1) and the bias (Equation A.4).

3.4 Results and discussion

3.4.1 Zone of influence

The results in Figure 3.6 show that in soil, the zone of influence ranges from 3 cm to 4 cm from the middle prong of the 5TM sensors. This is smaller than the propagation distance of 6 cm in air found by Cobos (2015) and larger than the propagation distance of 2.2 cm in deionized water found by Vaz et al. (2013). Open air does not affect the 5TM readings at the shallowest installation depth of 5 cm that is used in the

Raam network. The results also indicate that SMC does not affect the extent of the zone of influence.

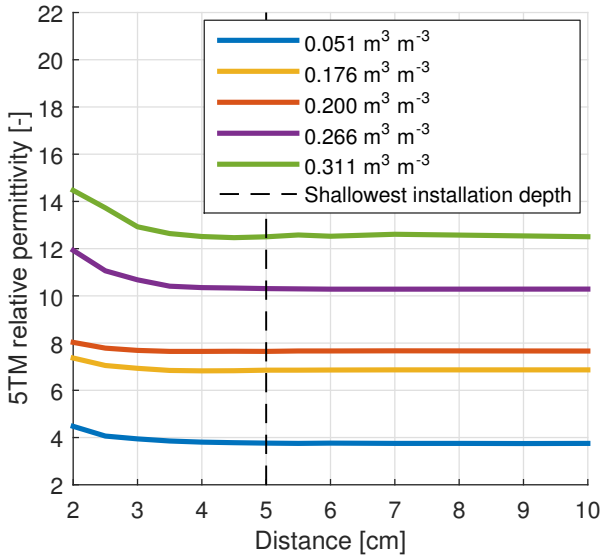

Figure 3.6 Relative permittivity readings of a 5TM sensor in a soil sample from station 1, obtained by moving a steel knife towards the sensor. The lines are the average of measurements obtained by performing the procedure described in Section 3.3.3 five times for each of the SMC conditions.

3.4.2 Calibration 5TM sensors

The results of the calibration procedure in Figure 3.7 show that the 5TM readings and gravimetric measurements correlate well. The relations between the 5TM readings and GVSMCs can best be approximated by two-term power functions. This is preferred over polynomial functions because power functions keep increasing beyond the range of GVSMCs obtained during the calibration procedure, which occurs in the field (further explained in Section 3.4.3.2). The power function between relative permittivity sensor readings and volumetric SMC reads

$$\theta_{cp} = c_A \times {\varepsilon_a}^{c_B} + c_C, \tag{3.2}$$

where θ_{cp} ($m^3\,m^{-3}$) is the calibrated volumetric SMC probe measurement, ε_a ($-$) is the measured relative permittivity, and c_A, c_B and c_C are calibration coefficients. The optimum calibration coefficients, listed in Table 3.4, are determined with the Matlab Curve Fitting Toolbox by non-linear least squares fitting.

Lab calibration has reduced *RMSD* values from $0.03\,m^3\,m^{-3}$–$0.07\,m^3\,m^{-3}$ to $0.02\,m^3\,m^{-3}$ and has eliminated the bias between the 5TM readings and GVSMCs (Table 3.5). The *RMSD* values using the Topp function are comparable or slightly worse than the values

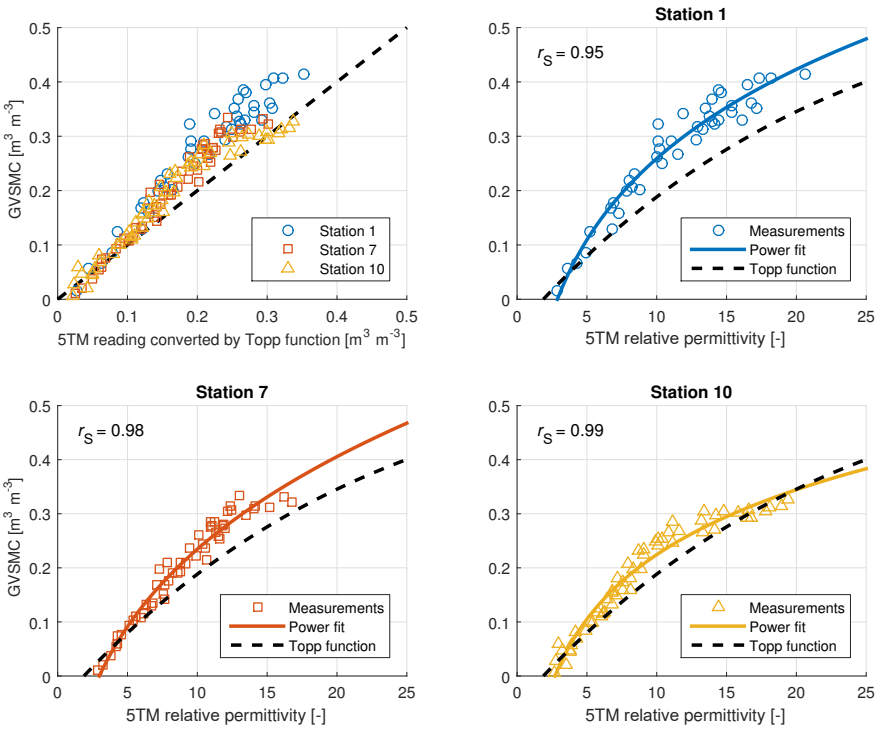

Figure 3.7 5TM relative permittivity readings against GVSMCs, measured in the laboratory in soil from a selection of fields. The power fits are used as calibration functions for converting the relative permittivity measurements by 5TM sensors to volumetric SMC.

Table 3.4 Calibration coefficients for converting relative permittivity measurements by 5TM sensors to volumetric SMC.

Station	Representative of stations	Coefficients		
		c_A	c_B	c_C
1	1, 2, 4, 5, 8, 12, 14, 15	1.276	0.1310	−1.466
7	6, 7	0.4853	0.2571	−0.6427
10	3, 9, 10, 11, 13	24.16	0.007038	−24.33

obtained by other studies using METER Group sensors. The *RMSD* values after the soil-specific calibration are comparable to the values obtained by other studies that performed a soil-specific calibration (Table 3.6).

Table 3.5 Accuracy metrics between GVSMCs and 5TM readings converted to volumetric SMC with the Topp function and the soil-specific calibration functions.

Station	Topp function			Number of pairs	Soil-specific calibration functions		
	r_S [–]	*RMSD* [$m^3\ m^{-3}$]	Bias [$m^3\ m^{-3}$]		r_S [–]	*RMSD* [$m^3\ m^{-3}$]	Bias [$m^3\ m^{-3}$]
1	0.95	0.0721	−0.0643	42	0.95	0.0235	0.000
7	0.98	0.0448	−0.0357	53	0.98	0.0177	0.000
10	0.99	0.0343	−0.0237	56	0.99	0.0190	0.000

Table 3.6 Accuracy metrics between the GVSMCs and readings by various METER Group sensors reported in previous studies.

Study	Study area and soil type	Sensor	*RMSD* with Topp function [$m^3\ m^{-3}$]	*RMSD* with soil-specific calibration function [$m^3\ m^{-3}$]
Bircher et al. (2012)	Western Denmark: Podzol sandy and loamy soils.	5TE	Agricultural land: 0.030 Forest: 0.026 Heath: 0.022	Not reported
Dente et al. (2009), Su et al. (2011)	Maqu, Tibetan Plateau: organic and silt loam soils.	EC-TM	0.06	0.02
Dente et al. (2011, 2012)	Twente, the Netherlands: sand and loamy sand.	EC-TM	0.054	0.023
Kizito et al. (2008)	Oso Flaco, USA: sand. Columbia, USA: silt loam.	TE	Not reported	Combined: 0.026 Sand: 0.015 Silt loam: 0.018
Matula et al. (2016)	Prague, Czech Republic: Haplic chernozem substrate loess.	EC-5 TE	EC-5: 0.031 TE: 0.029	EC-5: 0.018 TE: 0.023
Van der Velde et al. (2012b)	Naqu, Tibetan Plateau: loamy sand with gravel and high organic matter content.	EC-10	Not reported	0.029
Vaz et al. (2013)	Arizona, USA: sandy to clayey soils.	5TE	0.040	0.026
Varble and Chávez (2011)	Colorado, USA: see the fourth and fifth column.	5TE	Sandy clay loam: 0.022 Loamy sand: 0.025 Clay loam: 0.038	Sandy clay loam: 0.021 Loamy sand: 0.007 Clay loam: 0.028

3.4.3 Data verification

3.4.3.1 Data series completeness

The Raam network has generated data since April 2016. After 12 months of operations, the data series completeness is 96 %. Data gaps are caused by probes not being properly connected for a time and by the malfunctioning of sensors and loggers (specified in a readme file attached to the measurement data).

3.4.3.2 Data series analysis

We performed an initial data analysis of the behaviour and trends of SMC in the Raam. This includes an evaluation against the wilting point and saturated SMC for the soils in which the stations are placed. The wilting point and saturated SMC are estimated using the Staring series (Wösten et al., 2001), which provide the Van Genuchten parameters for soil water retention and soil hydraulic conductivity. These parameters can be used to estimate the SMC for a specific pressure head using the Van Genuchten (1980) equation:

$$\theta(h) = \theta_r + \frac{\theta_s - \theta_r}{[1 + (\alpha_G|h|)^{n_G}]^{1-1/n_G}}, \tag{3.3}$$

where h is the pressure head (cm of water), $\theta(h)$ is the SMC at h ($m^3\,m^{-3}$), θ_r is the residual SMC ($m^3\,m^{-3}$), θ_s is the saturated SMC ($m^3\,m^{-3}$), α_G is a scale parameter inversely proportional to the air entry value (cm^{-1}) and n_G is a parameter related to the pore size distribution (−). BOFEK2012 provides the Staring series at the station locations (Wösten et al., 2013).

Figure 3.8 shows that, generally, the station measurements are within the range expected based on BOFEK2012. However, the measurements of stations 1, 8 and 13 slightly exceed the saturated SMC, and stations 12 and 15 exceed the saturated SMC to a larger extent. Furthermore, the measurements at 80 cm depth at stations 1, 4, 6, 8 and 12 exceed the saturated SMC for about 25 % (station 8) to 100 % (station 6) of the time. This may be explained by local soil variability that is not captured by BOFEK2012 and macroporosity that is not considered by BOFEK2012. As BOFEK2012 only considers soil matrix porosity, deviations may occur when additional cracks, biopores or other macropores exist.

SMC measurements recorded in the field (Figure 3.8) exceed the maximum GVSMC obtained at saturated conditions in the laboratory (Figure 3.7). Reasons may be the presence of roots and macropores in the field, which can never be reproduced with the disturbed soil samples used for the calibration. In the field, macropores may be present, which increase the saturated SMC. Also the presence of large roots increases recorded water contents.

Figure 3.9 shows a time series plot of SMC measurements at station 1 for all measured depths, along with daily precipitation data of the Volkel weather station. The SMC series show a clear response to the precipitation events. The SMC at the upper layers shows larger dynamics than the

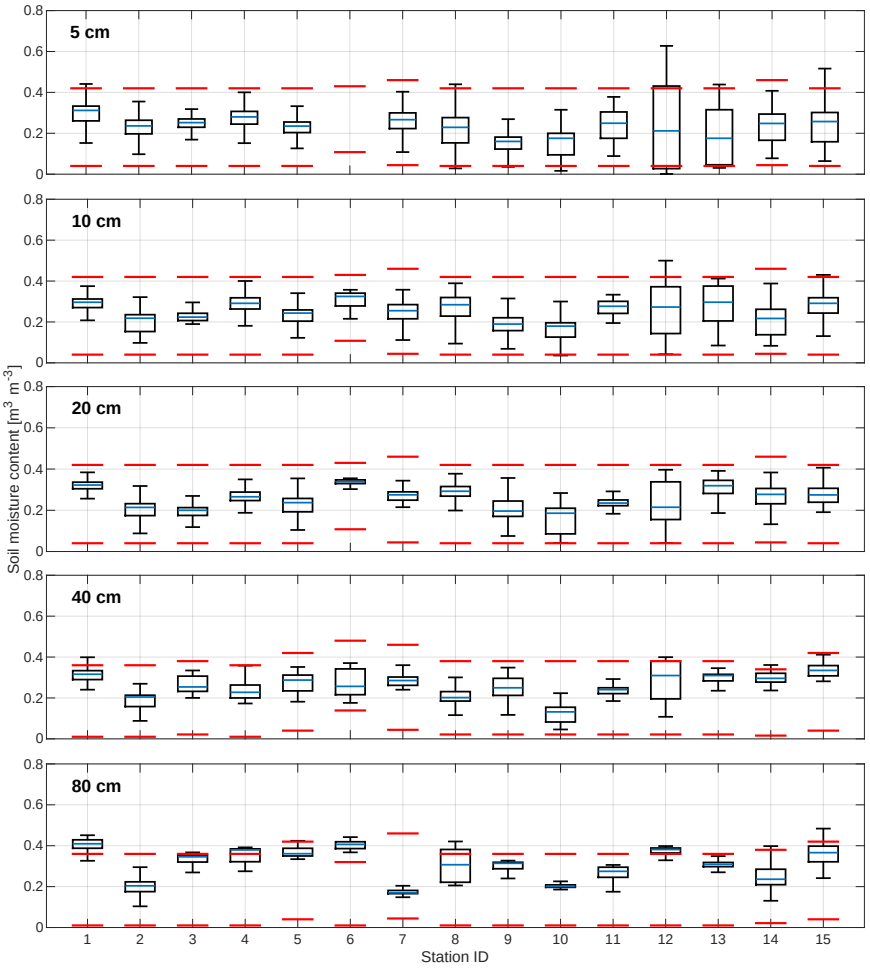

Figure 3.8 Box plots of the SMC measurements with theoretical wilting point and saturated SMC from BOFEK2012 (red lines), for each depth measured (5 April 2016–4 April 2017). Note that the box plot of 5 cm depth of station 6 is not shown: these data are removed from the dataset because of sensor malfunctioning.

SMC at deeper layers. The SMC at 80 cm is stable because it is controlled by the high phreatic groundwater level (GHG is 0.58 m below surface at the location of station 1; see Figure 3.3).

Figure 3.10a shows that the average SMC increases with depth from $0.23\,m^3\,m^{-3}$ at 5 cm to $0.30\,m^3\,m^{-3}$ at 80 cm. Indeed, one can expect the topsoil to be drier than the deeper parts due to infiltration and evapotranspiration. Figure 3.10b shows the relative standard deviation, which is defined as the ratio of the standard deviation of the SMC measurements to the average SMC, for each depth averaged over time and over all stations. A higher relative standard deviation indicates a larger vari-

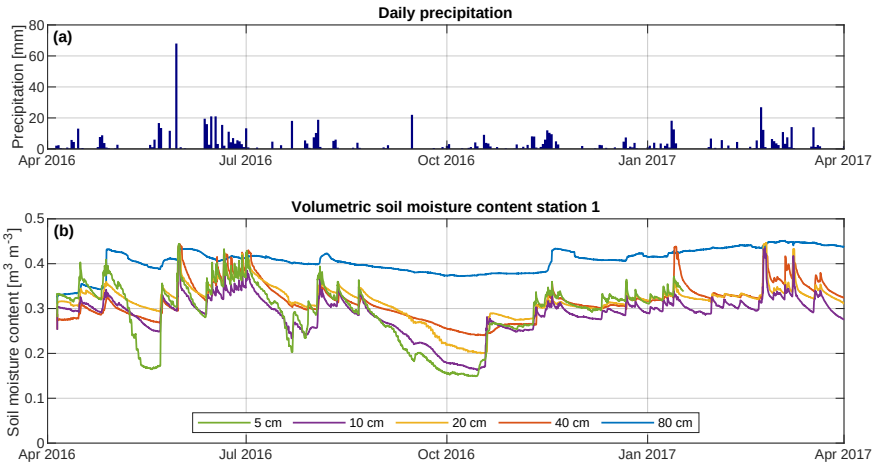

Figure 3.9 **(a)** Daily precipitation measured at Volkel weather station during the hydrological year 2016. **(b)** SMC measurements at station 1 during the hydrological year 2016 at 5 cm, 10 cm, 20 cm, 40 cm and 80 cm depth.

ability in SMC. Figure 3.10b indicates a decreasing variability in SMC with increasing depth, which was also visible for station 1 in Figure 3.9. The upper layers are mainly controlled by precipitation and evapotranspiration, which are variable in time. The deeper layers are mainly controlled by the generally high phreatic groundwater levels (Figure 3.3), which provide a continuous source of water by capillary rise.

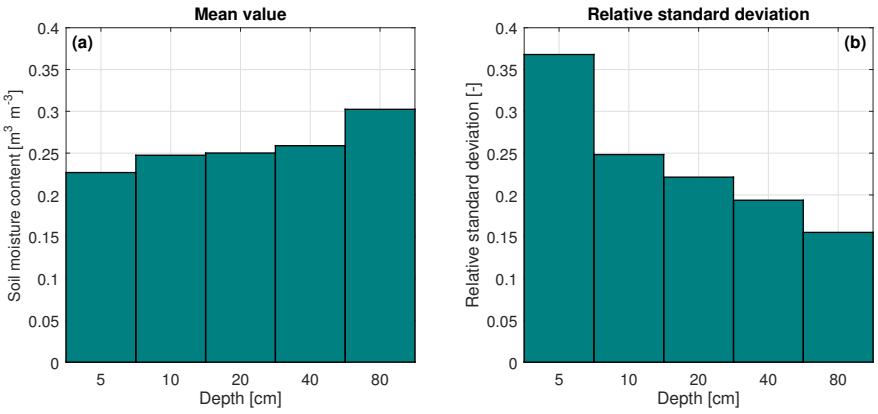

Figure 3.10 SMC average and relative standard deviation (ratio of the standard deviation to the average SMC), averaged over time (5 April 2016–4 April 2017) and over all stations for each depth measured.

We explored the influence of various factors on the dynamics of SMC. Figure 3.11a confirms our expectation that sandy soils have lower and more dynamic SMC than loamy/clayey soils. Figure 3.11b shows that locations with deep groundwater levels (> 1 m) are drier than loca-

tions with shallow groundwater levels (< 1 m). The situation of shallow groundwater levels applies to the stations 1, 6, 8, 11, 12, 13 and 15, based on groundwater level measurements by Waterschap Aa en Maas. Figure 3.11c shows that, in general, the SMC of maize fields is largest. Also, in the 2016/2017 winter period grasslands tended to be wetter than fields with sugar beets and onions. The observed dynamics of SMC on the catchment scale are as expected. However, local differences in surface elevation, soil composition and land cover play an important role in local-scale variation. Over time, changes in land cover and macroporosity, and soil temperature effects (Section 3.4.3.3) introduce uncertainties.

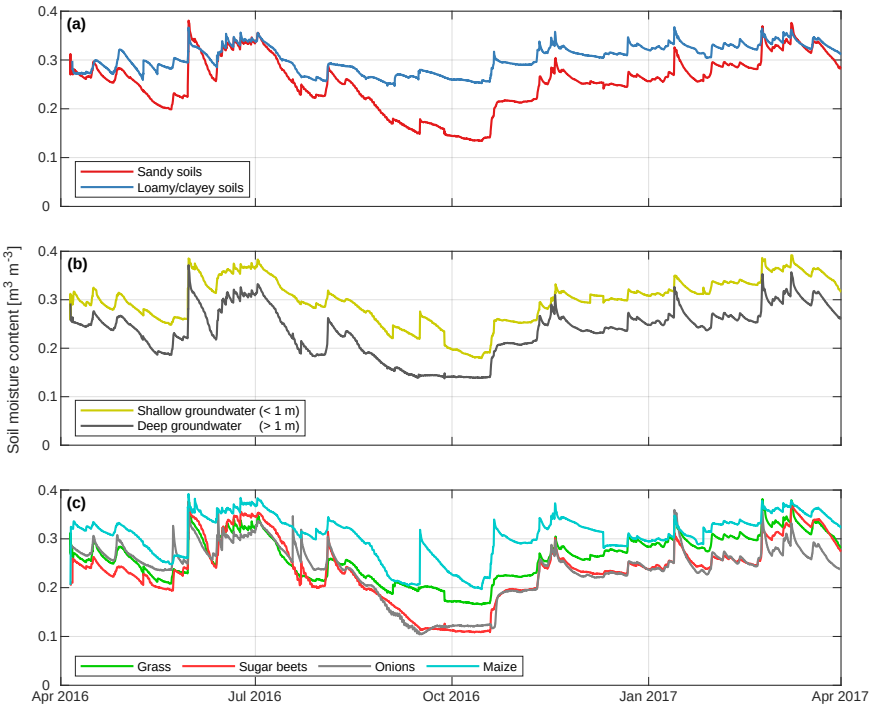

Figure 3.11 Influence of **(a)** soil type (Table 3.2), **(b)** groundwater depth (based on groundwater level measurements by Waterschap Aa en Maas) and **(c)** vegetation type (Table 3.3) on the SMC dynamics at 20 cm depth.

3.4.3.3 Effect of soil temperature

The SMC measurements at 5 cm, 10 cm and 20 cm depth show diurnal variations at all stations. Potential hydrological causes are the presence of dew and adsorption of water vapour by the soil, which cause an increase in SMC during the night and morning (Agam and Berliner, 2006; Kosmas et al., 1998). Alternatively, the SMC sensors might be sensitive to temperature. A number of studies found that the relative permittivity readings of SMC sensors are affected by soil temperature, varying from $-0.002\,\mathrm{m^3\,m^{-3}\,{}^\circ C^{-1}}$ to $0.004\,\mathrm{m^3\,m^{-3}\,{}^\circ C^{-1}}$ (Bogena et al.,

2007; Kizito et al., 2008; Rosenbaum et al., 2011; Verhoef et al., 2006). Figure 3.12 shows the largest SMC-to-temperature sensitivities measured at 5 cm depth, between 08:00 CET at day 1 and 08:00 CET at day 2, under the conditions of no precipitation on the day itself and the preceding 2 days, a maximum temperature difference between start and end time of 1.0 °C, and a maximum SMC difference between start and end time of 0.005 $m^3\,m^{-3}$. The SMC series are linearly detrended, assuming constant drainage and evaporation over the period of investigation (Cobos and Campbell, 2016). Then, we found the SMC-to-temperature sensitivities by applying a linear fit between the detrended SMC series and the soil temperature series. At station 7 in wet conditions (Figure 3.12a), there is a lag between the trends of SMC and soil temperature. This suggests that a soil hydrological process caused the diurnal variation in SMC, such as the addition of water by dew. At station 13 in dry conditions (Figure 3.12b), there is probably a direct effect of soil temperature on the SMC signal. Over all stations and all diurnal cycles satisfying the conditions introduced above, the average absolute sensitivity of SMC to soil temperature is 0.0006 $m^3\,m^{-3}\,°C^{-1}$. The difference between the minimum and maximum daily average soil temperature at 5 cm over the measurement period 5 April 2016 to 4 April 2017 is 19 °C to 28 °C. This translates into an effect of 0.011 $m^3\,m^{-3}$ to 0.017 $m^3\,m^{-3}$ on the SMC measurements by seasonal soil temperature variation. We consider this a small effect compared to local variations and other measurement uncertainties, and since there might also be a soil hydrological cause, we do not correct for the effect of soil temperature variation.

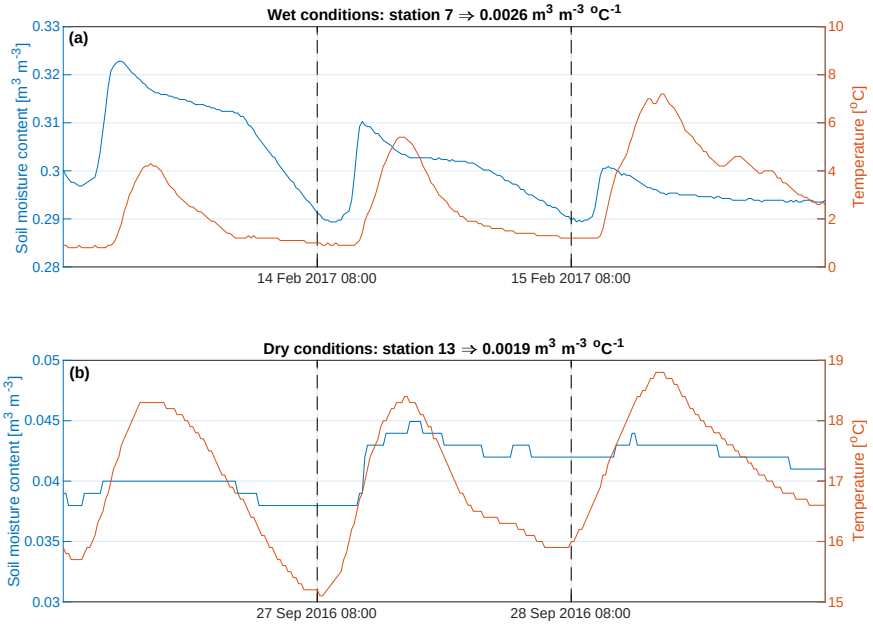

Figure 3.12 Largest sensitivities of SMC (blue line, left y-axis) to soil temperature variation (red line, right y-axis) in **(a)** wet conditions and **(b)** dry conditions.

The freezing of soils has a distinct effect on SMC measurements. When soils are frozen, the free water content decreases and this affects the bulk relative permittivity. These measurements do, however, give information about the free and frozen water contents. Together with the simultaneous soil temperature measurements, this could support research on the freezing of soils. However, the affected measurements are not usable as SMC measurements, so users of the SMC data are recommended to remove these from the measurement series.

3.5 Conclusions

The Raam SMC and soil temperature profile monitoring network contains 15 stations distributed over the Raam region. In total, 12 stations are located within the Raam catchment (catchment area of 223 km^2), and 5 of these stations are located within a closed sub-catchment of the Raam catchment (catchment area of 41 km^2). The stations consist of 5TM sensors installed at 5 cm, 10 cm, 20 cm, 40 cm and 80 cm depth. The measurements at 5 cm depth provide a reference for surface SMC estimations from earth observations, and the measurements at deeper layers enable the investigation of soil hydrological processes throughout the unsaturated zone. The experiment on the sensor's zone of influence shows that the sensor integrates a soil volume of 3 cm to 4 cm above and below the sensor's middle prong, so the installation depth of 5 cm is required to avoid effects of the open air. Soil-specific calibration functions for the 5TM sensors that have been developed under laboratory conditions lead to an accuracy of 0.02 $m^3\,m^{-3}$, which is lower than the accuracy range of 0.03 $m^3\,m^{-3}$–0.07 $m^3\,m^{-3}$ when applying the Topp function. Analysis of the first year of data shows that the station measurements are generally within the range expected based on the classified soil units and associated soil physical characteristics from the soil map of the Netherlands (BOFEK2012). Exceedance of the expected saturated SMC occurs at stations 1, 4, 6, 8, 12, 13 and 15, which could be the effect of local soil variability not captured by BOFEK2012 and macroporosity not considered by BOFEK2012. The measurements show expected SMC trends across the soil profile, with the average SMC increasing and the SMC variability decreasing with depth. The measurements confirm that sandy soils have lower and more dynamic SMC than loamy/clayey soils and locations with deep groundwater levels are drier than locations with shallow groundwater levels. Among the stations of the Raam network, on average, maize fields and grasslands are wetter than fields with sugar beets and onions.

The Raam SMC and soil temperature monitoring network and the mentioned additional datasets provide a valuable and ongoing dataset for investigating water management applications, for the calibration and validation of SMC estimations from earth observations on a coarse scale and a field scale, for the understanding of processes affected by SMC in the unsaturated zone, and for the assessment of land process models.

Stations 1 to 7, 10 and 12 to 15 can also be used for modelling the behaviour of the Raam catchment.

4 The uncertainty of in situ station measurements as reference for field-scale soil moisture content

The method and results in this chapter are based on parts (especially Supplement 2) of:

Benninga, H. F., Van der Velde, R., and Su, Z.: Sentinel-1 soil moisture content and its uncertainty over sparsely vegetated fields, J. Hydrol. X, 9, 100066, doi:10.1016/j.hydroa.2020.100066, 2020.

Abstract

A horizontal and a vertical mismatch between the soil moisture content (SMC) retrievals from satellites and the references from station measurements cause a spatial mismatch uncertainty between the two. This spatial mismatch uncertainty was estimated by calculating the unbiased root mean square deviation ($uRMSD$), i.e. the standard deviation, of station measurements at 5 cm depth with field measurements that were collected inside four agricultural fields and following uncertainty propagation rules. First, the field probe measurements were calibrated against gravimetrically determined volumetric SMC measurements, which results in an uncertainty of the field probe measurements of $0.020\,m^3\,m^{-3}$–$0.032\,m^3\,m^{-3}$. After correcting for the uncertainty of the field probe measurements, the estimates of spatial mismatch uncertainty for the four study fields are between $0.036\,m^3\,m^{-3}$ and $0.068\,m^3\,m^{-3}$. The average value of $0.051\,m^3\,m^{-3}$ is found as common measure for the spatial mismatch uncertainty.

Keywords: Soil moisture content, station measurements, reference uncertainty, field measurements.

4.1 Introduction

Soil moisture content (SMC) retrievals from satellite observations rely on references for calibration and validation purposes (e.g. Dorigo et al., 2011). The SMC references are typically obtained from in situ measurements. Continuous SMC monitoring stations can provide the references for a long time period and for a range of surface and hydrometeorological conditions.

A difference in sampling depth, however, exists between the SMC retrievals from satellite observations and the references from station measurements (Van der Velde et al., 2021; Escorihuela et al., 2010; Kornelsen and Coulibaly, 2013; Rondinelli et al., 2015; Zheng et al., 2019; Lv et al., 2018; Lee et al., 2017). C-band microwave observations, such as from the Sentinel-1 satellites, sample the soil from the surface to a depth of 1 cm–10 cm (Nolan and Fatland, 2003; Ulaby et al., 1996). In contrast, SMC stations are equipped with measurement probes at discrete depths, with the shallowest probe often at 5 cm or 10 cm depth. Consequently, a vertical mismatch is introduced.

Furthermore, a scale gap exists between SMC retrievals and (point-scale) station measurements (Western et al., 2002; Cosh et al., 2006). Many SMC monitoring networks, such as the Twente network (Van der Velde and Benninga, in preparation, in Chapter 2) and the Raam network (Benninga et al., 2018c, in Chapter 3) in the Netherlands, were developed on a regional scale. These two networks have densities of approximately 100 km^2 and 33 km^2 per station, and up to 80 km^2 and 8.2 km^2 per station in denser monitored areas. The distributed stations of a network can be averaged to obtain a regional estimate of SMC (e.g. Van der Velde et al., 2021; Crow et al., 2012; Colliander et al., 2017; Balenzano et al., 2021; Singh et al., 2020). Regarding fine- and field-scale SMC estimates, because of the large distance between the stations, this thesis and several other studies (e.g. Lievens and Verhoest, 2012; Van der Velde et al., 2015; Bauer-Marschallinger et al., 2019; Carranza et al., 2019; Pathe et al., 2009; Balenzano et al., 2021) rely on single SMC stations for providing the references. This is justified by the SMC temporal stability concept, from which can be inferred that single stations may be used for representing the SMC at larger scales, but this does involve a spatial mismatch uncertainty (Cosh et al., 2006; Vachaud et al., 1985; Cosh et al., 2016; Lievens and Verhoest, 2012; Pathe et al., 2009). Moreover, in the case of agricultural fields, SMC stations are generally installed at the border of fields for safety and continuity reasons. A horizontal mismatch between the SMC at an in situ station and field-averaged SMC originates from the spatial scale mismatch, differences in land cover, soil texture and structure, and local features such as nearby ditches and subsurface drainage pipes.

The vertical and horizontal mismatches cause uncertainty in the SMC station measurements as references for field-scale satellite (Sentinel-1 in the context of this thesis) observed SMC. The horizontal and vertical

mismatch uncertainties will together be referred to as spatial mismatch uncertainty ($U_{s,S1}$). The objective of this chapter is to estimate the $U_{s,S1}$. The measurements from continuous SMC monitoring stations at 5 cm depth were compared with field measurements that were collected inside four agricultural fields. Taking into account the uncertainty of the field probe measurements (U_{fp}), the $U_{s,S1}$ was estimated following uncertainty propagation rules.

4.2 Data

4.2.1 Station measurements

The SMC station measurements were collected by monitoring stations in the eastern part of the Netherlands. These monitoring stations are collectively known as the Twente network (Van der Velde et al., 2021; Dente et al., 2011, 2012) and further described in Van der Velde and Benninga (in preparation, in Chapter 2). They are equipped with 5TM probes (METER Group, 2019) installed at nominal depths of 5 cm, 10 cm, 20 cm, 40 cm and 80 cm, of which the readings are stored every 15 min. Van der Velde and Benninga (in preparation, in Chapter 2) calibrated the 5TM probes under laboratory conditions for the soils found in the study region. This resulted in an expected accuracy of 0.028 $m^3\,m^{-3}$. We used the 5 cm SMC measurements, which provide an integrated measurement over a soil depth of 1 cm to 9 cm (Benninga et al., 2018c, in Chapter 3).

4.2.2 Field measurements

Adjacent to monitoring stations, we selected two meadows (hereafter field I and II) and two cultivated fields (field III and IV) inside which we collected field measurements. The study fields are shown in Figure 4.1. Field I and III are adjacent to the same monitoring station. The study fields have loamy sandy surface layers (detailed in Appendix A.1). In the period of the field measurements, field III and IV were used to cultivate maize. The vegetation conditions vary from sparse or fallow outside the growing seasons (see the photos in Figure 4.1) up to leaf area indices (LAI) of 8.0 $m^2\,m^{-2}$, 7.7 $m^2\,m^{-2}$, 3.9 $m^2\,m^{-2}$ and 3.8 $m^2\,m^{-2}$ for field I–IV inside the growing seasons (Figure 7.6).

SMC field measurements of the 0 cm–5.7 cm layer were collected inside field I–IV with a handheld Stevens HydraProbe (Stevens Water Monitoring Systems, 2020). The field measurements were collected between May 2016 and April 2018 on 87 occasions in total. Fields I–IV have net surface areas, excluding a 20 m distance from the borders of the fields and a 40 m distance from trees and buildings to avoid possible influences on the satellite observations (Chapter 6), of 2.0 ha, 2.4 ha, 0.45 ha and 2.4 ha, respectively. Depending on the size of the field, we took field measurements at three to six locations (50 m–100 m apart). The locations are shown in Figure 4.1. At each location, four measurements were acquired with the field probe to reduce the uncertainty.

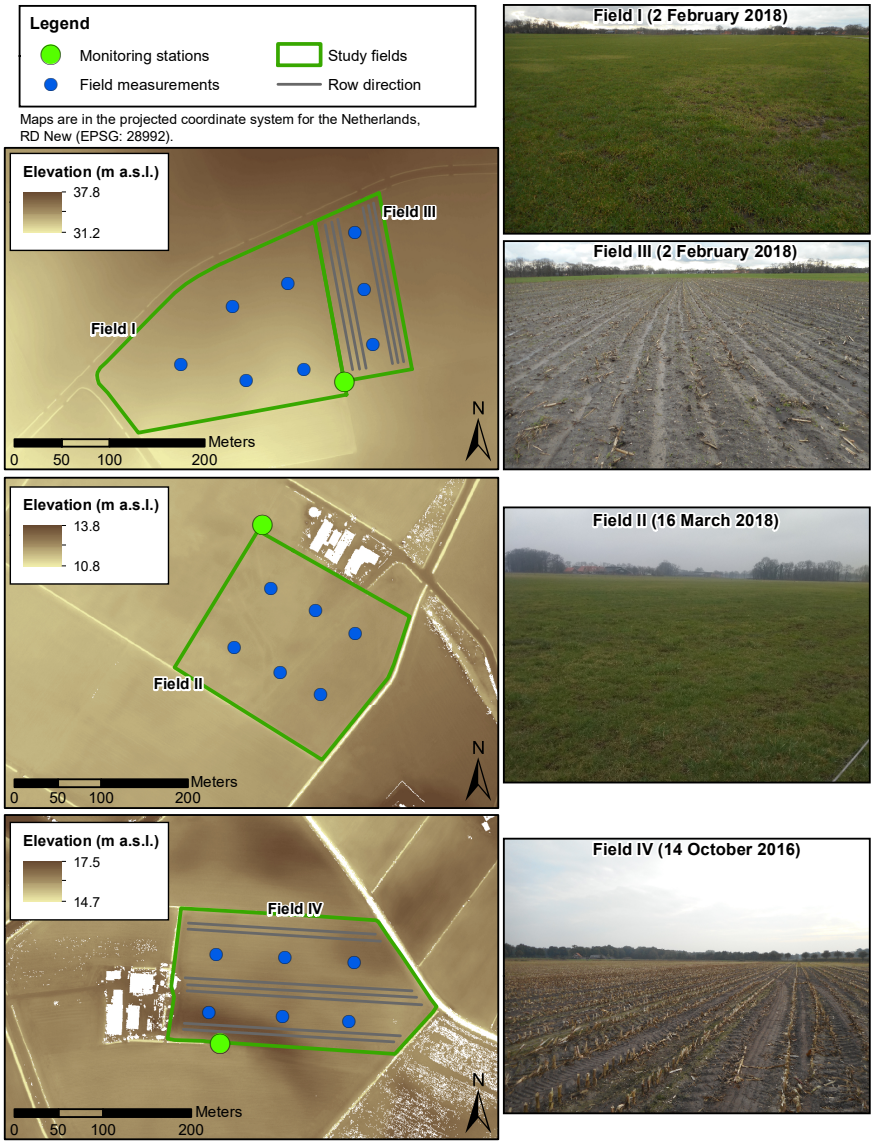

Figure 4.1 The locations of the SMC monitoring stations and SMC field measurements. Background is the digital terrain model AHN2 (Actueel Hoogtebestand Nederland, 2012b).

For the calibration of the field probe, on each measurement day gravimetrically determined volumetric SMC (GVSMC) measurements were taken immediately adjacent to field measurements. This follows the calibration procedure described in Cosh et al. (2005). Then, a power function, fitted through the match-ups of field probe temperature-corrected relative permittivity (ε_r) measurements and adjacent GVSMC measure-

ments, acts as calibration function in a similar fashion as described in Benninga et al. (2018c, in Chapter 3). The uncertainty of the field probe measurements (U_{fp}) is estimated between the calibrated probe measurements and the GVSMC references.

The field measurements are considered to be representative for Sentinel-1 observed SMC. Therefore, the field measurements were filtered according to the masking rules for frozen conditions, wet snow and intercepted rain that have been developed in Benninga et al. (2019, in Chapter 5) for Sentinel-1 backscatter (σ^0) observations. This reduces the number of field measurements, from the 87 occasions in total, to 66 used for estimating the $U_{s,S1}$.

4.3 Method

4.3.1 Definition of uncertainty

Differences between the field and station SMC have a systematic and variable component (Lee et al., 2017; Gruber et al., 2020). The systematic component is a correctable bias, which is further considered in Chapter 6. The variable component is the (random) uncertainty.

The standard deviation is selected as uncertainty measure. The standard deviation of the differences between two datasets, such as SMC retrievals and references, is often referred to as the unbiased root mean square deviation ($uRMSD$; Kerr et al., 2016):

$$uRMSD = \sqrt{\frac{\sum_{t=1}^{N}\left(Y_e(t) + \left(\overline{Y_r} - \overline{Y_e}\right) - Y_r(t)\right)^2}{N}}, \tag{4.1}$$

where N stands for the number of match-ups between estimates (Y_e) and references (Y_r), t stands for the observation number and the bars denote the means of Y_e and Y_r.

4.3.2 Spatial mismatch uncertainty

Both the measurement uncertainty of the SMC station probes (U_{sp}) and the representativeness of the SMC station measurements at 5 cm depth for the surface SMC at adjacent fields ($U_{s,f}$) contribute to the $U_{s,S1}$. Under the assumption that U_{sp} and $U_{s,f}$ are uncorrelated, their combined uncertainty can be calculated by following the addition rule for variances of independent random variables (Moore et al., 2017):

$$U_{s,S1} = \sqrt{{U_{sp}}^2 + {U_{s,f}}^2}. \tag{4.2}$$

Ultimately, the $U_{s,f}$ is retrieved by comparing the station measurements with the spatial mean of the field measurements. However, in addition to the $U_{s,f}$, the U_{sp} and U_{fp} constitute the uncertainty between the station measurements and the spatial mean of the field measurements. As the field measurements are averaged over a number of measurements

inside the study fields, from the standard deviation of a sample mean (Moore et al., 2017) follows that the U_{fp} decreases according to $1/\sqrt{M}$, where M is the number of measurements inside a field. Under the assumption that $U_{s,f}$, U_{sp} and U_{fp} are uncorrelated, the total uncertainty between the station measurements and the spatial mean of the field measurements ($U_{s,\overline{F}}$) can be formulated as:

$$U_{s,\overline{F}} = \sqrt{{U_{s,f}}^2 + \left(\frac{U_{fp}}{\sqrt{M}}\right)^2 + {U_{sp}}^2}. \tag{4.3}$$

Equation 4.3 can be converted to:

$$U_{s,f} = \sqrt{{U_{s,\overline{F}}}^2 - \left(\frac{U_{fp}}{\sqrt{M}}\right)^2 - {U_{sp}}^2}. \tag{4.4}$$

Combining Equation 4.2 and Equation 4.4 drops out U_{sp} and results in the final equation to estimate the $U_{s,S1}$:

$$U_{s,S1} = \sqrt{{U_{s,\overline{F}}}^2 - \left(\frac{U_{fp}}{\sqrt{M}}\right)^2}. \tag{4.5}$$

The U_{fp} is quantified in Section 4.4.1. The $U_{s,\overline{F}}$ is calculated with the $uRMSD$ (Equation 4.1) between the station measurements at the timestamps the field measurements were collected and the spatial mean of the field measurements.

4.3.3 Performance metrics

Next to estimates of U_{fp} and $U_{s,S1}$, the bias, Pearson correlation coefficient (r_P) and root mean square deviation ($RMSD$) were calculated between datasets. This was done between the calibrated probe measurements and the GVSMC references, and between the station and field-averaged SMC measurements. The equations for the bias, r_P and $RMSD$ are defined in Appendix A.2.

4.4 Results and discussion

4.4.1 Calibration and uncertainty of the field probe

Figure 4.2a shows the field probe ε_r measurements against the GVSMC references as well as the fitted calibration function between the two. Table 4.1 lists the performance metrics of the field measurements after the calibration. One (regional) calibration function for the measurements at the four study fields is justified by the overlapping point clouds (Figure 4.2a), the small remaining bias and high r_P (Table 4.1) for the individual fields. The match between the field probe measurements after application of the regional calibration function with the GVSMC references is shown in Figure 4.2b.

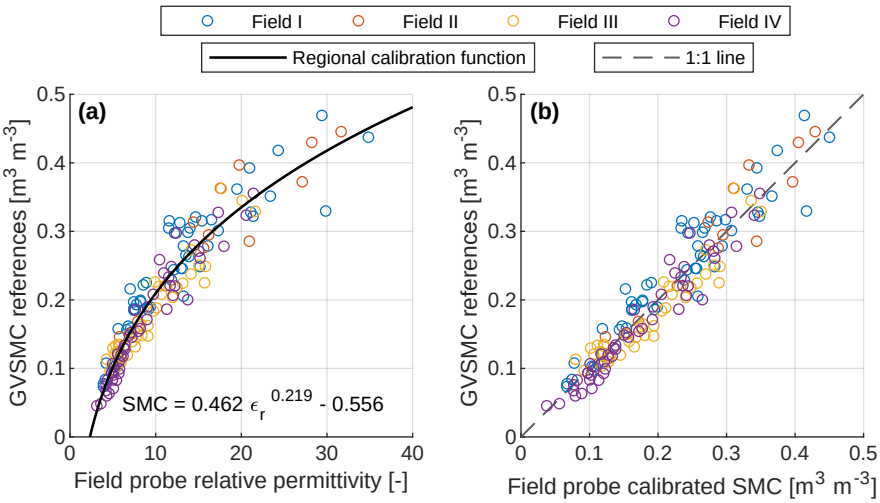

Figure 4.2 Field probe measurements against GVSMC references. **(a)** The calibration function between the field probe ε_r measurements and the references, and **(b)** the match between the calibrated field probe measurements and the references.

Table 4.1 The performance metrics of the SMC field measurements after the calibration against GVSMC references.

Field	Number of pairs	Bias [$m^3\,m^{-3}$]	r_P [−]	$RMSD$ [$m^3\,m^{-3}$]	$uRMSD$ (U_{fp}) [$m^3\,m^{-3}$]
I	52	−0.014	0.95	0.034	0.031
II	13	−0.0080	0.95	0.033	0.032
III	39	0.010	0.94	0.026	0.024
IV	50	0.0084	0.97	0.021	0.020

The measurement uncertainty of the field probe (U_{fp}) was quantified with the $uRMSD$ (Equation 4.1) between the calibrated field probe measurements and the GVSMC references. The values of $0.020\,m^3\,m^{-3}$ to $0.032\,m^3\,m^{-3}$ are comparable to the calibration accuracy of $0.028\,m^3\,m^{-3}$ estimated for the 5TM probes of the Twente network (Van der Velde and Benninga, in preparation, in Chapter 2) and $0.029\,m^3\,m^{-3}$ for a HydraProbe (Cosh et al., 2016).

4.4.2 Spatial mismatch uncertainty

Figure 4.3 shows the SMC station measurements, the measurements at the different locations within the fields, and the spatial mean of the field measurements. Table 4.2 lists the bias and r_P between the SMC field means and the station measurements. For field IV an inconsistency was found in the station measurements between May 2016–November 2016 and April 2017–September 2017 (see Figure 4.3 and the biases in Table 4.2), so these periods are listed separately in Table 4.2. The

inconsistency between these periods is further discussed in Chapter 6. The high r_P values in Table 4.2 correspond with the temporal stability concept that single stations can have a high correlation with the mean SMC at a larger scale (Vachaud et al., 1985; Cosh et al., 2006), and support the use of the station measurements at 5 cm depth as representative for the surface SMC of the adjacent fields (Lievens and Verhoest, 2012).

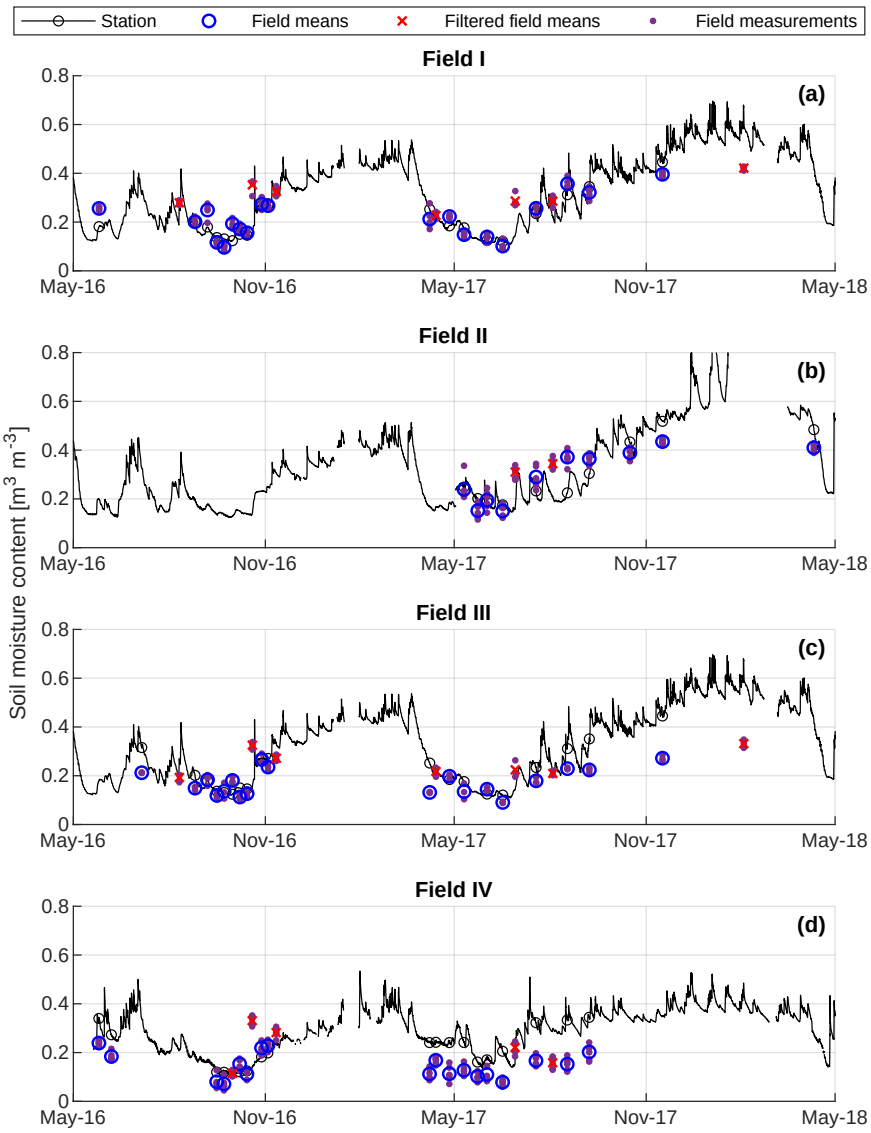

Figure 4.3 SMC station measurements and SMC field measurements. Both the measurements at the separate field locations in Figure 4.1 and the spatial mean of the field measurements are shown.

Equation 4.1 and Equation 4.5 were applied to estimate $U_{s,\overline{F}}$ and $U_{s,S1}$. Table 4.2 lists the results for the study fields. By first averaging for field IV the $U_{s,S1}$ for the two separate periods and then calculating the mean over field I–IV, a value of 0.051 $m^3\,m^{-3}$ is found as the common measure for $U_{s,S1}$.

Table 4.2 Comparison between the station and field-averaged SMC measurements.

Field	Number of pairs	Bias [$m^3\,m^{-3}$]	r_P [–]	$U_{s,\overline{F}}$ [$m^3\,m^{-3}$]	$U_{s,S1}$ [$m^3\,m^{-3}$]
I	19	0.0079	0.90	0.037	0.036
II	10	−0.0014	0.83	0.068	0.068
III	19	−0.042	0.80	0.056	0.056
		All measurements: −0.076 (18)	0.55	0.064	0.064
IV	18	May '16–Nov '16: −0.024 (8)	0.75	0.051	0.051
		April '17–Sep '17: −0.12 (10)	0.81	0.039	0.039

Measurements were collected at three to six locations within a field. Furthermore, at each field location four measurements were acquired. This brings the number of measurements per study field on 12 for field III, 20 for field I, and 24 for field II and IV. From Equation 4.5 can be seen that the effect of U_{fp} is decreased by a factor $1/\sqrt{M}$. As such, the considerable number of measurements that was used to estimate the SMC field mean causes that the effect of U_{fp} is small and the $U_{s,S1}$ values are almost equal to the $U_{s,\overline{F}}$ values.

The field measurements are considered representative for satellite-observed SMC. To be consistent with the estimation of SMC from satellite observations, the field measurements were filtered according to masking rules developed for Sentinel-1 σ^0 observations (Benninga et al., 2019, in Chapter 5). The filtered field measurements are also shown in Figure 4.3. Only the masking rule for rain interception applied to the field measurements as the masking rule conditions for snow and frozen conditions were not met during field measurements. Including both the unfiltered and the filtered field measurements results in the $U_{s,S1}$ values listed in Table 4.3. The $U_{s,S1}$ values are lower with (Table 4.2) than without the filtering. This indicates that the masking rule for rain interception, developed for Sentinel-1 σ^0 observations, is applicable to these field measurements and effective in reducing the uncertainty. Whether this is also the case for station measurements at 5 cm or 10 cm depth should be investigated.

Time-invariant $U_{s,S1}$ values per study field and a common $U_{s,S1}$ value were estimated, but this approach could be a simplification of reality. Several studies showed that the spatial variability of SMC depends on the SMC conditions. The SMC spatial variability is generally lowest in dry and wet conditions and increases during intermediate SMC conditions, as a result of (at this scale) homogeneous precipitation, causing homogeneous wet conditions, and dry-down processes which are first heterogenizing and then homogenizing (Ryu and Famiglietti, 2005; Kornelsen and Coulibaly, 2013). Based on more than 36 000 measurements

Table 4.3 Same as Table 4.2, but without filtering the field measurements according to the masking rules developed for Sentinel-1 σ^0 observations.

Field	Number of pairs	Bias [m^3 m^{-3}]	r_P [–]	$U_{s,\overline{F}}$ [m^3 m^{-3}]	$U_{s,S1}$ [m^3 m^{-3}]
I	26	0.012	0.78	0.074	0.074
II	12	0.022	0.74	0.082	0.081
III	26	−0.039	0.68	0.088	0.088
IV	23	All measurements: −0.053 (23)	0.26	0.087	0.087
		May '16–Nov '16: 0.0037 (11)	0.52	0.076	0.075
		April '17–Sep '17: −0.10 (12)	0.39	0.060	0.060

collected in two sub-humid regions in central USA, Famiglietti et al. (2008) developed the empirical functions of SMC spatial variability shown in Figure 4.4. As the spatial variability of SMC depends on the SMC conditions, the $U_{s,S1}$ may actually also depend on the SMC conditions. The $U_{s,S1}$ values were estimated mainly on SMC measurements in the regime for which the highest spatial variability was found, namely in intermediate SMC conditions between 0.1 m^3 m^{-3} and 0.25 m^3 m^{-3} (Figure 4.4), so the $U_{s,S1}$ value may be interpreted as probably being quite close to the upper limit and the value may decrease for wetter and drier soil conditions.

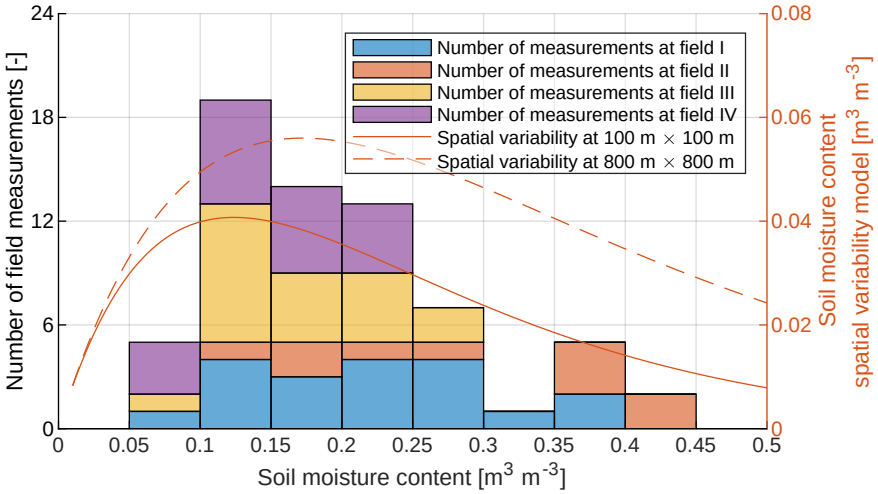

Figure 4.4 The number of measurements at field I–IV and the SMC spatial variability as a function of SMC and extent. The SMC spatial variability is adopted from the empirical functions developed by Famiglietti et al. (2008).

In contrast, the sampling depth of the field measurements likely causes an underestimation of the $U_{s,S1}$. Although sampling depths of up to 10 cm are reported for C-band σ^0 observations, this is for very dry soils and it is 1 cm–3 cm in the general SMC regime (Nolan and Fatland, 2003; Ulaby et al., 1996). 0 cm–5.7 cm layer field measurements were collected and compared with station measurements to estimate the $U_{s,S1}$, but larger differences with the station measurements are expected because Sentinel-1's sampling depth will generally be smaller.

Besides, the study by Famiglietti et al. (2008) suggests that the spatial variability of SMC increases with extent. Figure 4.4 shows this for $100\,\mathrm{m} \times 100\,\mathrm{m}$ and $800\,\mathrm{m} \times 800\,\mathrm{m}$, which are the extents in Famiglietti et al. (2008) closest to the surface areas of the study fields. The $U_{s,S1}$ estimates for the study fields in Table 4.2 do not directly show a relation with their surface areas. However, care should be taken when extrapolating the $U_{s,S1}$ estimates to fields with different surface areas. Furthermore, SMC variability may depend on field conditions regarding e.g. land cover, soil characteristics and agricultural management. Such effects on $U_{s,S1}$ require further investigation.

4.5 Conclusion

The uncertainty of SMC station measurements as references for satellite (Sentinel-1) observed field-scale SMC ($U_{s,S1}$) was estimated by comparing station measurements against measurements that were collected inside four study fields with a handheld device. In the calculation, we corrected for the uncertainty of the field probe measurements (U_{fp}). A significant amount of uncertainty is detected between SMC station measurements and field-scale SMC estimates. The estimates of $U_{s,S1}$ for the four study fields are between $0.036\,\mathrm{m^3\,m^{-3}}$ and $0.068\,\mathrm{m^3\,m^{-3}}$. The average value of $0.051\,\mathrm{m^3\,m^{-3}}$ is found as common measure for $U_{s,S1}$. It may be expected that the $U_{s,S1}$ decreases in wet and dry conditions, is underestimated due to the station probes' sampling depth being closer to the sampling depth of the field measurements than to that of the satellite observations as well as depends on the extent of fields and possibly more field conditions; aspects which require further investigation.

5 Impacts of radiometric uncertainty and weather-related surface conditions on soil moisture content retrievals with Sentinel-1

This chapter is based on:

Benninga, H. F., Van der Velde, R., and Su, Z.: Impacts of Radiometric Uncertainty and Weather-Related Surface Conditions on Soil Moisture Retrievals with Sentinel-1, Remote Sens., 11, 2025, doi:10.3390/rs11172025, 2019.

Abstract

The radiometric uncertainty of synthetic aperture radar (SAR) observations and weather-related surface conditions, caused by frozen conditions, snow and intercepted rain, affect the backscatter (σ^0) observations and limit the accuracy of soil moisture content (SMC) retrievals. This study estimates Sentinel-1's radiometric uncertainty, identifies the effects of weather-related surface conditions on σ^0 and investigates their impact on SMC retrievals for various conditions regarding SMC, surface roughness and incidence angle. Masking rules for the surface conditions that disturb σ^0 were developed based on meteorological measurements and timeseries of Sentinel-1 observations collected over five forests, five meadows and five cultivated fields in the eastern part of the Netherlands. The Sentinel-1 σ^0 observations appear to be affected by frozen conditions below an air temperature of 1 °C, snow during Sentinel-1's morning overpasses on meadows and cultivated fields and interception after more than 1.8 mm of rain in the 12 h preceding a Sentinel-1 overpass, whereas dew was not found to be of influence. After the application of these masking rules, the radiometric uncertainty was estimated by the standard deviation of the seasonal anomalies timeseries of the Sentinel-1 forest σ^0 observations. By spatially averaging the σ^0 observations, the Sentinel-1 radiometric uncertainty improves from 0.85 dB for a surface area of 0.25 ha to 0.30 dB for 10 ha for the VV polarization and from 0.89 dB to 0.36 dB for the VH polarization, following approximately an inverse square root dependency on the surface area over which the σ^0 observations are averaged. Deviations in σ^0 were combined with the σ^0 sensitivity to SMC as simulated with the integral equation method (IEM) surface scattering model, which demonstrated that both the disturbing effects by the weather-related surface conditions (if not masked) and radiometric uncertainty have a significant impact on the SMC retrievals from Sentinel-1. The SMC retrieval uncertainty due to radiometric uncertainty ranges from 0.01 $m^3\,m^{-3}$ up to 0.17 $m^3\,m^{-3}$ for wet soils and small surface areas. The impacts on SMC retrievals are found to be weakly dependent on the surface roughness and the incidence angle, and strongly dependent on the surface area (or the σ^0 disturbance caused by a weather-related surface condition for a specific land cover type) and the SMC itself.

Keywords: Sentinel-1, radiometric uncertainty, disturbing surface conditions, masking rules, soil moisture content.

5.1 Introduction

Earth observations made by synthetic aperture radar (SAR) instruments can be used to estimate soil moisture content (SMC) at field scale (e.g. El Hajj et al., 2017; Lievens and Verhoest, 2012; Su et al., 1997; Amazirh et al., 2018; Kornelsen and Coulibaly, 2013). However, SAR backscatter (σ^0) observations contain inaccuracies due to calibration uncertainties, sensor instabilities and speckle effects (Ulaby and Long, 2014; Torres et al., 2012; Schwerdt et al., 2017; Schmidt et al., 2018), hereafter combined and referred to as radiometric uncertainty. In addition to imperfections inherent to a retrieval algorithm, the radiometric uncertainty controls the accuracy of SMC retrievals.

The radiometric uncertainty of SAR observations can be determined by analysing the temporal σ^0 variability of a target for which the σ^0 is time-invariant (El Hajj et al., 2016; Baghdadi et al., 2015; Hawkins et al., 1999). The C-band Sentinel-1 signal is unlikely to penetrate dense canopies (Link et al., 2018; Guerriero et al., 2016; Ulaby et al., 1990; Ulaby and Long, 2014). Therefore, forest σ^0 can be assumed to be unaffected by variations in SMC and surface roughness, which can cause large and abrupt changes in the σ^0 over other land covers, and forests should behave as fairly time-invariant targets (Baghdadi et al., 2015; El Hajj et al., 2016; Hawkins et al., 1999). This property of the forest σ^0 was exploited to estimate the radiometric stability of SAR observations by calculating the standard deviation of the σ^0 timeseries (El Hajj et al., 2016; Baghdadi et al., 2015; Hawkins et al., 1999).

Previous studies (El Hajj et al., 2016; Baghdadi et al., 2015; Hawkins et al., 1999) determined the radiometric stability of σ^0 timeseries from targets with surface areas ranging from a pine tree forest of 8.1 ha (856 Sentinel-1 pixels) to an Amazon rainforest area of 10 000 km^2. Calibration uncertainties and sensor instabilities will mainly determine the variability in the mean forest σ^0 over such large surface areas, because the large number of independent samples leads to the suppression of the speckle effects (Ulaby and Long, 2014; Hawkins et al., 1999). Radiometric uncertainty from smaller surface areas, which contains a larger contribution of speckle due to the lower number of independent samples, is particularly relevant for the retrieval of SMC at field scale. If speckle is not completely suppressed, this is a contributing factor to the SMC retrieval accuracy. For example, with synthetically generated speckled σ^0 representing Sentinel-1 observations of bare soil, Pierdicca et al. (2014) obtained an improvement in SMC retrieval accuracy (root mean square deviation, *RMSD*) from 0.035 m^3 m^{-3} at the native resolution (1 pixel) to 0.025 m^3 m^{-3} at field scale (10×10 pixels). For the quantification of radiometric uncertainty and its effect on SMC retrieval uncertainty, radiometric uncertainty needs to be determined as a function of the surface area over which the σ^0 observations are aggregated.

Besides radiometric uncertainty, several weather-related surface conditions may disturb σ^0 observations, e.g., inundation (Henry et al., 2006;

Huang et al., 2018), frozen conditions (Hallikainen et al., 1985; Mironov et al., 2017; Baghdadi et al., 2018), wet snow (Ulaby and Long, 2014; Nagler and Rott, 2000; Baghdadi et al., 1997), intercepted rain (El Hajj et al., 2016; De Jong et al., 2000; Cisneros Vaca and Van der Tol, 2018; Dobson et al., 1991) and dew (Jackson and Moy, 1999; Gillespie et al., 1990; Ulaby and Long, 2014; Riedel et al., 2002), and thus affect the forthcoming SMC retrievals. Masking satellite observations for conditions under which SMC retrieval is not possible or more uncertain is common for existing coarse resolution (> 9 km) products, such as from the Advanced Scatterometer (ASCAT; Naeimi et al., 2012; Wagner et al., 2013), Soil Moisture and Ocean Salinity (SMOS; Kerr et al., 2016; Wigneron et al., 2017) and Soil Moisture Active Passive (SMAP; Wigneron et al., 2017). Previous studies (Bauer-Marschallinger et al., 2019; Molijn et al., 2018) have acknowledged that geophysical products derived from Sentinel-1 are also subject to elevated uncertainty levels if unwanted disturbances in the σ^0 observations are not addressed and further development of operational products would benefit from a masking procedure for disturbing surface conditions.

The objectives of this study are (1) to develop a masking procedure for the weather-related surface conditions that disturb Sentinel-1 σ^0 observations, (2) to estimate Sentinel-1's radiometric uncertainty as a function of surface area, and (3) to determine their impact on SMC retrievals. We investigated the weather-related surface condition effects of frozen conditions, snow, intercepted rain and dew, which are represented by nearby meteorological measurements, on Sentinel-1 σ^0 observations collected over five meadows, five cultivated fields and five forests in the Twente region in the east of the Netherlands. The results from these analyses are used to define a set of rules that could be taken as a starting point for the development of a formal masking procedure. After the application of the developed masking rules, the Sentinel-1 σ^0 observations of the five forests are used to estimate Sentinel-1's radiometric uncertainty (s_{S1}) as a function of the forest surface area (A) over which the Sentinel-1 σ^0 observations are averaged (from 0.25 ha to 10 ha). With the quantifications of s_{S1} and the disturbing effects on σ^0 by the weather-related surface conditions, we determined their impact on SMC retrievals from Sentinel-1 σ^0 for various bare surface conditions. The widely applied integral equation method (IEM) surface scattering model (Fung et al., 1992) was employed to simulate the σ^0 sensitivity to SMC for a surface representing meadows and a surface representing cultivated fields, for the incidence angles at which Sentinel-1 observes the Twente region and for dry to wet soil conditions. With these analyses we aim to provide insight in the role that the s_{S1} and the weather-related surface conditions (if not masked) play in the accuracy of SMC retrievals from Sentinel-1 σ^0.

5.2 Study area and data

5.2.1 Twente region and meteorological measurements

The Twente region, located in the eastern part of the Netherlands (Figure 5.1a), has a temperate oceanic climate. In the region are 20 stations equipped with 5TM SMC and soil temperature sensors (METER Group, 2019) at depths of 5 cm, 10 cm, 20 cm, 40 cm and 80 cm (Dente et al., 2012, 2011). The Twente region and the SMC and temperature monitoring network are further described in Van der Velde and Benninga (in preparation, in Chapter 2).

The Twente region is rather flat with some elevated glacial ridges, see Figure 5.1b. The land cover in the region is a mosaic of cultivated crop fields, meadows, forested and built-up areas. The masking rules for weather-related surface conditions have been developed on Sentinel-1 σ^0 observations over five forests, five meadows and five cultivated fields (Figure 5.1b), and the s_{S1} has been estimated using the σ^0 observations of the five forests. These forest areas (Figures 5.1c–g) were selected because they consist of dense forest, they are approximately homogeneous and have an area larger than 10 ha. The CORINE Land Cover maps 2012 and 2018 (Copernicus Land Monitoring Service, 2019) and the High Resolution Layer Forest 2012 and 2015 (Copernicus Land Monitoring Service, 2018) show that forest I–III are coniferous forest. Forest IV is dominated by coniferous forest (classified as coniferous forest in the CORINE Land Cover maps) and forest V contains a significant portion of deciduous forest (classified as deciduous forest in the CORINE Land Cover maps). Field visits have confirmed these classifications and revealed that most parts of the forests I–V have an understory of deciduous bush and trees, and that the soil surfaces are covered by litter.

According to laboratory analyses (Dente et al., 2011) and the soil physical units map of the Netherlands ('bodemfysische eenhedenkaart 2012' in Dutch, or BOFEK2012; Wösten et al., 2013), sandy to loamy sandy soils dominate the surface layer in the Twente region. The average soil texture from BOFEK2012 for the selected meadows and cultivated fields is 81.5 % sand, 14 % silt and 4.5 % clay, with a bulk density of 1.36 g cm^{-3}.

The Royal Netherlands Meteorological Institute ('Koninklijk Nederlands Meteorologisch Instituut' in Dutch, or KNMI) operates three automated weather stations in the Twente region (Figure 5.1b). The stations provide hourly measurements (KNMI, 2019), of which air temperature (1.5 m above ground) and relative humidity (1.5 m above ground) at hourly time steps, rainfall as hourly sums and wind speed (10 m above ground) as hourly averages were used to develop the masking rules for frozen conditions, rain interception and dew (see Section 5.3.2). Table 5.1 lists some statistics on the measurements by the KNMI weather stations in the Twente region.

Adjacent to one of the selected meadows (since 13 April 2017) and two of the selected cultivated fields (since 27 May 2016 and 13 April 2017) rainfall was measured by a tipping bucket rain gauge (Davis Rain Col-

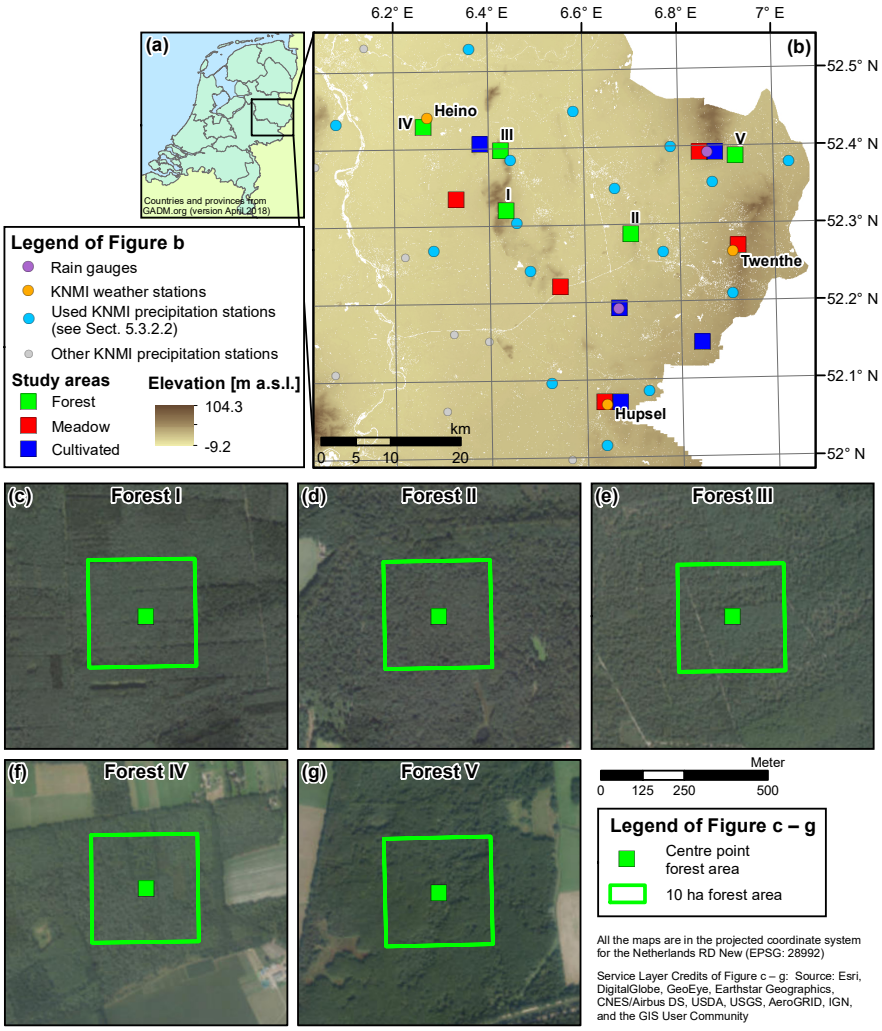

Figure 5.1 **(a)** Location of the Twente region in the Netherlands. **(b)** The Twente region with the selected study fields and the meteorological measurement locations. Background is the digital terrain model AHN2 (Actueel Hoogtebestand Nederland, 2012b). The grid shows WGS84 coordinates. **(c–g)** Zoom-ins of the selected forest areas I to V.

lector 7857M; Davis Instruments, 2015) with a resolution of 0.2 mm, also shown in Figure 5.1b. If available, these measurements were used to develop the masking rule for rain interception (see Section 5.3.2.3).

KNMI also operates a network of precipitation stations (Figure 5.1b) that record precipitation and snow depth daily at 09:00 CET (KNMI, 2019). These measurements were used to develop the masking rule for snow (see Section 5.3.2.2). Over 2014–2019 the surface was covered by snow on average 10 days per year, varying between 5 days in the hydrological

Table 5.1 Summary statistics of the measurements by the three KNMI weather stations (KNMI, 2019) in the Twente region, averaged over five hydrological years (1 April 2014–31 March 2019).

Condition	Twenthe	Hupsel	Heino
Minimum monthly mean air temperature [°C]	2.9 (January)	3.2 (January)	3.0 (January)
Maximum monthly mean air temperature [°C]	19.0 (July)	19.0 (July)	18.7 (July)
Number of days per year on which the air temperature dropped below 0 °C	53	49	49
Annual amount of rainfall [mm]	830	744	740
Number of days per year with rain (minimum 1 mm d^{-1})	139	124	131

year 2015 (1 April 2015–31 March 2016) and 23 days in the hydrological year 2016 (1 April 2016–31 March 2017).

5.2.2 Sentinel-1 imagery

The Sentinel-1 constellation (Sentinel-1A and Sentinel-1B) provides over land images in Interferometric Wide Swath (IW) mode at VV and VH polarization, C-band (5.405 GHz), with a reported radiometric accuracy of 1 dB (three standard deviations) and, after multi-looking, a spatial resolution of 20 m × 22 m (4.4 equivalent number of looks) for the Ground Range Detected (GRD) High Resolution (HR) product (Torres et al., 2012; Bourbigot et al., 2016). By analysing timeseries of Sentinel-1 σ^0 observations from point targets with a well-specified σ^0, radiometric accuracy standard deviations of 0.30 dB (one standard deviation) for Sentinel-1A (Schmidt et al., 2018), and 0.29 dB (one standard deviation) for Sentinel-1B (Schwerdt et al., 2017) have been obtained.

Level-1 GRD HR IW Sentinel-1 images were downloaded from the Copernicus Open Access Hub (Copernicus, 2019). We processed the images using the following operations available in the European Space Agency (ESA)'s Sentinel Application Platform (SNAP) V6.0 (ESA, 2019): (1) Apply Orbit File, (2) Thermal Noise Removal, and (3) Range Doppler Terrain Correction, including radiometric normalization to σ^0 (in $m^2\,m^{-2}$) with projected local incidence angles on a geographic grid (WGS84) with a pixel spacing of 9.0E−5° (equivalent to 10 m × 6.1 m at the study region's latitude). Subsequently, we averaged the Sentinel-1 σ^0 observations separately over the five individual forests for surface areas ranging from 0.25 ha (41 pixels) to 10 ha (1626 to 1631 pixels) taken from the centre points (see Figures 5.1c–g), the five individual meadows and the five individual cultivated fields, and we converted the σ^0 values to decibel (dB). In the averaging, we excluded the area within 20 m from borders of fields and 40 m from trees (obviously not for the forests) and buildings to avoid possible influences on the σ^0 values from outside the study fields. Sentinel-1A (since 3 October 2014) and Sentinel-1B (since 28 September 2016) together make observations of the Twente region with a temporal resolution of 1.5 days. Table 5.2 specifies the orbits that cover the study region. We included all Sentinel-1 images available for the

Twente region from 3 October 2014 until 1 November 2018, which are in total 676 images.

Table 5.2 Specifications of the Sentinel-1 orbits that cover the Twente region.

Relative orbit number	Pass	Acquisition time (CET)	Number of Sentinel-1 images	Projected incidence angle over the study fields
15	Ascending	18:16	165	32.8°–36.8°
37	Descending	6:49	166	33.7°–38.4°
88	Ascending	18:24	171	41.2°–45.1°
139	Descending	6:41	174	41.5°–46.2°

5.3 Methods

5.3.1 Sentinel-1 seasonal anomalies

Seasonal σ^0 dynamics, if not removed from the σ^0 timeseries, would obscure the assessment of the effects of weather-related surface conditions on Sentinel-1 σ^0 and would cause an overestimation of the s_{S1}.

The σ^0 observations from meadows and cultivated fields vary due to variations in SMC and vegetation. As the σ^0 increases with increasing SMC (e.g. Kornelsen and Coulibaly, 2013; Ulaby and Long, 2014; Altese et al., 1996), the Sentinel-1 σ^0 observations over the meadows and cultivated fields are expected to be higher in winter than in summer. The SMC measurements at 5 cm depth in the Twente region indicate that the SMC is generally at a high level from mid-November to mid-March (mean is $0.42\,m^3\,m^{-3}$) and at a low level from mid-May to mid-October (mean is $0.23\,m^3\,m^{-3}$). However, the exact surface SMC cycle is different each year and also contains dynamics on shorter timescales in response to meteorological events. The growing season typically starts in April and ends in October, during which the meadows are cut multiple times and/or being grazed and the crops on the cultivated fields are sowed and harvested. Depending on the crop type and the development stage, the vegetation decreases the σ^0 when attenuation is dominant or increases the σ^0 when the scattering from the vegetation and the soil-vegetation pathways are dominant (e.g. Kornelsen and Coulibaly, 2013; Ulaby and Long, 2014; Joseph et al., 2010).

Although the Sentinel-1 signal is unlikely to penetrate forest canopies, forest σ^0 might still vary seasonally (Cisneros Vaca and Van der Tol, 2018; Dobson et al., 1991; Hawkins et al., 1999) because canopy development in the leafy period leads to an increase in foliar and stem biomass, and to changes in the vegetation's dielectric properties (Dobson et al., 1991). On top of the seasonal development in forest biomass, the leave and trunk water content (and thus the vegetation's dielectric properties) may vary in response to the hydrological conditions (Steele-Dunne et al., 2017; Frolking et al., 2011). For example, Frolking et al. (2011) identified a decrease in Ku-band σ^0 observations over the southwestern Amazon forest during a prolonged drought.

In addition to the σ^0 variations in response to changes in land surface parameters, there may be instabilities in the Sentinel-1 σ^0 observations over time (El Hajj et al., 2016; Schmidt et al., 2018). For example, El Hajj et al. (2016) reported an offset of +0.9 dB in Sentinel-1A σ^0 observations over three time-invariant targets (an asphalt racetrack, a pine tree forest and a tropical forest) between 19 March 2015 and 25 November 2015 compared to observations outside this period, which they attributed to changes in the calibration of the Sentinel-1 products. In the period from 25 November 2015 to August 2017 the Sentinel-1A σ^0 observations varied between −0.75 dB (in October 2016) and +0.6 dB (in May 2016) relative to the σ^0 that is expected from point targets (Schmidt et al., 2018), which Schmidt et al. (2018) explained by seasonal changes of the atmospheric attenuation and temporal trends of transmission and receive modules in the instrument's front-end.

To remove the seasonal variation in Sentinel-1 σ^0 observations, we considered the anomalies of Sentinel-1 σ^0 observations with the moving average that resembles their seasonality ($d\sigma^0$, in dB):

$$d\sigma^0(T) = \sigma^0(T) - \frac{1}{N_W} \sum_{i=T-W}^{i=T+W} \sigma^0(i), \tag{5.1}$$

where T is an observation timestamp in the σ^0 timeseries, W is the length of the moving average window applied both forwards and backwards and N_W is the number of observations in the window from $T - W$ to $T + W$.

At the moving average window that resembles the seasonality of the σ^0 timeseries, anomalies are assumed to be exclusively due to measurement noise and speckle (i.e., random). Therefore, at this window length the autocorrelation of the $d\sigma^0$ timeseries should be 0. A too small window will result in a negative autocorrelation of $d\sigma^0$, because the moving average will tend to follow the σ^0 timeseries and a negative anomaly will likely be followed by a positive anomaly (and vice versa). As a consequence, part of the uncertainty in which we are interested is removed. A too large window will result in a positive autocorrelation of $d\sigma^0$, because the moving average underestimates the seasonal dynamics of σ^0. To find the moving average window that resembles the seasonal dynamics of σ^0, we evaluated the autocorrelation at a lag of 1 for varied window lengths (the results are in Section 5.4.1).

5.3.2 Sentinel-1 masks for weather-related surface conditions

Masks for frozen conditions, snow, rain interception and dew were developed by comparing meteorological measurements that represent these surface conditions against the Sentinel-1 $d\sigma^0$ of the five forests (the 10 ha forest areas), the five meadows and the five cultivated fields. We used standard meteorological measurements, which adds to the general applicability of the resulting masking rules. The results are presented in Section 5.4.2.

5.3.2.1 Frozen conditions

Both the water in the soil and in the vegetation can freeze, which we together refer to as frozen conditions. Its effect on Sentinel-1 σ^0 observations was investigated by comparing Sentinel-1 $d\sigma^0$ against the linear interpolation result of the two hourly air temperature measurements that are closest in time to a Sentinel-1 overpass, made by the KNMI weather station nearest to a study field.

5.3.2.2 Snow

For the assessment of the effect of snow on Sentinel-1 $d\sigma^0$, we averaged the snow depth measurements of the three KNMI precipitation stations nearest to a study field. Subsequently, the daily snow depth measurements at 9:00 CET were linearly interpolated to the Sentinel-1 overpass times (listed in Table 5.2).

5.3.2.3 Rain interception

Local rain gauge measurements are available for one meadow and two cultivated fields. For rainfall at the other study fields we used the hourly measurements from the nearest KNMI weather station. To denote the possibility of rain interception on the surface and the canopy, we summed the precipitation in the hour in which the Sentinel-1 observation was acquired and the 12 preceding hours following Cisneros Vaca and Van der Tol (2018) for a coniferous and a deciduous forest in the Netherlands. Iida et al. (2005, 2017) also used a period of 12 h to separate rainfall interception events.

5.3.2.4 Dew

Dew consists of water droplets that have condensed from the air on cooler objects, such as leaves (Conti, 2005; Jackson and Moy, 1999). Dew is not measured directly in the Twente region, but it is known that relative humidity conditions larger than 90 % are optimal for dew formation (Jackson and Moy, 1999).

Rao et al. (1998) showed that a relative humidity threshold of 90 % is a rather good predictor of dew onset and duration on maize, and they found only limited improvement with physically-based models. Because of the limited availability of the variables that are required as input to physically-based models (Rao et al., 1998), we opted for using relative humidity as an estimation for the likelihood of dew. The two hourly relative humidity measurements closest in time, made by the KNMI weather station nearest to a study field, were linearly interpolated to a Sentinel-1 overpass time.

Dew most likely forms during the night/morning and other stimuli are low wind speeds of about $1\,\mathrm{m\,s^{-1}}$ to $2\,\mathrm{m\,s^{-1}}$, clear skies and a temperature gradient between the object and the ambient atmosphere of about 1 °C to 2 °C (Conti, 2005; Gleason et al., 1994; Jackson and Moy, 1999).

Gleason et al. (1994) used a threshold of 2.5 m s^{-1} for wind speed (at 10 m above the ground) below which dew is more likely to form. Based on these studies, we analysed the effect of relative humidity on $d\sigma^0$ for the morning and the evening overpasses of Sentinel-1 and for wind speeds below and above 2.5 m s^{-1}.

5.3.3 Sentinel-1 radiometric uncertainty

After masking the Sentinel-1 σ^0 timeseries, we assume that the remaining anomalies in the forest $d\sigma^0$ timeseries are due to Sentinel-1 measurement noise and speckle. The standard deviation of the $d\sigma^0$ timeseries is a measure for the radiometric uncertainty (s_{S1}, in dB), formulated as:

$$s_{S1} = \sqrt{\frac{\sum_{i=1}^{i=N} (d\sigma^0(i) - \overline{d\sigma^0})^2}{N-1}}, \tag{5.2}$$

where $\overline{d\sigma^0}$ is the mean of the $d\sigma^0$ timeseries (in dB) and N is the total number of observations in the timeseries.

We estimated s_{S1} with Equation 5.2 for the five forests for surface areas (A) ranging from 0.25 ha to 10 ha. Subsequently, a second-order power function between A (in ha) and s_{S1} (in dB) of the following form was fitted:

$$s_{S1} = c_1 A^{c_2} + c_3. \tag{5.3}$$

The first term on the right-hand side of Equation 5.3 describes the dependency of s_{S1} to A. According to the Rayleigh fading model for speckle, each σ^0 observation is a sample from a Rayleigh distribution (Ulaby and Long, 2014). By averaging independent σ^0 observations, like spatially averaging them over an area (A), the uncertainty of the mean σ^0 decreases with $1/\sqrt{M}$, where M is the number of independent samples (Ulaby and Long, 2014). This follows from the standard deviation of a sample mean which decreases with $1/\sqrt{M}$, as is also formulated as part of the central limit theorem (Moore et al., 2017). Thus, the expected value for c_2 is -0.5 ($A^{-0.5} = 1/\sqrt{A}$). For a very large A (infinite number of samples) the uncertainty due to speckle approaches 0 dB. The second term on the right-hand side of Equation 5.3 specifies the s_{S1} which is present due to the variation in a σ^0 timeseries as a result of inherent sensor instabilities and calibration uncertainties. The model coefficients c_1 to c_3 were obtained by the 'Trust-Region' algorithm in the Matlab Curve Fitting toolbox. The results are presented in Section 5.4.3.

5.3.4 Impact on soil moisture content retrieval accuracy

The physically-based IEM surface scattering model (Fung et al., 1992), of which various versions have widely been used (e.g. Baghdadi et al., 2018; Verhoest et al., 2008; Kornelsen and Coulibaly, 2013; El Hajj et al., 2017; Lievens and Verhoest, 2012; Su et al., 1997; Altese et al., 1996; Verhoest et al., 2007; Paloscia et al., 2013; He et al., 2017; Guo et al.,

2019; Van der Velde et al., 2012b), simulates the σ^0 of bare land surfaces as a function of the land surface's geometric and dielectric properties. For more background on the IEM model, readers are referred to Ulaby and Long (2014). We employed IEM to simulate the σ^0 sensitivity to SMC for various bare surface conditions.

The geometry of the land, also known as the surface roughness, is parameterized by the root mean square surface height (s), the autocorrelation length (c_l) and an autocorrelation function. An exponential autocorrelation function was selected here, because it is viewed as most applicable to agricultural fields (Ulaby and Long, 2014; Verhoest et al., 2008). Table 5.3 lists the surface roughness scenarios that were investigated, representing the surfaces of meadows and cultivated fields. The found surface roughness parameters describe a slightly smoother surface for meadows than for cultivated fields. A very smooth surface scenario was added for reference purposes.

Table 5.3 The root mean square surface height (s) and the autocorrelation length (c_l) for three surface roughness scenarios. These surface roughness scenarios were used to evaluate the impacts of the weather-related surface conditions and s_{S1} on SMC retrievals.

Scenario	s [cm]	c_l [cm]	Source
Cultivated fields	1.1	11.5	Average of the measurements for maize fields during SMAPVEX12 (McNairn et al., 2015)
Meadows	0.94	14.8	Average of the measurements for pastures during SMAPVEX12 (McNairn et al., 2015)
Very smooth surface	0.5	10	Added for reference purposes

The land surface's dielectric properties, composed of the real and imaginary relative permittivity (ε_r), were estimated with the Mironov soil dielectric mixing model (Mironov et al., 2009) using the average soil texture of the meadows and cultivated fields (see Section 5.2.1) and SMC as input. For the impact of the weather-related surface conditions on SMC retrievals, we evaluated a SMC range of $0.05\,m^3\,m^{-3}$ to $0.50\,m^3\,m^{-3}$. For the impact of the s_{S1} on SMC retrieval uncertainty, we evaluated a dry scenario (SMC equal to $0.10\,m^3\,m^{-3}$) and a wet scenario (SMC equal to $0.35\,m^3\,m^{-3}$).

The σ^0 sensitivity to SMC was simulated with IEM for the three surface roughness scenarios (Table 5.3) and the SMC conditions as defined above, for incidence angles of 35° (representative for Sentinel-1 orbits 15 and 37, see Table 5.2) and 44° (representative for Sentinel-1 orbits 88 and 139, see Table 5.2). Figure 5.2 illustrates the methodology that was used to calculate the impact of a deviation in σ^0 ($\Delta\sigma^0$) on SMC retrievals: $\Delta\sigma^0$, either due to s_{S1} (both plus and minus) or a disturbing surface condition (single direction), is superimposed on the σ^0 for a specific SMC value (θ). The difference between the SMC that is retrieved with $\sigma^0 \pm \Delta\sigma^0$ and the

SMC starting point (θ) resembles the impact on the SMC retrieval ($\Delta\theta^{\pm}$). The performance of SMC retrievals is typically defined as the standard deviation of the differences between retrievals and a reference, i.e., the unbiased *RMSD* (Kerr et al., 2016). The standard deviation is also taken as a measure for the s_{S1}. Hence, the $\Delta\theta^{\pm}$ that is obtained from s_{S1} can be considered equivalent to the unbiased *RMSD* (both are in $m^3\,m^{-3}$).

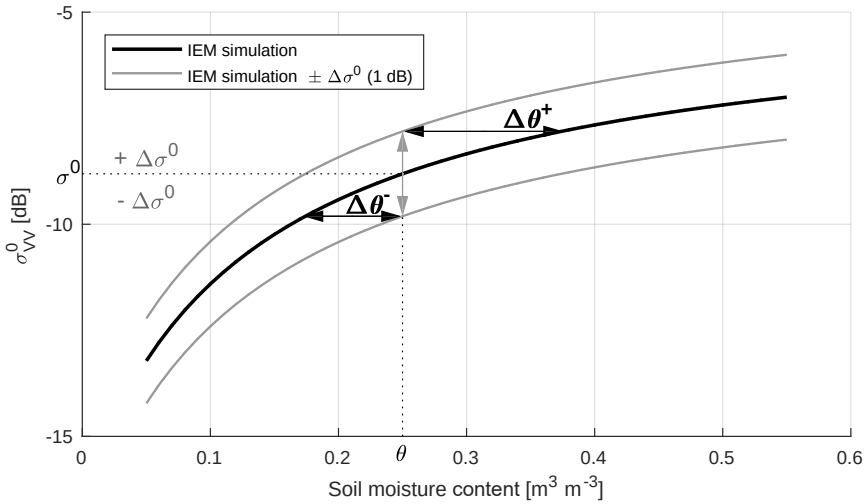

Figure 5.2 Illustration of the method to estimate the impact on SMC retrievals ($\Delta\theta$) at a specific SMC value (θ) due to a deviation ($\Delta\sigma^0$) in VV backscatter (σ^0_{VV}), for a certain relation between σ^0_{VV} and SMC simulated by IEM. This example uses the surface roughness parameters representative for meadows, listed in Table 5.3.

IEM can simulate the σ^0 for the VV polarization and the VH polarization. In Section 5.4.4 we show the results for the VV polarization, because this channel is generally used in SMC retrieval procedures for its larger sensitivity to SMC (e.g. El Hajj et al., 2017; Amazirh et al., 2018).

5.4 Results and discussion

5.4.1 Sentinel-1 timeseries and seasonal anomalies

Figure 5.3 shows the effect of varied moving average windows in Equation 5.1 on the standard deviation and autocorrelation of the $d\sigma^0$ timeseries to find the moving average window that resembles the seasonal dynamics in the Sentinel-1 σ^0 timeseries. The standard deviation is larger when no moving average is applied (Figures 5.3a and b), so the s_{S1} would be overestimated when the σ^0 seasonal dynamics are not removed. This is explained by the variations in the timeseries due to seasonal dynamics and instabilities in the Sentinel-1 σ^0 observations that are still included, which is also reflected in the autocorrelation being significantly above 0.0 (Figures 5.3c and d). Regarding forests the

autocorrelation is approximately 0.0 for a moving average window of 40 days. A moving average window of 40 days backwards and 40 days forwards is close to the three-month timescale of the meteorological seasons in the Twente region. Regarding meadows and cultivated fields the autocorrelation is approximately 0.0 for a moving average window of 25 days. The smaller window for meadows and cultivated fields can be explained by the shorter growth cycles of vegetation and harvesting and the shorter timescales of SMC dynamics, which strongly affect the σ^0 from these fields.

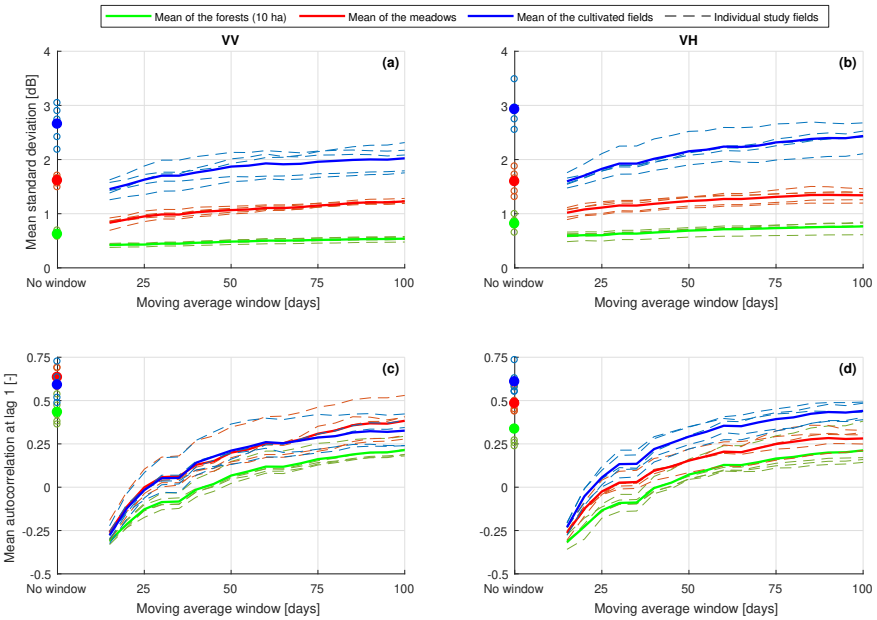

Figure 5.3 Standard deviation for the VV **(a)** and VH polarization **(b)** and autocorrelation at a lag of 1 for the VV **(c)** and VH polarization **(d)**, averaged over all orbits, for the $d\sigma^0$ timeseries calculated with Equation 5.1 using a moving average window varying from 15 days to 100 days. The values labelled as 'no window' were calculated for the anomalies of Sentinel-1 σ^0 observations with respect to the mean of the timeseries. The dashed lines represent the individual study fields and the solid lines are the means per land cover type.

Figure 5.4 shows examples of Sentinel-1 σ^0 and $d\sigma^0$ timeseries for a forest, a meadow and a cultivated field. For brevity only the VV polarization is shown. The Sentinel-1 σ^0, moving average and $d\sigma^0$ timeseries of all the study fields for both the VV and VH polarization are included in Supplement 1 of Benninga et al. (2019), see Chapter 9.

The variation in the moving average (the second term on the right-hand side of Equation 5.1) timeseries of the forest σ^0 is limited compared to the results from the meadows and cultivated fields. Excluding the Sentinel-1 observations that are masked for frozen conditions, snow or rain interception in the calculation of the moving averages, the minimum-to-maximum ranges of the moving average for the five

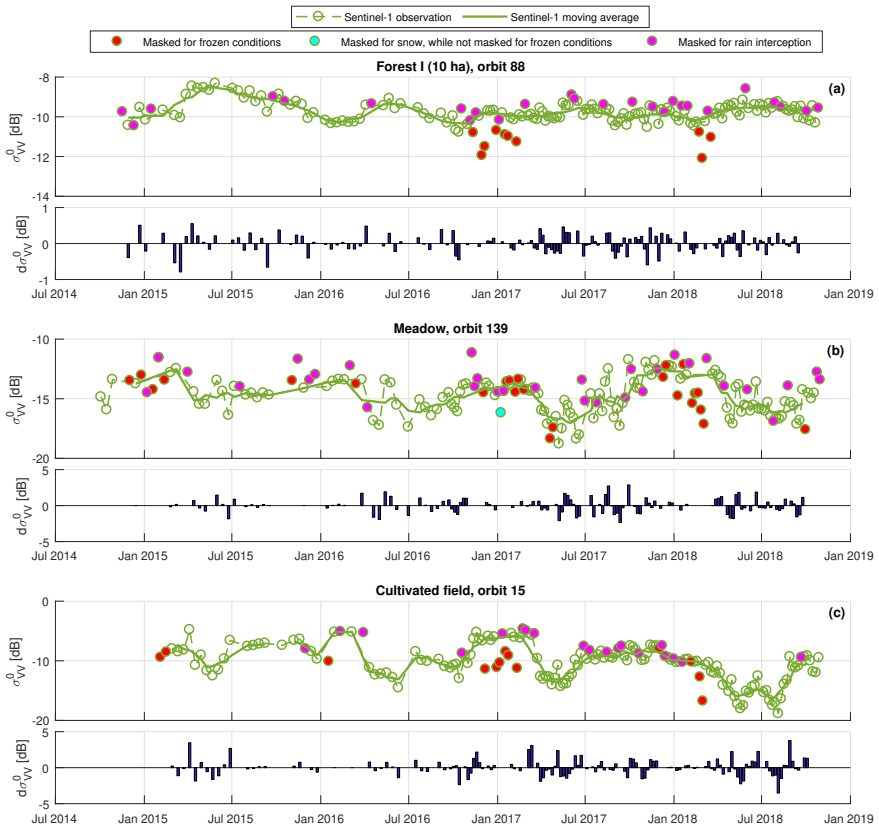

Figure 5.4 Sentinel-1 VV backscatter observations (σ^0_{VV}) and anomalies with the moving average ($d\sigma^0$) calculated with Equation 5.1, using a moving average window of 40 days for an example forest **(a)** and 25 days for an example meadow **(b)** and an example cultivated field **(c)**. The Sentinel-1 observations that are masked for frozen conditions, snow or rain interception are not included in the calculation of the moving averages. The masking rules are defined in Section 5.4.2.

forests are 1.04 dB–2.09 dB (mean is 1.57 dB) for the VV polarization and 0.91 dB–2.68 dB (mean is 1.52 dB) for the VH polarization. The mean minimum-to-maximum moving average range is 5.35 dB for the meadows and 8.57 dB for the cultivated fields for the VV polarization, and 4.83 dB and 9.17 dB, respectively, for the VH polarization. For C-band SAR observations, Cisneros Vaca and Van der Tol (2018) and Dobson et al. (1991) showed that summer conditions lead to an increase of 0.7 dB–1 dB in the σ^0 from a coniferous Douglas-fir forest and a coniferous pine forest, respectively. For a deciduous beech forest Cisneros Vaca and Van der Tol (2018) showed an increase of 0.5 dB at the VV polarization and a decrease of 1 dB at the VH polarization, whereas Dobson et al. (1991) identified a general decrease of 0 dB–2 dB for a deciduous forest. The seasonal variations found in these studies are of the same order of magnitude

as the moving average ranges that were estimated for the five selected forests. In Section 5.3.1 we also discussed an offset of +0.9 dB in Sentinel-1A σ^0 observations between 19 March 2015 and 25 November 2015 (El Hajj et al., 2016). Indeed, forest σ^0 increases in this period (see Figure 5.4a and Supplement 1), although part of the σ^0 offset will be due to the seasonal effect on σ^0. In the further analyses in this study these seasonal dynamics are removed from the σ^0 timeseries by considering the anomalies with the moving averages ($d\sigma^0$).

As can be seen in the examples in Figure 5.4 and deduced from Figures 5.3a–b, $d\sigma^0$ values are generally smaller for the forests than for the meadows and cultivated fields. The larger $d\sigma^0$ for meadows and cultivated fields relate to the effects of short-term variations in SMC and abrupt changes in vegetation, which superimpose on the seasonality in Sentinel-1 σ^0 as determined by the moving average.

5.4.2 Effects by weather-related surface conditions

The effects of frozen conditions, snow, intercepted rain and dew on Sentinel-1 $d\sigma^0$ are discussed in Sections 5.4.2.1–5.4.2.4. The meteorological measurements that are used to represent the weather-related surface conditions are introduced in Section 5.3.2, and $d\sigma^0$ follows from Equation 5.1 and the analysis in Section 5.4.1.

5.4.2.1 Frozen conditions

Figure 5.5 shows $d\sigma^0$ against air temperature. For the VV and the VH observations of the three land cover types, the bin means of 25 $d\sigma^0$ data points along the x-axis decrease with air temperature below approximately 1 °C. In other words, for low temperatures the Sentinel-1 observations are lower than their moving averages. This is also visible in Figure 5.4 in the majority of the Sentinel-1 observations that are masked for frozen conditions. From this analysis follows the masking rule for Sentinel-1 observations that were acquired when air temperature was below 1 °C, listed in Tables 5.4 and 5.5. The air temperature threshold of 1 °C could be explained by the measurement height of 1.5 m above ground, at which the temperature is generally higher than closer to the ground.

Hallikainen et al. (1985) and Mironov et al. (2017) demonstrated that for wet soils the real and imaginary parts of ε_r are considerably lower in frozen than in thawed conditions, because the ε_r of ice is much lower than that of liquid water: $\varepsilon_r \approx 3.2 - j0$ (ice) versus $\varepsilon_r \approx 73.3 - j21.5$ (water at 20 °C) for C-band (Ulaby and Long, 2014). Consequently, the σ^0 is lower for frozen than for thawed land surfaces. Figure 5.5 and the mean effects on $d\sigma^0$ when the masking rule for frozen conditions applies (listed in Tables 5.4 and 5.5) indicate that the effect is stronger for the σ^0 observations in the VH than in the VV polarization, which was also found by Baghdadi et al. (2018) for Sentinel-1 observations. The largest signal is observed for the cultivated fields.

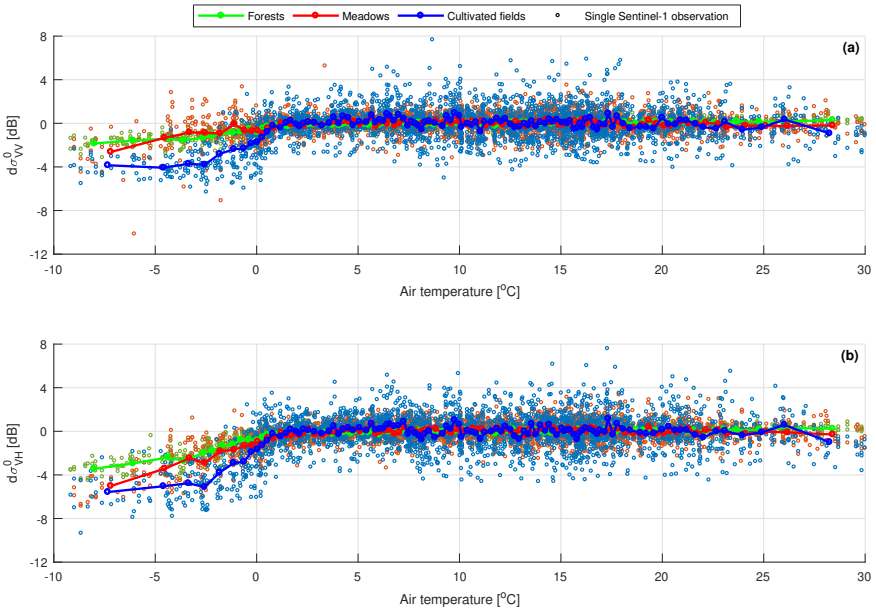

Figure 5.5 The effect of air temperature on the seasonal anomalies ($d\sigma^0$) of the Sentinel-1 σ^0 observations in VV polarization **(a)** and VH polarization **(b)**. Each point on the lines represents a bin of 25 Sentinel-1 observations along the x-axis. The Sentinel-1 observations masked for snow or rain interception are not included.

5.4.2.2 Snow

Snow is generally shallow and short-lived (couple of days) in the Twente region, so the number of Sentinel-1 observations under conditions with snow and the observed snow depth are limited. Moreover, during many Sentinel-1 observations when snow was present the masks for frozen conditions or rain interception also apply. Therefore, in Figure 5.6 ($d\sigma^0$ against snow depth) and Figure 5.7 ($d\sigma^0$ against air temperature, when snow was present) we also show the Sentinel-1 observations that would actually be masked for rain interception and frozen conditions, respectively.

Neither the presence of snow, the depth of the snow layer nor preceding precipitation seem to have an unambiguous effect on the $d\sigma^0$ in Figure 5.6. Some Sentinel-1 σ^0 observations are clearly lower than their moving average (for example for a snow depth of 0.70 cm), whereas other observations seem unaffected (for example for a snow depth of 0.87 cm). Based on simulations with a radiative transfer model, Ulaby and Long (2014) have deduced that a dry snow layer is optically thin for snowpacks below 2 m if $r/\lambda < 10^{-2}$, where r is the ice-crystal radius and λ is the wavelength. This condition holds for Sentinel-1's C-band, for typical ice-crystal radii of 0.25 mm to 2 mm (Ulaby and Long, 2014). In contrast, wet snow's ε_r is larger, and consequently wet snow has a larger reflectivity

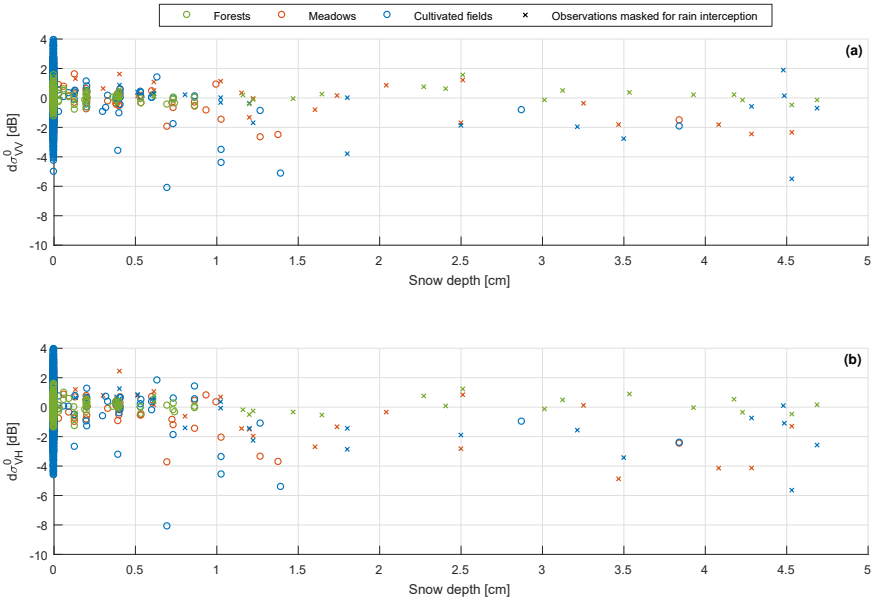

Figure 5.6 The effect of snow depth on the seasonal anomalies ($d\sigma^0$) of the Sentinel-1 σ^0 observations in VV polarization **(a)** and VH polarization **(b)**. Each data point represents a single Sentinel-1 observation. The Sentinel-1 observations masked for frozen conditions are not included, whereas the Sentinel-1 observations that are masked for rain interception are included (marked with a cross).

than dry snow (Ulaby and Long, 2014). Moreover, the absorption by wet snow is much larger than by dry snow, which also reduces the soil contribution to the σ^0 (Ulaby and Long, 2014). For a snowpack of 48 cm, HH σ^0 observations at a frequency of 5.5 GHz and an incidence angle of 50° reduce from −17 dB (snow liquid water content of 0 %) to −21 dB (snow liquid water content of 1.26 %) (Ulaby and Stiles, 1981). Using C-band HH (Radarsat) and VV (European Remote Sensing Synthetic Aperture Radar, or ERS SAR) observations and theoretical model simulations, Baghdadi et al. (1997) and Nagler and Rott (2000) also demonstrated that wet snow strongly reduces the σ^0 and both studies identified a change detection threshold of −3 dB compared to reference σ^0 from snow-free or dry snow surfaces for the classification of wet snow. As such, it is expected that dry snow does not affect the σ^0 and wet snow decreases the σ^0 observations.

Figure 5.7 plots $d\sigma^0$ against air temperature for the Sentinel-1 observations acquired in the morning and in the evening overpasses when snow was present. From Figure 5.7 it can be deduced that most of the large negative $d\sigma^0$ values in Figure 5.6 come from a Sentinel-1 morning overpass. The Sentinel-1 observations for the example with a snow depth of 0.70 cm (mentioned above in this section) were also acquired in a morning overpass, whereas the Sentinel-1 observations with a snow

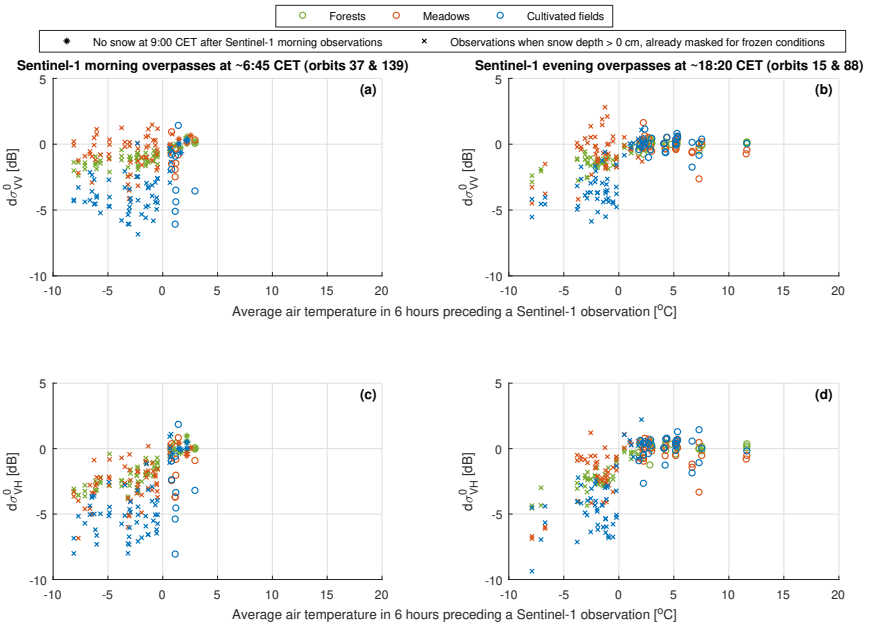

Figure 5.7 The effect of air temperature on the seasonal anomalies ($d\sigma^0$) when snow was present, for the Sentinel-1 VV σ^0 observations acquired in the morning overpasses **(a)** and the evening overpasses **(b)**, and the Sentinel-1 VH σ^0 observations acquired in the morning overpasses **(c)** and the evening overpasses **(d)**. Each data point represents a single Sentinel-1 observation. The Sentinel-1 observations masked for rain interception are not included, whereas the Sentinel-1 observations that are masked for frozen conditions are included (marked with a cross).

depth of 0.87 cm were acquired in an evening overpass.

When the average air temperature in the 6 h preceding a Sentinel-1 morning observation was above 0 °C and the snow depth at 9:00 CET shortly after the Sentinel-1 morning observation was 0 cm, it is likely that the snow at the time of the Sentinel-1 observation (at 6:45 CET) also already melted. Therefore, these Sentinel-1 morning observations are indicated with a different marker type in Figures 5.7a,c. Indeed, the $d\sigma^0$ values of those Sentinel-1 observations are around 0 dB. The remaining data points in Figures 5.7a,c, i.e. when a snow cover is assumed to be present, show that the meadow and cultivated field σ^0 observations acquired in the morning overpasses are disturbed even when the air temperature is above 1 °C. There are two possible explanations for this. Firstly, despite the air temperature being above 0 °C, the soil and the snow layer may still be frozen. This may be possible because the air temperature measurements are collected at 1.5 m above the ground surface. A frozen surface below the optically thin dry snow layer will reduce the σ^0. Secondly, the snow is melting (wet snow conditions). Both options would reduce the σ^0 compared to unfrozen and snow-

free conditions, but it is impossible to distinguish them with the snow and temperature measurements available in this study. Baghdadi et al. (2018) also noted that frozen soils and wet snow cannot reliably be distinguished with C-band σ^0 observations.

As with the effect of frozen conditions (see Section 5.4.2.1), the largest signal is observed for the cultivated fields. These fields are generally bare in winter. The Sentinel-1 forest σ^0 appears unaffected by snow when air temperature was above 1 °C. Baghdadi et al. (1997) also found that, in contrast to i.a. alfalfa, forage crop, oat and grass, wet snow cannot be identified over forested areas, which they attributed to the attenuation of the ground σ^0 signal by the canopy. Some snow may reside on the forest canopy, but this will melt fast when the air temperature is above 0 °C.

The Sentinel-1 observations acquired in the evening overpasses (Figures 5.7b and d) are unaffected by snow when the air temperature was above 0 °C. The maximum observed snow depth is 1.3 cm, which is the time-interpolated result of the snow depth recorded at 9:00 CET before and after the Sentinel-1 observation at 18:20 CET. In reality it is likely that (most of) such shallow snow has already melted in the time between the snow depth measurement at 9:00 CET and the Sentinel-1 observation at 18:20 CET, when the average air temperature was above 0 °C. For most of the Sentinel-1 observations in Figures 5.7b,d the three closest KNMI precipitation stations also recorded no snow or only a broken snow cover at 9:00 CET the day after the Sentinel-1 observation. Even though the majority of the Sentinel-1 evening observations is evidently unaffected, some suspicious data points can be identified in Figures 5.7b,d. However, we could not find any evidence for the presence of snow, and therefore, considered these points as outliers.

From the analyses above follows that the Sentinel-1 morning observations of meadows and cultivated fields are affected by snow and should be masked. The masking rules for snow are summarized in Tables 5.4 and 5.5, along with the mean $d\sigma^0$ when the masking rule applies. For a further development of the snow mask, Sentinel-1 σ^0 observations should be analyzed in combination with detailed snow information, regarding e.g., depth, wetness and where the snow resides, for a region where snowpacks are deeper and long-lived.

5.4.2.3 Rain interception

Figure 5.8 shows that the σ^0 increases after rainfall in the 12 h preceding a Sentinel-1 observation. Regarding meadows and cultivated fields this will not exclusively being the effect of intercepted rain, but also the effect of increased SMC. Therefore, for the development of the rain interception mask we focused on the effect on $d\sigma^0$ that is observed for forests.

We defined the masking rule for rain interception as minimum 1.8 mm of rain (listed in Tables 5.4 and 5.5), because from this amount of rainfall the effect on the bin-averaged $d\sigma^0$ is consistently positive. Starting from 1.8 mm of rain, the $d\sigma^0$ values generally increase with the amount

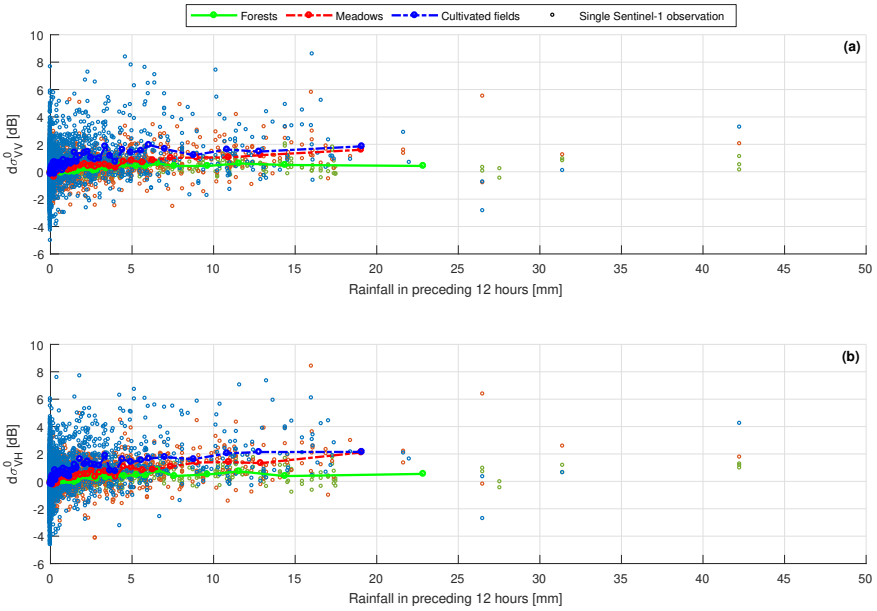

Figure 5.8 The effect of the rainfall sum in the preceding 12 h on the seasonal anomalies ($d\sigma^0$) of the Sentinel-1 σ^0 observations in VV polarization **(a)** and VH polarization **(b)**. Each point on the lines represents a bin of 25 Sentinel-1 observations along the x-axis. The Sentinel-1 observations masked for frozen conditions or snow are not included.

of rain until the bin-averaged $d\sigma^0$ values are approximately constant onwards from 4.2 mm of rain with an average effect of +0.47 dB for the VV polarization and +0.51 dB for the VH polarization. De Jong et al. (2000) and Riedel et al. (2002) explained that the σ^0 is influenced by the free-water content of the vegetation, and canopies intercept rainfall as a thin layer of free water on hydrophilic leaves or as drops on hydrophobic leaves (De Jong et al., 2000). Moreover, the orientation of the leaves can change due to the added weight (Jackson and Moy, 1999). Previous studies showed effects of rainfall on C-band σ^0 of +0.7 dB to +2.5 dB (mean is +1.3 dB) for a dense mixed forest (De Jong et al., 2000), +1 dB to +2 dB for a Douglas-fir canopy (Cisneros Vaca and Van der Tol, 2018), +2 dB to +3 dB for mature conifer and hardwood forests (Dobson et al., 1991), and +1 dB for a pine tree forest (El Hajj et al., 2016). Regarding crops, the X-band σ^0 observations by Allen and Ulaby (1984), as described by Jackson and Moy (1999), show an increase of about 3 dB directly after the canopies (wheat, maize and soybeans) had been sprayed with water, whereas the C-band σ^0 observations by Riedel et al. (2002) suggest that the effect on the σ^0 depends on the vegetation structure and the growth stadium.

Not only may the effect on the σ^0 by intercepted rain depend on the vegetation characteristics, also the amount and duration of the intercepted rain will vary. In this study we used the rainfall sum in

the 12 h preceding a Sentinel-1 observation as a rather simple proxy for rain interception. In reality, many more factors, including evaporation, the canopy's density and shape of elements, and the timing and intensity of the event(s) preceding a Sentinel-1 observation, control whether a canopy is wet at the moment of a Sentinel-1 overpass. A rain interception model, such as the Gash model (Gash, 1979), should be used to simulate these effects, but this goes beyond the scope of this study.

Standing water on fields after a heavy rain event might also affect the Sentinel-1 σ^0 observations. Complete inundation of an area shows a clear decrease in the σ^0 (e.g. Henry et al., 2006; Huang et al., 2018), but standing water on an agricultural field is generally a mosaic of wet soil and standing water in local depressions. We have not collected information about standing water on the selected agricultural fields. Given the high infiltration capacity of the sandy to loamy sandy soils in the Twente region, we assume that the most severe standing water situations will already be masked out by the masking rule for rain interception based on a minimum of 1.8 mm of rain in the 12 h preceding a Sentinel-1 observation.

5.4.2.4 Dew

Figure 5.9 shows $d\sigma^0$ against relative humidity for the Sentinel-1 morning and evening overpasses and for weak (wind speed $< 2.5\,\mathrm{m\,s^{-1}}$) and strong winds (wind speed $\geq 2.5\,\mathrm{m\,s^{-1}}$). In all figures $d\sigma^0$ seems unaffected by a high relative humidity. As explained in Section 5.3.2.4, the highest likelihood of dew is expected for the Sentinel-1 observations that were acquired during the morning overpasses when the wind speed was below $2.5\,\mathrm{m\,s^{-1}}$ and the relative humidity was above 90 %. Indeed, Figure 5.9 shows that the relative humidity is generally higher during Sentinel-1's morning overpasses, especially when the wind speed was low (Figures 5.9a and e). However, even Figures 5.9a,e exhibit no distinct systematic effect of high relative humidity (> 90 %) on $d\sigma^0$. In Figures 5.9a,e there is a peak in the cultivated field bin-averaged $d\sigma^0$ of about 1 dB at a relative humidity of 98 %, but $d\sigma^0$ is not systematically positive from the expected threshold of 90 % and for relative humidity higher than 98 % the bin-averaged $d\sigma^0$ values decrease again. This is probably just inherent variation in the bin-averaged $d\sigma^0$ values, which is also observed for example at relative humidities of 65 % and 85 %. We could not find a systematic effect of dew on the Sentinel-1 σ^0 observations, so we do not mask them for dew (also see Tables 5.4 and 5.5).

This is supported by Jackson and Moy (1999), who concluded, based on the work by Batlivala and Ulaby, that for frequencies between 1.1 GHz and 7.25 GHz there is no effect of dew on the σ^0. On the contrary, Gillespie et al. (1990) did find an increase in σ^0 observations due to a dew event for C-band HH, VV and HV observations taken from incidence angles of 10° to 40° parallel to the crop row direction. However, the Ku-and L-band observations are less affected, and the C-band VH observations, at an incidence angle of 60° or in across-row direction seem

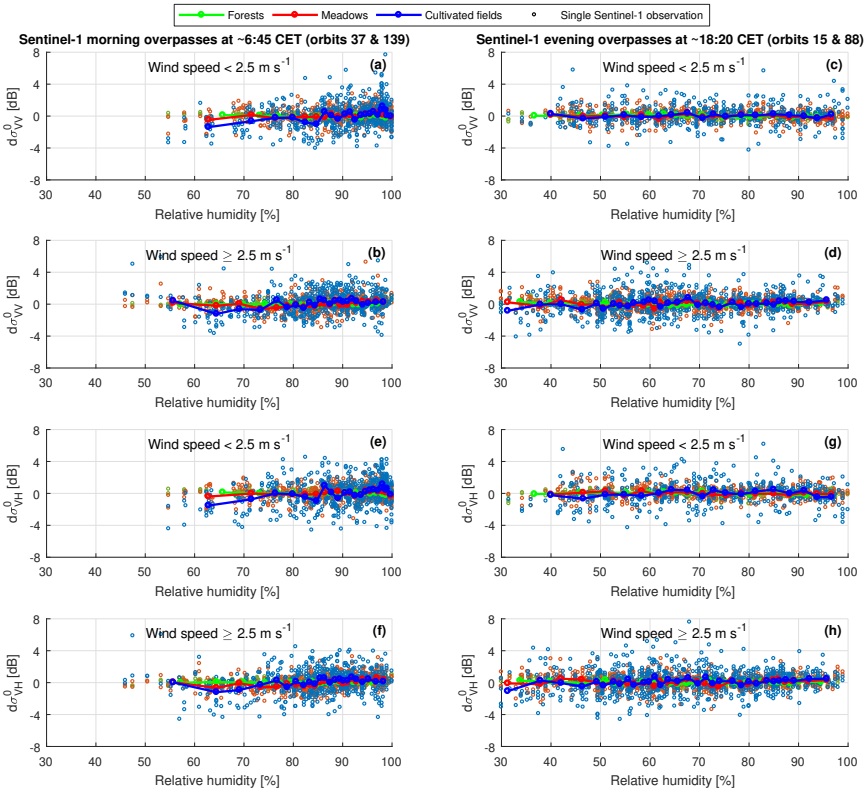

Figure 5.9 The effect of relative humidity on the seasonal anomalies ($d\sigma^0$), for the Sentinel-1 VV σ^0 observations acquired in the morning overpasses **(a–b)** and the evening overpasses **(c–d)**, and the Sentinel-1 VH σ^0 observations acquired in the morning overpasses **(e–f)** and the evening overpasses **(g–h)**. The Sentinel-1 observations are shown separately for weak and strong winds (average wind speeds in the hour of the Sentinel-1 observation below and above $2.5\,\mathrm{m\,s^{-1}}$, see the text in the sub-figures). Each point on the lines represents a bin of 25 Sentinel-1 observations along the x-axis. The Sentinel-1 observations masked for frozen conditions or rain interception are not included.

unaffected by dew (Gillespie et al., 1990). The C-band VV and VH σ^0 observations by Riedel et al. (2002) decrease by about 0.5 dB to 2 dB due to a dew event, whereas the X-band observations slightly increase and the L-band observations respond differently for different polarizations. These σ^0 observations show inconsistent σ^0 responses to dew for different radar settings and no explanations are provided for these differences (Jackson and Moy, 1999), and Ulaby and Long (2014) and Jackson and Moy (1999) stated that no general conclusions can be drawn regarding the effects of dew as a function of frequency, angle and polarization and the mechanisms behind it.

Both dew and intercepted rain wet the land surface. However, whereas the Sentinel-1 observations are affected by rain interception (see Sec-

tion 5.4.2.3), they seem unaffected by dew. Gillespie et al. (1990) and Riedel et al. (2002) suggested that the nature of the intercepted water by dew and rain interception may be different (i.e., drop size or thin layer) and that this can alter their effect on the σ^0. Moreover, dew deposits are relatively small, typically 0.1 mm to 0.3 mm per night with maxima of 0.5 mm per night (Jackson and Moy, 1999). The rain interception storage capacity is generally larger, in the order of 2 mm for a Douglas-fir forest (Cisneros Vaca et al., 2018) and a dense mixed forest (De Jong et al., 2000) in the Netherlands.

5.4.2.5 Summary of the masking rules

Tables 5.4 and 5.5 summarize the masking rules that result from the analyses in Sections 5.4.2.1–5.4.2.4 and list the mean effects on Sentinel-1 $d\sigma^0$ by the weather-related surface conditions.

Table 5.4 The masking rules for the weather-related surface conditions that result from the analyses in Sections 5.4.2.1–5.4.2.4. $T_{air}(T)$ is air temperature, $D_s(T)$ is snow depth and $P(T)$ is rainfall representative for the time of the Sentinel-1 observation (T). The calculation of these variables is explained in Section 5.3.2. The right columns list the mean $d\sigma^0$ of the Sentinel-1 VV observations to which a specific masking rule applies and none of the other masking rules apply.

Surface condition	Masking rule	Mean of $d\sigma^0_{VV}$ [dB]		
		Forests	Meadows	Cultivated fields
Frozen conditions	$T_{air}(T) \leq 1\,^\circ$C	−1.0	−0.88	−2.39
Snow	$D_s(T) > 0$ cm & D_s at 9:00 CET after $T > 0$ cm & Sentinel-1 morning observation & Land cover meadow or cultivated	Not masked	−0.52	−1.93
Rain interception	$\sum_{i=T-12\,hours}^{i=T} P(i) \geq 1.8$ mm	0.36	0.73	1.39
Dew	No masking	Not masked	Not masked	Not masked

Table 5.5 Same as Table 5.4, but for the Sentinel-1 VH observations.

Surface condition	Masking rule	Mean of $d\sigma^0_{VH}$ [dB]		
		Forests	Meadows	Cultivated fields
Frozen conditions	$T_{air}(T) \leq 1\,^\circ$C	−1.56	−1.96	−2.99
Snow	$D_s(T) > 0$ cm & D_s at 9:00 CET after $T > 0$ cm & Sentinel-1 morning observation & Land cover meadow or cultivated	Not masked	−1.09	−2.04
Rain interception	$\sum_{i=T-12\,hours}^{i=T} P(i) \geq 1.8$ mm	0.43	0.91	1.53
Dew	No masking	Not masked	Not masked	Not masked

The developed masking procedure for frozen conditions, snow, rain interception and dew is based on a rather simple set of masking rules

and standard meteorological measurements, which adds to their applicability. However, in Sections 5.4.2.1–5.4.2.4 various complexities in the representations of these weather-related surface conditions and their effects on σ^0 were discussed. In general, the representations of the weather-related surface conditions could be improved by using models that simulate these surface conditions and by using available spatially distributed products from land surface models and satellite observations. For example, Kerr et al. (2016) used the surface soil temperature and snow cover products from two models to mask SMOS observations, and Wagner et al. (2013) used SSM/I satellite information about snow to flag ASCAT SMC retrievals. Even the surface state flags that accompany coarse resolution SMC products could be used as information in the masking of Sentinel-1 products.

It should be realized that due to uncertainty in the representations of the weather-related surface conditions and uncertainty in the SAR observations, the masks will remain imperfect. Some σ^0 observations will unnecessarily be masked (false alarms), whereas other observations will be disturbed but missed by the masking rules (missed hits). For example, not all Sentinel-1 observations that were acquired when air temperature was below 1 °C are actually disturbed by frozen conditions, which is reflected in the dispersion of the points in Figure 5.5 and in Figure 5.4b for example in the period December 2016 to January 2017. This could be improved by utilizing the actual values of σ^0 observations (Naeimi et al., 2012), e.g., only masking for frozen conditions when the σ^0 or $d\sigma^0$ values of a Sentinel-1 observation indicate that it is affected. Further research is required to obtain the appropriate σ^0 or $d\sigma^0$ thresholds, thereby considering the σ^0 deviations that can be expected due to the s_{S1} for a certain surface area (see Section 5.4.3).

5.4.3 Radiometric uncertainty

Figure 5.10 shows the s_{S1}, calculated with Equation 5.2, as a function of A for the five selected forests and for each orbit in which Sentinel-1 collected data over the study region. As expected, the s_{S1} improves for larger A over which the Sentinel-1 σ^0 observations are averaged. The differences between the five forests in Figure 5.10 are rather small and there is no obvious systematic pattern between the forests, e.g., one forest consistently showing the highest radiometric uncertainty in each sub-figure. This provides a justification for combined fits over the five forests, of which the model coefficients are listed in Tables 5.6 and 5.7.

The s_{S1} is also rather similar for the different orbits, as can be seen from the blue and black lines in Figure 5.10. Only for the VV observations in orbit 15 there is a small underestimation of 0.03 dB at 10 ha by the combined fit, and for the VV observations in orbit 88 there is a small overestimation of 0.04 dB at 10 ha. These deviations are small and not seen in the other sub-figures, which suggests that there are no significant differences between the radiometric uncertainties of the different orbits due to the differences in incidence angle and pass direction (listed in

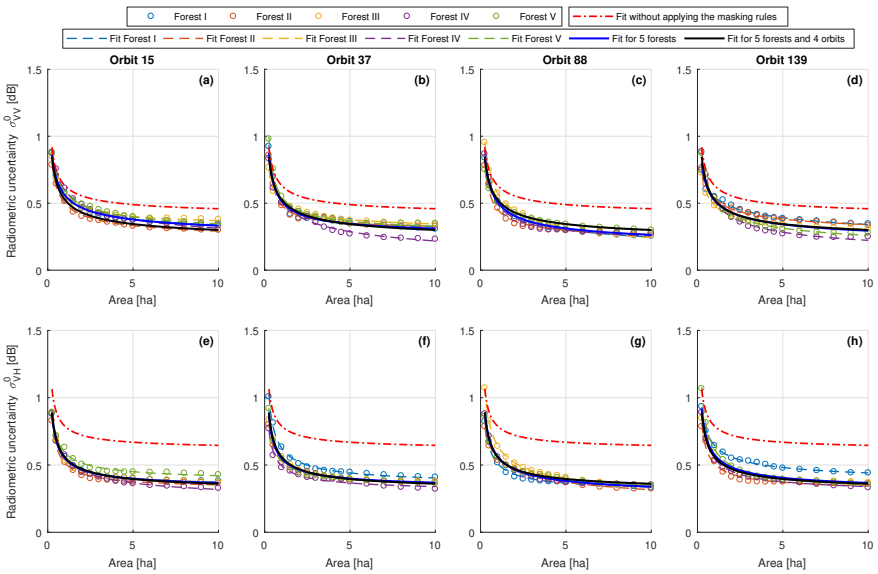

Figure 5.10 Radiometric uncertainty (s_{S1}) of the Sentinel-1 VV observations **(a–d)** and the Sentinel-1 VH observations **(e–h)**. The points are calculated s_{S1} values and the lines are the fitted second-order power functions (Equation 5.3). The s_{S1} is calculated on the forest σ^0 timeseries after application of the developed masking rules. For comparison the red lines show the combined fits over the four orbits and the five forests of s_{S1} without applying the masking rules. The model coefficients of the fits are listed in Tables 5.6 and 5.7.

Table 5.6 Model coefficients of the second-order power function between A and s_{S1} (Equation 5.3) of the Sentinel-1 VV observations over the five forests combined. The $RMSD$ is the root mean square deviation between the function and the underlying data points.

Relative orbit	c_1	c_2	c_3	$RMSD$ [dB]
All orbits in one fit	0.3381	−0.4809	0.1884	0.043
15	0.3556	−0.4443	0.2042	0.029
37	0.2710	−0.6091	0.2439	0.040
88	0.3706	−0.4703	0.1377	0.031
139	0.3756	−0.4035	0.1461	0.042

Table 5.2). This is in accordance with the results by Schmidt et al. (2018) and Schwerdt et al. (2017), who draw similar conclusions in their analyses of the radiometric accuracy of the Sentinel-1A and Sentinel-1B observations acquired in the IW mode.

The combined fits over the four orbits and the five forests indicate that the s_{S1} reduces from 0.85 dB (0.25 ha) to 0.30 dB (10 ha) for the VV polarization and from 0.89 dB (0.25 ha) to 0.36 dB (10 ha) for the VH polarization. Schwerdt et al. (2017) also found a lower radiometric accuracy standard deviation for the Sentinel-1B VV observations (0.23 dB) than for the VH observations (0.33 dB). The developed masking rules

Table 5.7 Same as Table 5.6, but for the s_{S1} of the Sentinel-1 VH observations.

Relative orbit	c_1	c_2	c_3	$RMSD$ [dB]
All orbits in one fit	0.2705	−0.5765	0.2891	0.041
15	0.2376	−0.6341	0.3125	0.030
37	0.2355	−0.6228	0.3128	0.039
88	0.3314	−0.4940	0.2325	0.037
139	0.2872	−0.5636	0.2888	0.049

have improved the s_{S1} by up to 0.16 dB and 0.29 dB at 10 ha, for the VV and VH polarization respectively.

Interesting to note is that the c_2 coefficients in Tables 5.6 and 5.7 are close to −0.5, especially for the combined fits over the five forests and the four orbits. This value of −0.5 for c_2 is in accordance with the theory about the standard deviation of sample means (decreasing with $1/\sqrt{M}$), as explained in Section 5.3.3.

El Hajj et al. (2016) obtained s_{S1} values of 0.35 dB for VV and 0.45 dB for Sentinel-1 VH observations of a 8.1 ha forest area (for the longest period that El Hajj et al. (2016) analysed). The s_{S1} values calculated with the model coefficients in Tables 5.6 and 5.7 for A equal to 8.1 ha are slightly lower (0.31 dB for VV and 0.37 dB for VH), which can be explained by the removal of the seasonal dynamics (see Section 5.4.1) and the extensive masking procedure in this study. The even lower c_3 coefficients in Tables 5.6 and 5.7 suggest that the s_{S1} further decreases for A larger than 10 ha. El Hajj et al. (2016) also found lower s_{S1} for A larger than 10 ha, namely 0.19 dB (VV σ^0) for a racetrack of 14.7 ha, and 0.18 dB (VV σ^0) and 0.29 dB (VH σ^0) for a tropical forest of 635.2 ha. The c_3 values are also lower than the specified radiometric accuracy standard deviations of Sentinel-1A and Sentinel-1B (see Section 5.2.2). It should, however, be realized that the relationships of s_{S1} versus A have been developed on Sentinel-1 σ^0 observations aggregated over areas up to 10 ha. The extrapolation to larger spatial domains should be tested on Sentinel-1 images collected over a study region with a time-invariant target of at least 100 ha (1 km × 1 km resolution, see Section 5.4.4).

5.4.4 Impact on soil moisture content retrievals

Figure 5.11 shows the deviations in SMC retrievals that are expected due to the disturbing effect on the σ^0 by the weather-related surface conditions, if the Sentinel-1 observations would not be masked. The methodology explained in Section 5.3.4 was used to estimate the impacts of the mean effects on Sentinel-1 VV σ^0 observations over meadows and cultivated fields by frozen conditions, snow and rain interception (listed in Table 5.4) on SMC retrievals. Rain interception causes an overestimation, and snow and frozen conditions cause an underestimation of SMC. It should be noted that the decrease in SMC retrievals during frozen conditions relates to an actual decrease in liquid water content and this

is, therefore, difficult to label as an error in SMC retrievals.

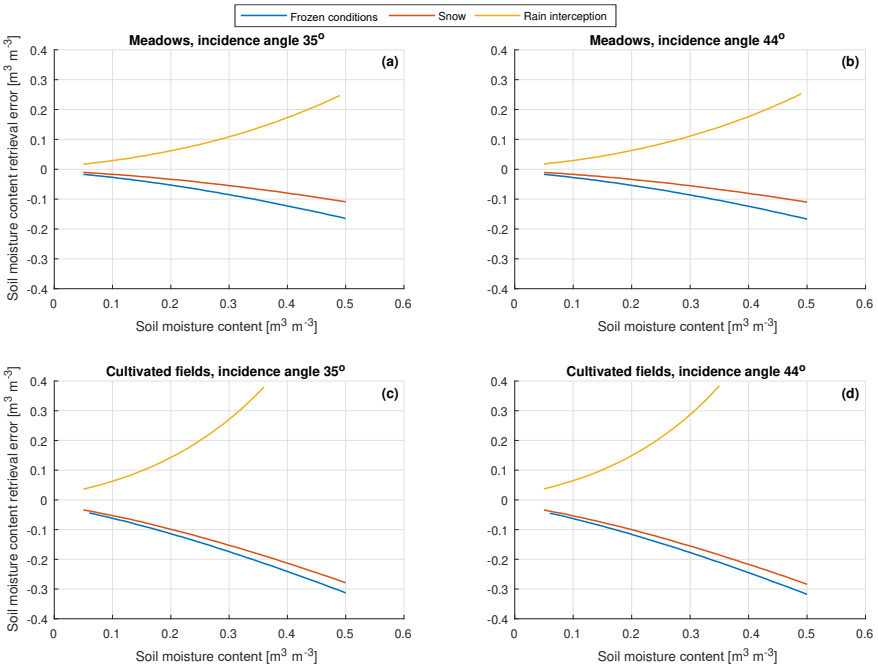

Figure 5.11 Impacts of frozen conditions, snow and rain interception on SMC retrieved from Sentinel-1 VV σ^0, for an incidence angle of $35°$ on meadows **(a)**, $44°$ on meadows **(b)**, $35°$ on cultivated fields **(c)** and $44°$ on cultivated fields **(d)**. For the effects of frozen conditions, snow and rain interception on Sentinel-1 σ^0, the mean effects listed in Table 5.4 are taken.

The penetration depth of C-band observations in wet snow is in the order of 3 cm to 1 m (Ulaby and Long, 2014; Casey et al., 2016; Nagler et al., 2016; Mätzler, 1987). This suggests that for shallow snowpacks, like they occur in the study region, the effects of frozen conditions and wet snow may superimpose to some extent, decreasing the σ^0 further and causing even a larger underestimation of the SMC.

Figure 5.12 shows the expected SMC retrieval uncertainties due to the s_{S1} as a function of A, for the surface conditions introduced in Section 5.3.4. The s_{S1} is estimated with Equation 5.3 and the model coefficients listed in Table 5.6 for the combined fit over all orbits. With this, we assume that the s_{S1} that has been estimated using forest σ^0 observations is applicable also to meadows and cultivated fields. This implicates that the the radiometric uncertainty sources are multiplicative, which is commonly adopted for speckle filtering (Lee, 1986; Touzi, 2002; Esch et al., 2011).

The impacts on SMC retrievals are larger for the cultivated fields than for the meadows for two reasons. Firstly, regarding the impacts of the disturbing effects on the σ^0 by the weather-related surface conditions (Figure 5.11), the mean effects of frozen conditions, snow and

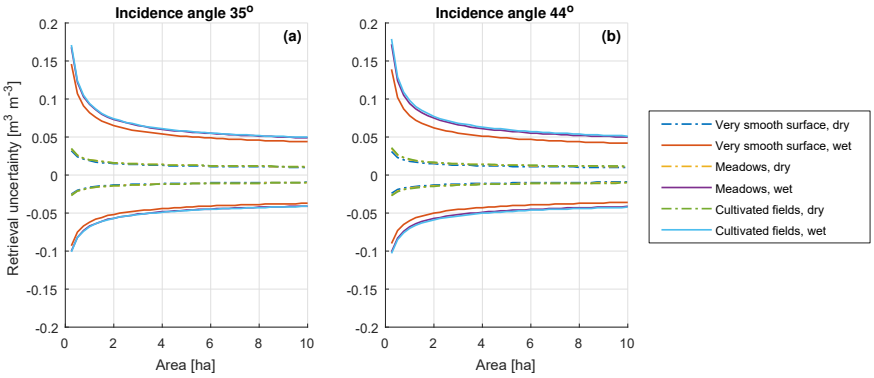

Figure 5.12 Upper ($\Delta\theta^+$) and lower boundary ($\Delta\theta^-$) of the SMC retrieval uncertainty due to the s_{S1} at VV polarization as a function of A, for incidence angles of $35°$ **(a)** and $44°$ **(b)**, for the three surface roughness scenarios (Table 5.3) and for dry soil (SMC equal to $0.10\,\mathrm{m^3\,m^{-3}}$) and wet soil (SMC equal to $0.35\,\mathrm{m^3\,m^{-3}}$).

rain interception on σ^0 are larger for the cultivated fields than for the meadows (see Table 5.4). Secondly, the σ^0 sensitivity to SMC is slightly larger for the surface roughness parameters taken as representative for meadows than for cultivated fields. As a result, a similar deviation in σ^0 results in a larger deviation in SMC for cultivated fields. However, as can be deduced from Figure 5.12, this effect is small in comparison to the first-mentioned reason.

The differences between the incidence angles of $35°$ and $44°$ are very small. In contrast to the small effects of surface roughness and incidence angle is the effect of SMC large. This is explained by the σ^0 sensitivity to SMC, which diminishes with increasing SMC according to IEM simulations (Altese et al., 1996). This is also reflected in the larger values for $\Delta\theta^+$ in comparison to $\Delta\theta^-$ shown in Figure 5.12. Verhoest et al. (2007) also showed SMC retrieval distributions that are skewed towards the higher SMC levels due to the non-linear relation between SMC and σ^0.

Paloscia et al. (2013) proposed a spatial resolution of 1 km or finer for an operational Sentinel-1 based SMC product. Figure 5.13 shows the SMC retrieval uncertainty for the s_{S1} that is estimated for a 1 km resolution (0.23 dB for the VV polarization), assuming that the obtained relations between A and s_{S1} can be applied to A larger than 10 ha. The figure shows that the s_{S1} consumes a significant portion of the $0.05\,\mathrm{m^3\,m^{-3}}$ accuracy requirement proposed for the operational SMC product by Paloscia et al. (2013), especially in the wet SMC range.

With IEM we demonstrated the effect of various surface conditions on the SMC retrieval errors and uncertainty, for a surface without vegetation. Vegetation typically reduces the σ^0 sensitivity to SMC (e.g. Guerriero et al., 2016). As such, the impacts of the disturbing effects by the weather-related surface conditions and s_{S1} on SMC retrievals are expected to increase with vegetation present. The impacts on SMC retrievals that we obtained with IEM, therefore, resemble the lower limits. The vegetation

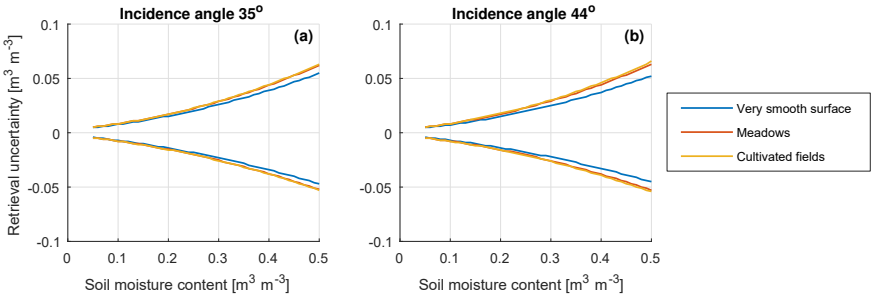

Figure 5.13 Upper ($\Delta\theta^+$) and lower boundary ($\Delta\theta^-$) of the SMC retrieval uncertainty due to the s_{S1} at VV polarization at 1 km resolution as a function of SMC, for incidence angles of $35°$ **(a)** and $44°$ **(b)** and for the three surface roughness scenarios (Table 5.3).

type and the vegetation stage can have a large effect on the σ^0 sensitivity to SMC, and further research is required to determine their effect on the SMC retrieval errors and uncertainty due to the weather-related surface conditions and the radiometric uncertainty.

5.5 Conclusions

In the scope of SMC retrieval from SAR observations, we have developed a masking procedure for weather-related surface conditions that disturb Sentinel-1 σ^0 observations and we have estimated the radiometric uncertainty of Sentinel-1 as a function of the surface area over which the σ^0 observations are aggregated. The impacts of the weather-related surface conditions and the radiometric uncertainty on SMC retrievals from Sentinel-1 σ^0 were investigated for various bare surface conditions using the IEM surface scattering model.

The effects of frozen conditions, snow, rain interception and dew on σ^0 were investigated by analysing meteorological measurements representing these surface conditions against seasonal anomalies of Sentinel-1 observations for five forests, five meadows and five cultivated fields in the eastern part of the Netherlands. From these analyses we have developed a set of masking rules for Sentinel-1 observations. From our results it follows that:

1. Sentinel-1 σ^0 observations of forests, meadows and cultivated fields are affected by frozen conditions below an air temperature of 1 °C, on average by −1.80 dB. Intercepted rain affects the σ^0 after more than 1.8 mm of rain in the 12 h preceding an observation, on average by +0.89 dB. Snow affects the σ^0 observations of meadows and cultivated fields that were acquired in the Sentinel-1 morning overpasses on average by −1.40 dB. We could not find a systematic effect of dew on the Sentinel-1 σ^0 observations, so no masking rule for dew was formulated.

2. Frozen conditions, snow and intercepted rain have the largest effect on the Sentinel-1 σ^0 observations of cultivated fields in comparison to forest and meadow σ^0 observations.
3. The effects of frozen conditions, snow and intercepted rain are larger on the Sentinel-1 σ^0 observations in VH than in VV polarization.

After masking the Sentinel-1 σ^0 timeseries of the five forests using the masking rules defined at point 1 above, Sentinel-1's radiometric uncertainty has been estimated by the standard deviation of the seasonal anomalies timeseries of the σ^0 observations averaged over forest surface areas ranging from 0.25 ha to 10 ha. From our results it follows that:

1. The Sentinel-1 radiometric uncertainty improves from 0.85 dB (0.25 ha) to 0.30 dB (10 ha) for the VV polarization and from 0.89 dB (0.25 ha) to 0.36 dB (10 ha) for the VH polarization.
2. The radiometric uncertainty is approximately inversely proportional to the square root of the surface area over which the Sentinel-1 σ^0 observations are averaged.

With the quantifications of radiometric uncertainty and the disturbing effects on the σ^0 by the weather-related surface conditions, we have determined their impact on SMC retrievals from Sentinel-1 VV σ^0. With the IEM model the σ^0 sensitivity to SMC was simulated for a surface representing meadows and a surface representing cultivated fields, for the incidence angles at which Sentinel-1 observes the study region and for dry to wet soil conditions. Based on the results, we draw the following conclusions:

1. If not masked, intercepted rain causes a significant overestimation of SMC ranging from $+0.047\,m^3\,m^{-3}$ for dry soils (SMC equal to $0.10\,m^3\,m^{-3}$) up to $+0.26\,m^3\,m^{-3}$ for wet soils (SMC equal to $0.35\,m^3\,m^{-3}$), averaged over the meadows and cultivated fields. Snow and frozen conditions lead to a significant decrease in SMC retrievals, from $-0.035\,m^3\,m^{-3}$ and $-0.045\,m^3\,m^{-3}$ for dry soils up to $-0.13\,m^3\,m^{-3}$ and $-0.16\,m^3\,m^{-3}$ for wet soils respectively.
2. The SMC retrieval uncertainty as a result of radiometric uncertainty is minimum $-0.01\,m^3\,m^{-3}$ to $+0.01\,m^3\,m^{-3}$ for dry soils and large surface areas, and maximum $-0.10\,m^3\,m^{-3}$ to $+0.17\,m^3\,m^{-3}$ for wet soils and small surface areas.
3. At the 1 km spatial resolution that Paloscia et al. (2013) proposed for an operational Sentinel-1 SMC product, radiometric uncertainty still leads to SMC retrieval uncertainty ranging from $0.01\,m^3\,m^{-3}$ for dry soils to $0.033\,m^3\,m^{-3}$ for wet soils. Especially in the wet SMC range the radiometric uncertainty consumes a significant portion of the $0.05\,m^3\,m^{-3}$ accuracy requirement proposed for this SMC product (Paloscia et al., 2013).
4. The impact on SMC retrievals by a σ^0 deviation, either due to a weather-related surface condition or radiometric uncertainty, is

weakly dependent on the surface roughness and the incidence angle, and strongly dependent on the SMC itself.

This study demonstrates that the weather-related surface conditions disturbing Sentinel-1 σ^0 observations and Sentinel-1's radiometric uncertainty have a major impact on SMC retrieval uncertainty especially in wet soil conditions and for retrievals based on a small number of independent σ^0 samples (fine spatial resolutions). This understanding aids appreciating the application value of SAR-based SMC products under various surface conditions and spatial resolutions. The reported uncertainty estimates represent the lower limits because the effects of vegetation are not accounted for in the simulations of σ^0 sensitivity to SMC. Further development of the masking procedure and characterization of other error contributions to SMC retrievals, such as imperfections in retrieval algorithms, would further benefit SMC product development and utilization.

6 Sentinel-1 soil moisture content and its uncertainty over sparsely vegetated fields

This chapter is based on parts of:

Benninga, H. F., Van der Velde, R., and Su, Z.: Sentinel-1 soil moisture content and its uncertainty over sparsely vegetated fields, J. Hydrol. X, 9, 100066, doi:10.1016/j.hydroa.2020.100066, 2020.

Abstract

Soil moisture content (SMC) retrievals from synthetic aperture radar (SAR) observations do not exactly match with in situ references due to imperfect retrieval algorithms, and uncertainties in the model parameters, SAR observations and in situ references. Information on the uncertainty of SMC retrievals would contribute to their applicability. This chapter presents a methodology for deriving the SMC retrieval uncertainty and decomposing this in its constituents. A Bayesian calibration framework was used for deriving the total uncertainty and the model parameter uncertainty. The methodology was demonstrated with the integral equation method (IEM) surface scattering model, which was employed for reproducing Sentinel-1 backscatter (σ^0) observations and the retrieval of SMC over four sparsely vegetated fields in the Netherlands. For two meadows the calibrated surface roughness parameter distributions are remarkably similar between the ascending and the descending Sentinel-1 orbits as well as between the two meadows, and yield consistent SMC retrievals for the calibration and validation periods ($RMSD$s of $0.076\,m^3\,m^{-3}$ to $0.11\,m^3\,m^{-3}$). These results are promising for operational retrieval of SMC over meadows. In contrast, the surface roughness parameter distributions of two fallow maize fields differ significantly and the surface roughness conditions changing over time result in less consistent SMC retrievals (calibration $RMSD$s of $0.096\,m^3\,m^{-3}$ and $0.13\,m^3\,m^{-3}$ versus validation $RMSD$s of $0.26\,m^3\,m^{-3}$). The SMC retrieval uncertainty derived with the Bayesian calibration successfully reproduces the uncertainty estimated empirically using in situ references. The main uncertainty originates from the in situ references and the Sentinel-1 observations, whereas the contribution from the surface roughness parameters is relatively small. The presented research yields further insights into the surface roughness of agricultural fields and SMC retrieval uncertainties, and these insights can be used to guide SAR-based SMC product developments.

Keywords: Soil moisture content, remote sensing, Sentinel-1 satellites, retrieval uncertainty, uncertainty sources, soil surface roughness.

6.1 Introduction

The soil moisture content (SMC) is a key state variable in climatological, meteorological, hydrological and ecological processes. Its control on the exchanges of water and energy at the land surface plays an important role in the development of climate and weather systems (Global Climate Observing System (GCOS), 2016; Massari et al., 2014; Seneviratne et al., 2010). In addition, it is important for the partitioning of rainfall in infiltration and runoff (Beck et al., 2009; Massari et al., 2014; Wanders et al., 2014), regarded as an indicator for the onset of droughts (Miralles et al., 2016; Seneviratne et al., 2010; Vautard et al., 2007), and essential for vegetation growth (Feddes et al., 1976; Ines et al., 2013). Hence, information about the SMC would benefit a number of applications.

Microwave remote sensing observations from satellites can be used to monitor SMC over large spatial domains. Examples of satellite-based SMC products are from the Advanced Scatterometer (ASCAT) at 25 km and 50 km (Wagner et al., 2013), Advanced Microwave Scanning Radiometer 2 (AMSR2) at 0.1° and 0.25° (Zhang et al., 2017; Kim et al., 2015), Soil Moisture and Ocean Salinity (SMOS) at on average 43 km (Kerr et al., 2010, 2016) and Soil Moisture Active Passive (SMAP) at 3 km, 9 km and 36 km resolution (Chan et al., 2016, 2018; Das et al., 2019). However, these products have a too coarse spatial resolution for many hydrological and agricultural applications (De Lange et al., 2014; Carranza et al., 2019; Pierdicca et al., 2014).

Backscatter (σ^0) observations by synthetic aperture radar (SAR) instruments can be used to estimate the SMC at much finer scale, even up to agricultural field scale (e.g. El Hajj et al., 2017; Lievens and Verhoest, 2012; Su et al., 1997; Amazirh et al., 2018). Bauer-Marschallinger et al. (2019) developed an operational 1 km resolution SMC product from Sentinel-1 SAR σ^0 observations, based on a change detection algorithm that assumes static surface roughness and vegetation conditions. However, at the field scale this assumption is unlikely to hold because spatial surface roughness and vegetation effects on the σ^0 are not averaged out over a large area (Bauer-Marschallinger et al., 2019). In those situations, the relation between the σ^0 signal and SMC must be separated from the effects of surface roughness and vegetation before the SMC can be estimated reliably (Kornelsen and Coulibaly, 2013; Paloscia et al., 2013; Verhoest et al., 2008). Physically based scattering models, such as the integral equation method (IEM) for surfaces (Fung et al., 1992) and the Tor Vergata model for vegetation (Bracaglia et al., 1995), simulate the scattering contributions from soil-vegetation systems based on prescribed electromagnetic characteristics. This supports the application of these models to various site conditions and sensor configurations (Paloscia et al., 2013; Petropoulos et al., 2015), the understanding of backscattering processes (Baghdadi et al., 2002; Balenzano et al., 2012; Wang et al., 2018) and the propagation of uncertainty sources (Satalino et al., 2002; Van der Velde et al., 2012b).

Surface scattering models, including the frequently-used IEM model, simulate the scattering of electromagnetic waves from a surface and are used to estimate the σ^0 from soils (Ulaby and Long, 2014). The surface roughness essentially governs the σ^0 response and, thus, the sensitivity to SMC. The parameterisation of the surface roughness is, therefore, an important input. Measuring the surface roughness was part of many field campaigns, such as EMAC'94 (Su et al., 1997), FLOODGEN in 1994, 1998 and 1999 (Baghdadi et al., 2004), Orgeval'94 (Zribi et al., 1997), OPE3 in 2002 (Joseph et al., 2010), SMAPVEX12 (McNairn et al., 2015), SMAPVEX16-IA (Hornbuckle et al., 2017) and SMAPVEX16-MB (McNairn et al., 2016). However, Baghdadi et al. (2002, 2004) and Su et al. (1997) have shown that the IEM model does not accurately reproduce σ^0 observations using measured surface roughness parameters. Lievens et al. (2011) and Verhoest et al. (2008) attributed this to both uncertainties in the surface roughness measurements and simplifications in the representation of surfaces.

A pragmatic approach for applying surface scattering models to land surfaces is considering the surface roughness parameters as 'effective parameters', obtained by model calibration instead of field measurements (Baghdadi et al., 2002; Lievens et al., 2011; Lievens and Verhoest, 2012; Rahman et al., 2008; Su et al., 1997; Verhoest et al., 2008, 2007). The calibration of the surface roughness parameters is accomplished by searching for a parameter set that results in a match between σ^0 observations and model simulations. Subsequently, the calibrated surface roughness parameters can be used to retrieve SMC from other σ^0 observations and/or on other fields (Su et al., 1997).

In addition to the surface roughness parameterisation, the SMC estimates from σ^0 observations will contain uncertainties specific for the selected retrieval algorithm (De Lannoy et al., 2014; Pathe et al., 2009) and due to uncertainty in the σ^0 observations (Benninga et al., 2019; Pathe et al., 2009). The σ^0 observations contain uncertainty from calibration uncertainties, sensor instabilities and speckle effects, which are together referred to as radiometric uncertainty (Benninga et al., 2019, in Chapter 5). Furthermore, SMC references are required for the calibration of scattering models and the validation of the SMC retrievals. The SMC references are typically obtained from in situ measurements. This introduces uncertainties due to a SMC probe's measurement uncertainty (Cosh et al., 2005) and spatial mismatches with satellite-observed SMC (Western and Blöschl, 1999; Cosh et al., 2006). A horizontal mismatch between the SMC at an in situ monitoring station and field-averaged SMC originates from differences in land cover, soil texture and structure, and local features such as nearby ditches and subsurface drainage pipes. A vertical mismatch originates from the (Sentinel-1 C-band) σ^0 observations having a sampling depth that varies from the surface to a depth of 1 cm–10 cm (Nolan and Fatland, 2003; Ulaby et al., 1996), whereas in practice SMC measurements at 5 cm or 10 cm depth, with an influence zone of e.g. 4 cm above and below the probe (Benninga et al., 2018c, in Chapter 3), often have to be adopted for calibration and validation pur-

poses (e.g. Bauer-Marschallinger et al., 2019; Chan et al., 2018; Kornelsen and Coulibaly, 2013; Pathe et al., 2009; Van der Velde et al., 2015).

Information on the uncertainty of SMC retrievals is essential to assess their reliability and for their applicability, for example for the assimilation of SMC retrievals into land surface models and for combining SMC products (Pierdicca et al., 2014; Verhoest et al., 2007; De Lannoy et al., 2014). Verhoest et al. (2007) estimated the uncertainty of SMC retrievals with the IEM model by defining uncertainty distributions for the surface roughness parameters. As a result of assumed surface roughness parameter uncertainties of ±7.5 %, ±15 % and ±25 %, Verhoest et al. (2007) reported SMC retrieval uncertainties (standard deviations) of $0.023\,m^3\,m^{-3}$, $0.041\,m^3\,m^{-3}$ and $0.060\,m^3\,m^{-3}$, respectively. Vernieuwe et al. (2011) continued on the study by Verhoest et al. (2007) by considering the correlation between the parameters based on a synthetically generated surface roughness dataset. Doubková et al. (2012) and Pathe et al. (2009) estimated the uncertainty of SMC retrievals from parameter uncertainty assumptions and the radiometric uncertainty. Pulvirenti et al. (2018) defined fuzzy logic rules in order to assign a degree of uncertainty (low, medium, high) to each SMC retrieval. These previous studies, however, relied on assumptions regarding the uncertainty of model parameters for the estimation of the SMC retrieval uncertainty. This is reflected in the applied calibration methods in general, which ignore uncertainties and aim for one optimal parameter set that results in a match between observations and simulations (e.g. Joseph et al., 2008; Lievens et al., 2011; Verhoest et al., 2007).

Bayesian calibration approaches allow for the derivation of parameter distributions and the separation of parameter uncertainty from the total simulation uncertainty, based on statistical assumptions of which the validity can be verified (Barber et al., 2012; De Lannoy et al., 2014; Haddad et al., 1996; Notarnicola et al., 2006; Notarnicola and Posa, 2004; Pierdicca et al., 2014). For example, using semi-empirical Oh surface scattering models (Oh et al., 1992, 2002), Haddad et al. (1996) and Pierdicca et al. (2014, 2010) formulated Bayesian frameworks for the retrieval of surface roughness parameters and SMC along with estimates of their retrieval uncertainty.

Bayesian frameworks cannot be solved analytically for highly nonlinear models (Vrugt, 2016), such as physically based scattering models. To provide an efficient solution for such models, the DiffeRential Evolution Adaptive Metropolis package (DREAM; Vrugt, 2016) implements a multichain Markov chain Monte Carlo simulation algorithm for generating samples from the posterior distributions that describe the parameter uncertainty and the total simulation uncertainty. De Lannoy et al. (2014) used DREAM to calibrate a radiative transfer model for simulating SMOS L-band brightness temperatures and to estimate the uncertainty of the parameters and the total simulation uncertainty.

In this study, the uncertainties involved in surface scattering model simulations and SMC retrievals were investigated. We focused on the calibration of the IEM surface roughness parameters, and, therefore, used

Sentinel-1 σ^0 observations and SMC measurements from sparsely vegetated fields, namely two meadows and two fallow cultivated parcels. The Bayesian calibration was performed with DREAM. The chapter extends on previous research on SMC retrieval from SAR σ^0 observations by (1) adopting a Bayesian calibration framework for deriving the uncertainty of the IEM surface roughness parameters and the total uncertainty, (2) assessing the derived SMC retrieval uncertainty against the uncertainty estimated empirically using in situ references, and (3) decomposing the total uncertainty in its four constituents.

6.2 Definitions of uncertainties

The standard deviation is selected as uncertainty measure. The standard deviation of the differences between two datasets, such as SMC retrievals and references, is often referred to as the unbiased root mean square deviation (*uRMSD*; Kerr et al., 2016):

$$uRMSD = \sqrt{\frac{\sum_{t=1}^{N}\left(Y_e(t) + \left(\overline{Y_r} - \overline{Y_e}\right) - Y_r(t)\right)^2}{N}}, \tag{6.1}$$

where N stands for the number of match-ups between estimates (Y_e) and references (Y_r), t stands for the observation number and the bars denote the means of Y_e and Y_r.

A SMC retrieval, its total uncertainty and constituents are illustrated in Figure 6.1. The surface roughness parameters for retrieving the SMC, as well as the parameter uncertainty (U_p) and total uncertainty were derived with Bayesian calibrations, using DREAM as described in Section 6.4. We refer to the total uncertainty that is derived with the Bayesian calibration as $U_{total\text{-}B}$. The surface roughness parameter set with the highest posterior probability, also referred to as the 'maximum a posteriori' (MAP; Vrugt, 2016; De Lannoy et al., 2014; Lu et al., 2017), was used for the optimal SMC retrieval. $U_{total\text{-}B}$ should be of similar magnitude as the empirical uncertainty of SMC retrievals for cases that the Bayesian calibration was statistically valid (De Lannoy et al., 2014). The empirical SMC retrieval uncertainty can be calculated with Equation 6.1 using in situ references. The $U_{total\text{-}B}$ and U_p are visualized by two histograms in Figure 6.1, which partly overlap and show that the distribution of the $U_{total\text{-}B}$ is wider than the distribution of the U_p. This is expected as U_p is one of the constituents of the total uncertainty.

The other constituents are inherent to the in situ references and the satellite observations, namely the measurement uncertainty of the station probes providing the in situ references (U_{sp}), the in situ references' uncertainty attributable to a spatial mismatch with Sentinel-1 observed SMC ($U_{s,S1}$), and Sentinel-1's radiometric uncertainty (U_{S1}). Figure 6.1 illustrates that U_{sp} and $U_{s,S1}$ apply to the in situ references, and U_{S1} applies to the SMC retrievals. In Section 6.3, the U_{sp}, $U_{s,S1}$ and U_{S1} are quantified.

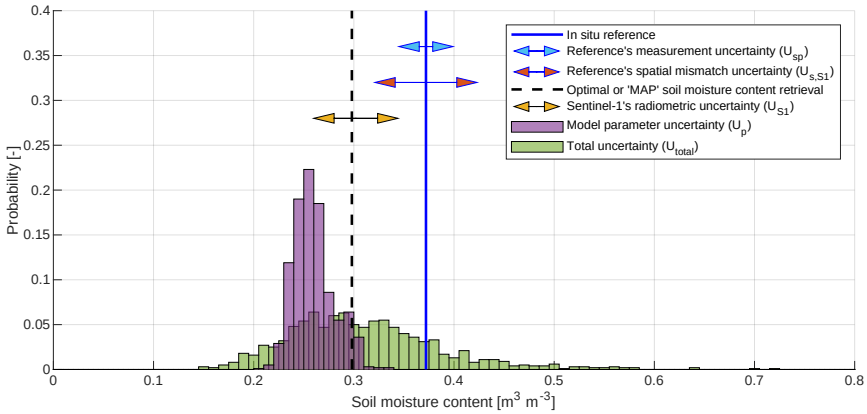

Figure 6.1 The SMC total retrieval uncertainty and its constituents, which are quantified in this study. The arrows represent one standard deviation. The two histograms partly overlap.

Next to its estimation with the Bayesian calibration, the total uncertainty can be found by combining its constituents. This is referred to as $U_{total\text{-}C}$ and can be calculated by following the addition rule for variances (Moore et al., 2017):

$$U_{total\text{-}C} = \sqrt{{U_{sp}}^2 + {U_{s,S1}}^2 + {U_{S1}}^2 + {U_p}^2 + Cov}, \tag{6.2}$$

where Cov stands for the covariance terms between the uncertainty constituents. The constituents are assumed to be uncorrelated, whereby Cov reduces to 0. The relative contributions of U_{sp}, $U_{s,S1}$, U_{S1} and U_p can then be calculated in a similar fashion as was done in Van der Velde et al. (2012a):

$$RC_{sp} = \frac{{U_{sp}}^2}{{U_{total\text{-}C}}^2}, \tag{6.3}$$

$$RC_{s,S1} = \frac{{U_{s,S1}}^2}{{U_{total\text{-}C}}^2}, \tag{6.4}$$

$$RC_{S1} = \frac{{U_{S1}}^2}{{U_{total\text{-}C}}^2}, \tag{6.5}$$

and

$$RC_{p} = \frac{{U_{p}}^2}{{U_{total\text{-}C}}^2}. \tag{6.6}$$

With Equation 6.2 we can evaluate to what extent $U_{total\text{-}C}$ explains $U_{total\text{-}B}$, and with Equations 6.3–6.6 we can assess their individual relative contributions.

6.3 Data

6.3.1 Study region, fields and periods

The SMC measurements used as references were collected by monitoring stations in the Twente region, located in the eastern part of the Netherlands (Figure 6.2). The Twente region is flat with some elevated glacial ridges and it has a temperate oceanic climate with a *Cfb* Köppen-Geiger climate classification (Beck et al., 2018). The SMC monitoring stations in this region are collectively known as the Twente network (Van der Velde et al., 2021; Dente et al., 2011, 2012), further described in Van der Velde and Benninga (in preparation, in Chapter 2).

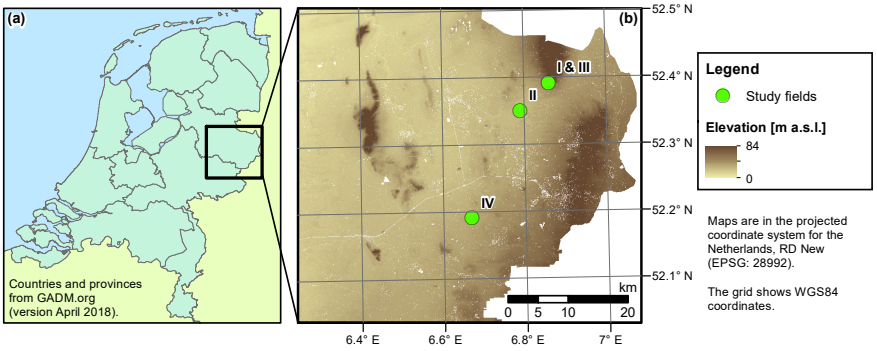

Figure 6.2 **(a)** Location of the Twente region in the Netherlands. **(b)** The locations of the study fields. Background is the digital terrain model AHN2 (Actueel Hoogtebestand Nederland, 2012b).

Stations are installed at the border of fields for safety and continuity reasons. Adjacent to monitoring stations, we selected two meadows (hereafter field I and II) and two fallow cultivated fields (field III and IV) as study fields for which we collected additional field measurements in total on 87 occasions. The study fields and the locations of the field measurements are shown in Figure 4.1. Field I and III are adjacent to the same monitoring station. The study fields have loamy sandy surface layers. Appendix A.1 details the study fields' surface layer soil textures and bulk densities from the soil physical units map of the Netherlands ('bodemfysische eenhedenkaart 2012' in Dutch, or BOFEK2012; Wösten et al., 2013).

Table 6.1 lists the study periods. We used the winter season of October 2016–March 2017 for the calibration of the surface roughness parameters and the winter season of October 2017–March 2018 for the validation of σ^0 simulations and SMC retrievals. The study periods are taken outside the growing season, from October (after harvesting and other agricultural practices) to March (before ploughing and sowing), so that the fields were fallow or covered with non-growing sparse vegetation and no agricultural practices were applied during the study periods. In between the winter seasons, several agricultural practices are applied on

cultivated fields (field III and IV), such as sowing, harvesting, manuring and ploughing. On meadows (field I and II) typically no ploughing is applied and the surface roughness is expected to change little.

Table 6.2 lists the land covers at the locations of the SMC monitoring stations and on the study fields during the calibration and validation period. Field I and II are covered with grass which is virtually static and sparse during winters: field measurements with the LI-COR LAI-2000 (LI-COR, 1992) indicated leaf area indices (LAI) of $1.1\,m^2\,m^{-2}$ and $1.3\,m^2\,m^{-2}$ outside the growing season versus maximums of $8.0\,m^2\,m^{-2}$ and $7.7\,m^2\,m^{-2}$ in the growing season for field I and II, respectively (Benninga et al., 2021a). Field III and IV were fallow with remaining maize stubble in the winter of 2016/2017. In the winter of 2017/2018 field III was again fallow with maize stubble, whereas field IV was used to grow winter wheat. Table 6.2 indicates that also the land cover at station IV changed between the calibration and the validation period. This station was installed on 20 May 2016. In the first period after installation the land cover at the station's location was similar to the study field. The second year it was covered with grassy vegetation because the area with the station probes was no longer directly subjected to agricultural practices.

Table 6.1 Study periods.

Field	Calibration	Validation
I	14 Oct 2016–21 March 2017	14 Oct 2017–21 March 2018
II	31 Oct 2016–16 March 2017	31 Oct 2017–1 April 2018
III	7 Oct 2016–21 March 2017	14 Oct 2017–21 March 2018
IV	14 Oct 2016–21 March 2017	17 Oct 2017–21 March 2018

Table 6.2 Size and land covers of the study fields.

Field	Net area [ha]	Calibration period		Validation period	
		Land cover at the station's location	Field's land cover	Land cover at the station's location	Field's land cover
I	2.0	Grass	Grass	Grass	Grass
II	2.4	Grass	Grass	Grass	Grass
III	0.45	Grass	Fallow with maize stubble	Grass	Fallow with maize stubble
IV	2.4	Fallow with maize stubble	Fallow with maize stubble	Grass	Winter wheat

6.3.2 Soil moisture content references

The SMC monitoring stations are equipped with 5TM probes (METER Group, 2019) installed at nominal depths of 5 cm, 10 cm, 20 cm, 40 cm and 80 cm, of which the readings are stored every 15 min. We used the 5 cm SMC measurements collected at Sentinel-1 overpass times as the in situ references. The probes at 5 cm depth provide an integrated

measurement over a soil depth of 1 cm to 9 cm (Benninga et al., 2018c, in Chapter 3).

The SMC measurements inside the study fields revealed an inconsistency in the station measurements of field IV. During the period May 2016–November 2016 the station measurements had a bias of $-0.024\,m^3\,m^{-3}$ with respect to the field measurements, whereas for the period April 2017–September 2017 the bias increased to $-0.12\,m^3\,m^{-3}$ (see Table 4.2). This likely is a consequence of the change in the land cover at the station's location from fallow with maize stubble to grassy vegetation (see Table 6.2 and Section 6.3.1).

6.3.2.1 Measurement uncertainty

A soil-specific calibration function was developed for the station probes of the Twente network (Van der Velde et al., 2021). The calibration accuracy, quantified by Equation 6.1 between the calibrated probe measurements and gravimetrically determined volumetric SMC (GVSMC) references, is $0.027\,m^3\,m^{-3}$. We adopted this value as general measure for the U_{sp} (it should be noted that later we found a value of $0.0277\,m^3\,m^{-3}$; see Van der Velde and Benninga (in preparation), in Chapter 2).

6.3.2.2 Spatial mismatch uncertainty

The horizontal and vertical mismatches have a systematic and a variable impact on differences between the SMC references and Sentinel-1 observed SMC. The systematic component is a bias which will implicitly be accounted for via the calibration of the surface roughness parameters. The variable component is $U_{s,S1}$, which contributes to the uncertainty of Sentinel-1 SMC retrievals.

The $U_{s,S1}$ was quantified by Equation 6.1 between the station measurements and the spatial mean of the 0 cm–5.7 cm layer SMC measurements inside field I–IV. Chapter 4 provides further information on the estimation of $U_{s,S1}$. The values for $U_{s,S1}$ in Table 4.2 demonstrate that adopting the station measurements as reference for the Sentinel-1 SMC retrievals introduces a significant amount of uncertainty, varying from $0.036\,m^3\,m^{-3}$ to $0.068\,m^3\,m^{-3}$. We adopted the mean of $0.051\,m^3\,m^{-3}$ over field I–IV as the common measure for $U_{s,S1}$.

6.3.3 Sentinel-1 imagery

6.3.3.1 Data processing

The Sentinel-1 constellation provides images in C-band (5.405 GHz), over land in Interferometric Wide Swath (IW) mode at VV and VH polarization. We only used the Sentinel-1 σ^0 observations in VV polarization because of the higher expected sensitivity to SMC than the VH polarization (e.g. Amazirh et al., 2018; El Hajj et al., 2017) and because the definitions of the surface roughness parameters in the IEM model are different for VV and VH due to underlying assumptions. The radiometric accuracy

is specified at 1 dB (three standard deviations). After multi-looking, the Ground Range Detected (GRD) High Resolution (HR) product has a resolution of 20 m × 22 m (4.4 equivalent number of looks) (Torres et al., 2012; Bourbigot et al., 2016).

To obtain Sentinel-1 backscatter (σ^0), we downloaded Level-1 GRD HR IW Sentinel-1 images from the Copernicus Open Access Hub (Copernicus, 2019) and processed them using the following operations in the European Space Agency (ESA)'s Sentinel Application Platform (SNAP) V6.0 (ESA, 2019): (1) Apply Orbit File, (2) Thermal Noise Removal, and (3) Range Doppler Terrain Correction, including radiometric normalization to σ^0 (in $m^2\,m^{-2}$) with projected local incidence angles on a geographic grid (WGS84) with a pixel spacing of 9.0E−5° (equivalent to 10 m × 6.1 m at the study region's latitude). Subsequently, the Sentinel-1 σ^0 observations were averaged over the study fields, excluding a 20 m distance from the borders of the fields and 40 m from trees and buildings to avoid possible influences of features outside the fields (see the net area in Table 6.2). The last step was to convert the σ^0 values to decibel (dB).

Table 6.3 specifies the orbits that cover the study region. Sentinel-1A provides images since 3 October 2014 and Sentinel-1B since 28 September 2016. The combination of Sentinel-1A and Sentinel-1B gives a temporal resolution of 1.5 days over the study region. However, frozen conditions, wet snow and intercepted rain can disturb σ^0 observations and we masked the Sentinel-1 observations for these weather-related surface conditions with the masking rules presented in Benninga et al. (2019, in Chapter 5). Furthermore, in situ references that decreased during frozen soil periods (Van der Velde et al., 2021) were removed, and from 18 January 2018 to 16 March 2018 the SMC monitoring station adjacent to field II was malfunctioning and no references are available for this period. Table 6.4 lists the number of Sentinel-1 observations with a matching in situ reference, before and after masking for the above-mentioned weather-related surface conditions.

Table 6.3 Specifications of the Sentinel-1 orbits that cover the Twente region.

Relative orbit number	Pass	Acquisition time (CET)	Platform heading relative to north	Projected incidence angle over the study fields
15	Ascending	18:16	−15.4°	34.4°–35.3°
37	Descending	6:49	−164.6°	35.4°–36.1°
88	Ascending	18:24	−15.3°	42.6°–43.4°
139	Descending	6:41	−164.6°	43.6°–44.2°

6.3.3.2 Radiometric uncertainty

Sentinel-1's radiometric uncertainty (s_{S1}, in dB) was estimated by the standard deviation of Sentinel-1 σ^0 observations from a target which is assumed time-invariant (Benninga et al., 2019, in Chapter 5). This resulted in a second-order power function between s_{S1} and the surface area over which the Sentinel-1 σ^0 observations are averaged. The SMC retrieval uncertainty due to the s_{S1} (being U_{S1}) is then derived through

Table 6.4 The number of Sentinel-1 observations for which a matching in situ reference is available.

Field	Calibration		Validation	
	Total	After masking	Total	After masking
I	87	50	96	54
II	74	42	63	40
III	92	54	96	54
IV	79	55	98	56

combination with the σ^0 to SMC sensitivity, which follows from simulations with the IEM model. The upper and lower boundaries of the uncertainty interval, as in Benninga et al. (2019, in Chapter 5) and Figure 6.1, were averaged for providing U_{S1}.

6.4 Methods

6.4.1 Surface scattering model application

IEM is a physically based surface scattering model (Fung et al., 1992) that has widely been used to simulate the σ^0 from bare and sparsely vegetated land surfaces. Readers are referred to Ulaby and Long (2014) for more background on the IEM model and to Kornelsen and Coulibaly (2013) for a discussion of previous studies in which IEM was used.

Vegetation effects are not accounted for by the IEM model, and accordingly, we limited the calibration and validation periods to the fallow or non-growing sparse vegetation conditions outside the growing season (see Section 6.3.1). The applicability of the IEM model to sparse grass covers is justified by the results of Van der Velde and Su (2009) and Van der Velde et al. (2012b). Van der Velde and Su (2009) found that for C-band σ^0 observations the effects of grass, with a normalized difference vegetation index (NDVI) varying from 0.15 in winters to 0.55 in summers, are small throughout the entire year. These NDVI values correspond to LAI values of approximately $0.38\,m^2\,m^{-2}$ to $1.63\,m^2\,m^{-2}$ (Knyazikhin et al., 1999; Tesemma et al., 2014), which is comparable to our LAI measurements outside the growing season. Moreover, the SMC retrieval uncertainties attributable to vegetation effects were found to be fairly small compared to uncertainties caused by the surface roughness parameterisation (Van der Velde et al., 2012b).

The IEM model requires parameterisations on the dielectric and geometric properties of the land surface. The dielectric properties were estimated with the Mironov soil dielectric mixing model (Mironov et al., 2009). SMC and the soil textures from Appendix A.1 served as input to the Mironov model. The geometry of the land, also known as the surface roughness, is parameterised by the root mean square surface height (s), the autocorrelation length (c_l) and an autocorrelation func-

tion. The exponential autocorrelation function was selected, because it is viewed as most appropriate for agricultural fields (Ulaby and Long, 2014; Verhoest et al., 2008). Callens et al. (2006) have shown that changes in surface roughness due to heavy rainfall are limited when no agricultural practices were applied recently. The study periods were taken such that no agricultural practices were applied within them (see Section 6.3.1) and, therefore, surface roughness can be assumed time-invariant. This assumption is discussed in Section 6.5.3.

Agricultural surfaces are generally anisotropic (Verhoest et al., 2008) and the fields are viewed from a different direction in Sentinel-1's ascending and descending orbits, causing that the surface roughness would be different for these orbits. This is especially expected for the fallow maize fields, which have tillage rows (see Figure 4.1). The meadows do not have a clear row structure. The anisotropy of the study fields was considered by separating the calibration of s and c_l for the Sentinel-1 σ^0 observations made in the ascending and in the descending orbits. By combining the two ascending orbits (15 and 88) and the two descending orbits (37 and 139) respectively, the surface roughness parameters were calibrated on two incidence angles (see Table 6.3) and the varying SMC conditions encountered during the calibration period.

6.4.2 Bayesian model calibration

Bayesian model calibration derives posterior parameter distributions conditioned on prior parameter distributions ($prior$) and the match between model simulations and reference data ($likelihood$), by solving Bayes' rule (Vrugt, 2016):

$$p(\vartheta|z) \propto likelihood \times prior, \tag{6.7}$$

where $p(\vartheta|z)$ is the resulting posterior probability density function (PDF) of the parameters (ϑ) given the reference data (z). The likelihood function evaluates how well the model reproduces z given ϑ, by describing the PDF of the residuals between simulations and references.

The generalized likelihood function, derived by Schoups and Vrugt (2010), offers a wide flexibility in heteroscedasticity, distribution and autocorrelation of the residuals. The likelihood model parameters have to be inferred jointly with the model parameters or must be given a fixed value. The validity of the residual model can be verified with a residual analysis. For more background on residual analysis, readers are referred to Lu et al. (2017), Scharnagl et al. (2011), Schoups and Vrugt (2010) and Thyer et al. (2009).

6.4.3 Application of DREAM

We adopted a simple implementation of the generalized likelihood function, and assumed homoscedastic, Gaussian and uncorrelated residuals. These assumptions are often made and convenient to use (e.g. Lu et al., 2017; Raj et al., 2018; Scharnagl et al., 2011), and lead to the common

standard least squares approach (Schoups and Vrugt, 2010). In Section 6.5.1, the validity of the residual model is verified with a residual analysis. The standard deviation of the residuals (σ_0) has to be inferred with the calibration. The two surface roughness parameters in combination with σ_0 bring the dimensionality (number of unknowns) at three.

The validity of the IEM model is limited to medium surface roughness conditions with $ks \leq 3$, where k is the free-space wavenumber (Baghdadi et al., 2004; Su et al., 1997). For the wavelength of Sentinel-1, this corresponds to a maximum s of 2.68 cm. For c_l no IEM validity domain has been formulated. Calibration ranges of 0.2 cm to 400 cm have been used, and the resulting calibrated c_l values ranged from 1.4 cm to 13 cm for maize and bare agricultural fields (Joseph et al., 2010, 2008; Lievens et al., 2011; Satalino et al., 2002; Verhoest et al., 2007) and from 0.2 cm to 7 cm for a mosaic of grasslands and wetlands (Van der Velde et al., 2012b). Non-informative (uniform) priors are preferred for scientific objectivity (Lunn et al., 2013; Notarnicola and Posa, 2004; Notarnicola et al., 2006). We defined the prior distributions as uniform distributions with the ranges (0.1 cm, 2.68 cm) for s and (0.1 cm, 100 cm) for c_l. The prior distribution of σ_0 is defined as a uniform distribution with ranges (0 dB, 2 dB).

We used the standard DREAM settings (Vrugt, 2016), with ten Markov chains. A burn-in of 50 % of the realizations is recommended to allow initialization to the posterior parameter distributions (Vrugt, 2016). Convergence of the chains was assessed by the multivariate Gelman-Rubin convergence diagnostic $\hat{R}^d$, where $\hat{R}^d$ below 1.2 indicates convergence (Brooks and Gelman, 1998; Vrugt, 2016), and by visual inspection of the mixing of the Markov chains (Raj et al., 2018; Vrugt, 2016). 7000 realizations per chain appeared sufficient to reach convergence after 50 % of the realizations, which results in 35 000 samples describing the posterior parameter distributions.

6.4.4 Soil moisture content retrieval

The MAP surface roughness parameter set was used for the optimal σ^0 simulations and SMC retrievals. These were evaluated against the Sentinel-1 σ^0 observations and in situ SMC references, respectively, with the root mean square deviation ($RMSD$), the unbiased $RMSD$ ($uRMSD$) and the Pearson correlation coefficient (r_P), defined in Appendix A.2.

For the retrieval of SMC from the Sentinel-1 σ^0 observations, we generated look-up tables of σ^0 simulations for SMC values ranging from 0.01 $m^3\,m^{-3}$ to 0.75 $m^3\,m^{-3}$, with an increment of 0.001 $m^3\,m^{-3}$, and combinations of soil textures, incidence angles and surface roughness parameter sets. A SMC retrieval is then taken equal to the SMC value for which the minimum difference between σ^0 simulations and a Sentinel-1 σ^0 observation is found.

For deriving $U_{total\text{-}B}$, we generated 1000 σ^0 residual samples from the skew exponential power distribution that underlies the likelihood function (Schoups and Vrugt, 2010), using the σ_0 that was found for the

MAP surface roughness parameter set. The resulting 1000 SMC retrievals with the MAP surface roughness parameters, after superimposing the σ^0 residual samples on a Sentinel-1 σ^0 observation, describe $U_{total\text{-}B}$. For the computation of U_p, we randomly sampled 1000 surface roughness parameter sets from their posterior distributions and derived 1000 SMC retrievals.

6.5 Results and discussion

6.5.1 Residual analysis

The residual analysis plots for the Bayesian calibrations are included in Appendix A.3.1. The figures (a) in Figures A.1–A.4 show for fields I to IV that the residual variances are generally independent of the simulated σ^0, which justifies the use of a homoscedastic residual model. The figures (b) show that the deviations from the theoretical quantiles for a Gaussian distribution are only substantial for a few σ^0 simulations at the tails and not systematic among the calibration cases, so we accepted the validity of the Gaussian residual distribution. Only for field IV a number of outliers can be observed, which is further discussed with regard to the σ^0 simulations in Section 6.5.3.

The calibration cases show some autocorrelation, with mean values of 0.40 at a lag of one time step and 0.28 at a lag of two time steps (figures (c) in Figures A.1–A.4). In the Bayesian calibration of process models, such as rainfall-runoff models (Schoups and Vrugt, 2010) and terrestrial ecosystem models (Lu et al., 2017), autocorrelation in the residuals can be accounted for with autoregressive residual models. However, the IEM model does not contain state variables. Using autoregressive residual models, therefore, does not change the posterior parameter distributions nor the residual analysis plots of our calibration results. In Appendix A.4 this is demonstrated by showing for field I the calibration results obtained with a first-order and a second-order autoregressive residual model.

Appendix A.3.2 contains the residual analysis plots for the validation period. Figures A.5–A.8 show that the homoscedastic Gaussian residual model is generally also valid for the validation period. The quantile-quantile plots already give an outlook on the performances of the σ^0 simulations and SMC retrievals in the validation period. Regarding field I, the quantile-quantile plot (Figure A.5b) is steeper (larger dispersion) than the quantile-quantile plot for the calibration period and it reveals a bias (compare to the plot's origin, $(0, 0)$). Hence, a 'slightly' degraded performance and a bias are expected for the validation period. For field II the quantile-quantile plots for the calibration and the validation period (Figures A.2b and A.6b) are comparable, so we expect similar performances. For field III (Figure A.3b) and field IV (Figure A.4b) steep lines and high biases are observed, suggesting worse performances for the validation period.

6.5.2 Posterior parameter distributions

Figures 6.3–6.6 show the posterior parameter sets and the MAP s and c_l for fields I to IV. Joseph et al. (2008), Lievens et al. (2011), Rahman et al. (2008) and Verhoest et al. (2007) already reported that multiple optimal combinations of s and c_l are possible. The scatter plots in Figures 6.3–6.6 illustrate that the posterior distributions of the surface roughness parameters actually cover a large part of the solution space, and that the s and c_l are highly correlated (Spearman's rank correlation coefficient, r_S, is 0.97 to 1.0).

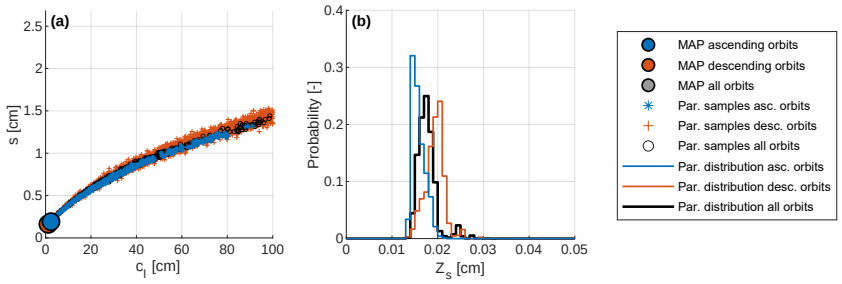

Figure 6.3 **(a)** The posterior combinations of s and c_l, and **(b)** histograms of the posterior Z_s distributions, for field I.

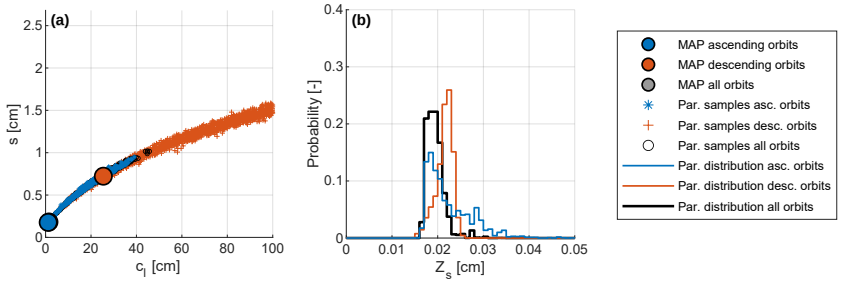

Figure 6.4 Same as Figure 6.3, but for field II.

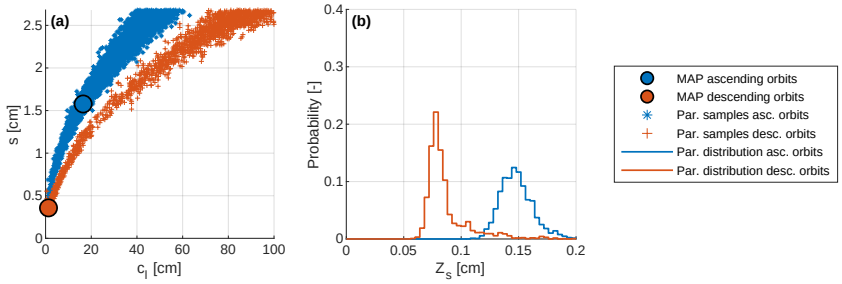

Figure 6.5 Same as Figure 6.3, but for field III.

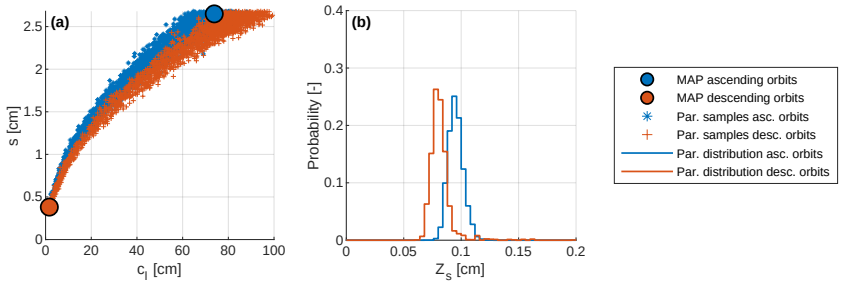

Figure 6.6 Same as Figure 6.3, but for field IV.

Individual values of s or c_l, therefore, do not contain much information about the surface roughness. For example, s values of 0.5 cm to 1.5 cm are found in the posterior parameter distributions of all the fields. Hence, both s and c_l or a ratio between them should be used to characterize the roughness of a surface. From Figures 6.3–6.6 it is clear that the relation between s and c_l is non-linear and that the simple s/c_l ratio will not suffice. Instead, it is approximately a square root relation and the parameter $Z_s = s^2/c_l$ (Zribi and Dechambre, 2002) is suitable for characterizing the roughness of the surfaces.

For the meadows (Figures 6.3 and 6.4), the ascending and the descending orbits' posterior distributions coincide. In other words, the surface roughness is similar for the Sentinel-1 σ^0 observations made in the ascending and in the descending orbits. This is an indication that the meadows have an isotropic surface roughness, at least in Sentinel-1's ascending and descending orbit viewing directions. Therefore, we also calibrated the surface roughness parameters with the Sentinel-1 σ^0 observations from both passes combined, of which the results are also shown in Figures 6.3 and 6.4. The parameter sets obtained from the combined calibration were used in the remainder of this chapter.

Furthermore, the posterior parameter distributions of the two meadows are quite similar. The MAP s values are 0.16 cm and 0.18 cm, and the c_l values are 1.31 cm and 1.49 cm for field I and field II, respectively. In Section 6.5.3 we discuss the cross-validation results of the MAP surface roughness parameters of field I applied to retrieve the SMC for field II, and vice versa.

For the fallow maize fields (Figures 6.5 and 6.6), the ascending and the descending orbits' posterior distributions are different. This was expected, as these fields do have an anisotropic surface due to tillage rows and these are viewed from different angles in the ascending and descending orbits.

6.5.3 Retrievals

The MAP SMC retrievals, U_p and $U_{total\text{-}B}$ are plotted as time series in Figure 6.7, and Table 6.5 lists the performance metrics of the MAP SMC retrievals for the calibration and the validation period. Time series

and performance metrics of the forward σ^0 simulations, using the SMC references and calibrated surface roughness parameters as input to the IEM model, are shown in Figure 6.8 and Table 6.6 respectively.

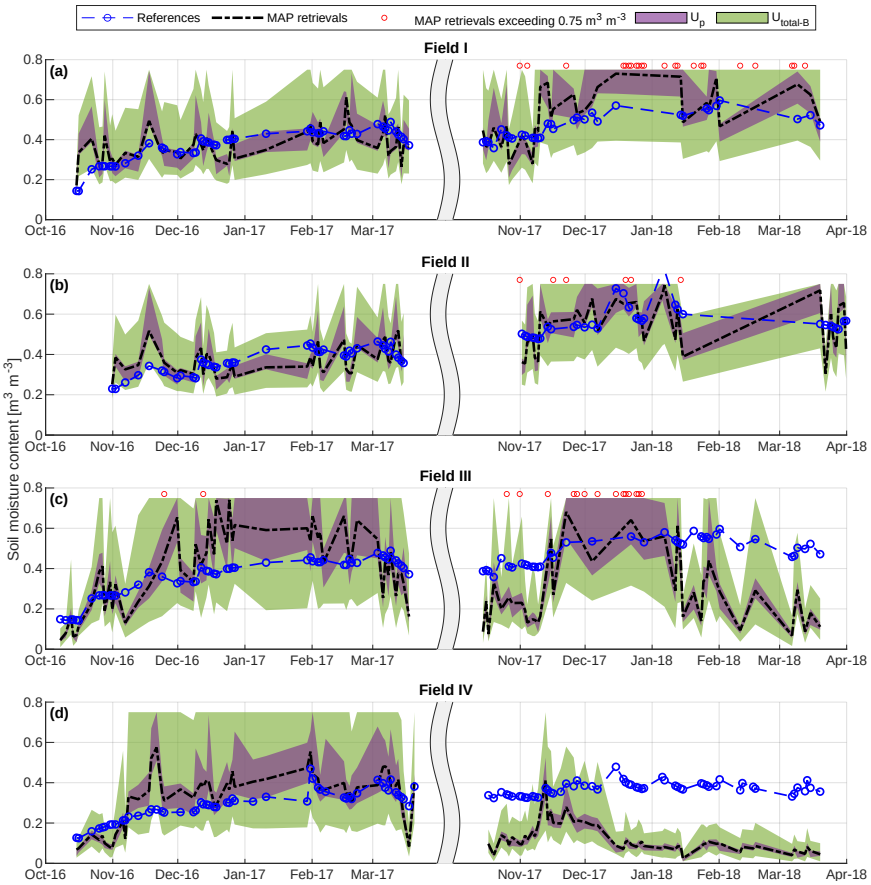

Figure 6.7 The SMC retrievals and in situ references. The U_p and $U_{total\text{-}B}$ are visualized by the 95 % confidence interval.

6.5.3.1 Meadows

The performance of the meadows' MAP σ^0 simulations is comparable for the calibration and the validation period. This indicates that the surface roughness remained similar, which can be explained by the fact that no ploughing was applied on the meadows. The increase in the empirical uncertainty ($uRMSD$, Equation 6.1) of the SMC retrievals can be explained by the wetter conditions during the validation period. IEM model simulations show that the σ^0 to SMC sensitivity diminishes with increasing SMC, see for example Figure 3 in Altese et al. (1996) and the results in Benninga et al. (2019, in Chapter 5), which results in larger SMC deviations for equal σ^0 deviations under wetter conditions. Because

Table 6.5 Performance metrics of the MAP SMC retrievals against the in situ references.

Field	Note	Calibration			Validation		
		r_P [−]	$RMSD$ [$m^3\,m^{-3}$]	$uRMSD$ [$m^3\,m^{-3}$]	r_P [−]	$RMSD$ [$m^3\,m^{-3}$]	$uRMSD$ [$m^3\,m^{-3}$]
I	-	0.50	0.079	0.079	0.65	0.11	0.10
	With parameters II	0.51	0.10	0.070	0.55	0.12	0.12
II	-	0.30	0.076	0.076	0.54	0.10	0.10
	With parameters I	0.28	0.14	0.098	0.14	0.10	0.10
III	All orbits	0.70	0.15	0.14	0.51	0.25	0.14
	Excluding orbit 15	0.70	0.13	0.12	0.43	0.26	0.15
IV	-	0.76	0.096	0.088	−0.056	0.26	0.077

Table 6.6 Performance metrics of the MAP σ^0 simulations against the Sentinel-1 σ^0 observations.

Field	Note	Calibration			Validation		
		r_P [−]	$RMSD$ [dB]	$uRMSD$ [dB]	r_P [−]	$RMSD$ [dB]	$uRMSD$ [dB]
I	-	0.67	0.72	0.72	0.69	0.99	0.77
	With parameters II	0.68	0.99	0.72	0.68	0.78	0.77
II	-	0.54	0.62	0.62	0.66	0.63	0.63
	With parameters I	0.52	0.92	0.62	0.66	0.92	0.63
III	All orbits	0.88	1.13	1.13	0.62	2.41	2.19
	Excluding orbit 15	0.88	0.93	0.93	0.54	2.48	2.21
IV	-	0.85	1.10	1.10	0.49	4.07	1.56

of this, the SMC retrieval uncertainty distributions in Figure 6.7 are also wider at higher SMC and they are skewed towards the higher SMC levels.

The posterior surface roughness parameter distributions and the MAP values are quite similar for the two meadows. To further verify this, we performed a cross-validation by retrieving the SMC for field II using the MAP surface roughness parameters of field I, and vice versa. Table 6.5 lists the SMC retrieval performances, and Appendix A.5 includes the SMC and σ^0 time series figures. The calibration has aimed to optimize the $RMSD$ of the σ^0 simulations, so it could be expected that the $RMSD$ for the calibration period is higher using the MAP parameter set of the other meadow. In general, the SMC retrieval performances are comparable using the MAP surface roughness parameter sets obtained for the other meadow.

6.5.3.2 Fallow fields

The validation performances for the fallow fields are considerably worse than the calibration performances. Field III was fallow with maize stubble during both the calibration and the validation period, but the surface roughness is likely to be different due to agricultural practices in between. Furthermore, Figures 6.7c (and 6.8c) show in the validation period three distinctive periods: from 14 October 2017 to 10 November 2017 with low SMC retrievals (high σ^0 simulations), from 15 November 2017 to 14 January 2018 with high SMC retrievals (low σ^0 simulations), and from

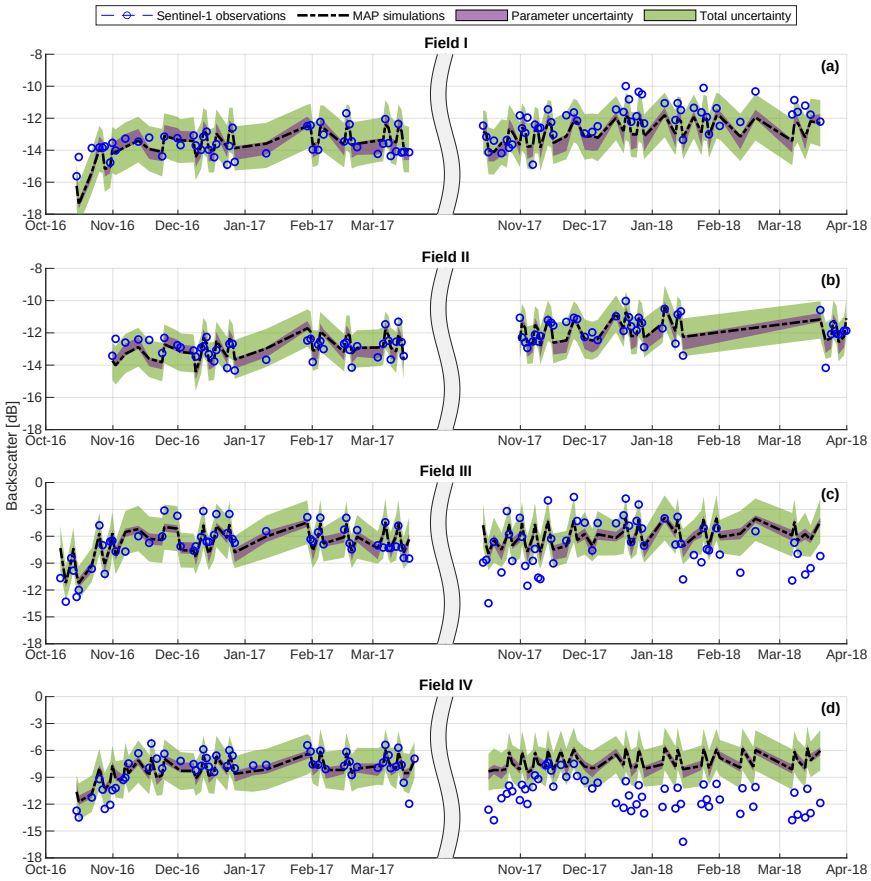

Figure 6.8 Sentinel-1 σ^0 observations and simulations. The parameter and total simulation uncertainty are visualized by the 95 % confidence interval.

15 January 2018 to 21 March 2018 with low SMC retrievals (high σ^0 simulations). However, the field was harvested in September/October 2017 and not ploughed after May 2017, so changes in surface roughness due to agricultural practices and heavy rainfall were not expected. This result demonstrates that even under these circumstances, the fallow field cannot be simulated with a single set of surface roughness parameters.

Besides, Sentinel-1 σ^0 observations of up to -3 dB in the calibration period and -2 dB in the validation period were acquired for field III, with a maximum of -1.62 dB. These Sentinel-1 observations all originate from relative orbit number 15. The IEM model with an exponential autocorrelation function for the surface roughness cannot reproduce such high σ^0 observations with any set of surface roughness parameters. Therefore, we omitted the Sentinel-1 σ^0 observations of field III acquired in relative orbit 15 for further analysis in this study. An additional calibration was performed exclusively on the Sentinel-1 observations acquired in relative orbit 88, of which the results are presented in Appendix A.6. The

posterior parameter distributions (Figure A.14) and the σ^0 simulation performances (Figure A.17) for this calibration are, however, similar to the calibration on both ascending orbits. Using the original surface roughness parameter sets and omitting the orbit 15 Sentinel-1 σ^0 observations does improve the σ^0 simulation and SMC retrieval performances (Tables 6.5 and 6.6).

For field IV, the validation performances are more degraded than for field III. This can be explained by the different land covers in the calibration and the validation period (Table 6.2) and by the bias in the in situ references during the validation period (Section 6.3.2). Figure 6.9a shows the residuals of the MAP SMC retrievals with the original references and with the references corrected for the bias of $-0.12\,\mathrm{m^3\,m^{-3}}$. Part of the residuals can indeed be explained by this bias. However, still three periods can be distinguished in the residuals: between 17 October 2017 and the sowing of the winter wheat on 10 November 2017 the *RMSD* against the bias-corrected references is $0.10\,\mathrm{m^3\,m^{-3}}$ (13 observations), between 13 November 2017 and 6 December 2017 the *RMSD* is smallest with a value of $0.050\,\mathrm{m^3\,m^{-3}}$ (10 observations), and after 15 December 2017 the *RMSD* is $0.19\,\mathrm{m^3\,m^{-3}}$ (32 observations). The development of the winter wheat vegetation on this field during the validation period does not have a large effect, as this should otherwise be visible as a gradual trend in the residuals extending to April 2018. Moreover, at the end of the validation period the wheat cover is still sparse, as is shown in Figure 6.9b. A number of heavy rainfall events occurred between 6 December 2017 and 15 December 2017 (in total 64 mm). Callens et al. (2006) demonstrated that rainfall smoothens the surface and reduces the surface roughness on recently tilled fields. Indeed, the Sentinel-1 σ^0 observations being lower after 15 December 2017 is in accordance with a reduced surface roughness.

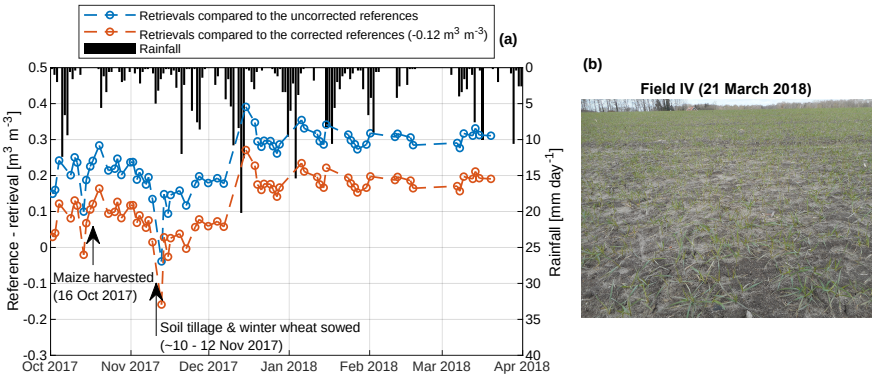

Figure 6.9 **(a)** Residuals between the MAP SMC retrievals and the in situ references of field IV over the validation period. **(b)** Field IV on 21 March 2018.

A number of outliers were observed in the residual analysis plots of the calibrations on field IV. As visualized in Figure A.4, the σ^0 simulations in the first part of the calibration period, between 14 October 2016 and

6 November 2016, hold the largest residuals and all these residuals are on one side of the quantile-quantile plots. This indicates that the surface roughness conditions have changed within the calibration period. As discussed in the previous paragraphs, for both fallow fields the same holds between the calibration and the validation period as well as within the validation periods.

6.5.3.3 Note on the soil moisture content references

It should be noted that the SMC references extend to higher levels than saturated SMCs generally observed. BOFEK2012 (Wösten et al., 2013) lists saturated SMC values of 0.44 $m^3\,m^{-3}$–0.45 $m^3\,m^{-3}$ for the surface layers (0 cm to 23 cm depth) of field I to IV. These values are exceeded by the station SMC measurements. This can be partly attributed to higher organic matter content and root density near the soil surface. Organic matter increases SMC values especially in sandy and loamy sandy soils (Minasny and McBratney, 2018). In addition, local soil variability is not captured by BOFEK2012, local soil variability is not considered in the probes' calibration function, and roots and macropores in the probes' influence zone can increase measured SMC (Benninga et al., 2018c, in Chapter 3). However, even with consideration of these factors, the very high SMC measurements, especially for field II, seem unrealistic in absolute sense. Nevertheless, the correlations between the station and field measurements, listed in Table 4.2, are high. It can, therefore, be expected that the station measurements capture the temporal variability of the adjacent field's SMC.

The absolute SMC measurement values may still deviate from realistic values. This will affect the surface roughness parameters obtained by the calibration, and for the SMC retrieval over independent periods or fields it may be necessary to apply an unbiasing procedure. This is reflected in the meadows' cross-validation results, see Tables 6.5 and 6.6: the $RMSD$s, which include the bias in the mean, are generally higher than the original calibration metrics, whereas the r_P and $uRMSD$s, which exclude this bias, are comparable.

6.5.4 Retrieval uncertainty

Figure 6.10 shows $U_{total\text{-}B}$ in comparison to the uncertainty of the MAP SMC retrievals estimated empirically using the SMC references and Figure 6.11 shows $U_{total\text{-}B}$ relative to $U_{total\text{-}C}$, for bins of SMC references. The empirical uncertainty is quantified with Equation 6.1, but without removing the bias for each bin separately to preserve the integrity of the time series' PDFs. For field I and II both the calibration and the validation period are included (Figures 6.10a and b). Since it was found that the parameters calibrated for the cultivated fields (field III and IV) are invalid for the validation period, the latter period is not included in Figures 6.10c–f. As a consequence of that and because the ascending and descending orbits are separated for field III and IV, the total number of

pairs is larger for field I and II and for visualization purposes the number of pairs per bin in Figures 6.10 and 6.11 is ten for field I and II and five for field III and IV.

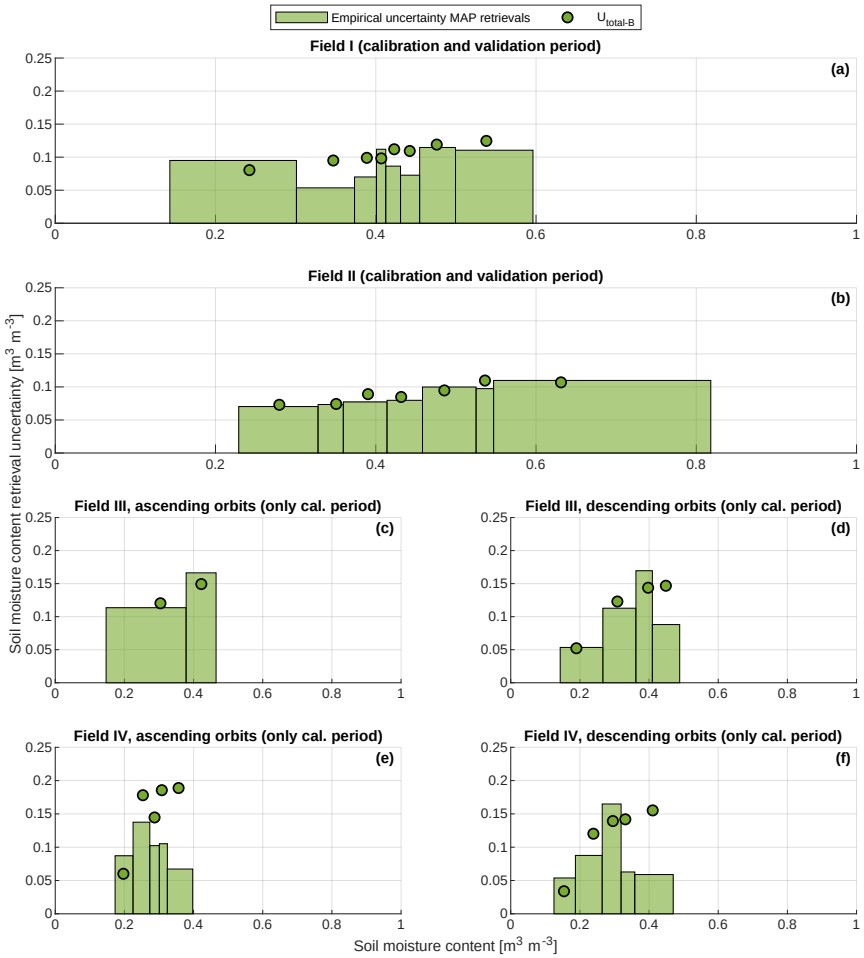

Figure 6.10 The empirical uncertainty of SMC retrievals and $U_{total\text{-}B}$, for bins of SMC references. The number of pairs per bin is ten for field I **(a)** and II **(b)** and five for field III **(c–d)** and IV **(e–f)**.

The increasing empirical uncertainty and $U_{total\text{-}B}$ with increasing SMC in Figure 6.10 are explained by the diminishing σ^0 to SMC sensitivity with increasing SMC, as was discussed in Section 6.5.3.1. Both the increasing trend and the magnitude of the empirical uncertainty are rather closely approximated by $U_{total\text{-}B}$. In other words, the SMC retrieval uncertainty derived with the Bayesian calibration does successfully reproduce the uncertainty estimated empirically. This does, however, not hold for field IV. As explained in Section 6.5.3.2, the IEM model does not correctly reproduce the σ^0 of field IV within the calibration period with a single set of surface roughness parameters. As a consequence, the likelihood func-

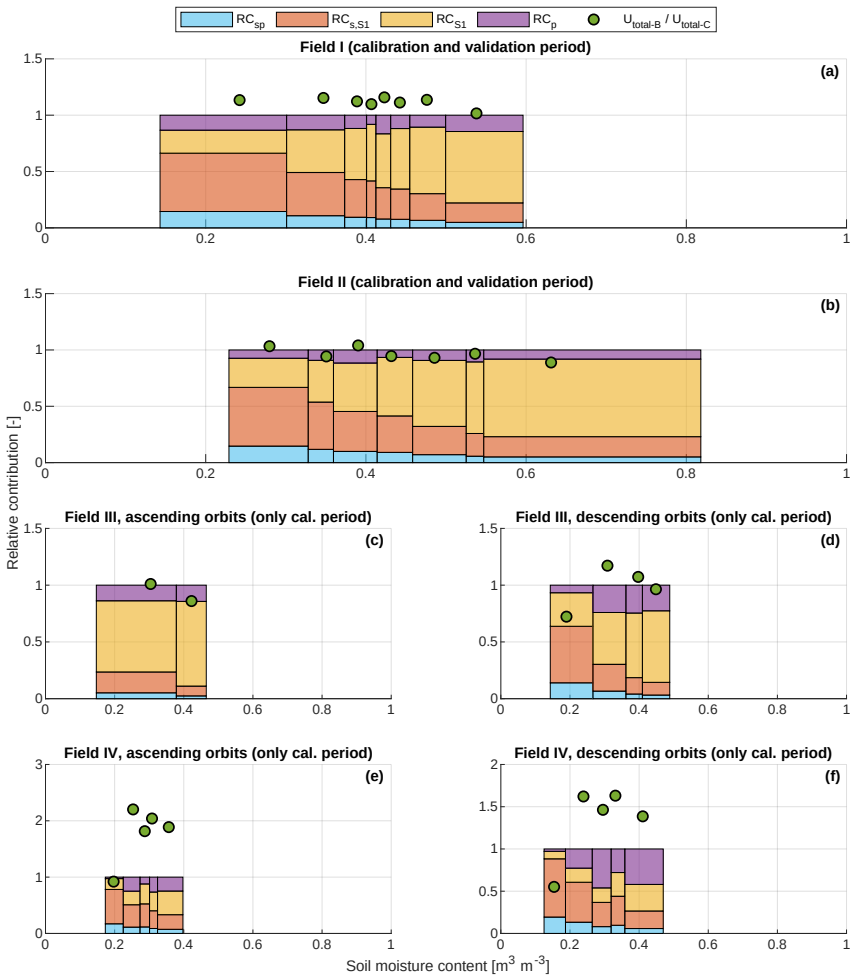

Figure 6.11 $U_{total\text{-}B}$ and its four constituents relative to $U_{total\text{-}C}$. The bins are the same as in Figure 6.10.

tion implementation with a homoscedastic residual standard deviation is not valid over the complete calibration period.

Figure 6.11 shows that the combination of U_{sp}, $U_{s,S1}$, U_{S1} and U_p, i.e. $U_{total\text{-}C}$, approximately explains $U_{total\text{-}B}$, except for field IV again. Figure 6.11 also shows the relative squared contributions of U_{sp}, $U_{s,S1}$, U_{S1} and U_p, namely RC_{sp}, $RC_{s,S1}$, RC_{S1} and RC_p. The RC_p is relatively small and constant across the investigated SMC domain, with an average of 13 % over the SMC domain and fields I to III. This means that the U_p increases with SMC because the total uncertainty increases with increasing SMC. From the assumption that U_{sp} and $U_{s,S1}$ are equal to $0.027\,\mathrm{m^3\,m^{-3}}$ and $0.051\,\mathrm{m^3\,m^{-3}}$ across the entire SMC domain follows that their relative contributions (RC_{sp} and $RC_{s,S1}$) decrease with increasing SMC because the total uncertainty increases with SMC. The average RC_{sp} and $RC_{s,S1}$

decrease, respectively, from 13 % and 46 % at a SMC of 0.26 $m^3\,m^{-3}$ to 4 % and 15 % at a SMC of 0.53 $m^3\,m^{-3}$. The average RC_{S1} increases from 31 % at a SMC of 0.26 $m^3\,m^{-3}$ to 67 % at a SMC of 0.53 $m^3\,m^{-3}$, which is explained by the increasing U_{S1} with increasing SMC (Benninga et al., 2019, in Chapter 5). The U_{S1} is found to be the dominant driver for the increasing SMC retrieval uncertainty with increasing SMC. For field III, the RC_{S1} is even larger than for the other fields (at an equal SMC level) because of field III's smaller surface area.

6.6 Conclusions

The total uncertainty and its constituents were investigated for SMC retrievals from Sentinel-1 σ^0 observations over four sparsely vegetated fields (two meadows and two fallow cultivated fields). A Bayesian framework was used for calibrating the surface roughness parameters that are input to the IEM surface scattering model, and for deriving the parameter and total uncertainty distributions. Subsequently, these distributions were used to retrieve the SMC and its uncertainty, and the relative contributions of four uncertainty sources were evaluated. This resulted in the following conclusions:

1. The simplest implementation of the likelihood function, using a homoscedastic Gaussian residual model, describes the simulation residuals. An exception is when the IEM model is not capable of reproducing the Sentinel-1 σ^0 observations in a calibration or validation period with a single set of surface roughness parameters.
2. The surface roughness parameters (s and c_l) are highly correlated, with Spearman's rank correlation coefficients (r_S) of 0.97 to 1.0. The s and c_l have approximately a square root relation and the parameter $Z_s = s^2/c_l$, which was already introduced in Zribi and Dechambre (2002), is shown to be suitable for characterizing the roughness of the surfaces. This result also implies that it is valid to fix one of the parameters s or c_l for simplifying the calibration while still acquiring the same posterior Z_s distribution.
3. For the two meadows the surface roughness parameter distributions coincide for Sentinel-1's ascending and descending orbits, despite the different directions from which Sentinel-1 views the fields in these passes. Furthermore, the surface roughness parameter distributions of the two meadows are quite similar. In contrast, for the two fallow fields the surface roughness parameter distributions depend on the pass direction and the distributions differ between the two fields. This is attributed to the anisotropic nature of these surfaces caused by tillage rows.
4. The performance of the SMC retrievals for the calibration period, expressed by the $RMSD$, is between 0.076 $m^3\,m^{-3}$ and 0.13 $m^3\,m^{-3}$. The validation results for an independent period confirm that, for the meadows, the surface roughness parameters can be used across

years. For the fallow fields, however, the surface roughness conditions change; not only between the calibration and the validation period, but even within single winter periods.

5. The total SMC retrieval uncertainty derived with the Bayesian calibration successfully reproduces the uncertainty estimated empirically using in situ references, including the trend of increasing uncertainty with increasing SMC.
6. The in situ references' measurement uncertainty (U_{sp}) and spatial mismatch uncertainty ($U_{s,S1}$), the SMC retrieval uncertainty due to Sentinel-1's radiometric uncertainty (U_{S1}) and the parameter uncertainty (U_p) constitute the total uncertainty. The main uncertainty originates from the in situ references and the Sentinel-1 σ^0 observations, whereas the contribution from the surface roughness parameters is relatively small.

The two meadows' coinciding surface roughness parameter distributions for the ascending and descending orbits, their similar surface roughness and consistent SMC retrievals for the calibration and validation period are promising results for operational retrieval of SMC over meadows. The value of such a SMC product would be substantial as meadows cover a major portion of the land in use for agriculture, e.g. 71 % in the study region Twente and 55 % in the Netherlands in 2017 (Ministry of Economic Affairs and Climate Policy, 2020). Therefore, further research to the selection of a common surface roughness parameter set for meadows and the associated retrieval uncertainty would be interesting.

To improve the performance of the Sentinel-1 SMC retrievals it will be essential to reduce the in situ references' uncertainties and the radiometric uncertainty. The references' uncertainties can be reduced by averaging multiple spatially distributed measurements. Reducing the impact of radiometric uncertainty can be achieved by accepting a coarser spatial resolution or a further improvement of the SAR image processing.

By the Bayesian calibration of the IEM model, further insights into the surface roughness of agricultural fields and SMC retrieval uncertainties have been derived. These insights can be used to guide SAR-based SMC product developments. Moreover, the study shows the utility of Bayesian calibration approaches for deriving such new insights and the presented methodology may serve as an example for the Bayesian calibration of other scattering model applications.

7 Sentinel-1 soil moisture content retrieval over meadows using a physically based scattering model

This chapter is based on:

Benninga, H. F., Van der Velde, R., and Su, Z.: Sentinel-1 soil moisture content retrieval over meadows using a physically based scattering model, submitted.

Abstract

Soil moisture content (SMC) information at field scale could have important applications in agricultural and regional water management. This study presents an operationally applicable scheme for SMC retrieval over meadows from synthetic aperture radar (SAR) backscatter (σ^0) observations. We parameterised the vegetation scattering and absorption model developed at the Tor Vergata University of Rome (TV) and the integral equation method (IEM) surface scattering model for grass-covered soil surfaces. Leaf area index (LAI) estimates from a Sentinel-2 product provide field-scale vegetation information, as is demonstrated by validation against in situ measurements. The SMC retrieval scheme is applied with field-averaged Sentinel-1 σ^0 observations from November 2015 to November 2018 and evaluated on 21 meadows against adjacent in situ station measurements, without (IEM) and with a vegetation correction (TV-IEM). Masking the IEM and TV-IEM SMC retrievals for dense vegetation conditions improves their performance, but this is a trade-off with the number of retrievals. By setting the SMC retrievals that exceed the upper retrieval limit of $0.75\,m^3\,m^{-3}$ during the wet period to the maximum SMC, the performance metrics improve to mean Pearson correlation coefficients of 0.55 for IEM and 0.64 for TV-IEM, root mean square deviations ($RMSD$) of $0.14\,m^3\,m^{-3}$ for IEM and $0.13\,m^3\,m^{-3}$ for TV-IEM, and $RMSD$s relative to the range of the SMC references of 24 % for both IEM and TV-IEM. The slightly better SMC retrieval performance with TV-IEM is caused by invalid SMC retrievals under dense vegetation conditions, and the performance metrics for IEM and TV-IEM are practically equal by considering the same retrieval-reference pairs. The IEM and TV-IEM retrieval performances are also similar to the performance of two other Sentinel-1 based products at field scale. They are, on average, outperformed by NASA's Soil Moisture Active Passive (SMAP) 9 km and 36 km products evaluated at field scale, but these products are expected to deviate if larger regional differences are present and in field-specific situations.

Keywords: Soil moisture content, Sentinel-1 satellites, vegetation correction, LAI validation, operationally applicable scheme.

7.1 Introduction

Microwave backscatter (σ^0) observations by synthetic aperture radar (SAR) instruments are known for their potential to monitor soil moisture content (SMC). Recently, interest has grown in the Sentinel-1 satellites because of the combination of its fine spatiotemporal resolutions, high radiometric accuracy and the operational ambition of the programme (Balenzano et al., 2021; Bauer-Marschallinger et al., 2019; Hornacek et al., 2012; Pulvirenti et al., 2018). Balenzano et al. (2021), Bauer-Marschallinger et al. (2019) and Pulvirenti et al. (2018) developed algorithms for the retrieval of SMC from Sentinel-1 observations at resolutions of 1 km, 1 km and 500 m, respectively.

Several studies noted the potential of Sentinel-1 σ^0 observations for monitoring SMC even at finer scales, up to agricultural field scale (e.g. Amazirh et al., 2018; El Hajj et al., 2017). Especially over heterogeneous landscapes with relatively small agricultural fields, such as in western Europe, new applications may be anticipated with SMC information at field scale. This includes agricultural water management for field trafficability and irrigation (Carranza et al., 2019; Lei et al., 2020; Vereecken et al., 2014), and regional catchment management in dry and wet periods (Cenci et al., 2017; Mahanama et al., 2008; Pauwels et al., 2001; Pezij et al., 2019b).

For the SMC to be estimated from Sentinel-1 observations, the relation between σ^0 and SMC must be separated from the effects of surface roughness and vegetation (Kornelsen and Coulibaly, 2013; Paloscia et al., 2013; Verhoest et al., 2008). Surface scattering models, such as the frequently-used 'integral equation method' (IEM) model, simulate the σ^0 from surfaces based on the surface roughness and SMC (via relative permittivity) given the sensing configurations regarding frequency and incidence angle (Ulaby and Long, 2014). The results in Benninga et al. (2020b, in Chapter 6) show that the IEM surface roughness parameters can be assumed time-invariant, independent of the ascending/descending orbit and similar for different meadows. This is a promising finding for the retrieval of SMC over meadows across a larger region because it suggests that using a single set of surface roughness parameters would be allowed. The value of such a product would be substantial as meadows cover a major portion of the land in use for agriculture. However, this finding was obtained only for two meadows. Furthermore, the meadows were in relatively wet and sparsely vegetated (winter) conditions. Hence, further research is required over additional meadows and for a range of hydrometeorological and vegetation conditions.

The development of vegetation throughout a year complicates the retrieval of SMC. Interactions of the microwave signal with vegetation results in attenuation of the soil σ^0, direct σ^0 from the vegetation and σ^0 from soil-vegetation pathways (Ulaby and Long, 2014). These effects are enhanced by Sentinel-1's sub-optimal specifications for SMC retrieval, notably the C-band (wavelength 5.6 cm) observations at relatively large

incidence angles and in VV polarization (Fascetti et al., 2017; Pulvirenti et al., 2018). Based on the theory it is, thus, expected that correcting Sentinel-1 σ^0 observations for vegetation effects contributes to more accurate SMC retrievals. The discrete electromagnetic Tor Vergata (TV) model coupled with the IEM surface scattering model (Bracaglia et al., 1995; Dente et al., 2014; Wang et al., 2018) is a physically based model. Advantages of using a physically based model are the application to various site conditions and sensor configurations (Paloscia et al., 2013; Petropoulos et al., 2015) as well as propagation of uncertainty sources (Benninga et al., 2020b, in Chapter 6; Satalino et al., 2002; Van der Velde et al., 2012b) and the understanding of backscattering processes (Baghdadi et al., 2002; Balenzano et al., 2012; Wang et al., 2018). However, deficiencies in the models, their parameterisations and uncertainty in the input variables, such as current vegetation conditions, will also influence the accuracy of SMC retrievals.

This study presents an operationally applicable scheme for SMC retrieval over meadows from SAR σ^0 observations. For this purpose, we parameterised the TV and IEM models for grass-covered soil surfaces. For representing field-scale vegetation conditions, we utilized a leaf area index (LAI) product derived from Sentinel-2 optical imagery (Paepen and Wens, 2017; VITO, 2019). The Sentinel-2 LAI estimates were validated against in situ measurements collected on six agricultural fields in the east of the Netherlands. The parameters required for the TV and IEM models were adopted from previous studies, except for the vegetation water content (VWC) for which various time-invariant and time-varying VWC values were tested. Then, the SMC retrieval scheme was demonstrated by retrieving the SMC from Sentinel-1 σ^0 observations for 21 meadows and validated against measurements from adjacent in situ monitoring stations. The retrieval results with IEM (without vegetation correction) and TV-IEM (with vegetation correction) are compared to evaluate whether the vegetation correction improves the SMC estimates. Furthermore, we tested whether the performance improves by incorporating information from SMC retrievals that exceed the upper SMC retrieval limit and by masking SMC retrievals for dense vegetation conditions. Eventually, the SMC retrieval performance is compared with the performance of three other Sentinel-1 based products at field scale, three Sentinel-1 based products at 1 km resolution and the Soil Moisture Active Passive (SMAP) 9 km and 36 km products evaluated at field scale.

7.2 Soil moisture content retrieval scheme

Figure 7.1 shows the SMC retrieval scheme, separated in the boxes A–C.

7.2.1 A: Input data

The preparation of the input data starts with the selection of meadows within a study region. In case of the Netherlands this can be done

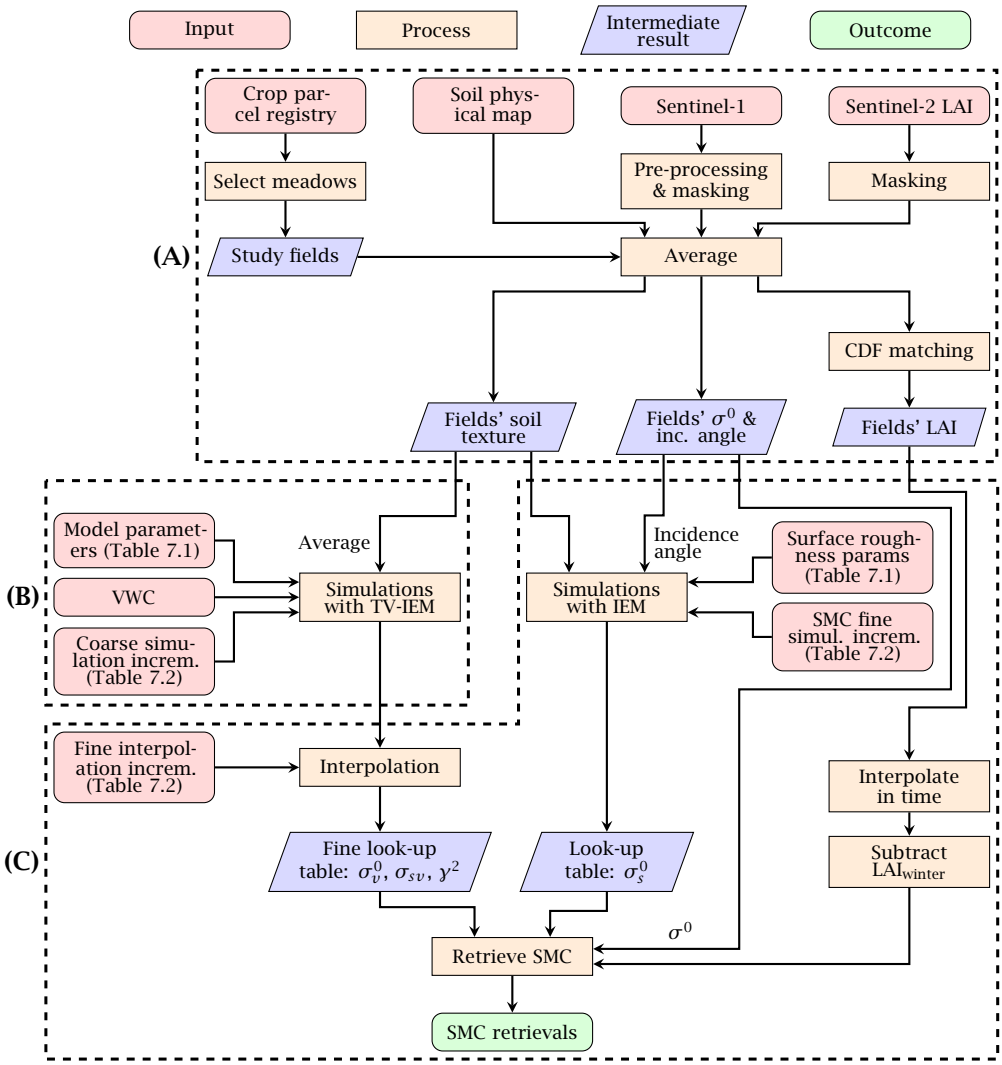

Figure 7.1 Flowchart of the SMC retrieval scheme, separated in the preparation of the input data **(A)**, the parameterisation of the TV-IEM model **(B)**, and the retrieval of SMC from σ^0 observations **(C)**.

with the crop parcel registry ('Basisregistratie Gewaspercelen' in Dutch; Ministry of Economic Affairs and Climate Policy, 2020). This database contains, on an annual basis, the type of crop for each agricultural parcel in the Netherlands. For the selected meadows the average soil texture, Sentinel-1 σ^0 and incidence angle, and Sentinel-2 LAI were calculated. For the soil texture we could use the soil physical properties map of the Netherlands ('bodemfysische eenhedenkaart 2012' in Dutch, or BOFEK2012; Wösten et al., 2013). The preparation steps that were applied to the Sentinel-1 imagery and Sentinel-2 LAI maps are described below.

7.2.1.1 Sentinel-1 imagery

The Sentinel-1 constellation consists of the Sentinel-1A and Sentinel-1B satellites, which provide imagery since October 2014 and September 2016 (Bourbigot et al., 2016; Torres et al., 2012). Their imaging revisit time over the European landmasses, which is one of the high priority areas in Sentinel-1's acquisition strategy (Bauer-Marschallinger et al., 2019; Torres et al., 2012), is approximately 3 to 8 days with Sentinel-1A and improves to 1.5 to 3 days with both Sentinel-1A and -1B. Inconsistencies in the Sentinel-1 σ^0 time series were found before 25 November 2015 (Benninga et al., 2019, in Chapter 5; El Hajj et al., 2016), so the SMC retrieval scheme was started from 25 November 2015 and it was continued until 1 November 2018.

Sentinel-1 σ^0 and local incidence angle values for study fields were obtained from Level-1 Ground Range Detected (GRD) High Resolution (HR) Interferometric Wide Swath (IW) imagery. The images were downloaded from the Copernicus Open Access Hub (Copernicus, 2019). The operations (1) Apply Orbit File, (2) Thermal Noise Removal and (3) Range Doppler Terrain Correction, including radiometric normalization to σ^0 (in $m^2\,m^{-2}$) with projected local incidence angles, available in the European Space Agency (ESA)'s Sentinel Application Platform (SNAP) V6.0 (ESA, 2019), were used to pre-process the Sentinel-1 images.

The Level-1 GRD HR IW Sentinel-1 images have, after multi-looking, a resolution of $20\,m \times 22\,m$ (Bourbigot et al., 2016; Torres et al., 2012). The Range Doppler Terrain Correction included projection of the Sentinel-1 σ^0 and local incidence angles on a geographic grid (WGS84) with a pixel spacing of $9.0E{-}5^\circ$ (equivalent to $10\,m \times 6.1\,m$ at the study region's latitude). After the pre-processing operations the Sentinel-1 σ^0 and incidence angle values were averaged over study fields, excluding the area within 20 m from borders of fields and 40 m from trees and buildings to avoid possible influences from outside fields. The final steps were to mask the Sentinel-1 σ^0 observations of study fields for frozen conditions, wet snow and intercepted rain with the masking rules for weather-related surface conditions presented in Benninga et al. (2019, in Chapter 5) and to express the σ^0 intensity values in dB.

Sentinel-1 provides σ^0 observations in VV and VH polarization. The σ^0 observations in VV polarization have a higher expected sensitivity to SMC (e.g. Amazirh et al., 2018; El Hajj et al., 2017; Pulvirenti et al., 2018). Therefore, only the VV polarization σ^0 observations were used in the presented SMC retrieval scheme.

7.2.1.2 Sentinel-2 leaf area index

The Sentinel-2A and -2B satellites provide imagery in 13 spectral bands in the visible, near infrared and short wave infrared parts of the electromagnetic spectrum (Drusch et al., 2012). The resolution is 10 m, 20 m or 60 m, depending on the spectral band. The revisit period over the Netherlands

is 12 to 6 days from 1 July 2015 to 1 July 2017 (Sentinel-2A) and 5 to 2.5 days from 1 July 2017 onwards (Sentinel-2A and Sentinel-2B).

Using Sentinel-2 imagery, the Flemish Institute for Technological Research ('Vlaamse Instelling voor Technologisch Onderzoek' in Dutch, or VITO) generates 10 m grid maps of various vegetation indicators, namely the fraction of absorbed photosynthetically active radiation, fraction of green vegetation cover, LAI, normalized difference vegetation index (NDVI), chlorophyll canopy content and chlorophyll water content (Paepen and Wens, 2017; VITO, 2019). The maps are masked for the scene classifications cloud shadow, medium probability for clouds and high probability for clouds. For this study, V102 vegetation indicator maps as well as scene classification maps were downloaded from the VITO Product Distribution Portal (VITO, 2019). Recently, V200 replaced V102 and the distribution moved to Terrascope (Piccard et al., 2020).

Figure 7.2 illustrates that individual fields can be distinguished on the Sentinel-2 LAI maps. Differences between the LAI values of meadows exist due to different management practices: part of them is being grazed and others are cut at several moments in the year. On 15 September 2016 (the example map in Figure 7.2) part of the crop fields had already been harvested, whereas on others the crop was still there.

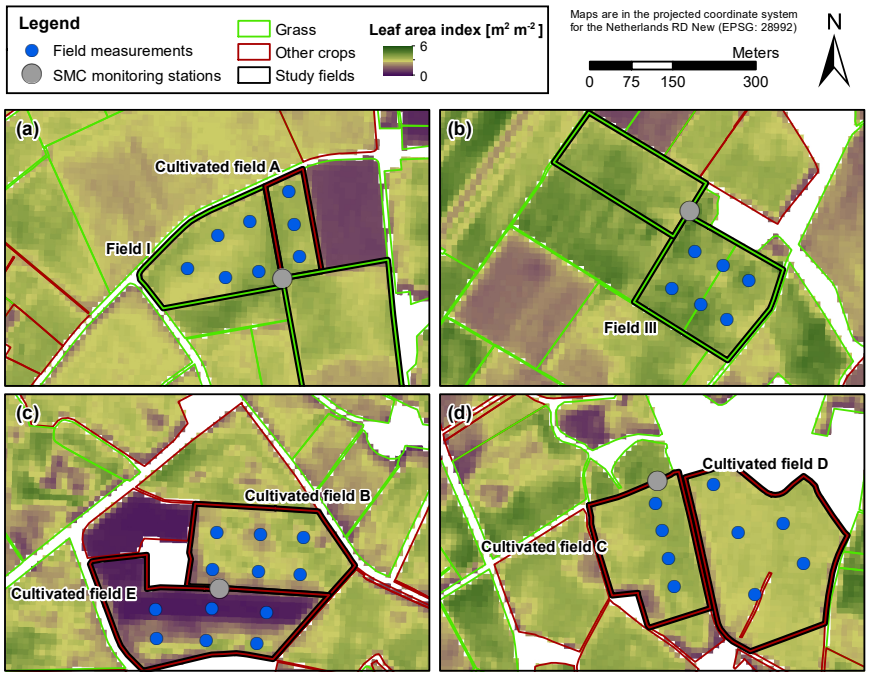

Figure 7.2 Sentinel-2 LAI maps on 15 September 2016 for the fields where we collected in situ LAI measurements. The outlines of the agricultural fields originate from the crop parcel registry 2016 (Ministry of Economic Affairs and Climate Policy, 2020).

The Sentinel-2 LAI images are not collected at the same time as Sentinel-1 images. Furthermore, only about 40 % of the LAI estimates is available after the masking for cloud shadow, medium probability and high probability for clouds. To provide LAI information at the time of Sentinel-1 images we, therefore, had to interpolate the Sentinel-2 LAI estimates. We assumed that we do not have local information available, such as when a study field was sowed or harvested, to enable region-wide application of the Sentinel-2 LAI information. Instead, we linearly interpolated two subsequent Sentinel-2 LAI estimates if the time gap between them is less than 15 days and the LAI does not decrease more than $2\,m^2\,m^{-2}$, thereby assuming that a larger decrease associates with the harvesting of a crop. For the winter period between 1 November and 1 March no variation in LAI is expected and we adopted the mean of Sentinel-2 LAI estimates over this period for a field. Furthermore, if no interpolated Sentinel-2 LAI estimate is available for a Sentinel-1 observation, a maximum time gap of 1.5 days is assumed to adopt a Sentinel-2 LAI estimate. The interpolated Sentinel-2 LAI estimates are validated against in situ LAI measurements in Section 7.5.1.

7.2.2 B: Forward backscattering model

7.2.2.1 Surface and vegetation models

The total σ^0 constitutes of three contributions as follows (in $m^2\,m^{-2}$):

$$\sigma^0 = \gamma^2\sigma_s^0 + \sigma_v^0 + \sigma_{sv}^0, \tag{7.1}$$

where γ^2 is the two-way transmissivity of the vegetation (= 1−two-way attenuation), σ_s^0 is the σ^0 from the soil surface, σ_v^0 is the direct vegetation σ^0 and σ_{sv}^0 is the σ^0 from soil-vegetation pathways. The IEM surface scattering model (Fung et al., 1992) simulates the scattering in all upward directions from the soil by representing it as a rough dielectric surface. The TV electromagnetic model, developed at the Tor Vergata University of Rome, represents the vegetation as a medium of discrete scatterers and simulates the γ^2, σ_v^0 and σ_{sv}^0 based on radiative transfer theory. Readers are referred to Bracaglia et al. (1995) and Dente et al. (2014) for more background on the TV-IEM model.

7.2.2.2 Parameterisation

We implemented the TV model for grass-covered surfaces using the vegetation parametrisation reported in Dente et al. (2014), excluding the litter layer, and the IEM surface roughness parameter values that were calibrated on sparsely vegetated meadows in Benninga et al. (2020b, in Chapter 6). The TV vegetation and IEM surface roughness parameter values are listed in Table 7.1. For the soil texture parameters, we used the average sand, silt and clay content, and soil bulk density of the study fields (i.e. regional averages).

The LAI determines the number of discs that represent the vegetation (Bracaglia et al., 1995). In Benninga et al. (2020b, in Chapter 6) it has been

Table 7.1 The surface and vegetation parameters used for simulating a grass-covered soil surface with the TV-IEM model.

Module	Parameter	Symbol	Value	Source
Surface	Root mean square surface height	s	0.16 cm	Benninga et al. (2020b, in Chapter 6)
Surface	Autocorrelation length	c_l	1.31 cm	Benninga et al. (2020b, in Chapter 6)
Surface	Soil texture: sand, silt and clay content, and soil bulk density	-	Averages for the study fields, see Section 7.4.1	
Vegetation	Leaves' disc radius	R_{leaf}	1.4 cm	Dente et al. (2014)
Vegetation	Leaves' disc thickness	D_{leaf}	0.02 cm	Dente et al. (2014)

assumed that the sparse grass cover on meadows in winter conditions does not affect the Sentinel-1 σ^0 observations. To enable adopting the surface roughness parameter values from Benninga et al. (2020b, in Chapter 6), we subtracted from the Sentinel-2 LAI estimates the LAI during winter before they were used as input to the SMC retrieval scheme.

Regarding the VWC vegetation variable, previous studies adopted time-invariant values of 0.8 kg kg^{-1} (Dente et al., 2014) and 0.59 kg kg^{-1} (Wang et al., 2018) for grass. These VWC values were obtained after optimizing TV simulations with regard to passive and active microwave observations over Tibetan alpine meadows. However, given the water-limited conditions that can occur in our study region, the VWC may vary over time as well. Therefore, besides searching for one optimum VWC value, we also investigated implementation of a time-varying VWC. The VWC is adapted each Sentinel-1 time step by optimizing the VWC value on the match between the SMC retrieval and reference of the previous time step. This is based on the assumptions that the residual between a SMC retrieval and reference is caused by an imperfect VWC value and that the VWC value of the previous time step can be used for the current time step. Two methods were tested, namely: (i) combining the Sentinel-1 observations in the ascending and descending orbits, and (ii) separating the ascending (afternoon) and descending (morning) orbits, i.e. using for a descending orbit Sentinel-1 observation the optimum VWC value of the previous descending observation.

7.2.3 C: Retrieval of soil moisture content from backscatter observations

The retrieval of SMC from a Sentinel-1 σ^0 observation involves finding the SMC value for which the minimum difference between σ^0 simulations and the Sentinel-1 σ^0 observation is achieved. This would require a large number of TV-IEM simulations over a broad range of incidence angle, LAI, VWC and SMC combinations, which is not feasible in operational settings because of the considerable run time of single TV-IEM simulations. Appendix A.7 details the estimation of TV-IEM's and IEM's run time. On an Intel Core(TM) i7-4790 CPU @ 3.60 GHz processor, the run time is 26.1 s per TV-IEM simulation.

As an alternative, we performed the TV-IEM simulations and stored the σ^0 contributions (σ_v^0, σ_s^0, σ_{sv}^0 and γ^2) in look-up tables. The TV-IEM simulations were first executed on the ranges and coarse simulation increments listed in Table 7.2. Second, similar to Kim et al. (2014), the TV-IEM simulations were linearly interpolated to the finer increments that are listed in Table 7.2. This two-step procedure increases the number of nodes from a limited number of simulations, i.e. from 11 880 simulations to 278 633 043 nodes. The validity of the linear interpolations is discussed in Section 7.3.

Table 7.2 Discretisation of the TV-IEM look-up tables. Regarding LAI, the simulation nodes are [0 $m^2\,m^{-2}$, 1 $m^2\,m^{-2}$, ..., 10 $m^2\,m^{-2}$] with an additional simulation for 0.1 $m^2\,m^{-2}$. Regarding SMC, the simulations nodes are [0.05 $m^3\,m^{-3}$, 0.1 $m^3\,m^{-3}$, ..., 0.75 $m^3\,m^{-3}$] with an additional simulation for 0.01 $m^3\,m^{-3}$.

Variable	Lower limit	Upper limit	Coarse simulation increment	Fine interpolation increment
Incidence angle [°]	29	47	2	0.25
LAI [$m^2\,m^{-2}$]	0, 0.1	10	1.0	0.1
VWC [$kg\,kg^{-1}$]	0.4	0.9	0.05	0.01
SMC [$m^3\,m^{-3}$]	0.01, 0.05	0.75	0.1	0.001

To limit the number of TV-IEM simulations, we only performed them for a study region's average soil texture and at discrete incidence angles. IEM's short run time (0.0556 ms per simulation, see Appendix A.7) allows to combine the TV-IEM σ_v^0, σ_{sv}^0 and γ^2 simulations, during the retrieval process, with IEM σ_s^0 simulations for the fine interpolation increments and field-specific soil textures and incidence angles.

7.3 TV-IEM model sensitivity to soil and vegetation variables

The σ_v^0, $\gamma^2\sigma_s^0$ and σ_{sv}^0 relative contributions to the total σ^0, as simulated with the TV-IEM model, are shown in Figure 7.3. The fine grid simulated contributions, as functions of LAI and VWC, show small random deviations from the coarse grid simulations. As a function of SMC, the coarse grid simulations align with the fine grid simulations — for the 35° case — because the coarse grid simulations were combined with IEM simulations at fine increments. However, in contrast with the LAI and VWC, interpolating the simulations for the coarse incidence angle increments to the fine interpolation increments has a systematic effect on the simulations, as can be seen from the systematic deviations in Figures 7.3b, d and f. Nevertheless, the linear interpolations of the coarse grid simulations approximately follow the lines of fine grid simulations and in this study we consider the linear interpolations as acceptable approximations for establishing the σ^0 contributions look-up tables.

Figures 7.3a–b show that the σ^0 originates completely from the soil surface for a LAI of 0 $m^2\,m^{-2}$, which is expected because the σ_v^0 and σ_{sv}^0

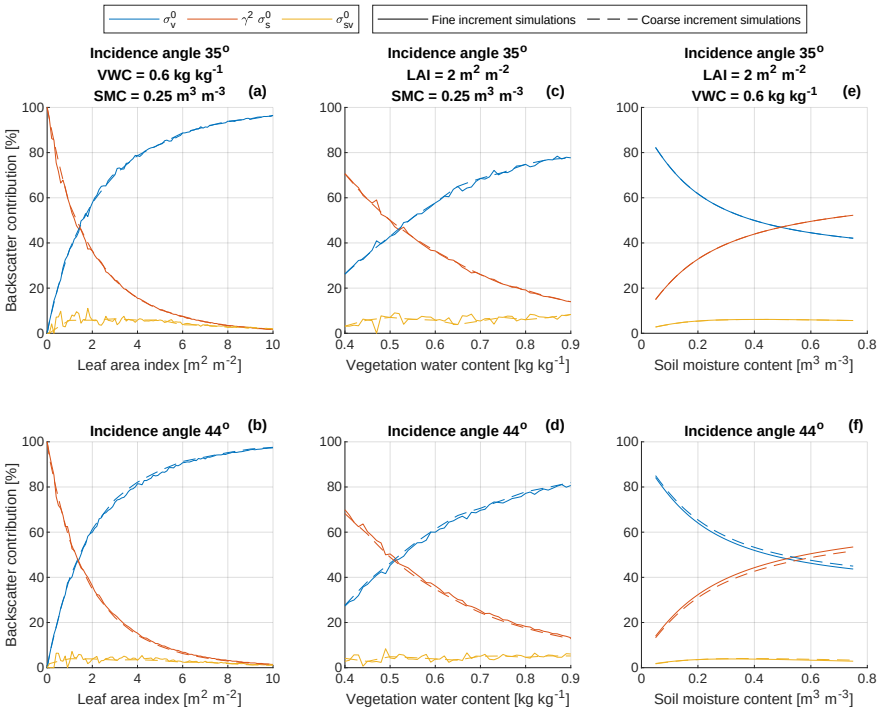

Figure 7.3 The σ_v^0, $\gamma^2\sigma_s^0$ and σ_{sv}^0 relative contributions for varied LAI, VWC and SMC conditions, and incidence angles of $35°$ and $44°$. The solid lines represent TV-IEM simulations with fine increments of $0.1\,\mathrm{m^2\,m^{-2}}$ **(a–b)**, $0.01\,\mathrm{kg\,kg^{-1}}$ **(c–d)** and $0.01\,\mathrm{m^3\,m^{-3}}$ **(e–f)**, and the dashed lines represent simulations with the coarse increments listed in Table 7.2.

will be $0\,\mathrm{m^2\,m^{-2}}$ and γ^2 will be 1 when no vegetation is present. However, the $\gamma^2\sigma_s^0$ contribution already reduces significantly with a limited grass cover. The σ_v^0 is larger than the $\gamma^2\sigma_s^0$ from a LAI of approximately $1.5\,\mathrm{m^2\,m^{-2}}$ and onwards (for a VWC of $0.6\,\mathrm{kg\,kg^{-1}}$). Figures 7.3c–d show that the $\gamma^2\sigma_s^0$ contribution also reduces with increasing VWC. Hence, both an increasing LAI and VWC cause a diminishing σ^0 to SMC sensitivity. Figures 7.3e–f show that the relative $\gamma^2\sigma_s^0$ contribution is larger for higher SMC. This is because σ_s^0 increases with increasing SMC. The σ^0 to SMC sensitivity diminishes with increasing SMC (Altese et al., 1996; Benninga et al., 2019, in Chapter 5), as is illustrated in Figure 7.4. Figure 7.4 also reflects the reduced σ^0 to SMC sensitivity under a vegetation cover: the higher the LAI and VWC are, the more the σ^0 to SMC sensitivity reduces because the σ_s^0 is increasingly more attenuated and the σ_v^0 relative contribution to the total σ^0 increases. The $\gamma^2\sigma_s^0$ relative contribution is slightly smaller for the $44°$ incidence angle than for the $35°$ incidence angle. This is explained by the longer path through the vegetation for larger incidence angles. For example, for a LAI of $2\,\mathrm{m^2\,m^{-2}}$ and a VWC of $0.6\,\mathrm{kg\,kg^{-1}}$ the γ^2 values are 0.49 and 0.48 for incidence angles of $35°$

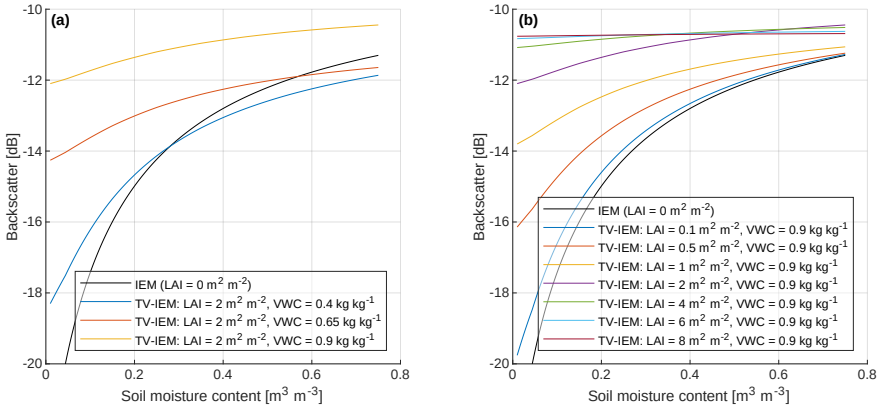

Figure 7.4 The sensitivity of σ^0 to SMC. The simulations in this figure are for a 35° incidence angle.

and 44°, respectively, and for a LAI of $4\,m^2\,m^{-2}$ they are 0.23 and 0.22.

The σ^0_{sv} relative contribution is small for all grass cover and SMC conditions. The mean σ^0_{sv} values are 5.5% of the total σ^0 for the 35° incidence angle (Figures 7.3a, c and e) and 3.6% for the 44° incidence angle (Figures 7.3b, d and f). In contrast to the $\gamma^2\sigma^0_s$, the σ^0_{sv} relative contribution is fairly independent of the LAI and VWC, and under dense grass conditions its contribution is similar to that of the $\gamma^2\sigma^0_s$. Whereas in the frequently-used water cloud model (WCM), which was introduced by Attema and Ulaby (1978) and used in e.g. El Hajj et al. (2017), Paloscia et al. (2013) and Pulvirenti et al. (2018) for SMC mapping from Sentinel-1 imagery, multiple scattering interactions between the soil surface and the vegetation are neglected, these results suggest that σ^0_{sv} should be included because of its significant contribution to the total σ^0 for grass-covered soil surfaces. Furthermore, σ^0_{sv} may still contribute to σ^0 to SMC sensitivity under dense vegetation conditions (Chiu and Sarabandi, 2000; Joseph et al., 2010; Stiles et al., 2000).

7.4 Validation references and method

7.4.1 Study region and period

The study region is located in the eastern part of the Netherlands (Figure 7.5a). For an extensive description of the study region's landscape, soils and climate, we refer to Van der Velde and Benninga (in preparation, in Chapter 2). From mid-November to mid-March (winter period) the SMC is generally at a high level and from mid-May to mid-October (summer period) at a low level mainly due to a higher evaporative demand (Benninga et al., 2019, in Chapter 5; Van der Velde et al., 2021). Moreover, the general SMC cycle contains dynamics on shorter time-scales in response to meteorological events. In the study period of 25 November 2015 to 1 November 2018, the 2018 summer was exceptionally dry due to high

evaporative demands and low rainfall (Bakke et al., 2020; Buitink et al., 2020; Buras et al., 2020). The grass growing season is approximately from 1 March to 1 November (Pellikaan, 2017; Veeneman et al., 2017). Outside the growing season, grass covers are virtually static and sparse. Within the growing season meadows are being grazed or cut at several moments, which is why the LAI can be very different between adjacent meadows (see Figure 7.2).

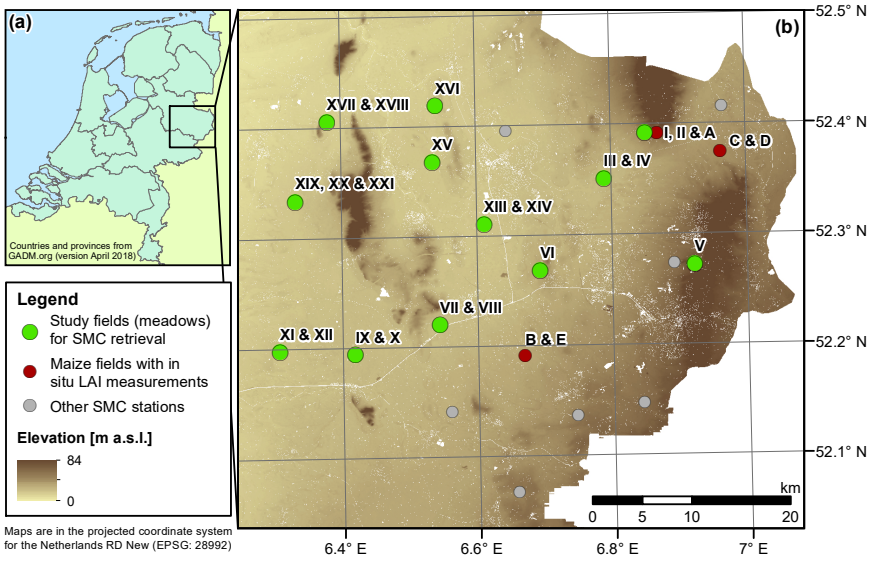

Figure 7.5 **(a)** Location of the study region in the Netherlands. **(b)** The locations of the study fields, adjacent to stations of the SMC monitoring network Twente. Background is the digital terrain model AHN2 (Actueel Hoogtebestand Nederland, 2012b).

The imaging revisit time of the Sentinel-1 satellites over a region is controlled by a region's latitude and Sentinel-1's acquisition strategy (Bauer-Marschallinger et al., 2019; Torres et al., 2012). Sentinel-1 images are collected relatively intensively over our study region because this region is covered by two ascending and two descending orbits. The characteristics of these orbits are listed in Table 7.3. Sentinel-1's imaging revisit time over the study region with these four orbits combined and both Sentinel-1A and -1B is 1.5 days. The Sentinel-2 LAI maps were available for specific time periods and specific parts of Europe (Paepen and Wens, 2017; VITO, 2019): for the northern part of our study region throughout the study period, but for the southern part the period from 1 January 2017 to 1 July 2018 was not available and for the most eastern part only half of the Sentinel-2 images were processed. This gives temporal resolutions of 4 days for the western and middle part and 8 days for the eastern part of the study region.

Table 7.3 Specifications of the Sentinel-1 orbits that cover the study region. The number of Sentinel-1 images is for the study period from 25 November 2015 to 1 November 2018 and before masking the σ^0 observations for weather-related surface conditions.

Relative orbit number	Pass	Acquisition time (CET)	Number of Sentinel-1 images	Projected local incidence angle over the study fields
15	Ascending	18:16	145	32.3°–36.3°
37	Descending	6:49	148	34.0°–37.8°
88	Ascending	18:24	143	40.8°–44.4°
139	Descending	6:41	146	42.2°–45.6°

7.4.1.1 In situ soil moisture content

The study region is equipped with a network of twenty SMC monitoring stations, known as the Twente network (Dente et al., 2012; Dente et al., 2011; Van der Velde and Benninga, in preparation, in Chapter 2; Van der Velde and Benninga, 2020) and shown in Figure 7.5b. The retrieval scheme was applied to estimate SMC for the meadows adjacent to monitoring stations. Table A.3 lists the study fields and their surface areas. Multiple meadows can be adjacent to a single SMC station, as can also be seen in Figure 7.2.

Table A.3 also lists the soil characteristics of the study fields. Sandy to loamy sandy soils dominate the surface layer in the study region, with some remnants of loamy soils and organic soils (Van der Velde and Benninga, in preparation, in Chapter 2; Wösten et al., 2013). This study was limited to the meadows with sandy to loamy sandy surface layers. We generated TV look-up tables for the study fields' average soil texture of 80 % sand, 15 % silt and 5 % clay, with a bulk density of 1.33 g cm^{-3}, derived from BOFEK2012 (Wösten et al., 2013). As explained in Section 7.2.3, IEM was run for the field-specific soil textures.

The monitoring stations measure SMC with 5TM probes (METER Group, 2019) at nominal depths of 5 cm, 10 cm, 20 cm, 40 cm and 80 cm and store the readings every 15 min. The 5TM probes have an influence zone of approximately up to 4 cm above and below the sensor's middle prong (Benninga et al., 2018c, in Chapter 3). We used the 5 cm depth SMC measurements, being representative for a soil depth of 1 cm to 9 cm, that are collected at Sentinel-1 overpass times as the in situ references.

7.4.1.2 In situ leaf area index

The interpolated Sentinel-2 LAI estimates were validated against in situ references. During the growing seasons of 2016 and 2017, we measured the LAI on two meadows (fields I and III) on a two-weekly basis. In order to increase the number of available LAI references and evaluate the general performance of the Sentinel-2 LAI estimates, we also validated them with in situ LAI measurements that were collected on four maize fields (fields A–D). In situ LAI measurements were also collected on a

fifth maize field (field E), but no concurrent Sentinel-2 LAI estimates are available here.

Figure 7.5b shows the locations of fields I, III and A–E, and Figure 7.2 shows the locations of the LAI measurements within these fields. The LAI measurements were collected at three to six locations, about 50 m to 100 m apart, within a field. The optical instrument LI-COR LAI-2000 (LI-COR, 1992) was used for the measurements. This instrument estimates the LAI based on the ratio between light intensity readings above and below the canopy. We operated the instrument with a sensor opening of 90° to remove the operator and the sun from the sensor's view (LI-COR, 1992). On the meadows we acquired one above-canopy reading and four below-canopy readings about 0.5 m apart to reduce the measurement uncertainty. On the maize fields we acquired, at each measurement location, four below-canopy readings with the sensor opening along the rows and four below-canopy readings with the sensor opening facing a maize row, each set accompanied with an above-canopy reading. Of the four measurements below a maize canopy, the first was in/adjacent to the maize row, the second was at 1/4 between rows, the third was halfway, and the fourth was at 3/4 between rows, following the LAI-2000 manual (LI-COR, 1992). The LAI-2000 File Viewer (FV2000) application (LI-COR, 2004), using the default horizontal uniform canopy model, converted the light intensity readings to LAI.

The Sentinel-2 LAI estimates and the in situ references are shown in Figure 7.6. Following the conditions for the interpolation of Sentinel-2 LAI estimates as defined in Section 7.2.1.2, during harvesting periods the Sentinel-2 LAI estimates are indeed not interpolated. As a result, however, no validation pair is established for the in situ LAI references that were acquired just before or after a harvesting period. These in situ LAI references typically represent the most extreme LAI conditions. As the LAI will not vary much in the week before and the week after harvesting, we relaxed the maximum time gap of 1.5 days to maximum one week for these LAI references and included them as pairs with the Sentinel-2 LAI estimate just before or after.

7.4.2 CDF matching

Cumulative distribution function (CDF) matching suppresses systematic biases in the mean, variability and dynamic range of estimates — the Sentinel-2 LAI and Sentinel-1 SMC — with their respective references (Boé et al., 2007; Brocca et al., 2011; Drusch et al., 2005; Kornelsen and Coulibaly, 2015; Reichle and Koster, 2004). CDF matching was implemented by fitting a polynomial (correction function) to ranked estimates against the residuals between the ranked estimates and ranked references (Brocca et al., 2011; Drusch et al., 2005; Kornelsen and Coulibaly, 2015). The correction function is generated on estimate-reference pairs. We obtained the model coefficients of the correction function with the 'Trust-Region' algorithm in Matlab's Curve Fitting toolbox, by fitting, similar to Brocca et al. (2011), a fifth-order polynomial.

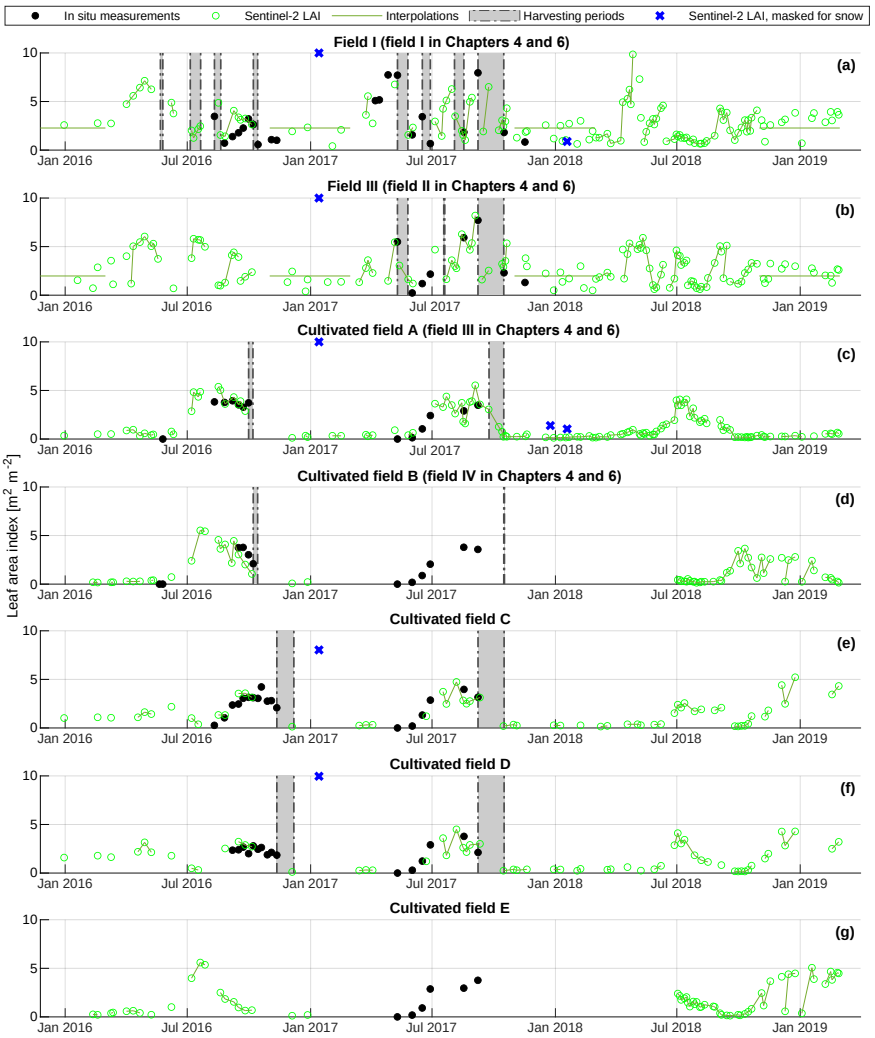

Figure 7.6 Sentinel-2 LAI estimates and in situ LAI references. The figure titles specify within the brackets the name for the same field as that is used in Chapters 4 and 6.

After generation of the correction function, the estimates were subjected to the correction function so that the estimates' CDF should match the references' CDF. The Kolmogorov-Smirnov test with a significance level of 5 % (Kornelsen and Coulibaly, 2015; Massey, 1951) was used to verify whether the correction function successfully aligned the CDFs. If this is confirmed, the correction function was also applied to the estimates for which no concurrent reference is available and beyond the range for which it was developed. Following Boé et al. (2007), the correction factor of the correction function's boundary was applied to estimates that exceed the ranges on which the correction function was established.

7.4.3 Performance metrics

The Sentinel-2 LAI estimates and Sentinel-1 SMC retrievals were evaluated against their in situ references with the Pearson correlation coefficient (r_P) and the root mean square deviation ($RMSD$), which are defined in Appendix A.2. The $RMSD$ is the standard deviation of the differences between estimates and references (Kerr et al., 2016), and can, as such, be considered as a measure for uncertainty.

The r_P and the relative $RMSD$ ($RRMSD$) were used for comparison of the SMC retrieval performance among fields and against the performance of other SMC products. The $RRMSD$ is defined as follows:

$$RRMSD = \frac{RMSD}{\max(Y_r) - \min(Y_r)}, \tag{7.2}$$

where Y_r stands for the references, and $\max(Y_r)$ and $\min(Y_r)$ for the maximum and minimum Y_r. The $RRMSD$ evaluates the retrieval uncertainty relative to the range of the SMC references. In contrast to the $RMSD$, of which the value depends on the range of SMC values that occur, the $RRMSD$ may be compared among fields, conditions or studies with different SMC ranges. We calculated the $RRMSD$ of other studies using the reported unbiased $RMSD$ values and SMC ranges or, if available, the original SMC retrievals and references.

7.5 Results and discussion

7.5.1 Sentinel-2 leaf area index

7.5.1.1 Validation

The time series of the Sentinel-2 LAI estimates and the in situ LAI references in Figure 7.6 show the same dynamics. The Sentinel-2 LAI product, thus, provides information of vegetation conditions at field scale. Table 7.4 lists the performance metrics between the linearly interpolated Sentinel-2 LAI estimates and the in situ references. However, the Sentinel-2 LAI estimates that were acquired when snow was present seem disturbed. Therefore, in addition to the default masking for cloud shadow, medium probability for clouds and high probability for clouds, we also masked the Sentinel-2 LAI maps when the scene classification of snow applies to a pixel. For the maize fields no in situ references are available in winter, but for the meadows the performance metrics (see Table 7.4) indeed slightly improve.

Figure 7.7 shows the CDFs of the Sentinel-2 LAI estimates before and after CDF matching against the in situ references. The aligning of the Sentinel-2 LAI's CDFs with the in situ LAI's CDFs was confirmed with the Kolmogorov-Smirnov test with a significance level of 5 % (Kornelsen and Coulibaly, 2015; Massey, 1951). The match between the final Sentinel-2 LAI estimates and the in situ references is presented in Figure 7.8. The r_P and $RMSD$ improve by the CDF matching, as is listed in Table 7.4.

Table 7.4 Performance metrics of three Sentinel-2 LAI products against the in situ references collected on the meadows and maize fields.

Study fields	LAI product	Number of pairs	r_P [−]	$RMSD$ [$m^2\,m^{-2}$]
Meadows	Original	21	0.93	1.15
	Masked for snow	21	0.93	1.11
	Masked for snow & CDF-matched	20	0.94	0.71
Maize	Original	23	0.63	0.83
	Masked for snow	23	0.63	0.83
	Masked for snow & CDF-matched	23	0.65	0.79

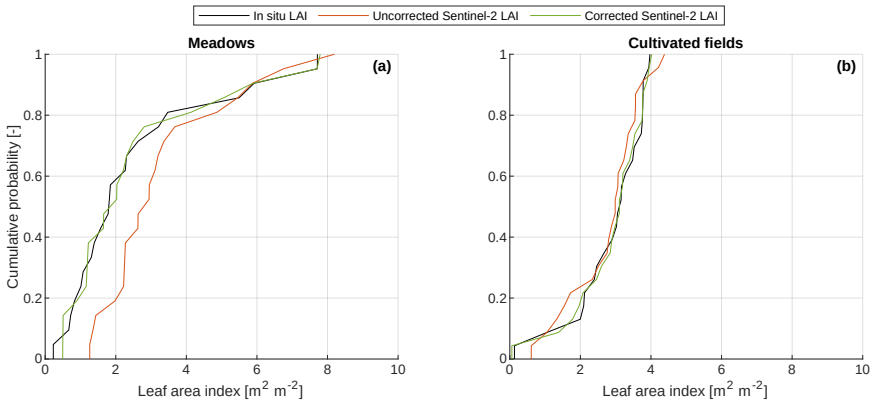

Figure 7.7 CDFs for the in situ LAI references and the Sentinel-2 LAI estimates before ('uncorrected') and after ('corrected') CDF matching.

The uncertainty of the linearly interpolated Sentinel-2 LAI estimates for the meadows is estimated at $0.71\,m^2\,m^{-2}$.

7.5.1.2 Propagation of Sentinel-2 leaf area index uncertainty

The uncertainty of the Sentinel-2 LAI estimates propagates through the TV-IEM SMC retrieval scheme and affects SMC retrievals. We investigated this effect by retrieving the SMC from a σ^0 value for a given LAI value as well as for this LAI value perturbed upwards and downwards with the Sentinel-2 LAI uncertainty of $0.71\,m^2\,m^{-2}$. This propagation principle can be deduced from Figure 7.4b and is illustrated in more detail in Appendix A.9.

Figure 7.9 shows the effect of the Sentinel-2 LAI uncertainty on the SMC retrievals. The σ^0 to SMC relation is more sensitive to the LAI in the lower LAI range, e.g. a LAI of $2\,m^2\,m^{-2}$, as is visible in Figure 7.4b. This causes in many cases even invalid SMC retrievals above or below the retrieval limit. In the upper range of LAI values the σ^0 to SMC sensitivity diminishes, causing that a same deviation in σ^0 results in a larger deviation in SMC.

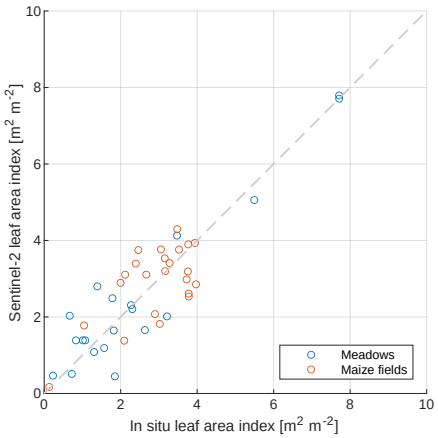

Figure 7.8 The Sentinel-2 LAI estimates, after masking for snow and CDF matching, against the in situ LAI references collected on the meadows and maize fields.

7.5.2 Calibration of the vegetation water content

Figure 7.10 shows the performance of SMC retrievals for a range of time-invariant VWC values and the time-varying methods, as explained in Section 7.2.2.2. Both the r_P and $RMSD$ are hardly affected by the used VWC. This suggests that other uncertainties, such as the Sentinel-1 radiometric uncertainty (Benninga et al., 2019, in Chapter 5; Pathe et al., 2009; Schmidt et al., 2018; Schwerdt et al., 2017), surface roughness parameter uncertainty (Benninga et al., 2020b, in Chapter 6), SMC reference uncertainties (Benninga et al., 2020b, in Chapter 6; Cosh et al., 2005; Cosh et al., 2006; Western et al., 2002) and Sentinel-2 LAI uncertainty (Section 7.5.1.2), dominate the retrieval uncertainty. Moreover, temporal variation in the vegetation status is included via the LAI time series: when the VWC is low, the LAI will also tend to be lower. This is illustrated in Figure 7.6a–b for example for the very dry 2018 summer and this reduces the sensitivity of the model performance to VWC.

The highest r_P and lowest $RMSD$ are obtained for a VWC of $0.90\,\mathrm{kg\,kg^{-1}}$. This value also outperforms the two time-varying VWC methods. In addition, the time-varying VWC methods have the disadvantage of requiring a SMC reference for the previous Sentinel-1 time step, which will generally not be available in operational applications. Therefore, the VWC value of $0.90\,\mathrm{kg\,kg^{-1}}$ was selected as input to the SMC retrieval scheme.

7.5.3 Soil moisture content retrievals

Figure 7.11 shows time series and CDFs of SMC retrievals and references for field XVIII, XIV and II, respectively the fields with the best, worst and a medium $RRMSD$ performance. The CDF matching is successful in aligning the SMC retrievals' CDFs to the references' CDFs. All fields pass

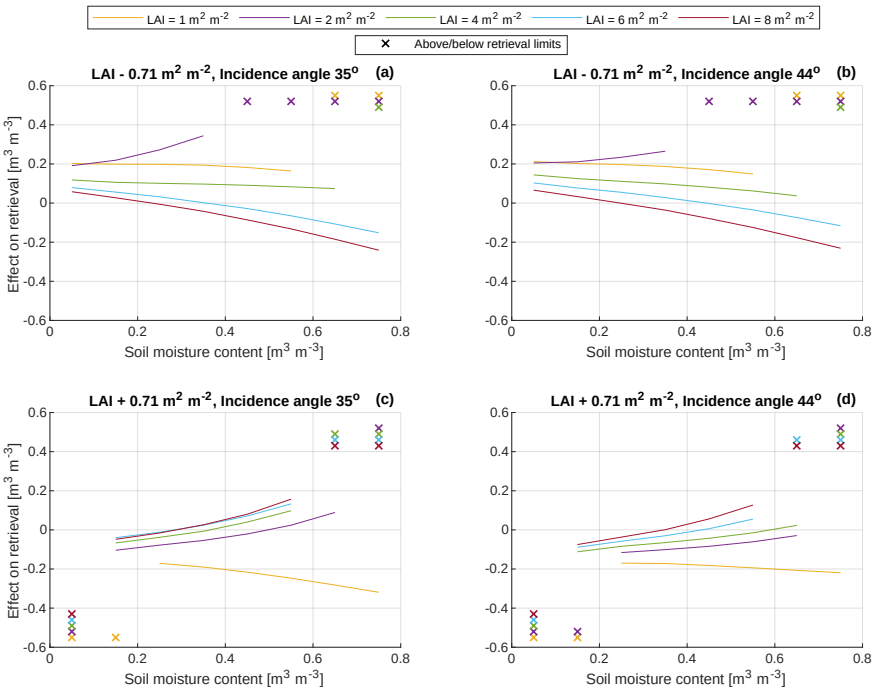

Figure 7.9 The propagation of the Sentinel-2 LAI uncertainty ($0.71\,\mathrm{m^2\,m^{-2}}$) into TV-IEM SMC retrievals. The SMC retrievals limits are $0.01\,\mathrm{m^3\,m^{-3}}$ and $0.75\,\mathrm{m^3\,m^{-3}}$. Exceedances of these limits after perturbation of the LAI are shown as crosses. These figures are for a VWC of $0.90\,\mathrm{kg\,kg^{-1}}$, which followed from its calibration (Section 7.5.2).

the Kolmogorov-Smirnov test with a significance level of 5 % (Kornelsen and Coulibaly, 2015; Massey, 1951). The time series in the left panels demonstrate that the retrievals match the SMC references pretty well, although the retrievals also exhibit a significant spread, i.e. uncertainty, and there are periods with systematic deviations from the references.

As a result of the successful CDF matching, over the complete period no systematic differences between the IEM and TV-IEM SMC retrievals are present. Nevertheless, their retrievals are different due to the different pairs that were used in the CDF matching and due to the vegetation correction. The vegetation correction (without considering the CDF matching) causes that the majority of the vegetation-corrected TV-IEM retrievals is lower than the IEM retrievals. For most combinations of LAI, VWC and SMC, the vegetation contributes more to the σ_v^0 and σ_{sv}^0 than that it attenuates the σ_s^0. This is shown in Figure 7.4b by the higher SMC-σ^0 lines with vegetation present.

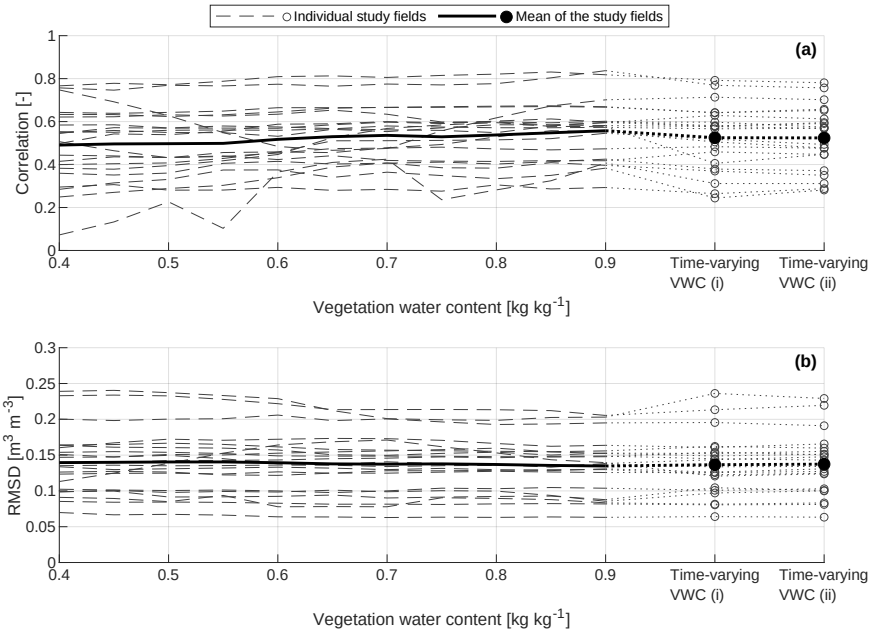

Figure 7.10 Performance metrics between SMC retrievals and references for a range of time-invariant VWC values and the time-varying VWC methods (i) and (ii).

7.5.3.1 The performance of IEM and TV-IEM retrievals

Figure 7.12 shows the performance metrics of the SMC retrievals. More SMC retrievals are possible if no vegetation correction is applied because not for every Sentinel-1 σ^0 observation a Sentinel-2 LAI estimate is available and because TV-IEM results in more invalid SMC retrievals above or below the retrieval limit. Averaged over the study fields, there are 164.0 and 322.9 SMC retrievals possible for the total period and 102.5 and 261.4 for the growing seasons with TV-IEM and IEM respectively. The performance metrics of the IEM retrievals for the same retrieval-reference pairs as TV-IEM are also shown in Figure 7.12.

The performance metrics of the SMC retrievals with TV-IEM are slightly better than the performance metrics of 'IEM all retrievals', especially regarding r_P. Comparison with the performance metrics of IEM shows, however, that this is effect is caused by the different retrieval-references pairs. The invalid TV-IEM retrievals occur mainly under denser vegetation conditions because the range of σ^0 values for which a SMC retrieval is possible becomes limited, as can be seen in Figure 7.4b. When a Sentinel-1 σ^0 observation is outside this range, the SMC retrieval will be invalid. Under denser vegetation cover, i.e. increasing LAI, the σ^0 to SMC sensitivity reduces (see Section 7.3). IEM does not account for the effect of vegetation, as a result of which the Sentinel-1 σ^0 observations that led to the invalid SMC retrievals by TV-IEM yield less accurate SMC

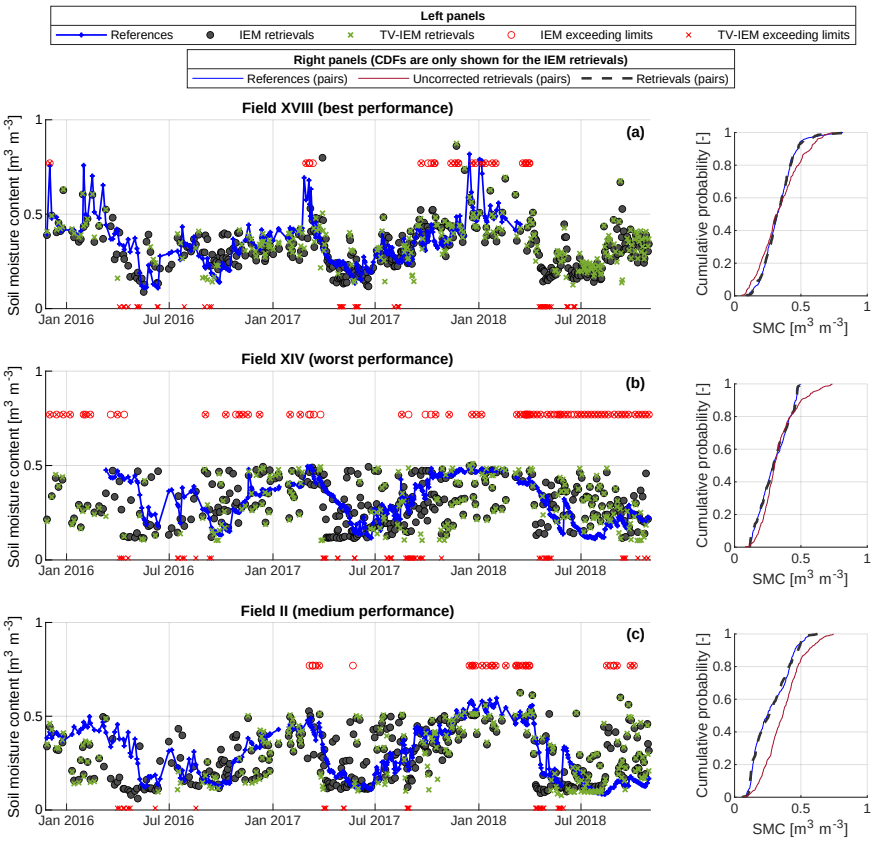

Figure 7.11 SMC retrievals and references for field XVIII (best retrieval performance), field XIV (worst performance) and field II (medium performance). The CDFs (right panels) are only shown for the IEM retrievals.

retrievals by IEM and negatively impact the performance metrics.

Although it could be expected that correcting σ^0 observations for vegetation effects contributes to better SMC retrieval performances, the similar performance metrics for TV-IEM and IEM may be explained by two factors. Firstly, Section 7.5.1.2 demonstrates the substantial effect of the Sentinel-2 LAI uncertainty on SMC retrievals. It is likely that the correction required for grass is dominated by the uncertainty that is introduced by the Sentinel-2 LAI estimates. Secondly, the effect of grass on the Sentinel-1 σ^0 may be not as large as simulated with the TV model, which would cause incorrect corrections for the vegetation effects. This is supported by the results in Benninga et al. (2020b, in Chapter 6), in which it was found that the uncertainty of SMC retrievals can be explained even when the vegetation effects are not considered. The LAIs for the meadows in that study were $1.1\,\mathrm{m^2\,m^{-2}}$ and $1.3\,\mathrm{m^2\,m^{-2}}$, and their results suggest that the vegetation effects could be neglected under these sparse vegetation conditions. Similar results were found by

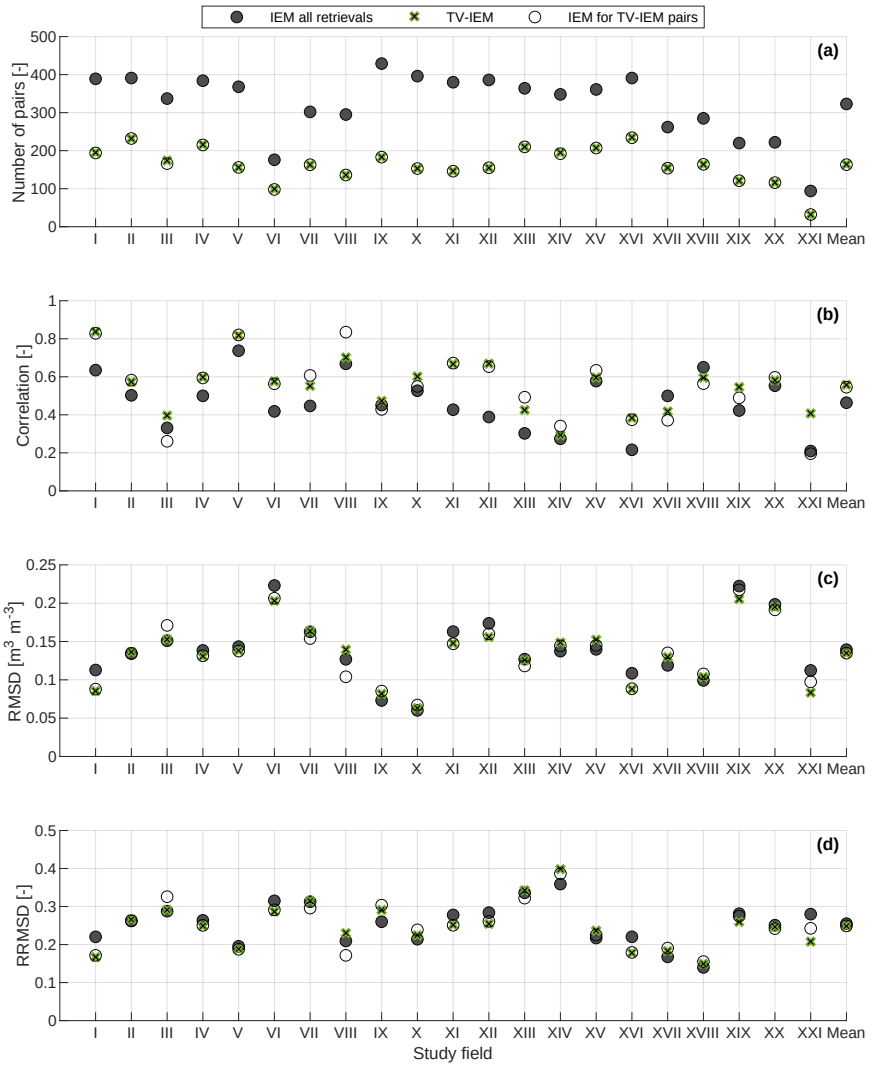

Figure 7.12 Performance metrics of the IEM and TV-IEM SMC retrievals against the SMC references. 'IEM for TV-IEM pairs' contains the same retrieval-reference pairs as 'TV-IEM' (i.e. a Sentinel-2 LAI estimate is available and TV-IEM resulted in a valid SMC retrieval), whereas 'IEM all retrievals' contains all the retrieval-reference pairs possible (i.e. from all the Sentinel-1 σ^0 observations).

Van der Velde et al. (2012b) and Van der Velde and Su (2009). In contrast, the vegetation effects as simulated by the TV model are significant at LAI values of $1.1\,\mathrm{m^2\,m^{-2}}$ and $1.3\,\mathrm{m^2\,m^{-2}}$, with, for a 35° incidence angle, γ^2 values of 0.50 and 0.45 and σ_v values of $-14.0\,\mathrm{dB}$ and $-13.6\,\mathrm{dB}$ respectively.

7.5.3.2 Exceedance of retrieval limits

One result we want to highlight is obtained for field XXI (Figure 7.13): hardly any Sentinel-1 σ^0 observation resulted in a valid SMC retrieval between 25 November 2015 and 26 March 2017. The crop parcel registry (Ministry of Economic Affairs and Climate Policy, 2020) lists that this field was used to grow maize in 2015 and 2016, and only since 2017 it has been in use as meadow. Figure 7.13 shows that this has a large effect on the SMC retrievals and results in many invalid retrievals, i.e. the Sentinel-1 σ^0 observation does not correspond to a SMC between 0.01 $m^3\,m^{-3}$ and 0.75 $m^3\,m^{-3}$ according to the modelled σ^0 to SMC relation. This can be explained by the surface roughness that is different for maize fields than for meadows (Benninga et al., 2020b, in Chapter 6). In all performance results, therefore, only the period after 26 March 2017 was evaluated for field XXI.

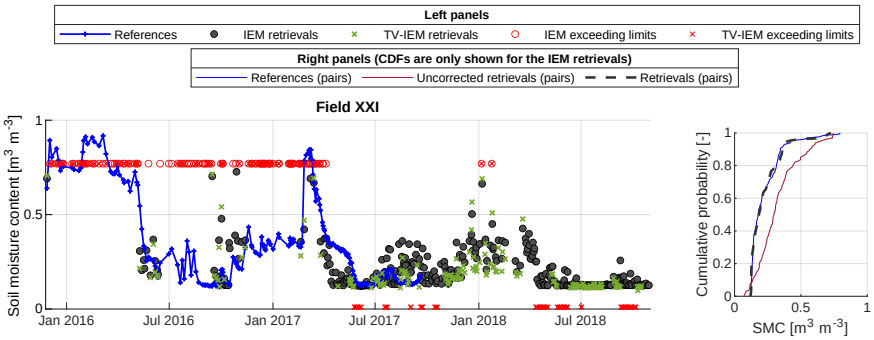

Figure 7.13 SMC retrievals and references for field XXI. Only since 2017 this field has been in use as meadow, resulting in many invalid retrievals in the period before due to a different surface roughness.

SMC retrievals for the other fields exceed the upper retrieval limit of 0.75 $m^3\,m^{-3}$ mainly in wet periods, and this may, as such, provide information about the SMC. To test this, we set the retrievals that exceed 0.75 $m^3\,m^{-3}$ to the maximum SMC. For example, for field II these retrievals (red data points in Figure 7.11c) were set to 0.63 $m^3\,m^{-3}$. This was applied to all the SMC retrievals exceeding the upper limit (variant 1) and only to those retrievals in the period from 15 November to 15 March (variant 2), which is the expected wet period in the study region. As shown in Figures A.21–A.22 and summarized in Table 7.5, both variants improve the r_P in particular. Variant 2 results in the best SMC retrieval performance for both IEM and TV-IEM. Setting retrievals that exceed the lower limit of 0.01 $m^3\,m^{-3}$ to the minimum SMC was also tested, but this does not improve the IEM and TV-IEM retrieval performances.

7.5.3.3 Masking for dense vegetation

The SMC retrievals will be less accurate under denser vegetation conditions. El Hajj et al. (2017) acknowledged this limitation of C-band SAR

Table 7.5 Performance metric means of the study fields for two variants of incorporating information from SMC retrievals that exceed the upper retrieval limit of $0.75\,m^3\,m^{-3}$. Variant 1 sets all the IEM retrievals that exceed $0.75\,m^3\,m^{-3}$ and variant 2 sets only the IEM retrievals that exceed $0.75\,m^3\,m^{-3}$ in the expected wet period (15 November to 15 March) to the maximum SMC. The performance metrics per study field are shown in Figures A.21–A.22.

SMC product	Variant	Number of pairs	r_P [−]	$RMSD$ [$m^3\,m^{-3}$]	$RRMSD$ [−]
IEM all retrievals	Original	322.9	0.46	0.14	0.25
	1	352.2	0.54	0.15	0.25
	2	339.5	0.55	0.14	0.24
TV-IEM	Original	164.0	0.56	0.13	0.25
	1	185.3	0.61	0.14	0.25
	2	178.1	0.64	0.13	0.24
IEM for TV-IEM pairs	Original	163.2	0.55	0.13	0.25
	1	185.3	0.59	0.14	0.25
	2	177.4	0.62	0.13	0.24

σ^0 observations by masking the σ^0 observations acquired under vegetation conditions with a NDVI higher than 0.75. Applying the relation reported in Knyazikhin et al. (1999) and Tesemma et al. (2014), a NDVI of 0.75 converts into a LAI of $5.63\,m^2\,m^{-2}$. This might even be a too high LAI threshold, as the σ^0 to SMC sensitivity, according to the TV model (Figure 7.4), is already significantly reduced at a LAI of $2\,m^2\,m^{-2}$.

The performance of the IEM SMC retrievals was analysed for a range of LAI thresholds used to mask the SMC retrievals. For example, for a LAI threshold of $4\,m^2\,m^{-2}$ we masked all SMC retrievals from Sentinel-1 σ^0 observations that were acquired when the Sentinel-2 LAI estimate was higher than $4\,m^2\,m^{-2}$. Figure 7.14 shows that the performance metrics improve with the LAI threshold. However, the number of pairs also reduces with application of a (lower) LAI threshold. Applying a certain LAI threshold for masking SMC retrievals is a trade-off between accuracy and number of retrievals.

7.5.4 Retrieval performance compared with other studies

The SMC retrieval performances are compared with the performance of two other Sentinel-1 based products at field scale, one Sentinel-1 and a priori SMC information based product at field scale, three Sentinel-1 based products at 1 km resolution, and the SMAP 9 km and 36 km products. The characteristics and performance metrics of these products are listed in Table 7.6.

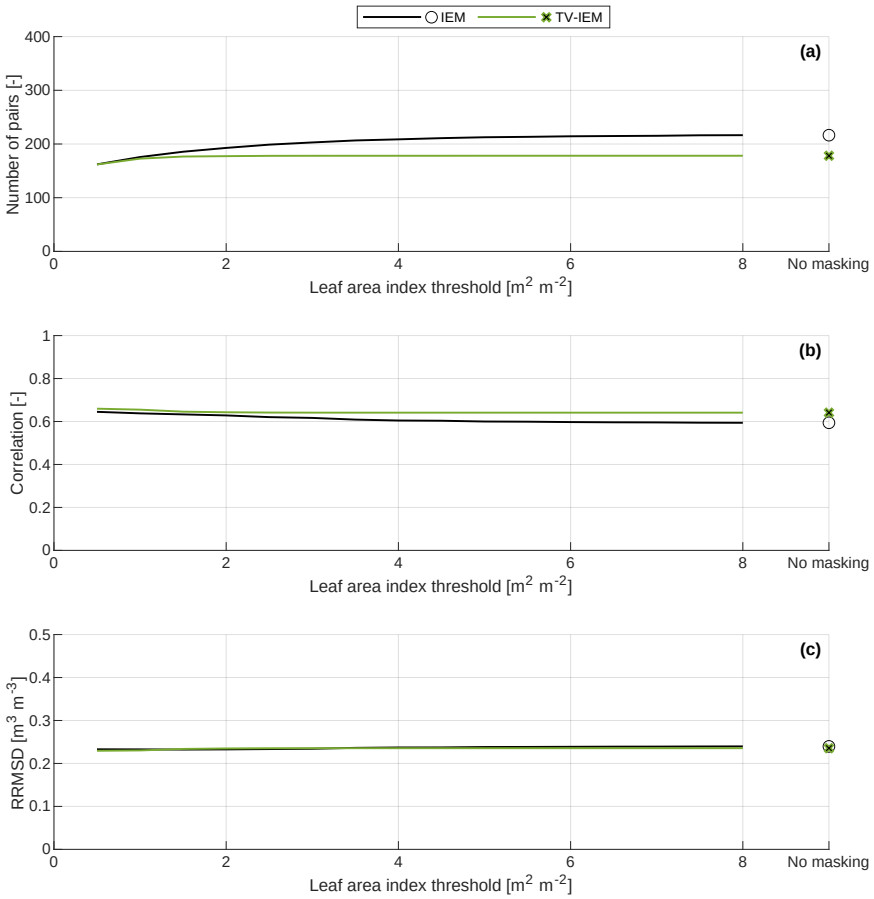

Figure 7.14 Performance metric means of the study fields, after first applying variant 2 from Section 7.5.3.2, for a range of LAI thresholds used to mask the SMC retrievals. Only the SMC retrievals for which a Sentinel-2 LAI estimate was available are included.

Table 7.6 The performance of other SMC products from satellite imagery.

Study	Product	r_P [−]	$RRMSD$ [−]	Evaluation
El Hajj et al. (2017)	Sentinel-1 VV, IEM combined with the WCM for incorporating vegetation effects. Field-scale product.	not reported	0.25	The averages of 25 to 30 measurements within a study field were used as references. The reported $RMSD$ values were unbiased, using Equation 3 in Entekhabi et al. (2010b), with the also reported mean bias.
	The first product and a priori information on SMC (wet/dry).	not reported	0.18	

Carranza et al. (2019)	Sentinel-1 VV, change detection method for a field-scale product. We subjected the retrievals to CDF matching.	0.44	0.25	Evaluated against the measurements from single stations.
Bazzi et al. (2019)	First product of El Hajj et al. (2017), at 1 km resolution.	0.77	0.14	The references from El Hajj et al. (2017) were used, averaged for the fields within 1 km by 1 km grid cells.
	The 1 km resolution Copernicus Surface Soil Moisture product, developed by Bauer-Marschallinger et al. (2019).	0.48	0.22	
Balenzano et al. (2021)	Sentinel-1, short term change detection approach for a 1 km resolution product.	0.71	0.18	The 1 km resolution product was evaluated at 1.6 km × 1.6 km by averaging the SMC retrievals and references from 11 stations that cover this area.
Pezij et al. (2020)	SMAP 9 km product (SCA-V morning overpasses). We subjected the retrievals to CDF matching.	0.77	0.16	The SMAP product (Chan et al., 2018) was extracted for the study region. Evaluated against the measurements from single stations (i.e. at field scale): stations 2, 3, 4, 5, 11, 13, 14, 15, 16, 17, 18 and 19.
Van der Velde et al. (2021)	SMAP 36 km product (SCA-V). We subjected the retrievals to CDF matching.	0.78	0.15	The SMAP product (Chan et al., 2016) was extracted for the study region, specifically SMAP reference pixel 3606. Evaluated against the measurements from single stations (i.e. field scale) in SMAP reference pixel 3606: stations 2, 3, 5, 11, 15, 16, 17.

7.5.4.1 Comparison with Sentinel-1 based products

The performance metrics of the two Sentinel-1 based products at field-scale — the first product in El Hajj et al. (2017) and the product in Carranza et al. (2019) — are similar to the performance we obtained. Note that the SMC retrievals in El Hajj et al. (2017) are compared to references based on 25 to 30 measurements within a study field. Benninga et al. (2020b, in Chapter 6) found that the references' sensor uncertainty and spatial mismatch uncertainty constitute, respectively, 13 % and 46 % of the retrieval uncertainty at a SMC of 0.26 $m^3\,m^{-3}$ to 4 % and 15 % at a

SMC of 0.53 $m^3\,m^{-3}$. These uncertainty contributions are reduced by averaging spatially distributed measurements (Balenzano et al., 2021; Singh et al., 2020; Vinnikov et al., 1999), as in El Hajj et al. (2017). As such, the actual *RRMSD*, which excludes the references' uncertainties, of the SMC products in this study are expected to be lower than that of the product in El Hajj et al. (2017). The second product in El Hajj et al. (2017) has a better SMC retrieval performance than the algorithm presented in this chapter, which is explained by the use of the a priori information on the SMC condition. The products in Bazzi et al. (2019) and in Balenzano et al. (2021) also show better performance metrics. This can be explained by the lower references' uncertainties and the lower radiometric uncertainty (Benninga et al., 2019, in Chapter 5) at the 1 km or 1.6 km scale than at the field scale of 0.16 ha to 6.3 ha that is studied here.

7.5.4.2 Comparison with SMAP products

The SMAP 36 km and 9 km products perform better at field scale than the Sentinel-1-based SMC products in this study and the other studies listed in Table 7.6. The SMAP imagery, which is in L-band, are less obstructed by vegetation and more sensitive to SMC as well as have a sampling depth closer to the references at 5 cm depth than the C-band Sentinel-1 observations (El Hajj et al., 2019; Entekhabi et al., 2010a). Furthermore, Gruber et al. (2020) points out that coarse scale products often better match local SMC dynamics than downscaled (finer) products. The result here does, however, not necessarily apply to other regions. The study region is rather flat and homogeneous regarding soil characteristics and meteorological conditions, so large regional differences in SMC dynamics are not expected. Moreover, information at field scale is still required in specific situations, such as after irrigation practices or in the presence of local drainage systems.

One period in which the Sentinel-1 SMC retrievals significantly deviate from the references is the end of the 2018 summer, which is shown in more detail with the examples in Figures 7.15 and 7.16. Whereas the SMC references remain low, the retrievals show an increased SMC level especially from mid-August. The same is visible in the SMAP retrievals (Chan et al., 2018, 2016; Van der Velde et al., 2021). At the end of July and in August 2018 a number of rainfall events occurred, but the 2018 summer was exceptionally dry in the months before and these rainfall events are not or only minorly reflected in the SMC references. The SMC references originate from measurements at 5 cm depth and due to the extreme dryness of the soil and high evaporative demand (Van der Velde et al., 2021), we expect that (most of) the rainfall did not fully infiltrate the sensor's influence zone of 1 cm–9 cm soil depth. Field V is located in a slightly wetter area than field II and the level of the SMC references increased from the end of August. Still, in this period the SMC retrievals show more dynamics in response to the rainfall than the references. The SMC estimates from satellites and from in situ sensors

provide information for different soil layers and, in an optimum setting, complement each other.

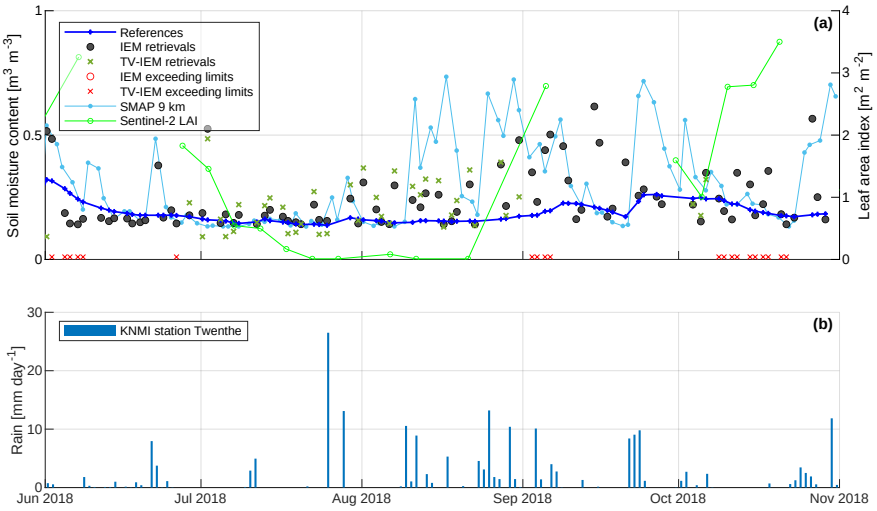

Figure 7.15 SMC retrievals and references for field V during the 2018 summer. Field V has the best $RRMSD$ retrieval performance after fields XVIII and XVII, for which no references are available in this period. The SMAP $9\,\mathrm{km}$ retrievals for the pixel in which field V is located are shown. Both the Sentinel-1 and SMAP SMC retrievals were CDF-matched against the references over the complete time period (25 November 2015 to 1 November 2018). The rainfall data originate from the weather station Twenthe, which is operated by the Royal Netherlands Meteorological Institute ('Koninklijk Nederlands Meteorologisch Instituut' in Dutch, or KNMI; KNMI, 2019).

Rainfall does not explain all of the increased SMC retrievals, as can be seen in July, beginning of August, mid-September and mid-October in Figures 7.15 and 7.16. Also the SMAP retrievals remain low in these periods, which indicates an issue in the Sentinel-1 SMC retrievals. The increased SMC retrievals originate from Sentinel-1 σ^0 observations acquired in orbits 88 & 139 (see Appendix A.11). The σ^0 observations acquired in orbits 88 & 139 have an incidence angle of 40.8°–45.6°, whereas the σ^0 observations from orbits 15 & 37 have an incidence angle of 32.3°–37.8° (Table 7.3). For larger incidence angles, the microwaves have a longer path through the vegetation to and from the soil surface and, consequently, experience more effect of vegetation and a lower sensitivity to SMC (e.g. Crow et al., 2010; Palmisano et al., 2018; Ulaby et al., 1979). This is also seen in the TV simulations, discussed in Section 7.3. The higher σ^0 to SMC sensitivity for lower incidence angles is reflected in better SMC retrieval performance metrics for orbits 15 & 37 than for orbits 88 & 139, shown in Figure A.31 and summarized in Table 7.7.

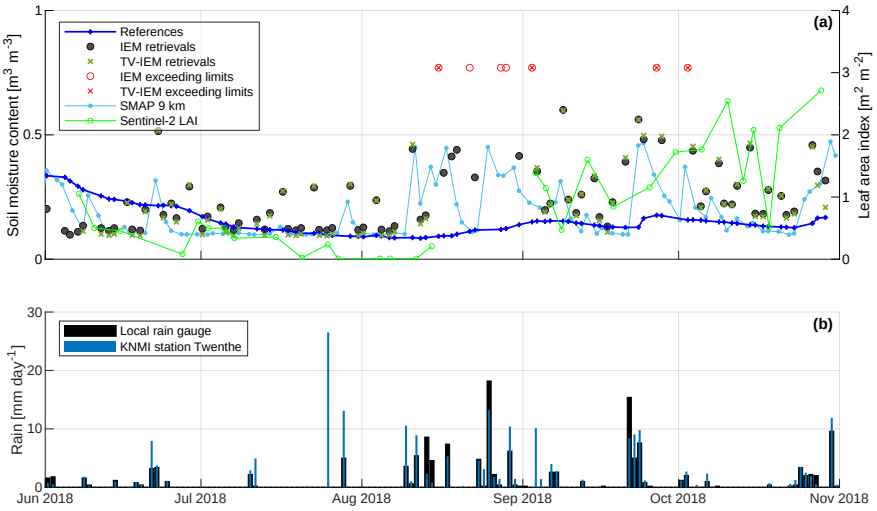

Figure 7.16 Same as Figure 7.15, but for field II. The rainfall data originate from the weather station Twenthe (KNMI, 2019) and from a local rain gauge adjacent to field II.

Table 7.7 Performance metrics means of the study fields, for the SMC retrievals from Sentinel-1 σ^0 observations acquired in orbits 15 & 37 and in orbits 88 & 139. The performance metrics per study field are shown in Figure A.31.

SMC product	Orbits	Number of pairs	r_P [−]	$RMSD$ [m^3 m^{-3}]	$RRMSD$ [−]
IEM all retrievals	All	322.9	0.46	0.14	0.25
	15 & 37	162.4	0.52	0.13	0.24
	88 & 139	160.4	0.41	0.15	0.29
TV-IEM	All	164.0	0.56	0.13	0.25
	15 & 37	82.0	0.63	0.12	0.23
	88 & 139	82.0	0.47	0.14	0.29

7.6 Conclusions

An operationally applicable scheme is presented for field-scale SMC retrieval over meadows from SAR σ^0 observations, and this scheme is evaluated without (IEM) and with vegetation correction (TV-IEM). The TV vegetation scattering and absorption model and the IEM surface scattering model were parameterised for grass-covered soil surfaces. To facilitate fast inversion of σ^0 observations to SMC, look-up tables of the TV-IEM-modelled direct vegetation σ^0 (σ^0_v), σ^0 from soil-vegetation pathways (σ^0_{sv}), soil surface σ^0 (σ^0_s) and the vegetation two-way transmissivity (γ^2) were generated on fine grids. The axes of these look-up tables are incidence angle, LAI, VWC and SMC. We used the look-up tables to invert field-averaged Sentinel-1 σ^0 observations into SMC for meadows. Field-scale LAI information was derived from a Sentinel-2 vegetation product.

The Sentinel-2 LAI estimates were validated against in situ measurements collected on two meadows and four maize fields. The r_Ps are

0.94 and 0.65 and the *RMSD*s are 0.71 $m^2\,m^{-2}$ and 0.79 $m^2\,m^{-2}$ for the meadows and the maize fields, respectively, after masking the Sentinel-2 LAI estimates for snow and CDF-matching them against the in situ references. The results demonstrate that the Sentinel-2 LAI product provides field-scale information. However, despite the rather good performance, the Sentinel-2 LAI uncertainty of 0.71 $m^2\,m^{-2}$ results in the lower LAI range in many invalid SMC retrievals because the modelled σ^0 to SMC relation is very sensitive to LAI and in the upper LAI range it propagates into large SMC retrieval deviations because the σ^0 to SMC sensitivity diminishes.

The SMC retrieval scheme was demonstrated by retrieving the SMC for 21 meadows and validating the results against references from adjacent in situ monitoring stations. By setting the SMC retrievals that exceed the upper retrieval limit of 0.75 $m^3\,m^{-3}$ during the wet period to the maximum SMC, the performance metrics improve to mean r_Ps of 0.55 for IEM and 0.64 for TV-IEM, *RMSD*s of 0.14 $m^3\,m^{-3}$ for IEM and 0.13 $m^3\,m^{-3}$ for TV-IEM, and *RMSD*s relative to the range of the SMC references (*RRMSD*) of 0.24 for both IEM and TV-IEM. Masking the SMC retrievals for dense vegetation also improves the performance metrics, but this is a trade-off with the number of retrievals. Because not for every Sentinel-1 σ^0 observation a Sentinel-2 LAI estimate is available and TV-IEM results in more invalid SMC retrievals under dense vegetation conditions, more SMC retrievals are possible without the vegetation correction. By considering the same retrieval-reference pairs as for TV-IEM, the performance metrics of the SMC retrievals that are obtained with IEM are practically equal to the performance metrics of the SMC retrievals with TV-IEM.

The IEM and TV-IEM retrieval performances are also similar to the performance of two other Sentinel-1 based products at field scale, of which one was obtained with a data-driven (change detection) method and one with a semi-empirical vegetation model (WCM) combined with IEM. The SMAP 36 km and 9 km products perform better at the field scale, with mean *RRMSD*s of 0.15 and 0.16 respectively, but they may be unsuitable if larger regional differences are present and in field-specific situations such as after irrigation practices or with local drainage systems.

The two scheme implementations (without and with the vegetation correction) and the SMC products to which their performance was compared are based on imagery from different satellites or on different algorithms. As a consequence, the individual retrievals of these products are different. However, the performance metrics indicate that all these SMC products provide information about SMC at field scale. It would, therefore, be interesting to (1) research the representation of field-scale SMC as an ensemble of SMC products, and (2) validate more products at field scale, such as the 500 m product from Sentinel-1 imagery retrieved with a multi-temporal algorithm (Pulvirenti et al., 2018), the 1 km Copernicus Surface Soil Moisture product with a change detection algorithm (Bauer-Marschallinger et al., 2019), the 1 km product from Sentinel-1 imagery with the short term change detection algorithm (Balenzano et al., 2021), the 1 km and 3 km products from a combination of SMAP and

Sentinel-1 imagery (Das et al., 2019), and several more, and potentially include them in an ensemble of SMC products. Analysing multiple SMC products in conjunction may provide further insights into these products, and ensembles of SMC retrievals could reveal the uncertainties and show the probability of SMC conditions.

Synthesis

8

With soil moisture content (SMC) information at field scale, new applications in water and agricultural management may be anticipated. Furthermore, at field scale more direct relations between the ground conditions (SMC, surface roughness and vegetation) and the backscatter (σ^0) observations are expected. This supports studying σ^0-SMC relations. This thesis aimed at developing a method for retrieving SMC at field scale from Sentinel-1 σ^0 observations and obtaining a better understanding of the uncertainties involved in such retrievals. Based on the research presented in Chapters 2–7, this chapter summarizes the answers to the research questions, formulates the general conclusions and recommends directions for future research.

8.1 Summary of the main findings

Research question 1: What is the uncertainty of in situ SMC measurements as reference for field-scale SMC retrievals?
Two regional SMC monitoring networks were employed, namely the Twente network in the east (Chapter 2) and the Raam network in the south (Chapter 3) of the Netherlands. Both regions mainly hold sandy to loamy sandy soils. Soil-specific calibration functions were established for the SMC sensors. The associated measurement uncertainty of the station probes (U_{sp}) is $0.018\,m^3\,m^{-3}$ to $0.023\,m^3\,m^{-3}$ for the Raam network and $0.028\,m^3\,m^{-3}$ for the Twente network. The sensor's influence zone, determined in Raam soil, is 3 cm–4 cm.

The networks' stations have sensors installed at depths of 5 cm, 10 cm, 20 cm, 40 cm and 80 cm. The SMC sensors at 5 cm depth measure the 1 cm–9 cm soil layer, whereas Sentinel-1's C-band observations are expected to be sensitive to SMC from the surface to a depth of 1 cm–10 cm. This difference in sampling depth introduces a vertical mismatch. Furthermore, the field-scale SMC retrievals are to be compared against the measurements from a single SMC monitoring station, which introduces a horizontal mismatch due to a spatial scale mismatch, differences in land cover, soil texture and structure, and local features such as nearby ditches and subsurface drainage pipes. These vertical and horizontal mismatches cause a spatial mismatch uncertainty in the

SMC station measurements as references for field-scale SMC estimates from satellite observations ($U_{s,S1}$). In Chapter 4, the $U_{s,S1}$ is estimated by comparing station measurements against measurements inside four agricultural fields with a handheld device. The $U_{s,S1}$ estimates for the four fields are between $0.036\,m^3\,m^{-3}$ and $0.068\,m^3\,m^{-3}$. The average value of $0.051\,m^3\,m^{-3}$ is adopted as common measure for the $U_{s,S1}$.

Research question 2: What is the impact of Sentinel-1 σ^0 uncertainty and weather-related surface conditions on SMC retrievals?
Chapter 5 focuses on the Sentinel-1 σ^0 observations. It presents masking rules for weather-related surface conditions, estimates Sentinel-1's radiometric uncertainty (s_{S1}) and investigates the impact of both on SMC retrievals. The masking rules were developed by analysing meteorological measurements against seasonal anomalies of Sentinel-1 σ^0 observations over five forests, five meadows and five cultivated fields. The Sentinel-1 (VV) σ^0 observations are affected by frozen conditions below an air temperature of 1 °C, on average by −1.80 dB, snow during Sentinel-1's morning overpasses on meadows and cultivated fields, on average by −1.40 dB, and interception after more than 1.8 mm of rain in the 12 h preceding a Sentinel-1 overpass, on average by +0.89 dB. Dew was not found to be of influence. Following these results, a set of masking rules was formulated for frozen conditions, snow and intercepted rain, and applied to all the Sentinel-1 σ^0 observations in this thesis.

The s_{S1} consists of calibration uncertainties, sensor instabilities and speckle effects. It was estimated from the seasonal anomalies timeseries of the Sentinel-1 forest σ^0 observations. The obtained s_{S1} values are 0.85 dB (VV polarization) and 0.89 dB (VH polarization) for a surface area of 0.25 ha. The s_{S1} values improve, by spatially averaging the σ^0 observations, to 0.30 dB (VV polarization) and 0.36 dB (VH polarization) for a surface area of 10 ha. In accordance with the theory about the standard deviation of sample means, the s_{S1} is approximately inversely proportional to the square root of the surface area over which the Sentinel-1 σ^0 observations are averaged.

The impacts on SMC retrievals, if not masking for the weather-related surface conditions and of the s_{S1}, were estimated via the σ^0 to SMC sensitivity modelled with the integral equation method (IEM) surface scattering model. This was done for three surface roughness scenarios, representing cultivated fields, meadows and a very smooth surface, the incidence angles at which Sentinel-1 observes the Twente region, specifically 35° and 44°, and SMC values from $0.05\,m^3\,m^{-3}$ to $0.50\,m^3\,m^{-3}$. The impact on SMC retrievals is shown to be weakly dependent on the surface roughness and the incidence angle, and strongly dependent on the SMC and the surface area (or the σ^0 disturbance caused by a weather-related surface condition for a specific land cover type). Averaged over the meadows and cultivated fields, intercepted rain causes a significant overestimation of SMC ranging from $+0.047\,m^3\,m^{-3}$ for dry soils up to $+0.26\,m^3\,m^{-3}$ for wet soils. Snow and frozen conditions lead to a significant decrease in SMC retrievals, respectively from $-0.035\,m^3\,m^{-3}$

and $-0.045\,m^3\,m^{-3}$ for dry soils up to $-0.13\,m^3\,m^{-3}$ and $-0.16\,m^3\,m^{-3}$ for wet soils. As a result of s_{S1} (U_{S1}), the SMC retrievals have a low uncertainty ($-0.01\,m^3\,m^{-3}$ to $+0.01\,m^3\,m^{-3}$) for dry soils and large surface areas and a high uncertainty ($-0.10\,m^3\,m^{-3}$ to $+0.17\,m^3\,m^{-3}$) for wet soils and small surface areas. Because the effects of vegetation are not accounted for in the simulations of the σ^0 to SMC sensitivity, the reported impacts and uncertainties represent the lower limits.

Research question 3: What are the relative uncertainty contributions to SMC retrievals under sparsely vegetated conditions?
In Chapter 6, SMC retrieval was implemented for two sparsely vegetated meadows and two fallow maize fields. In this way, the surface roughness parameters in the IEM surface scattering model could be investigated. A Bayesian framework was used to calibrate the surface roughness parameters, and to derive the model parameter (U_p) and total uncertainty. The resulting total SMC retrieval uncertainty successfully reproduces the uncertainty estimated empirically from the SMC retrievals against station references. This includes the trend of increasing SMC retrieval uncertainty with increasing SMC, which is explained by the diminishing σ^0 to SMC sensitivity with increasing SMC.

The combination of the derived U_p with the estimates of the U_{sp} from Chapter 2, the $U_{s,S1}$ from Chapter 4 and the U_{S1} from Chapter 5 also constitute total SMC retrieval uncertainty, which allows to decompose the total uncertainty in its four constituents. The main uncertainty originates from the in situ references (U_{sp} and $U_{s,S1}$) and the Sentinel-1 σ^0 observations (U_{S1}), whereas the contribution from the surface roughness parameters (U_p) is small. Their relative contributions depend on the SMC conditions. As the U_{sp} and $U_{s,S1}$ are assumed independent of SMC and the total uncertainty increases with SMC, their relative contributions decrease, respectively, from 13 % and 46 % at a SMC of $0.26\,m^3\,m^{-3}$ to 4 % and 15 % at a SMC of $0.53\,m^3\,m^{-3}$. The relative contribution of the U_{S1} increases with increasing SMC, namely from 31 % at a SMC of $0.26\,m^3\,m^{-3}$ to 67 % at a SMC of $0.53\,m^3\,m^{-3}$. The relative contribution of U_p is relatively constant and on average 13 % over the SMC domain.

The surface roughness parameter distributions, for the two fallow fields, are different and depend on the pass direction from which Sentinel-1 σ^0 observations were acquired. These fields have an anisotropic surface due to tillage rows and these are viewed with different angles from the ascending/descending orbits of Sentinel-1. Furthermore, the surface roughness conditions change between periods. This is in contrast with the surface roughness parameter distributions for the two meadows, which are time-invariant, independent of Sentinel-1's ascending/descending orbits and similar for the two meadows that were studied. These are promising results for the operational retrieval of SMC over meadows across a larger region because they suggest that using a single set of surface roughness parameters is allowed.

Research question 4: Can Sentinel-1 SMC retrievals be improved by accounting for vegetation in an operationally applicable scheme for SMC retrieval over meadows?
SMC retrieval over meadows is implemented as an operationally applicable scheme in Chapter 7. For this purpose, the IEM surface scattering model and the Tor Vergata (TV) vegetation scattering and absorption model were parameterised for grass-covered soil surfaces. The scheme is evaluated without (IEM) and with (TV-IEM) the vegetation correction applied to Sentinel-1 σ^0 observations.

Field-scale vegetation conditions, being input to the vegetation correction, were derived from a Sentinel-2 product. Validation of the Sentinel-2 leaf area index (LAI) estimates against in situ measurements on two meadows and four maize fields demonstrates that the Sentinel-2 LAI product provides field-scale information. However, uncertainty propagation also shows that the Sentinel-2 LAI uncertainty of $0.71\,\mathrm{m^2\,m^{-2}}$ has a large impact on SMC retrievals. In the lower LAI range it results in invalid SMC retrievals because the modelled σ^0 to SMC relation is very sensitive to LAI, and in the upper LAI range it propagates into large SMC retrieval deviations because the σ^0 to SMC sensitivity diminishes.

The validation of SMC retrievals for 21 meadows in the Twente region demonstrates that the performances of the IEM and TV-IEM retrievals are similar, i.e. without and with the vegetation correction. The final performance metrics have mean Pearson correlation coefficients of 0.55 for IEM and 0.64 for TV-IEM, root mean square deviations (*RMSD*) of $0.14\,\mathrm{m^3\,m^{-3}}$ for IEM and $0.13\,\mathrm{m^3\,m^{-3}}$ for TV-IEM, and *RMSD*s relative to the range of the SMC references (*RRMSD*) of 24 % for both IEM and TV-IEM, but the performance metrics are practically equal if the same retrieval-reference pairs are considered. Masking for dense vegetation conditions improves the performance metrics to the detriment of the number of retrievals, and this is a trade-off that deserves further investigation. Not only are the SMC retrieval performances similar with and without the vegetation correction, they are also similar to the performance of two other Sentinel-1 based products at field-scale. The Sentinel-1 based products are outperformed by the Soil Moisture Active Passive (SMAP) 9 km and 36 km products evaluated at field scale, with mean *RRMSD*s of 15 % and 16 %. However, the coarse SMAP products are expected to deviate if larger SMC differences within regions are present and in field-specific situations such as after irrigation practices or with local drainage systems.

8.2 General conclusions

Uncertainty information is essential to assess the reliability and for the applicability of SMC retrievals. Frozen conditions, snow and intercepted rain impact Sentinel-1 σ^0 observations. Rules were formulated for masking these weather-related surface conditions, so — if done perfectly — no impact would be expected. The in situ references' measurement

uncertainty and spatial mismatch uncertainty, Sentinel-1's radiometric uncertainty, and the retrieval algorithm and parameters are uncertainty contributions to SMC retrievals.

Synthetic aperture radar (SAR) σ^0 observations, such as acquired by the Sentinel-1 satellites, are often mentioned as a source for SMC information at field-scale. The SMC retrieval accuracies that were obtained for the sparsely vegetated fields seem low. However, the combination of the uncertainty sources demonstrates that this low accuracy can be explained and originates for a large part from the in situ references against which the SMC retrievals are validated and the Sentinel-1 σ^0 observations.

Vegetation effects on σ^0 and accounting for them adds to the SMC retrieval uncertainty over vegetated fields. The uncertainty contribution of vegetation model parameters has not yet been investigated, but uncertainty in the Sentinel-2 LAI estimates for representing field-scale vegetation conditions has a large impact on SMC retrievals. Both with and without correction for vegetation effects on Sentinel-1 σ^0, the presented SMC retrieval scheme results in accuracies of 24% relative to the SMC range. Insight in the uncertainty contributions helps to comprehend such SMC retrieval accuracies.

8.3 Recommendations

The topics that were studied in this thesis will be increasingly relevant, given the expected Earth's population growth as well as increase in floods and droughts due to climate change. Based on the thesis' methods and findings, directions for future research are suggested below.

Recommendation 1: Focus on the uncertainty sources with the largest contributions to effectively improve the SMC retrievals.
Information on the relative contributions of uncertainty sources can direct towards efforts that potentially are (most) effective in improving the accuracy of SMC retrievals (Karthikeyan et al., 2017a). Chapter 6 shows that the in situ references' measurement uncertainty (U_{sp}), the in situ references' spatial mismatch uncertainty ($U_{s,S1}$) and the SMC retrieval uncertainty due to Sentinel-1's radiometric uncertainty (U_{S1}) constitute large contributions to the total uncertainty.

References are required for the calibration of model parameters and the validation of the SMC retrievals. Although not directly, in this way the references' uncertainties (U_{sp} and $U_{s,S1}$) contribute to the total SMC retrieval uncertainty. This thesis had to rely on single sensors for providing field-scale references. Both the U_{sp} and $U_{s,S1}$ can be reduced by averaging spatially distributed measurements. Therefore, set-up of long-term field-scale SMC monitoring networks consisting of multiple stations is recommended. A minimum number of three stations is suggested, in order to reduce the spatial mismatch uncertainty to 0.041 $m^3\,m^{-3}$ for a 70% confidence interval as in Colliander et al. (2017). Besides, Gruber

et al. (2020) points out that coarse scale products often better match local SMC dynamics than downscaled (finer) products. A similar finding was obtained in Chapter 7 regarding the performances of the field-scale SMC retrieval and the SMAP 9 km and 36 km products. It should be evaluated whether finer scale SMC retrievals indeed represent real SMC variations. Hence the recommendation is to set-up multiple field-scale networks of at least three stations within the single grid cells of coarser (e.g. 1 km) products.

The s_{S1} is an inherent contribution to the SMC retrieval uncertainty (U_{S1}). Nevertheless, its contribution can be reduced and the SMC retrievals be improved. One way is by improvement of SAR image processing, which may include better SAR observation systems, temporal filtering and speckle filtering. Another way is by adopting a coarser spatial resolution.

Recommendation 2: Investigate the dependency of the uncertainty sources on field conditions.
The uncertainty sources were estimated for study fields in the Twente region. Characteristic for this region is the temperate oceanic climate, flat landscape, sandy to loamy sandy soils, small agricultural fields and specific agricultural practices regarding, e.g., crop types and tillage. These factors influence the total SMC retrieval uncertainty and the relative uncertainty contributions, meaning that the conclusions and recommendation 1 cannot directly be extrapolated to other climatic and landscape contexts. The methods presented in this thesis and the SMC measurement networks that are available globally (Dorigo et al., 2021; Colliander et al., 2017) may be used to broaden the conclusions on the contributions of the uncertainty sources.

A specific note to the $U_{s,S1}$ is that it was estimated for four agricultural fields and one common estimate was adopted. These estimates were assumed independent of SMC conditions. As already discussed in Chapter 4, however, several studies demonstrated that SMC spatial variability depends on the SMC conditions. Therefore, it may be expected that the $U_{s,S1}$ actually depends on the SMC conditions. Besides, the results by Famiglietti et al. (2008) suggest that the SMC spatial variability increases with spatial extent. The dependency of $U_{s,S1}$ on SMC conditions, field surface area and possibly more field conditions (e.g. vegetation, soil characteristics and agricultural management), could be further investigated by using the field measurements from the 2009 and 2015 measurement campaigns in Twente (Chapter 2) and from several other field campaigns (Gruber et al., 2020) in addition to the field measurements that were collected in the context of this thesis.

Recommendation 3: Assess the general applicability of the presented SMC retrieval scheme.
The SMC retrieval scheme that is presented is, potentially, operationally applicable for SMC retrieval over meadows. However, the SMC retrievals have only been validated on meadows in the study region Twente. The

characteristics of this region are described under recommendation 2. Besides, Chapter 7 validated the temporal dynamics with the match between SMC retrievals and references separately for each study field. Before operational implementation, it is recommended to study the general applicability of the SMC retrieval scheme and extend the validation to other soil types and field, SMC and vegetation conditions as well as validate spatial dynamics.

It should be noted, however, that a limitation of the SMC retrieval scheme, which probably degrades its performance, are the set of assumed surface roughness and vegetation parameters. Regarding the surface roughness parameters, Chapter 6 suggests that using a single set of surface roughness parameters is permitted for meadows across a larger region and multiple seasons. However, this finding was obtained for two meadows over two winter seasons and the assumption of using a single set of surface roughness parameters is not verified in Chapter 7. Regarding the vegetation parameters, values calibrated on Tibetan alpine grassland were adopted from Dente et al. (2014). Chapter 7 focuses on establishing a scheme for operational SMC retrieval and investigates whether, with the described implementation, the vegetation correction improves the SMC retrievals. Further research questions are if SMC retrieval performance would improve with (i) a region-specific calibration of vegetation parameters, (ii) field-specific roughness parameters and vegetation parameters, and (iii) how either can be established in a SMC retrieval scheme that is operationally applicable.

Recommendation 4: Functionally evaluate the surface SMC retrievals. The evaluation of SMC retrievals against SMC references involves several complexities, which is extensively described in this thesis. Moreover, from evaluating estimated accuracies against a target accuracy threshold, such as $0.04\,m^3\,m^{-3}$ for the Soil Moisture and Ocean Salinity (SMOS) and SMAP missions, a product cannot be declared 'valid' or 'invalid' because such thresholds do not relate to the suitability for a specific application (Entekhabi et al., 2010b; Gruber et al., 2020). Estimating the performance at different timescales could inform of prediction skill regarding e.g. seasonal and short wetting/drying events (Gruber et al., 2020; Beck et al., 2021). However, in many cases surface SMC is not even the actual variable of interest. Entekhabi et al. (2010b) and Gruber et al. (2020) stress that the user community should define SMC accuracy requirements inferred from the relation of SMC with another variable and the accuracy requirement of that variable.

Alternatively, to value SMC retrievals and bypass the direct validation against SMC references, the SMC retrievals could be functionally evaluated in potential applications (e.g. Crow, 2007; Crow et al., 2012; Bauer-Marschallinger et al., 2018). An example could be to assimilate SMC retrievals into a catchment model, and evaluate whether the river discharge can be simulated with sufficient or improved accuracy. Within the context of the research project OWAS1S (Optimizing Water Availability with Sentinel-1 Satellites), functional evaluation of SMC information

has been applied in the PhD theses by Carranza (2021) for agricultural water management and by Pezij (2020) for operational water management. Similar analyses could be performed with the SMC retrievals from this thesis.

Recommendation 5: Analyse SMC products in conjunction and present them as ensembles.
SMC retrievals are generally evaluated against in situ references to quantify their performance. From the comparison of the Sentinel-1 SMC retrievals against SMAP 9 km retrievals in Chapter 7, it was inferred that rainfall did not fully infiltrate the influence zone of the in situ sensors at 5 cm depth in the months after the exceptionally dry 2018 summer. The satellite retrievals and the in situ sensors provide information for different soil layers, as was also found for e.g. SMOS (Rondinelli et al., 2015; Escorihuela et al., 2010) and SMAP retrievals (Van der Velde et al., 2021; Shellito et al., 2016). In an optimum setting, the SMC estimates from satellites and from in situ sensors, thus, complement each other. The comparison also pointed to increased SMC retrievals from two Sentinel-1 orbits. These cases illustrate that analysing a SMC product against other SMC products may give additional insights into the SMC products.

The scheme implementations with and without vegetation correction, two other Sentinel-1 based products and the SMAP products in Chapter 7 each yield different SMC retrievals because they are based on imagery from different satellites or on different algorithms, but the performance metrics indicate that all these SMC products provide information about field-scale SMC. It would, therefore, be interesting to research the representation of field-scale SMC as an ensemble of SMC products. Ensemble representations provide multiple predictions of a quantity for the same location and time, based on multiple models ('super-ensembles' or 'grand-ensembles'), and initial condition, forcing and/or parameter uncertainties. These are common practice in other fields, such as for meteorological forecasts (e.g. Buizza et al., 2005; Bougeault et al., 2010) and river discharge forecasts (e.g. Cloke and Pappenberger, 2009; Fleming et al., 2015; He et al., 2009). SMC retrievals have in common with meteorological and river discharge forecasts that they are uncertain. Ensembles of SMC retrievals could reveal the uncertainties and provide information on the possibility of a certain (e.g. extreme) SMC condition to occur. An ensemble-like approach was already used in Chapter 6 for estimating the U_p and the total uncertainty, after taking 1000 samples from the surface roughness parameter and residual distributions. Quets et al. (2019) presented an ensemble approach for SMC retrievals, using SMOS observations, 5 parameter sets and 17 perturbed parameter values. Examples of SMC products that could be validated and potentially added to a field-scale SMC super-ensemble are the 500 m product from Sentinel-1 imagery retrieved with a multi-temporal algorithm (Pulvirenti et al., 2018), the 1 km Copernicus Surface Soil Moisture product with a change detection algorithm (Bauer-Marschallinger et al., 2019), the 1 km product from Sentinel-1 imagery with the short term change detection

algorithm (Balenzano et al., 2021), and the 1 km and 3 km products from a combination of SMAP and Sentinel-1 imagery (Das et al., 2019). The insights gained in this thesis on the contributing factors to SMC retrieval uncertainty can be used for generating ensembles of field-scale SMC retrievals from Sentinel-1.

Recommendation 6: Use the vegetation signal in Sentinel-1 backscatter observations.
The model study in Chapter 7 points out that vegetation highly attenuates the soil σ^0 signal and significantly contributes to the total Sentinel-1 σ^0. Actually, Sentinel-1's specifications are sub-optimal for SMC retrieval with its observations in C-band at relatively large incidence angles and in the VV and VH polarizations. Next to attempting to correct or mask for vegetation effects and focus on the soil signal, information may be extracted from the vegetation signal. For example, vegetation σ^0 signals were used to monitor vegetation water stress (Van Emmerik et al., 2017), SMC in the root zone (Carranza, 2021) and vegetation indices (Vreugdenhil et al., 2018).

Recommendation 7: Utilize upcoming L-band SAR missions for SMC retrieval.
L-band σ^0 observations are less obstructed by vegetation and penetrate deeper in the soil than C-band σ^0 observations (Entekhabi et al., 2010a; El Hajj et al., 2019). Hence, L-band σ^0 observations are more suitable for SMC retrieval. This could also be in combination with C-band σ^0 observations (Mengen et al., 2021). A next generation of satellite missions with selected operational land coverage will enable this. The SAOCOM-1A and -1B satellites (Azcueta et al., 2021) were launched in 2018 and 2020, launch of NISAR (Kellogg et al., 2020) is planned for 2023, Tandem-L (Moreira et al., 2015) for 2024 and ROSE-L (Davidson et al., 2021) for 2028.

Data availability

9

Chapter 2

The raw and processed soil moisture content (SMC) and temperature Twente network data from 2008 till 2020, the photos and notes taken during field visits as well as the measurements collected during the 2009, 2015, 2016 and 2017 field campaigns are publicly available at https://doi.org/10.17026/dans-zrn-n8nh (Van der Velde and Benninga, 2020). An updated version of the dataset is expected. The locations of the measurements are given in geographic (WGS84) and map projected coordinates (RD New). Table 2.7 lists open third-party datasets.

The following supplements will be made available with the scientific paper when published and until then may be requested from the authors of the paper, Table S1: the groundwater monitoring wells nearest to the Twente monitoring stations, Table S2: lists of maintenance practices applied to the Twente monitoring stations, Table S3: types of capacitance probes installed at each station and depth.

Chapter 3

The processed SMC and soil temperature data collected by the Raam network are available at:

- 5 April 2016–4 April 2017: https://doi.org/10.4121/uuid:276a8c0e-c9a9-4fdf-916a-75cfe06fa974 (Benninga et al., 2018a).
- 5 April 2017–4 April 2018: https://doi.org/10.4121/uuid:afb36ac8-e266-4968-8f76-0d1f6988e23d (Benninga et al., 2018b).
- 5 April 2018–4 April 2019: https://doi.org/10.4121/uuid:b68e3971-c73e-4d7f-b52f-9ef7d7fe1ed2 (Benninga et al., 2020a).

A readme file describes the structure of the files, contact information and locations. Also included is a file containing information about additional datasets available for the Raam catchment (elevation, soil physical, land cover, groundwater level and meteorological data).

Chapters 4 and 6

The SMC measurements that were collected inside four study fields, and the processed Sentinel-1 σ^0 observations, masks for weather-related surface conditions, SMC retrievals and SMC references are available at https://doi.org/10.17026/dans-xfs-3anu (Benninga et al., 2020c). This dataset contains modified Copernicus Sentinel data [2016–2018]. The Sentinel-1 images were downloaded from the Copernicus Open Access Hub (https://scihub.copernicus.eu/; Copernicus, 2019), the SMC references were collected by the Twente network, which is operated by the Faculty of Geo-Information Science and Earth Observation (ITC) - University of Twente (Van der Velde and Benninga, 2020), and meteorological measurements of the Royal Netherlands Meteorological Institute ('Koninklijk Nederlands Meteorologisch Instituut' in Dutch, or KNMI) were obtained from http://www.knmi.nl/nederland-nu/klimatologie-metingen-en-waarnemingen (KNMI, 2019).

Chapter 5

The following are available online at www.mdpi.com/2072-4292/11/17/2025/s1, Supplement 1: figures of Sentinel-1 σ^0 time series for all study fields, Supplement 2: tables with the processed masks for weather-related surface conditions, meteorological conditions and Sentinel-1 σ^0 observations for the study fields. Contain modified Copernicus Sentinel data [2014–2018]. The data sources are the same as for Chapters 4 & 6.

Chapter 7

The leaf area index (LAI) measurements collected inside two meadows and five maize fields and the Sentinel-2 LAI estimates for these fields are available at https://doi.org/10.17026/dans-xxv-sdez (Benninga et al., 2021a). Tables of processed Sentinel-1 σ^0 observations, masks for weather-related surface conditions, processed Sentinel-2 LAI estimates, SMC references, and the IEM and TV-IEM retrievals, as well as supplementary time series figures for the 21 study fields are available at https://doi.org/10.17026/dans-z9z-t36z (Benninga et al., 2021b). The datasets at Benninga et al. (2021a) and Benninga et al. (2021b) contain modified Copernicus Sentinel data [2015–2019]. The V102 vegetation indicator (LAI) maps and scene classifications were downloaded from the VITO Product Distribution Portal of the Flemish Institute for Technological Research ('Vlaamse Instelling voor Technologisch Onderzoek' in Dutch, or VITO; VITO 2019). The data sources of the Sentinel-1 images, KNMI meteorological measurements and SMC references are the same as for Chapters 4 & 6.

Author contributions

10

Chapter 2

Conceptualization: Rogier van der Velde (R.v.d.V.), Harm-Jan F. Benninga (H.F.B.); **Data curation:** R.v.d.V., H.F.B.; **Formal analysis:** R.v.d.V.; **Funding acquisition:** R.v.d.V.; **Investigation:** R.v.d.V., H.F.B.; **Methodology:** R.v.d.V., H.F.B.; **Project administration:** R.v.d.V.; **Resources:** R.v.d.V.; **Software:** R.v.d.V., H.F.B.; **Supervision:** R.v.d.V.; **Validation:** R.v.d.V., H.F.B.; **Visualization:** R.v.d.V., H.F.B.; **Writing–original draft preparation:** R.v.d.V., H.F.B.; **Writing–review & editing:** R.v.d.V., H.F.B.

R.v.d.V. coordinated the writing, and was (primarily) responsible for the introduction, description of the monitoring network and field campaigns, calibrations, and soil moisture content time series analyses. H.F.B. was (primarily) responsible for the description of the study area and open datasets, maintenance and quality control. Both authors contributed to the field data collection, and the organization of the Twente dataset.

Chapter 3

Conceptualization: Harm-Jan F. Benninga (H.F.B.), Coleen D. U. Carranza (C.D.U.C.), Michiel Pezij (M.P.), Pim van Santen (P.v.S.), Martine J. van der Ploeg (M.J.v.d.P.), Denie C. M. Augustijn (D.C.M.A.), Rogier van der Velde (R.v.d.V.); **Data curation:** H.F.B., C.D.U.C., M.P., P.v.S.; **Formal analysis:** H.F.B., C.D.U.C., M.P.; **Funding acquisition:** P.v.S., M.J.v.d.P., D.C.M.A., R.v.d.V.; **Investigation:** H.F.B., C.D.U.C., M.P., P.v.S., M.J.v.d.P., D.C.M.A., R.v.d.V.; **Methodology:** H.F.B., C.D.U.C., M.P.; **Project administration:** H.F.B., P.v.S., R.v.d.V.; **Resources:** P.v.S., R.v.d.V.; **Software:** H.F.B., M.P.; **Supervision:** M.J.v.d.P., D.C.M.A., R.v.d.V.; **Validation:** M.J.v.d.P., D.C.M.A., R.v.d.V.; **Visualization:** H.F.B., C.D.U.C., M.P.; **Writing–original draft preparation:** H.F.B., C.D.U.C., M.P., P.v.S; **Writing–review & editing:** H.F.B., C.D.U.C., M.P., P.v.S., M.J.v.d.P., D.C.M.A., R.v.d.V.

The complete author team designed the monitoring network and the paper's structure. H.F.B. coordinated the writing, whereby C.D.U.C. contributed specifically to the soil characterisation, M.P. to the data series analyses and P.v.S. to the study area descriptions.

Chapters 4, 6 and 7

Conceptualization: Harm-Jan F. Benninga (H.F.B.), Rogier van der Velde (R.v.d.V.), Zhongbo Su (Z.S.); **Data curation:** H.F.B., R.v.d.V.; **Formal analysis:** H.F.B.; **Funding acquisition:** R.v.d.V., Z.S.; **Investigation:** H.F.B., R.v.d.V.; **Methodology:** H.F.B., R.v.d.V.; **Project administration:** R.v.d.V., Z.S.; **Resources:** H.F.B., R.v.d.V., Z.S.; **Software:** H.F.B.; **Supervision:** R.v.d.V., Z.S.; **Validation:** R.v.d.V.; **Visualization:** H.F.B.; **Writing–original draft preparation:** H.F.B.; **Writing–review & editing:** H.F.B., R.v.d.V., Z.S.

Chapter 5

Conceptualization: Harm-Jan F. Benninga (H.F.B.), Rogier van der Velde (R.v.d.V.), Zhongbo Su (Z.S.); **Data curation:** H.F.B.; **Formal analysis:** H.F.B.; **Funding acquisition:** R.v.d.V., Z.S.; **Investigation:** H.F.B.; **Methodology:** H.F.B., R.v.d.V.; **Project administration:** R.v.d.V., Z.S.; **Resources:** H.F.B., R.v.d.V., Z.S.; **Software:** H.F.B.; **Supervision:** R.v.d.V., Z.S.; **Validation:** R.v.d.V.; **Visualization:** H.F.B.; **Writing–original draft preparation:** H.F.B.; **Writing–review & editing:** H.F.B., R.v.d.V., Z.S.

Appendices

A

A.1 Soil characteristics of the study fields in Chapters 4 and 6

Table A.1 The soil textures and bulk densities of the study fields in Chapter 4 and Chapter 6. The values are from the surface layer (0 cm to 23 cm depth) of the soil physical units map of the Netherlands ('bodemfysische eenhedenkaart 2012' in Dutch, or BOFEK2012; Wösten et al., 2013).

Field	Texture			Bulk density [g cm^{-3}]
	Sand [%]	Silt [%]	Clay [%]	
I	79	17	4	1.37
II	75	18	7	1.39
III	79	17	4	1.37
IV	78	17	5	1.40

A.2 Performance metrics definitions

Match-ups between estimates (Y_e) and references (Y_r) are evaluated with the root mean square deviation ($RMSD$), the unbiased $RMSD$ ($uRMSD$), the Pearson correlation coefficient (r_P) and the bias.

$$RMSD = \sqrt{\frac{\sum_{t=1}^{N} \left(Y_e(t) - Y_r(t)\right)^2}{N}}, \tag{A.1}$$

$$uRMSD = \sqrt{\frac{\sum_{t=1}^{N} \left(Y_e(t) + \left(\overline{Y_r} - \overline{Y_e}\right) - Y_r(t)\right)^2}{N}}, \tag{A.2}$$

$$r_P = \frac{\sum_{t=1}^{N} \left(Y_e(t) - \overline{Y_e}\right)\left(Y_r(t) - \overline{Y_r}\right)}{\sqrt{\sum_{t=1}^{N} \left(Y_e(t) - \overline{Y_e}\right)^2}\sqrt{\sum_{t=1}^{N} \left(Y_r(t) - \overline{Y_r}\right)^2}}, \tag{A.3}$$

and

$$bias = \overline{Y_e} - \overline{Y_r}, \tag{A.4}$$

where N stands for the number of pairs and t for the observation number. The bars denote the means of Y_e and Y_r.

A.3 Residual analysis plots

A.3.1 Calibration period

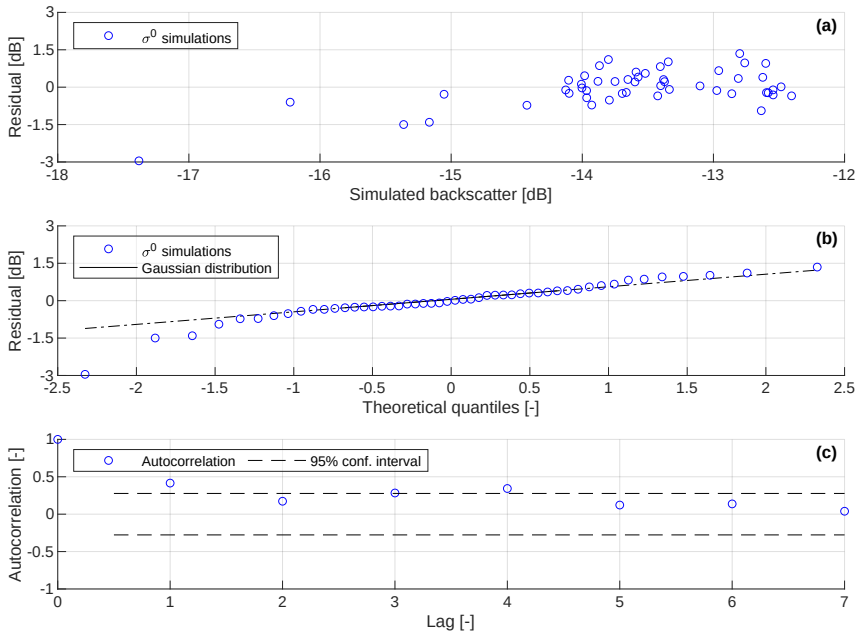

Figure A.1 Residual analysis plots of the MAP σ^0 simulations for the combined ascending & descending orbits calibration on field I. **(a)** Residuals against simulations, **(b)** quantile-quantile plot, **(c)** autocorrelation coefficients of the residuals.

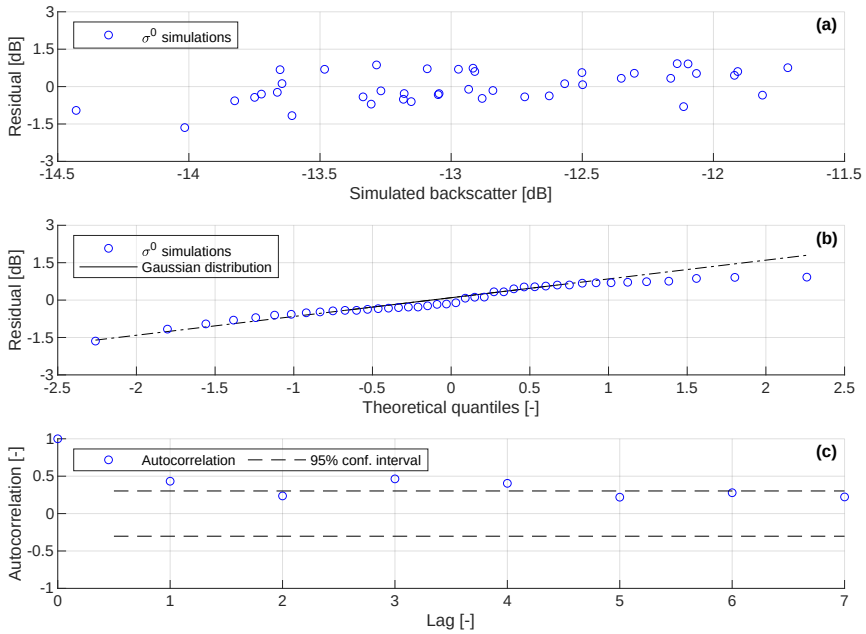

Figure A.2 Residual analysis plots of the MAP σ^0 simulations for the combined ascending & descending orbits calibration on field II. **(a)** Residuals against simulations, **(b)** quantile-quantile plot, **(c)** autocorrelation coefficients of the residuals.

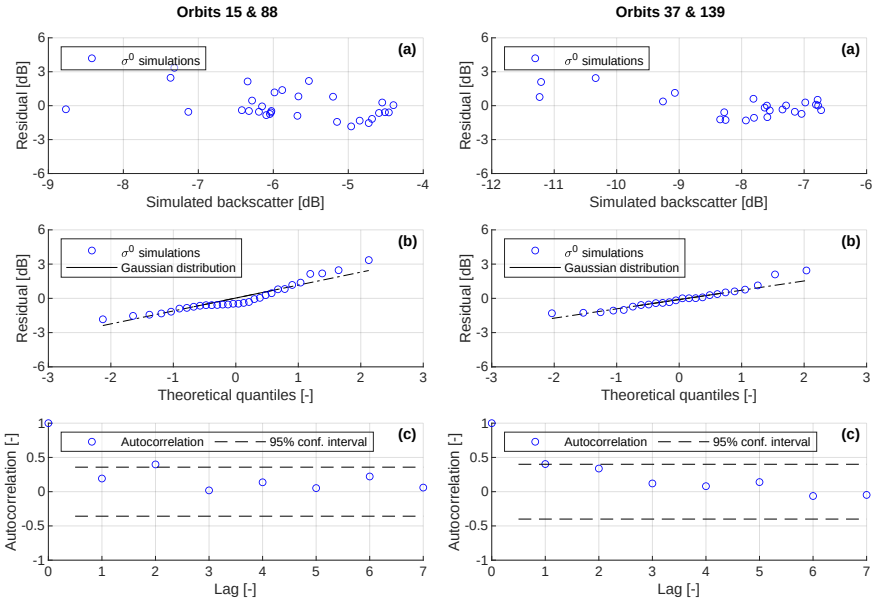

Figure A.3 Residual analysis plots of the MAP σ^0 simulations for the calibrations on field III. **(a)** Residuals against simulations, **(b)** quantile-quantile plot, **(c)** autocorrelation coefficients of the residuals.

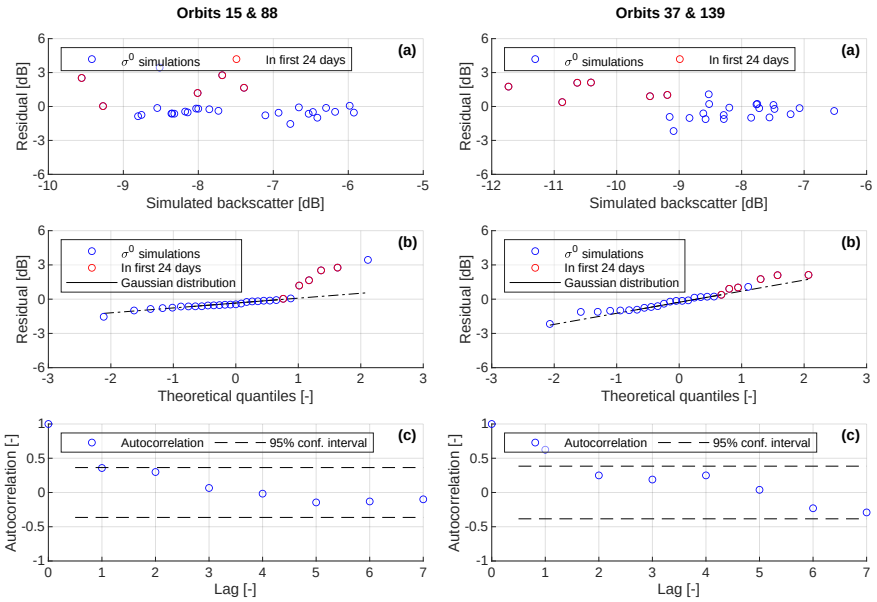

Figure A.4 Residual analysis plots of the MAP σ^0 simulations for the calibrations on field IV. **(a)** Residuals against simulations, **(b)** quantile-quantile plot, **(c)** autocorrelation coefficients of the residuals.

A.3.2 Validation period

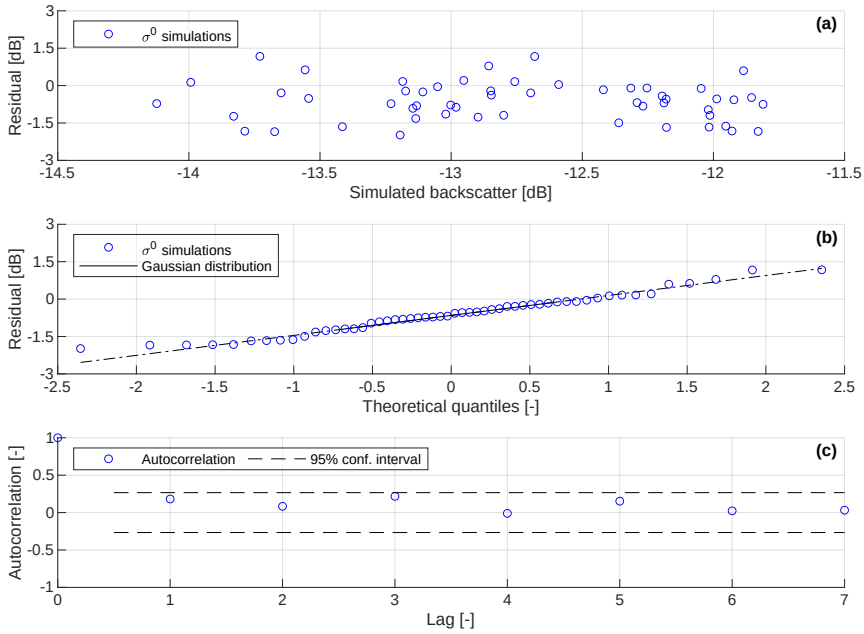

Figure A.5 Residual analysis plots of the MAP σ^0 simulations for the combined ascending & descending orbits validation on field I. **(a)** Residuals against simulations, **(b)** quantile-quantile plot, **(c)** autocorrelation coefficients of the residuals.

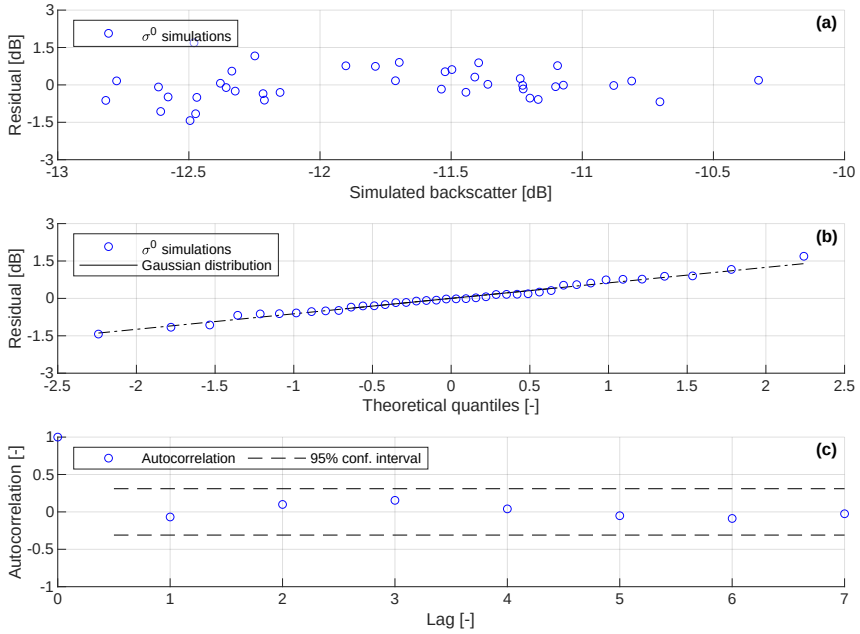

Figure A.6 Residual analysis plots of the MAP σ^0 simulations for the combined ascending & descending orbits validation on field II. **(a)** Residuals against simulations, **(b)** quantile-quantile plot, **(c)** autocorrelation coefficients of the residuals.

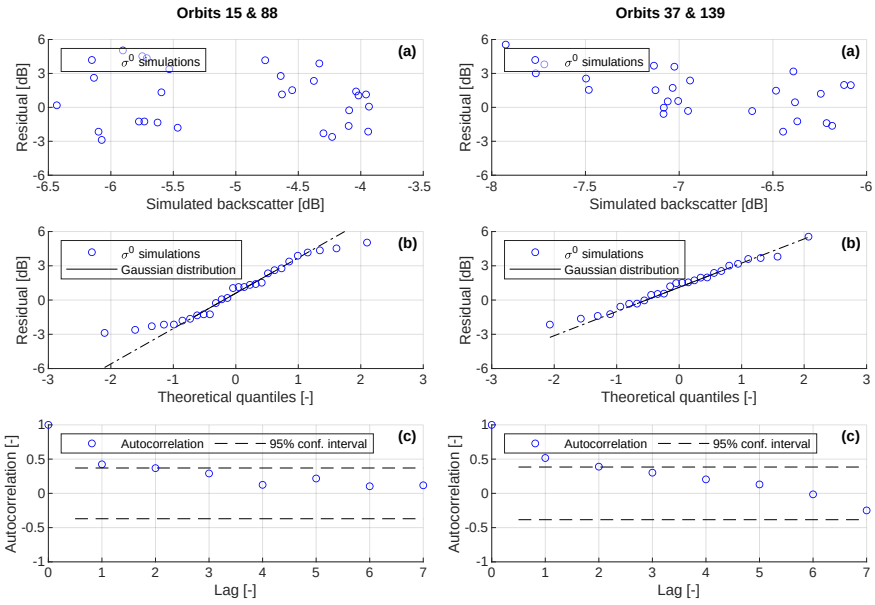

Figure A.7 Residual analysis plots of the MAP σ^0 simulations for the validations on field III. **(a)** Residuals against simulations, **(b)** quantile-quantile plot, **(c)** autocorrelation coefficients of the residuals.

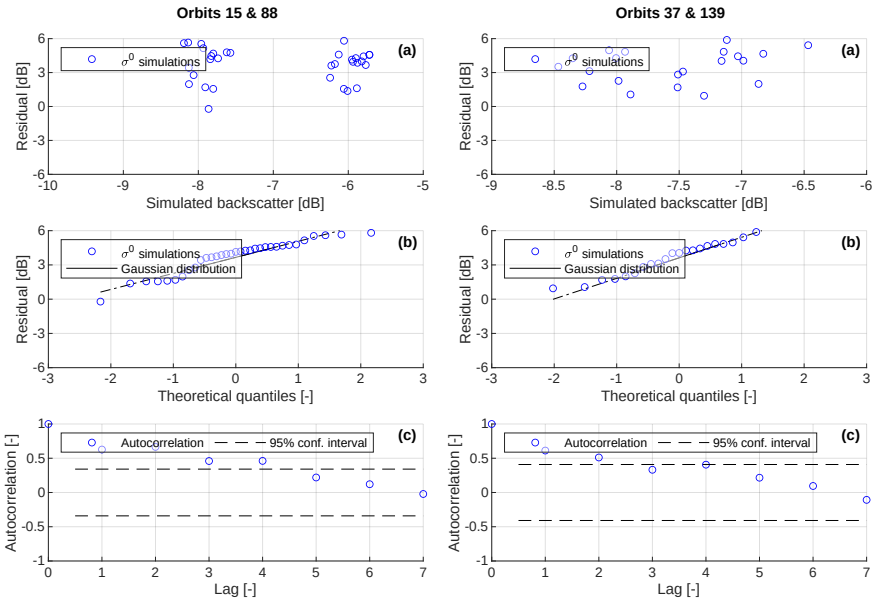

Figure A.8 Residual analysis plots of the MAP σ^0 simulations for the validations on field IV. **(a)** Residuals against simulations, **(b)** quantile-quantile plot, **(c)** autocorrelation coefficients of the residuals.

A.4 Calibration results with a first-order and a second-order autoregressive residual model

For the calibration with a second-order autoregressive residual model, which has two additional parameters to be inferred, 10 000 realizations per chain were used in order to reach convergence after 50 % of the realizations (burn-in realizations).

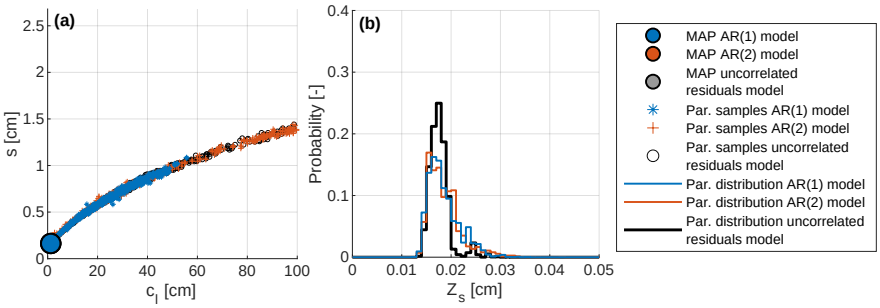

Figure A.9 **(a)** The posterior combinations of s and c_l, and **(b)** histograms of the posterior Z_s distributions for field I, using a residual model with uncorrelated residuals, a first-order (AR(1)) and a second-order (AR(2)) autoregressive model.

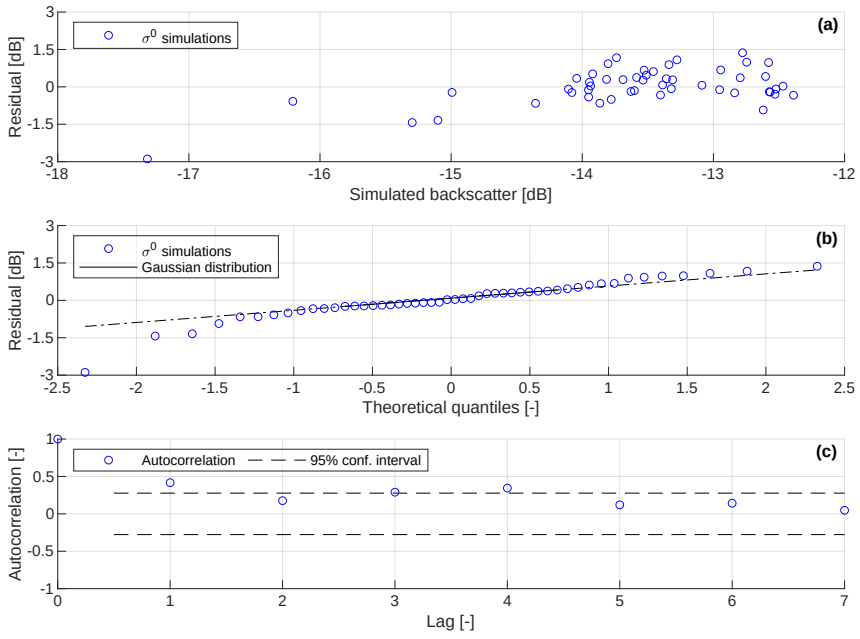

Figure A.10 Residual analysis of the MAP σ^0 simulations for the calibration on field I with an AR(1) residual model. **(a)** Residuals against simulations, **(b)** quantile-quantile plot, **(c)** autocorrelation coefficients of the residuals.

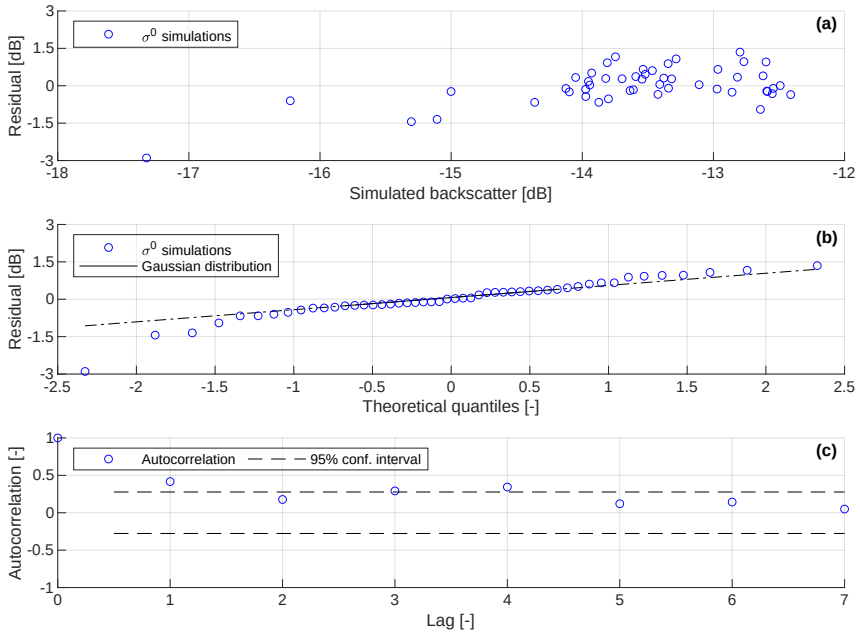

Figure A.11 Residual analysis of the MAP σ^0 simulations for the calibration on field I with an AR(2) residual model. **(a)** Residuals against simulations, **(b)** quantile-quantile plot, **(c)** autocorrelation coefficients of the residuals.

A.5 Time series figures of the meadows' surface roughness cross-validation

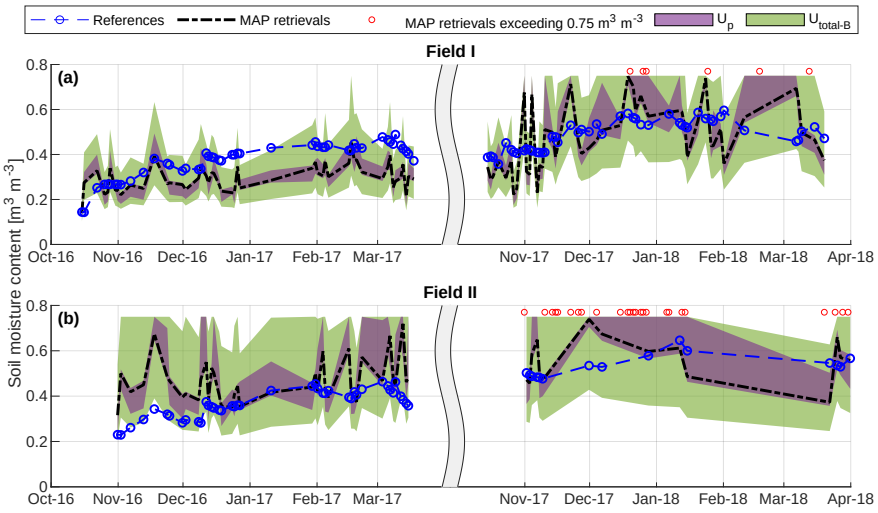

Figure A.12 SMC retrievals for field I using the MAP surface roughness parameter set of field II, and vice versa. The U_p and $U_{total\text{-}B}$ are visualized by the $95\,\%$ confidence interval.

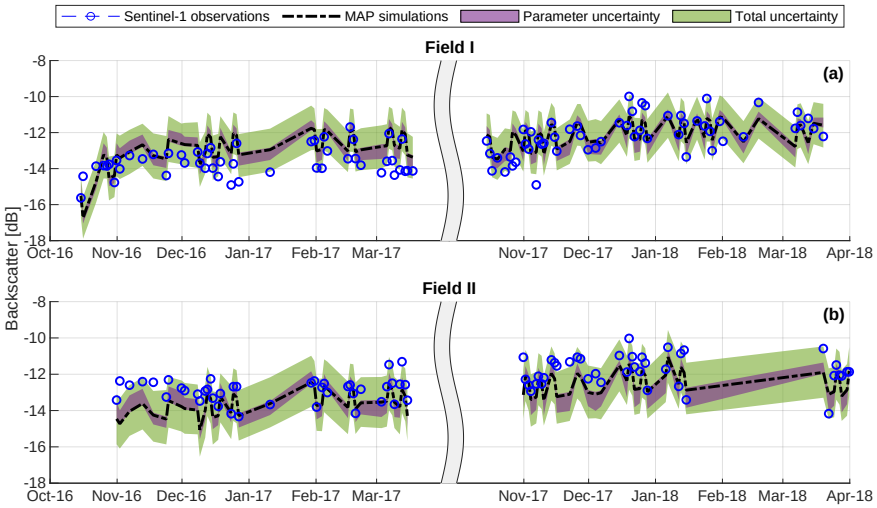

Figure A.13 σ^0 simulations for field I using the MAP surface roughness parameter set of field II, and vice versa. The parameter and total simulation uncertainty are visualized by the $95\,\%$ confidence interval.

A.6 Field III surface roughness calibration exclusively on Sentinel-1 observations acquired in relative orbit 88

The posterior surface roughness parameter distributions (Figure A.14) of the calibration on field III Sentinel-1 σ^0 observations acquired exclusively in relative orbit 88 are similar to the results obtained on the Sentinel-1 observations acquired in both ascending orbits (15 & 88), except for a limited number of parameter combinations having a Z_s around 1.0 cm.

Figures A.15 and A.16 show the residual analysis plots. Figure A.15 justifies the use of the homoscedastic Gaussian residual model for the calibration period. The residual analysis plots for the validation period (Figure A.16) are similar to the residual analysis plots of the old calibration on both ascending orbits (Figure A.7).

Figure A.17 shows that the performances of the orbit 88 σ^0 simulations with the parameter sets sampled from the posterior distributions obtained by the calibration on orbit 88 are similar to the performances with the parameter sets obtained by the calibration on both orbit 15 and 88.

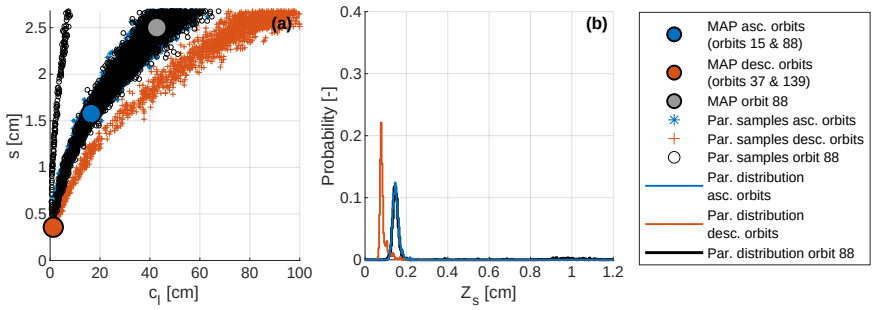

Figure A.14 **(a)** The posterior combinations of s and c_l, and **(b)** histograms of the posterior Z_s distributions for field III, including the calibration exclusively on Sentinel-1 observations acquired in relative orbit 88.

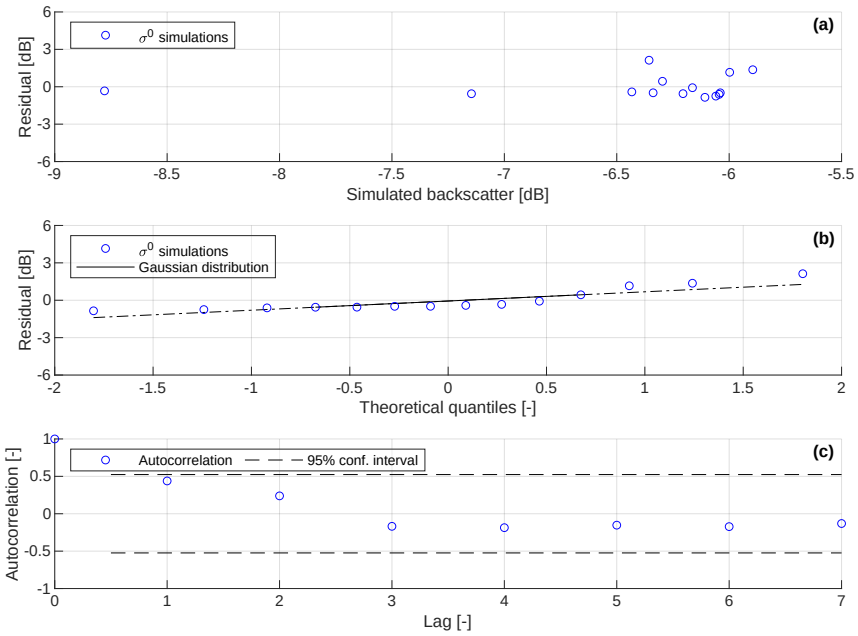

Figure A.15 Residual analysis plots of the MAP σ^0 simulations for the relative orbit 88 calibration on field III. **(a)** Residuals against simulations, **(b)** quantile-quantile plot, **(c)** autocorrelation coefficients of the residuals.

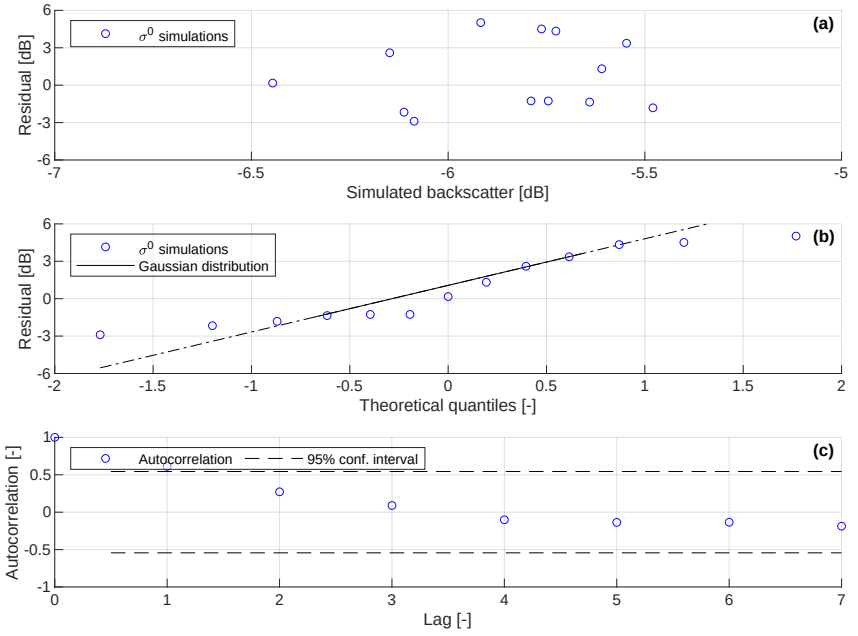

Figure A.16 Residual analysis plots of the MAP σ^0 simulations for the relative orbit 88 validation on field III. **(a)** Residuals against simulations, **(b)** quantile-quantile plot, **(c)** autocorrelation coefficients of the residuals.

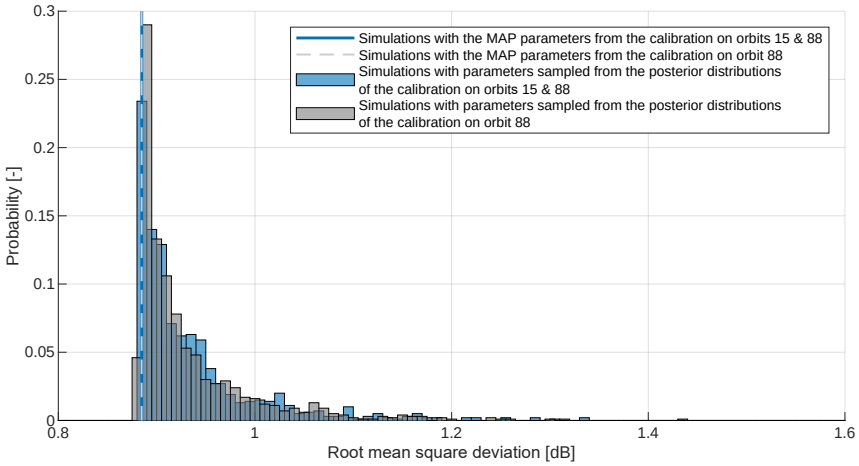

Figure A.17 $RMSD$ histogram for σ^0 simulations with 1000 parameter sets sampled from posterior surface roughness parameter distributions and with MAP parameter sets, against the Sentinel-1 σ^0 observations acquired in relative orbit 88 (field III).

A.7 Estimation of TV-IEM's and IEM's run time

The run times of TV-IEM (Tor Vergata - integral equation method) and IEM (integral equation method) were estimated by running the models for seven cases with a varied number of simulations and ten repetitions per case. The computer that was used was equipped with an Intel Core(TM) i7-4790 CPU @ 3.60 GHz processor. The results are shown in Figure A.18.

A linear equation can be fitted through the data points in Figure A.18a–b because both TV-IEM and IEM consist of a for-loop by which each input instance (combination of incidence angle, LAI, VWC and SMC) is independently simulated. The run times per simulation and the overhead times ($M = 0$) can be derived from the linear equations. Their estimates are listed in Table A.2.

A negative overhead time as found by the linear equation for TV-IEM is actually not possible. The estimated overhead time for TV-IEM is very small and its value is largely affected by uncertainty in the run times of the simulations. For both TV-IEM and IEM it can be considered negligible.

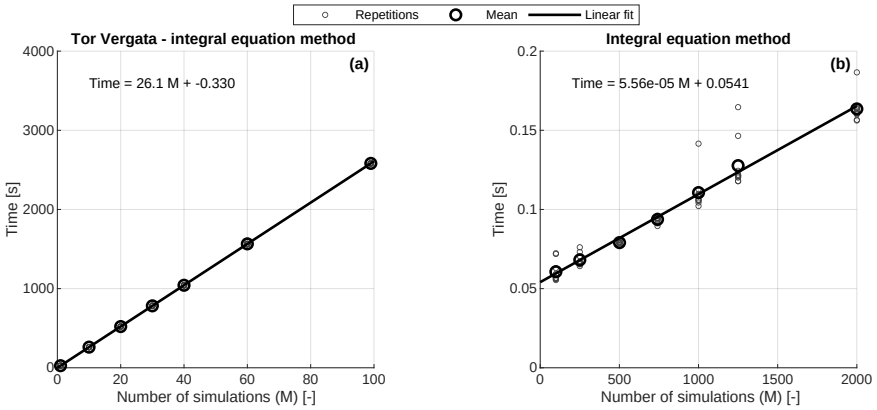

Figure A.18 The run time of the TV-IEM and the IEM model for a varied number of simulations (M).

Table A.2 Estimates of the run time per simulation and the overhead time for the TV-IEM and the IEM model.

Model	Run time per simulation [s]	Overhead time [s]
TV-IEM	26.1	−0.330
IEM	5.56×10^{-5}	0.0541

A.8 Details of the study fields in Chapter 7

Table A.3 Characteristics of the study fields in Chapter 7. The SMC monitoring stations, collectively known as the Twente network, are detailed in Van der Velde et al. (2021) and Van der Velde and Benninga (in preparation). The soil texture and soil bulk density originate from the soil physical properties map of the Netherlands and apply to the upper soil layer (BOFEK2012; Wösten et al., 2013). The net area refers to the net surface area of a field, excluding a 20 m distance from borders of fields and 40 m from trees and buildings (see Section 7.2.1.1).

Station	Field	Soil texture [%]			Soil bulk density [g cm^{-3}]	Net area [ha]
		Sand	Silt	Clay		
ITC_SM02	I	79	17	4	1.37	1.96
	II	79	17	4	1.37	4.12
ITC_SM03	III	75	18	7	1.39	2.38
	IV	65	22	13	1.21	1.53
ITC_SM04	V	78	14	8	1.36	1.83
ITC_SM05	VI	78	17	5	1.38	1.50
ITC_SM11	VII	87	9	4	1.06	6.32
	VIII	88	8	4	1.15	5.35
ITC_SM13	IX	87	10	3	1.38	2.43
	X	87	10	3	1.38	2.22
ITC_SM14	XI	77	17	6	1.42	1.48
	XII	77	17	6	1.42	1.39
ITC_SM15	XIII	67	21	12	1.24	0.70
	XIV	79	17	4	1.37	1.45
ITC_SM16	XV	87	9	4	1.26	0.60
ITC_SM17	XVI	87	10	3	1.38	0.93
ITC_SM18	XVII	77	17	6	1.42	0.16
	XVIII	77	17	6	1.42	0.80
ITC_SM19	XIX	78	18	4	1.35	1.31
	XX	78	18	4	1.35	3.88
	XXI	78	18	4	1.35	1.55

A.9 Effect of the Sentinel-2 LAI uncertainty on the backscatter to soil moisture content sensitivity

The propagation principle of the Sentinel-2 LAI uncertainty into SMC retrievals is illustrated in Figures A.19 and A.20. First, for a given LAI (e.g. LAI = $1\,m^2\,m^{-2}$) and SMC (e.g. SMC = $0.35\,m^3\,m^{-3}$) the σ^0 is determined. Next, the LAI is perturbed with the Sentinel-2 LAI uncertainty (LAI = $1\,m^2\,m^{-2} \pm 0.71\,m^2\,m^{-2}$) and two new SMC to σ^0 relations are established. Then, the SMC is determined from the σ^0 value and the new SMC to σ^0 relations (SMC^+ and SMC^- in Figures A.19a and A.20a). Finally, the effects on the SMC retrievals are determined as the differences of the original SMC with SMC^+ and SMC^- (ΔSMC^+ and ΔSMC^- in Figures A.19a and A.20a).

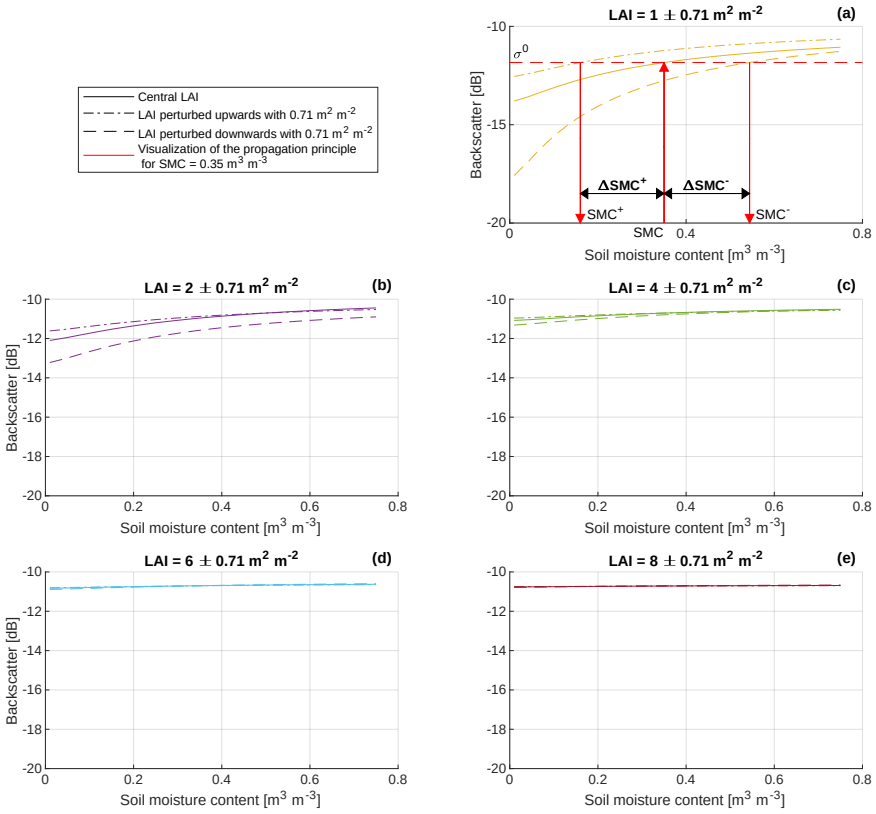

Figure A.19 The sensitivity of σ^0 to SMC for LAI values perturbed upwards and downwards by the Sentinel-2 LAI uncertainty of $0.71\,m^2\,m^{-2}$. The simulations in this figure are for a $35°$ incidence angle. The colours match Figure 7.4.

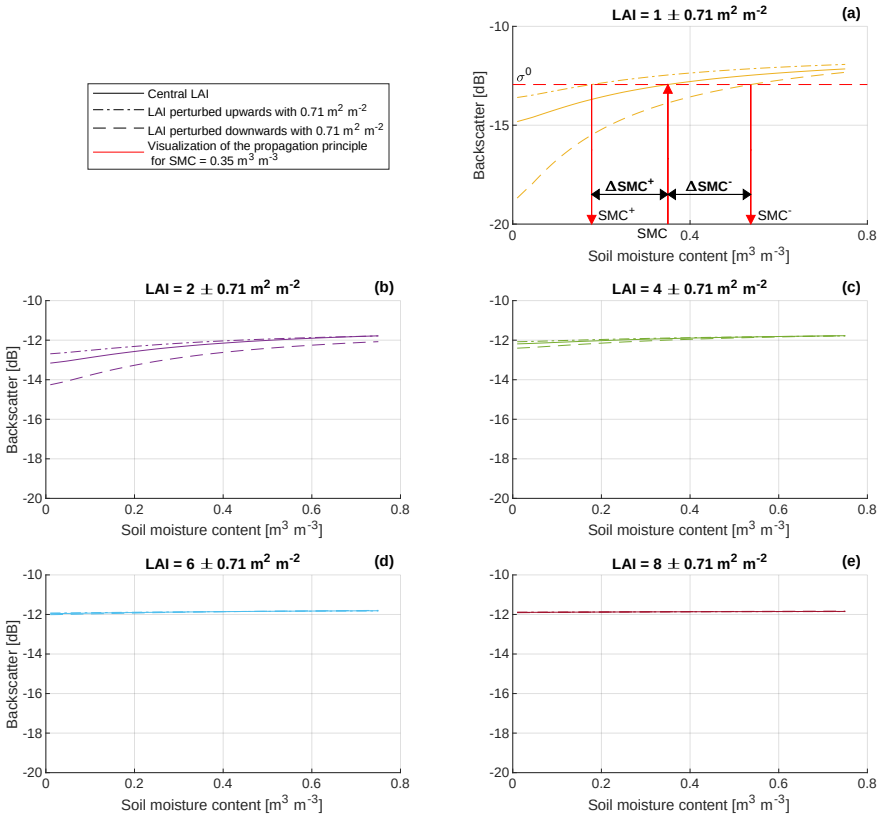

Figure A.20 Same as Figure A.19, but for a 44° incidence angle.

A.10 Performance metrics of all fields for two variants of incorporating upper limit exceedances

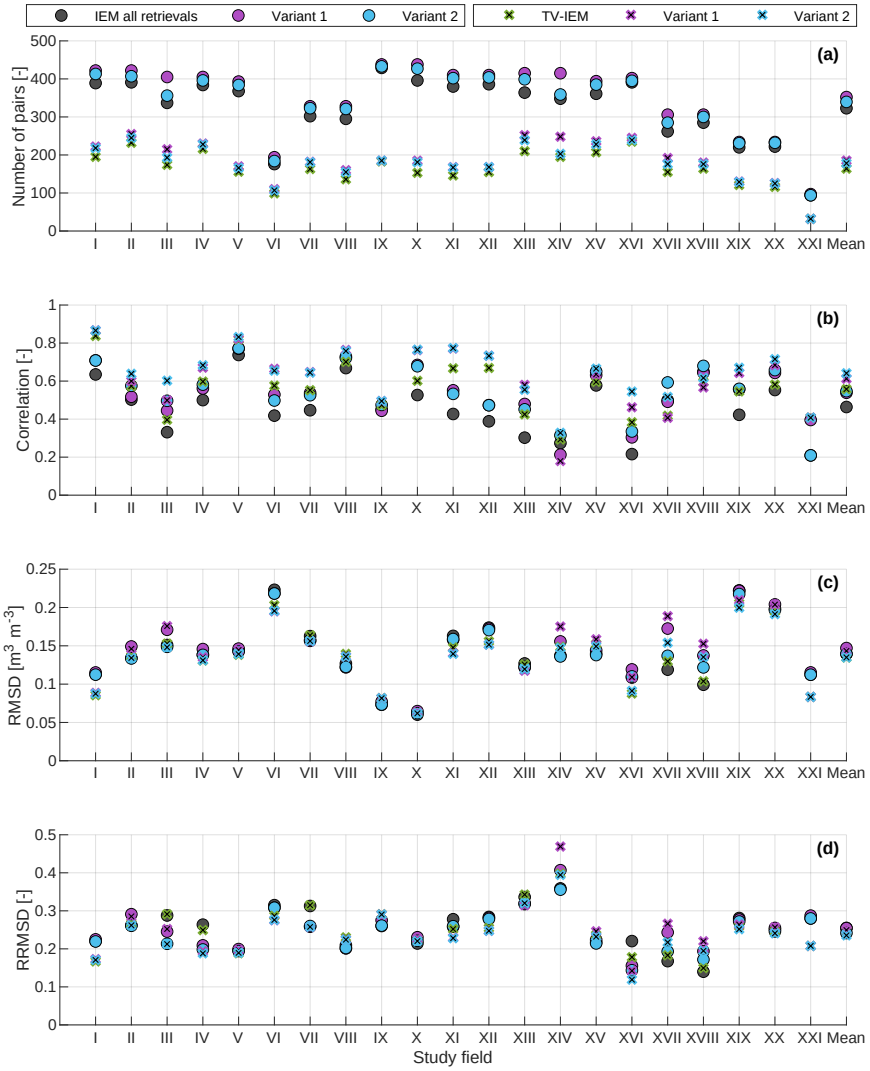

Figure A.21 Performance metrics of the IEM and TV-IEM SMC retrievals against the SMC references for two variants of incorporating information from SMC retrievals that exceed the upper retrieval limit of $0.75\,\mathrm{m^3\,m^{-3}}$. Variant 1 sets all the IEM retrievals that exceed $0.75\,\mathrm{m^3\,m^{-3}}$ and variant 2 sets only the IEM retrievals that exceed $0.75\,\mathrm{m^3\,m^{-3}}$ in the expected wet period (15 November to 15 March) to the maximum SMC.

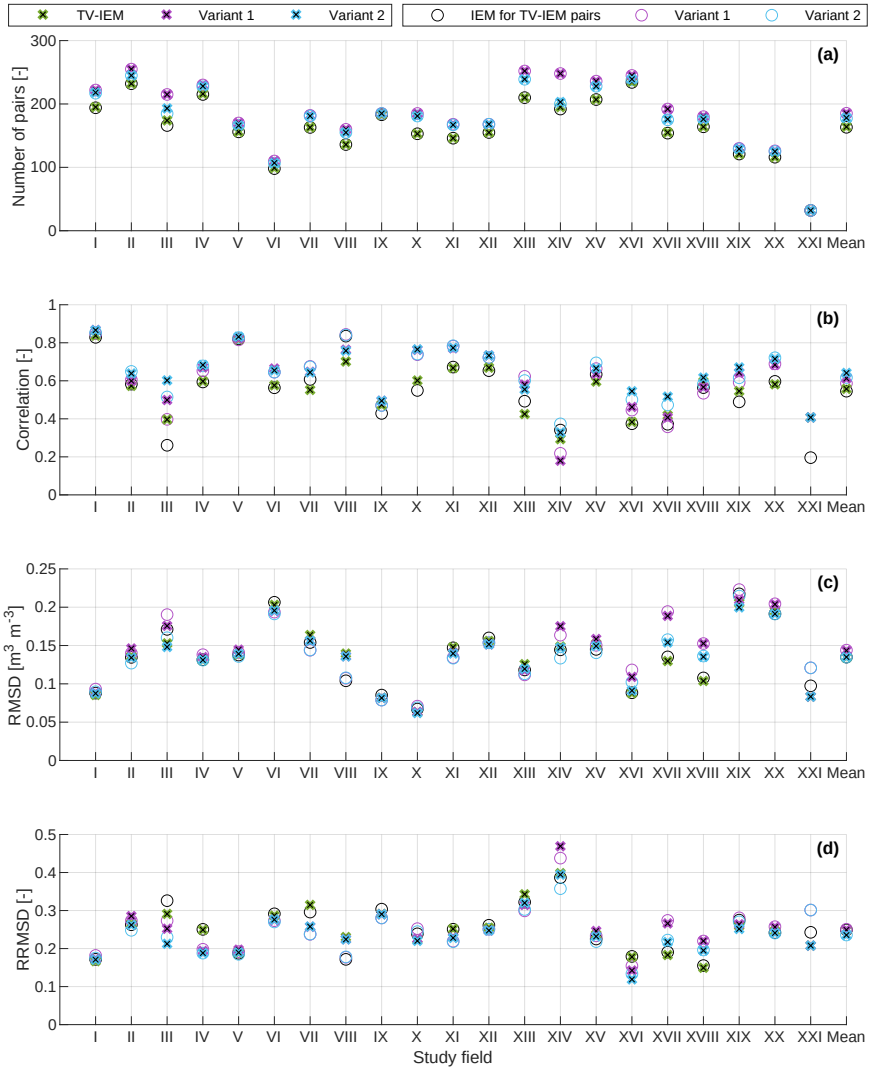

Figure A.22 Same as Figure A.21, but for TV-IEM and 'IEM for TV-IEM pairs'. 'IEM for TV-IEM pairs' contains the same retrieval-reference pairs as 'TV-IEM' (i.e. a Sentinel-2 LAI estimate is available and TV-IEM resulted in a valid SMC retrieval), whereas 'IEM all retrievals' (in Figure A.21) contains all the retrieval-reference pairs possible (i.e. from all Sentinel-1 σ^0 observations).

A.11 Sentinel-1 and SMAP soil moisture content retrieval time series

A.11.1 Field V

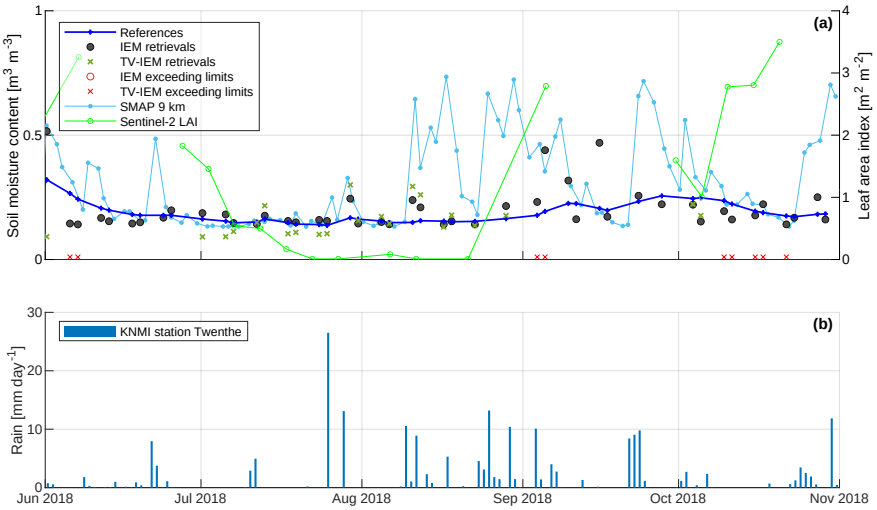

Figure A.23 SMC retrievals and references for field V during the 2018 summer. Only the Sentinel-1 SMC retrievals for orbits 15 & 37 are shown. More information about the data sources in this figure can be found in the caption of Figure 7.15.

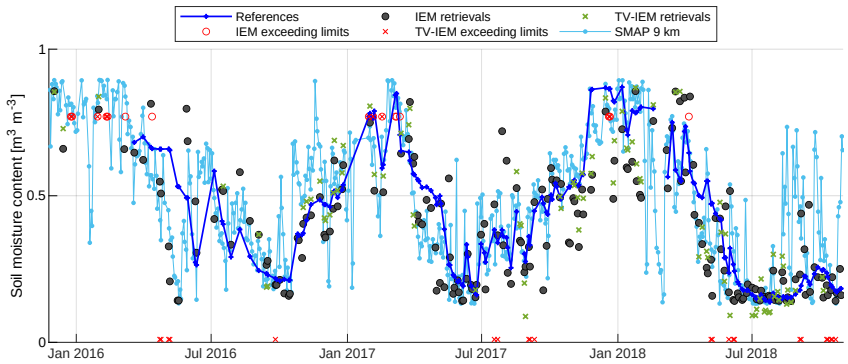

Figure A.24 SMC retrievals and references for field V. Only the Sentinel-1 SMC retrievals for orbits 15 & 37 are shown.

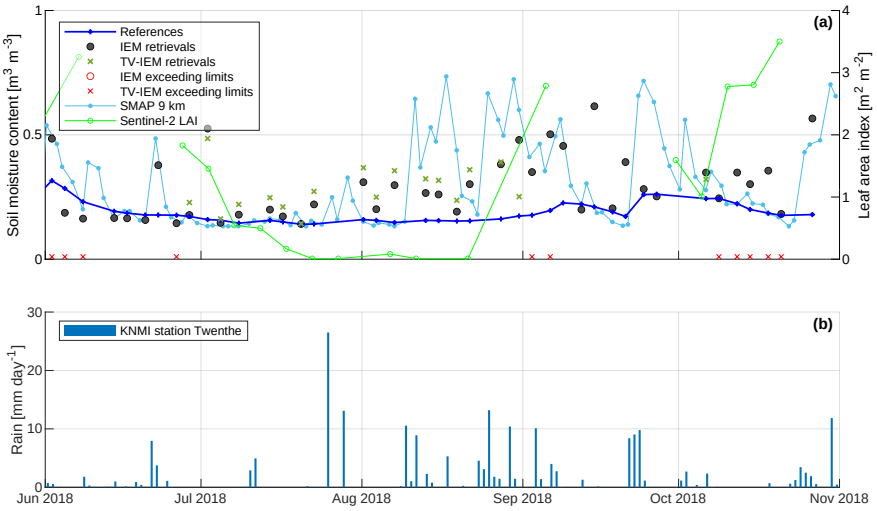

Figure A.25 SMC retrievals and references for field V during the 2018 summer. Only the Sentinel-1 SMC retrievals for orbits 88 & 139 are shown.

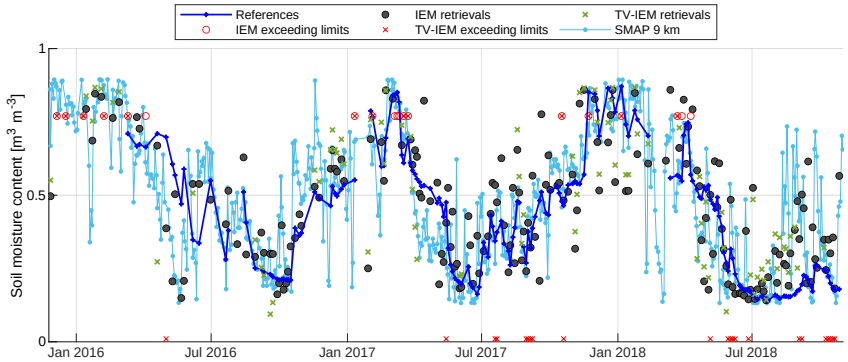

Figure A.26 SMC retrievals and references for field V. Only the Sentinel-1 SMC retrievals for orbits 88 & 139 are shown.

A.11.2 Field II

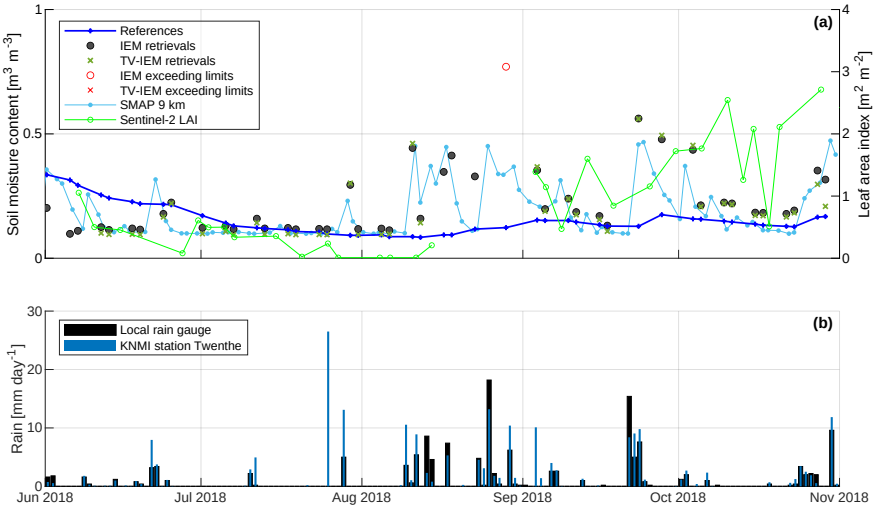

Figure A.27 SMC retrievals and references for field II during the 2018 summer. Only the Sentinel-1 SMC retrievals for orbits 15 & 37 are shown.

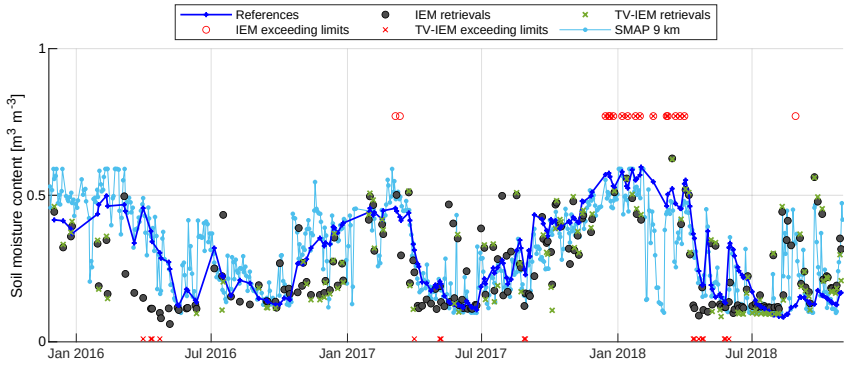

Figure A.28 SMC retrievals and references for field II. Only the Sentinel-1 SMC retrievals for orbits 15 & 37 are shown.

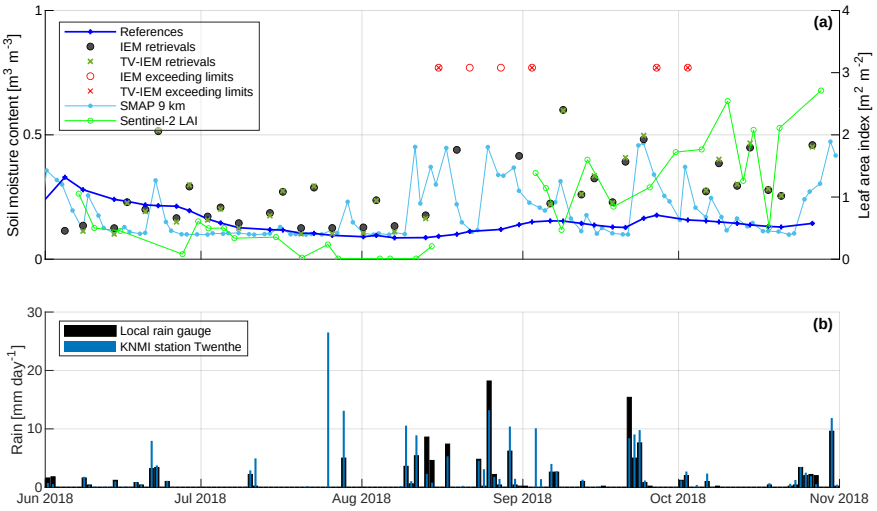

Figure A.29 SMC retrievals and references for field II during the 2018 summer. Only the Sentinel-1 SMC retrievals for orbits 88 & 139 are shown.

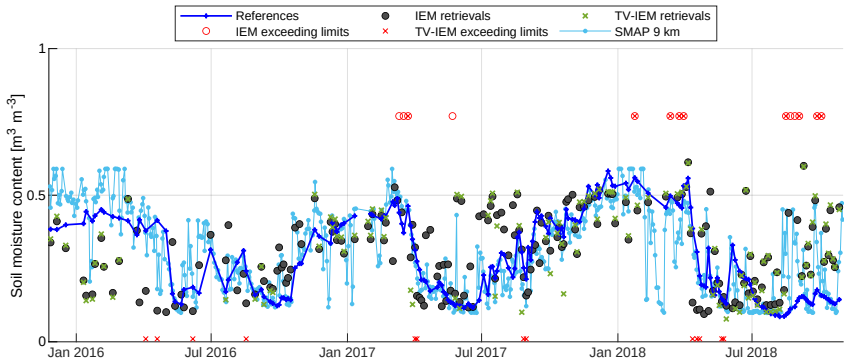

Figure A.30 SMC retrievals and references for field II. Only the Sentinel-1 SMC retrievals for orbits 88 & 139 are shown.

A.12 Performance metrics of all fields for orbits 15 & 37 and orbits 88 & 139

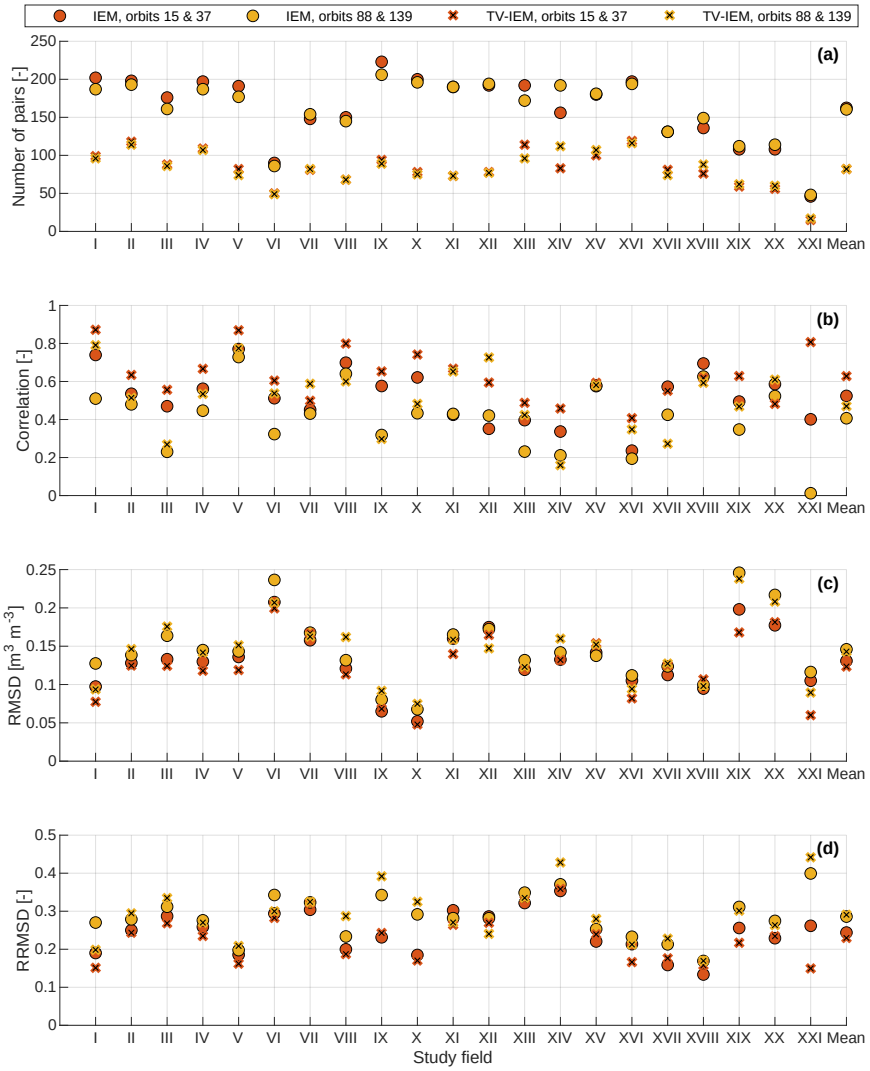

Figure A.31 Performance metrics of the IEM and TV-IEM SMC retrievals against the SMC references, for orbits 15 & 37 and orbits 88 & 139.

Bibliography

Actueel Hoogtebestand Nederland: Actueel Hoogtebestand Nederland. Version 2. Dataset, available online: http://www.ahn.nl (accessed on 1 Dec 2016), 2012a.

Actueel Hoogtebestand Nederland: Actueel Hoogtebestand Nederland. Version 2. Dataset, available online: http://www.ahn.nl (accessed on 11 Feb 2019), 2012b.

Actueel Hoogtebestand Nederland: Actueel Hoogtebestand Nederland. Version 3. Dataset, available online: http://www.ahn.nl (accessed on 19 Jul 2021), 2019.

Agam, N. and Berliner, P. R.: Dew formation and water vapor adsorption in semi-arid environments - A review, J. Arid Environ., 65, 572–590, doi:10.1016/j.jaridenv.2005.09.004, 2006.

Ahmad, M.-u.-d., Bastiaanssen, W. G. M., and Feddes, R. A.: Sustainable use of groundwater for irrigation: a numerical analysis of the subsoil water fluxes, Irrig. Drain., 51, 227–241, doi:10.1002/ird.59, 2002.

Albergel, C., Rüdiger, C., Pellarin, T., Calvet, J.-C., Fritz, N., Froissard, F., Suquia, D., Petitpa, A., Piguet, B., and Martin, E.: From near-surface to root-zone soil moisture using an exponential filter: an assessment of the method based on in-situ observations and model simulations, Hydrol. Earth Syst. Sci., 12, 1323–1337, doi:10.5194/hess-12-1323-2008, 2008.

Albergel, C., de Rosnay, P., Balsamo, G., Isaksen, L., and Muñoz-Sabater, J.: Soil Moisture Analyses at ECMWF: Evaluation Using Global Ground-Based In Situ Observations, J. Hydrometeorol., 13, 1442–1460, doi:10.1175/JHM-D-11-0107.1, 2012.

Ali, I., Greifeneder, F., Stamenkovic, J., Neumann, M., and Notarnicola, C.: Review of Machine Learning Approaches for Biomass and Soil Moisture Retrievals from Remote Sensing Data, Remote Sens., 7, 16 398–16 421, doi:10.3390/rs71215841, 2015.

Altese, E., Bolognani, O., Mancini, M., and Troch, P. A.: Retrieving Soil Moisture Over Bare Soil from ERS 1 Synthetic Aperture Radar Data: Sensitivity Analysis Based on a Theoretical Surface Scattering Model and Field Data, Water Resour. Res., 32, 653–661, doi:10.1029/95WR03638, 1996.

Amazirh, A., Merlin, O., Er-Raki, S., Gao, Q., Rivalland, V., Malbeteau, Y., Khabba, S., and Escorihuela, M. J.: Retrieving surface soil moisture at high spatio-temporal resolution from a synergy between Sentinel-1 radar and Landsat thermal data: A study case over bare soil, Remote Sens. Environ., 211, 321–337, doi:10.1016/j.rse.2018.04.013, 2018.

Attema, E., Bargellini, P., Edwards, P., Levrini, G., Lokas, S., Moeller, L., Rosich-Tell, B., Secchi, P., Torres, R., Davidson, M., and Snoeij, P.: Sentinel-1 – The Radar Mission for GMES Operational Land and Sea Services, ESA Bull. 131, pp. 10–17, available online: https://www.esa.int/esapub/bulletin/bulletin131/bul131a_attema.pdf (accessed on 23 Jul 2021), 2007.

Attema, E. P. W. and Ulaby, F. T.: Vegetation modelled as a water cloud, Radio Sci., 13, 357–364, doi:10.1029/RS013i002p00357, 1978.

Azcueta, M., Gonzalez, J. P. C., Zajc, T., Ferreyra, J., and Thibeault, M.: External Calibration Results of the SAOCOM-1A Commissioning Phase, IEEE Trans. Geosci. Remote Sens., 60, 1–8, doi:10.1109/TGRS.2021.3075369, 2021.

Baghdadi, N., Gauthier, Y., and Bernier, M.: Capability of multitemporal ERS-1 SAR data for wet-snow mapping, Remote Sens. Environ., 60, 174–186, doi:10.1016/S0034-4257(96)00180-0, 1997.

Baghdadi, N., King, C., Chanzy, A., and Wigneron, J. P.: An empirical calibration of the integral equation model based on SAR data, soil moisture and surface roughness measurement over bare soils, Int. J. Remote Sens., 23, 4325–4340, doi:10.1080/01431160110107671, 2002.

Baghdadi, N., Gherboudj, I., Zribi, M., Sahebi, M., King, C., and Bonn, F.: Semi-empirical calibration of the IEM backscattering model using radar images and moisture and roughness field measurements, Int. J. Remote Sens., 25, 3593–3623, doi:10.1080/01431160310001654392, 2004.

Baghdadi, N., El Hajj, M., Dubois-Fernandez, P., Zribi, M., Belaud, G., and Cheviron, B.: Signal Level Comparison Between TerraSAR-X and COSMO-SkyMed SAR Sensors, IEEE Geosci. Remote Sens. Lett., 12, 448–452, doi:10.1109/LGRS.2014.2342733, 2015.

Baghdadi, N., El Hajj, M., Zribi, M., and Bousbih, S.: Calibration of the Water Cloud Model at C-Band for Winter Crop Fields and Grasslands, Remote Sens., 9, 969, doi:10.3390/rs9090969, 2017.

Baghdadi, N., Bazzi, H., El Hajj, M., and Zribi, M.: Detection of Frozen Soil Using Sentinel-1 SAR Data, Remote Sens., 10, 1182, doi:10.3390/rs10081182, 2018.

Bai, X., He, B., Li, X., Zeng, J., Wang, X., Wang, Z., Zeng, Y., and Su, Z.: First Assessment of Sentinel-1A Data for Surface Soil Moisture Estimations Using a Coupled Water Cloud Model and Advanced Integral Equation Model over the Tibetan Plateau, Remote Sens., 9, 714, doi:10.3390/rs9070714, 2017.

Bakke, S. J., Ionita, M., and Tallaksen, L. M.: The 2018 northern European hydrological drought and its drivers in a historical perspective, Hydrol. Earth Syst. Sci., 24, 5621–5653, doi:10.5194/hess-24-5621-2020, 2020.

Balenzano, A., Mattia, F., Satalino, G., Ouellette, J., and Johnson, J. T.: An experimental and theoretical study on the sensitivity of cross-polarized backscatter to soil moisture, in: 2012 IEEE International Geoscience and Remote Sensing Symposium, pp. 3411–3414, Munich, Germany, doi:10.1109/IGARSS.2012.6350688, 2012.

Balenzano, A., Mattia, F., Satalino, G., Lovergine, F. P., Palmisano, D., Peng, J., Marzahn, P., Wegmüller, U., Cartus, O., Dąbrowska-Zielińska, K., Musial, J. P., Davidson, M. W. J., Pauwels, V. R. N., Cosh, M. H., McNairn, H., Johnson, J. T., Walker, J. P., Yueh, S. H., Entekhabi, D., Kerr, Y. H., and Jackson, T. J.: Sentinel-1 soil moisture at 1 km resolution: a validation study, Remote Sens. Environ., 263, 112 554, doi:10.1016/j.rse.2021.112554, 2021.

Barber, M., Grings, F., Perna, P., Piscitelli, M., Maas, M., Bruscantini, C., Jacobo-Berlles, J., and Karszenbaum, H.: Speckle Noise and Soil Heterogeneities as Error Sources in a Bayesian Soil Moisture Retrieval Scheme for SAR Data, IEEE J. Sel. Top. Appl. Earth Obs. Remote Sens., 5, 942–951, doi:10.1109/JSTARS.2012.2191266, 2012.

Barrett, B. W., Dwyer, E., and Whelan, P.: Soil Moisture Retrieval from Active Spaceborne Microwave Observations: An Evaluation of Current Techniques, Remote Sens., 1, 210–242, doi:10.3390/rs1030210, 2009.

Bartalis, Z., Wagner, W., Naeimi, V., Hasenauer, S., Scipal, K., Bonekamp, H., Figa, J., and Anderson, C.: Initial soil moisture retrievals from the METOP-A Advanced Scatterometer (ASCAT), Geophys. Res. Lett., 34, L20 401, doi:10.1029/2007GL031088, 2007.

Batey, T.: Soil compaction and soil management - a review, Soil Use Manag., 25, 335–345, doi:10.1111/j.1475-2743.2009.00236.x, 2009.

Bauer-Marschallinger, B., Paulik, C., Hochstöger, S., Mistelbauer, T., Modanesi, S., Ciabatta, L., Massari, C., Brocca, L., and Wagner, W.: Soil Moisture from Fusion of Scatterometer and SAR: Closing the Scale Gap with Temporal Filtering, Remote Sens., 10, 1030, doi:10.3390/rs10071030, 2018.

Bauer-Marschallinger, B., Freeman, V., Cao, S., Paulik, C., Schaufler, S., Stachl, T., Modanesi, S., Massari, C., Ciabatta, L., Brocca, L., and Wagner, W.: Toward Global Soil Moisture Monitoring With Sentinel-1: Harnessing Assets and Overcoming Obstacles, IEEE Trans. Geosci. Remote Sens., 57, 520–539, doi:10.1109/TGRS.2018.2858004, 2019.

Bazzi, H., Baghdadi, N., El Hajj, M., Zribi, M., and Belhouchette, H.: A Comparison of Two Soil Moisture Products S^2MP and Copernicus-SSM Over Southern France, IEEE J. Sel. Top. Appl. Earth Obs. Remote Sens., 12, 3366–3375, doi:10.1109/jstars.2019.2927430, 2019.

Beck, H. E., De Jeu, R. A. M., Schellekens, J., Van Dijk, A. I. J. M., and Bruijnzeel, L. A.: Improving Curve Number Based Storm Runoff Estimates Using Soil Moisture Proxies, IEEE J. Sel. Top. Appl. Earth Obs. Remote Sens., 2, 250–259, doi:10.1109/JSTARS.2009.2031227, 2009.

Beck, H. E., Zimmermann, N. E., McVicar, T. R., Vergopolan, N., Berg, A., and Wood, E. F.: Present and future Köppen-Geiger climate classification maps at 1-km resolution, Sci. Data, 5, 180 214, doi:10.1038/sdata.2018.214, 2018.

Beck, H. E., Pan, M., Miralles, D. G., Reichle, R. H., Dorigo, W. A., Hahn, S., Sheffield, J., Karthikeyan, L., Balsamo, G., Parinussa, R. M., Van Dijk, A. I. J. M., Du, J., Kimball, J. S., Vergopolan, N., and Wood, E. F.: Evaluation of 18 satellite- and model-based soil moisture products using in situ measurements from 826 sensors, Hydrol. Earth Syst. Sci., 25, 17–40, doi:10.5194/hess-25-17-2021, 2021.

Benninga, H. F., Carranza, C. D. U., Pezij, M., Van der Ploeg, M. J., Augustijn, D. C. M., and Van der Velde, R.: Regional soil moisture monitoring network in the Raam catchment in the Netherlands – 2016-04/2017-04 (corrected). Dataset, 4TU.ResearchData, doi:10.4121/uuid:276a8c0e-c9a9-4fdf-916a-75cfe06fa974, 2018a.

Benninga, H. F., Carranza, C. D. U., Pezij, M., Van der Ploeg, M. J., Augustijn, D. C. M., and Van der Velde, R.: Regional soil moisture monitoring network in the Raam catchment in the Netherlands – 2017-04/2018-04. Dataset, 4TU.ResearchData, doi:10.4121/uuid:afb36ac8-e266-4968-8f76-0d1f6988e23d, 2018b.

Benninga, H. F., Carranza, C. D. U., Pezij, M., Van Santen, P., Van der Ploeg, M. J., Augustijn, D. C. M., and Van der Velde, R.: The Raam regional soil moisture monitoring network in the Netherlands, Earth Syst. Sci. Data, 10, 61–79, doi:10.5194/essd-10-61-2018, 2018c.

Benninga, H. F., Van der Velde, R., and Su, Z.: Impacts of Radiometric Uncertainty and Weather-Related Surface Conditions on Soil Moisture Retrievals with Sentinel-1, Remote Sens., 11, 2025, doi:10.3390/rs11172025, 2019.

Benninga, H. F., Carranza, C. D. U., Pezij, M., Van der Ploeg, M. J., Augustijn, D. C. M., and Van der Velde, R.: Regional soil moisture monitoring network in the Raam catchment in the Netherlands – 2018-04/2019-04. Dataset, 4TU.ResearchData, doi:10.4121/uuid:b68e3971-c73e-4d7f-b52f-9ef7d7fe1ed2, 2020a.

Benninga, H. F., Van der Velde, R., and Su, Z.: Sentinel-1 soil moisture content and its uncertainty over sparsely vegetated fields, J. Hydrol. X, 9, 100 066, doi:10.1016/j.hydroa.2020.100066, 2020b.

Benninga, H. F., Van der Velde, R., and Su, Z.: Supplementary data of 'Sentinel-1 soil moisture content and its uncertainty over sparsely vegetated fields'. Dataset, DANS, doi:10.17026/dans-xfs-3anu, 2020c.

Benninga, H. F., Van der Velde, R., and Su, Z.: Leaf area index field measurements. Dataset, DANS, doi:10.17026/dans-xxv-sdez, 2021a.

Benninga, H. F., Van der Velde, R., and Su, Z.: Supplementary data of 'Sentinel-1 soil moisture content retrieval over meadows using a physically based scattering model'. Dataset, DANS, doi:10.17026/dans-z9z-t36z, 2021b.

Benninga, H. F., Van der Velde, R., and Su, Z.: Sentinel-1 soil moisture content retrieval over meadows using a physically based scattering model, submitted.

Beven, K., Cloke, H., Pappenberger, F., Lamb, R., and Hunter, N.: Hyperresolution information and hyperresolution ignorance in modelling the hydrology of the land surface, Sci. China Earth Sci., 58, 25–35, doi:10.1007/s11430-014-5003-4, 2015.

Bircher, S., Skou, N., Jensen, K. H., Walker, J. P., and Rasmussen, L.: A soil moisture and temperature network for SMOS validation in Western Denmark, Hydrol. Earth Syst. Sci., 16, 1445–1463, doi:10.5194/hess-16-1445-2012, 2012.

Bloemberg-Van der Hulst, M.: Stuw helpt boer bij wateroverlast en verdroging (in Dutch), available online: `https://www.nieuweoogst.nl/nieuws/2021/07/31/stuw-helpt-boer-bij-wateroverlast-en-verdroging` (accessed on 31 Aug 2021), 2021.

Blume, H.-P. and Leinweber, P.: Plaggen Soils: landscape history, properties, and classification, J. Plant Nutr. Soil Sci., 167, 319–327, doi:10.1002/jpln.200420905, 2004.

Boé, J., Terray, L., Habets, F., and Martin, E.: Statistical and dynamical downscaling of the Seine basin climate for hydro-meteorological studies, Int. J. Climatol., 27, 1643–1655, doi:10.1002/joc.1602, 2007.

Bogena, H. R., Huisman, J. A., Oberdörster, C., and Vereecken, H.: Evaluation of a low-cost soil water content sensor for wireless network applications, J. Hydrol., 344, 32–42, doi:10.1016/j.jhydrol.2007.06.032, 2007.

Bogena, H. R., Herbst, M., Huisman, J. A., Rosenbaum, U., Weuthen, A., and Vereecken, H.: Potential of Wireless Sensor Networks for Measuring Soil Water Content Variability, Vadose Zo. J., 9, 1002–1013, doi:10.2136/vzj2009.0173, 2010.

Bogena, H. R., White, T., Bour, O., Li, X., and Jensen, K. H.: Toward Better Understanding of Terrestrial Processes through Long-Term Hydrological Observatories, Vadose Zo. J., 17, 180 194, doi:10.2136/vzj2018.10.0194, 2018.

Bosch, D. D., Sheridan, J. M., and Marshall, L. K.: Precipitation, soil moisture, and climate database, Little River Experimental Watershed, Georgia, United States, Water Resour. Res., 43, W09 472, doi:10.1029/2006WR005834, 2007.

Bougeault, P., Toth, Z., Bishop, C., Brown, B., Burridge, D., Chen, D. H., Ebert, B., Fuentes, M., Hamill, T. M., Mylne, K., Nicolau, J., Paccagnella, T., Park, Y. Y., Parsons, D., Raoult, B., Schuster, D., Dias, P. S., Swinbank, R., Takeuchi, Y., Tennant, W., Wilson, L., and Worley, S.: The THORPEX Interactive Grand Global Ensemble, Bull. Am. Meteorol. Soc., 91, 1059–1072, doi:10.1175/2010BAMS2853.1, 2010.

Bourbigot, M., Johnsen, H., Piantanida, R., Hajduch, G., and Poullaouec, J.: Sentinel-1 Product Definition (Document Number: S1-RS-MDA-52-7440), Tech. rep., ESA, available online: `https://sentinel.esa.int/documents/247904/1877131/Sentinel-1-Product-Definition` (accessed on 12 Aug 2019), 2016.

Bousbih, S., Zribi, M., Lili-Chabaane, Z., Baghdadi, N., El Hajj, M., Gao, Q., and Mougenot, B.: Potential of Sentinel-1 Radar Data for the Assessment of Soil and Cereal Cover Parameters, Sensors, 17, 2617, doi:10.3390/s17112617, 2017.

Bracaglia, M., Ferrazzoli, P., and Guerriero, L.: A Fully Polarimetric Multiple Scattering Model for Crops, Remote Sens. Environ., 54, 170–179, doi:10.1016/0034-4257(95)00151-4, 1995.

Brocca, L., Hasenauer, S., Lacava, T., Melone, F., Moramarco, T., Wagner, W., Dorigo, W., Matgen, P., Martínez-Fernández, J., Llorens, P., Latron, J., Martin, C., and Bittelli, M.: Soil moisture estimation through ASCAT and AMSR-E sensors: An intercomparison and validation study across Europe, Remote Sens. Environ., 115, 3390–3408, doi:10.1016/j.rse.2011.08.003, 2011.

Brooks, S. P. and Gelman, A.: General Methods for Monitoring Convergence of Iterative Simulations, J. Comput. Graph. Stat., 7, 434–455, doi:10.1080/10618600.1998.10474787, 1998.

Brutsaert, W.: Hydrology – An introduction, Cambridge University Press, Cambridge, UK, 1 edn., 2005.

Buitink, J., Swank, A. M., Van der Ploeg, M., Smith, N. E., Benninga, H. F., Van der Bolt, F., Carranza, C. D. U., Koren, G., Van der Velde, R., and Teuling, A. J.: Anatomy of the 2018 agricultural drought in the Netherlands using in situ soil moisture and satellite vegetation indices, Hydrol. Earth Syst. Sci., 24, 6021–6031, doi:10.5194/hess-24-6021-2020, 2020.

Buizza, R., Houtekamer, P. L., Toth, Z., Pellerin, G., Wei, M., and Zhu, Y.: A Comparison of the ECMWF, MSC, and NCEP Global Ensemble Prediction Systems, Mon. Weather Rev., 133, 1076–1097, doi:10.1175/MWR2905.1, 2005.

Buras, A., Rammig, A., and Zang, C. S.: Quantifying impacts of the 2018 drought on European ecosystems in comparison to 2003, Biogeosciences, 17, 1655–1672, doi:10.5194/bg-17-1655-2020, 2020.

Burgin, M. S., Colliander, A., Njoku, E. G., Chan, S. K., Cabot, F., Kerr, Y. H., Bindlish, R., Jackson, T. J., Entekhabi, D., and Yueh, S. H.: A Comparative Study of the SMAP Passive Soil Moisture Product With Existing Satellite-Based Soil Moisture Products, IEEE Trans. Geosci. Remote Sens., 55, 2959 – 2971, doi:10.1109/TGRS.2017.2656859, 2017.

Caldwell, T. G., Bongiovanni, T., Cosh, M. H., Jackson, T. J., Colliander, A., Abolt, C. J., Casteel, R., Larson, T., Scanlon, B. R., and Young, M. H.: The Texas Soil Observation Network: A Comprehensive Soil Moisture Dataset for Remote Sensing and Land Surface Model Validation, Vadose Zo. J., 18, 190 034, doi:10.2136/vzj2019.04.0034, 2019.

Callens, M., Verhoest, N. E. C., and Davidson, M. W. J.: Parameterization of tillage-induced single-scale soil roughness from 4-m profiles, IEEE Trans. Geosci. Remote Sens., 44, 878–888, doi:10.1109/TGRS.2005.860488, 2006.

Calvet, J.-C., Fritz, N., Froissard, F., Suquia, D., Petitpa, A., and Piguet, B.: In situ soil moisture observations for the CAL/VAL of SMOS: The SMOSMANIA network, in: 2007 IEEE International Geoscience and Remote Sensing Symposium, pp. 1196–1199, Barcelona, Spain, doi:10.1109/IGARSS.2007.4423019, 2007.

Campbell, J. E.: Dielectric Properties and Influence of Conductivity in Soils at One to Fifty Megahertz, Soil Sci. Soc. Am. J., 54, 332–341, doi:10.2136/sssaj1990.03615995005400020006x, 1990.

Carranza, C. D. U.: Investigating soil moisture dynamics for improved applications of radar satellites in agricultural water management, Phd, Wageningen University, doi:10.18174/532848, available online: https://edepot.wur.nl/532848 (accessed on 24 Aug 2021), 2021.

Carranza, C. D. U., Van der Ploeg, M. J., and Torfs, P. J. J. F.: Using lagged dependence to identify (de)coupled surface and subsurface soil moisture values, Hydrol. Earth Syst. Sci., 22, 2255–2267, doi:10.5194/hess-22-2255-2018, 2018.

Carranza, C. D. U., Benninga, H. F., Van der Velde, R., and Van der Ploeg, M. J.: Monitoring agricultural field trafficability using Sentinel-1, Agric. Water Manag., 224, 105 698, doi:10.1016/j.agwat.2019.105698, 2019.

Carrão, H., Russo, S., Sepulcre-Canto, G., and Barbosa, P.: An empirical standardized soil moisture index for agricultural drought assessment from remotely sensed data, Int. J. Appl. Earth Obs. Geoinf., 48, 74–84, doi:10.1016/j.jag.2015.06.011, 2016.

Casey, J. A., Howell, S. E. L., Tivy, A., and Haas, C.: Separability of sea ice types from wide swath C- and L-band synthetic aperture radar imagery acquired during the melt season, Remote Sens. Environ., 174, 314–328, doi:10.1016/j.rse.2015.12.021, 2016.

Cenci, L., Pulvirenti, L., Boni, G., Chini, M., Matgen, P., Gabellani, S., Squicciarino, G., and Pierdicca, N.: An evaluation of the potential of Sentinel 1 for improving flash flood predictions via soil moisture-data assimilation, Adv. Geosci., 44, 89–100, doi:10.5194/adgeo-44-89-2017, 2017.

Chambers, C. and Crawford, L.: Customer notification – Attention: 5TM, 5TE, and GS3 calibrations, Tech. rep., Decagon Devices, Inc., Pullman, WA USA, 2014.

Chan, S. K., Bindlish, R., O'Neill, P. E., Njoku, E., Jackson, T., Colliander, A., Chen, F., Burgin, M., Dunbar, S., Piepmeier, J., Yueh, S., Entekhabi, D., Cosh, M. H., Caldwell, T., Walker, J., Wu, X., Berg, A., Rowlandson, T., Pacheco, A., McNairn, H., Thibeault, M., Martinez-Fernandez, J., Gonzalez-Zamora, A., Seyfried, M., Bosch, D., Starks, P., Goodrich, D., Prueger, J., Palecki, M., Small, E. E., Zreda, M., Calvet, J.-C., Crow, W. T., and Kerr, Y.: Assessment of the SMAP Passive Soil Moisture Product, IEEE Trans. Geosci. Remote Sens., 54, 4994–5007, doi:10.1109/TGRS.2016.2561938, 2016.

Chan, S. K., Bindlish, R., O'Neill, P., Jackson, T., Njoku, E., Dunbar, S., Chaubell, J., Piepmeier, J., Yueh, S., Entekhabi, D., Colliander, A., Chen, F., Cosh, M. H., Caldwell, T., Walker, J., Berg, A., McNairn, H., Thibeault, M., Martínez-Fernández, J., Uldall, F., Seyfried, M., Bosch, D., Starks, P., Holifield Collins, C., Prueger, J., Van der Velde, R., Asanuma, J., Palecki, M., Small, E. E., Zreda, M., Calvet, J., Crow, W. T., and Kerr, Y.: Development and assessment of the SMAP enhanced passive soil moisture product, Remote Sens. Environ., 204, 931–941, doi:10.1016/j.rse.2017.08.025, 2018.

Chaubell, M. J., Yueh, S. H., Scott Dunbar, R., Colliander, A., Chen, F., Chan, S. K., Entekhabi, D., Bindlish, R., O'Neill, P. E., Asanuma, J., Berg, A. A., Bosch, D. D., Caldwell, T., Cosh, M. H., Collins, C. H., Martinez-Fernandez, J., Seyfried, M., Starks, P. J., Su, Z., Thibeault, M., and Walker, J.: Improved SMAP Dual-Channel Algorithm for the Retrieval of Soil Moisture, IEEE Trans. Geosci. Remote Sens., 58, 3894–3905, doi:10.1109/TGRS.2019.2959239, 2020.

Chen, F., Crow, W. T., Starks, P. J., and Moriasi, D. N.: Improving hydrologic predictions of a catchment model via assimilation of surface soil moisture, Adv. Water Resour., 34, 526–536, doi:10.1016/j.advwatres.2011.01.011, 2011.

Chiu, T. and Sarabandi, K.: Electromagnetic Scattering from Short Branching Vegetation, IEEE Trans. Geosci. Remote Sens., 38, 911–925, doi:10.1109/36.841974, 2000.

Cisneros Vaca, C. and Van der Tol, C.: Sensitivity of Sentinel-1 to Rain Stored in Temperate Forest, in: IGARSS 2018 - 2018 IEEE International Geoscience and Remote Sensing Symposium, pp. 5330–5333, Valencia, Spain, doi:10.1109/IGARSS.2018.8517859, 2018.

Cisneros Vaca, C., Van der Tol, C., and Ghimire, C. P.: The influence of long-term changes in canopy structure on rainfall interception loss: a case study in Speulderbos, the Netherlands, Hydrol. Earth Syst. Sci., 22, 3701–3719, doi:10.5194/hess-22-3701-2018, 2018.

Cloke, H. L. and Pappenberger, F.: Ensemble flood forecasting: A review, J. Hydrol., 375, 613–626, doi:10.1016/j.jhydrol.2009.06.005, 2009.

Cobos, D.: Application Note: Measurement Volume of Decagon Volumetric Water Content Sensors, Tech. rep., Decagon Devices, Inc., Pullman, WA USA, Available online: http://manuals.decagon.com/Application%20Notes/14955_VWC%20Sensor%20Measurement%20Volumes_Web.pdf (accessed on 13 Nov 2017), 2015.

Cobos, D. and Campbell, C.: Application Note: Correcting Temperature Sensitivity of ECH$_2$O Soil Moisture Sensors, Tech. rep., METER Group, Inc., Pullman, WA USA, available online: https://www.onsetcomp.com/files/15923-C%20Correcting%20Temperature%20Sensitivity%20of%20ECH2O%20Soil%20Moisture%20Sensors.pdf (accessed on 13 Nov 2017), 2016.

Cobos, D. R. and Chambers, C.: Application Note: Calibrating ECH2O Soil Moisture Sensors, Tech. rep., METER Group, Inc., Pullman, WA USA, available online: https://www.onsetcomp.com/files/15922-C%20Calibrating%20ECH2O%20Soil%20Moisture%20Sensors.pdf (accessed on 30 Sep 2021), 2010.

Colliander, A., Jackson, T. J., Bindlish, R., Chan, S., Das, N., Kim, S. B., Cosh, M. H., Dunbar, R. S., Dang, L., Pashaian, L., Asanuma, J., Aida, K., Berg, A., Rowlandson, T., Bosch, D., Caldwell, T., Caylor, K., Goodrich, D., al Jassar, H., Lopez-Baeza, E., Martínez-Fernández, J., González-Zamora, A., Livingston, S., McNairn, H., Pacheco, A., Moghaddam, M., Montzka, C., Notarnicola, C.,

Niedrist, G., Pellarin, T., Prueger, J., Pulliainen, J., Rautiainen, K., Ramos, J., Seyfried, M., Starks, P., Su, Z., Zeng, Y., Van der Velde, R., Thibeault, M., Dorigo, W., Vreugdenhil, M., Walker, J. P., Wu, X., Monerris, A., O'Neill, P. E., Entekhabi, D., Njoku, E. G., and Yueh, S.: Validation of SMAP surface soil moisture products with core validation sites, Remote Sens. Environ., 191, 215–231, doi:10.1016/j.rse.2017.01.021, 2017.

Conti, A.: Dew, in: Water Encyclopedia: Oceanography; Meteorology; Physics and Chemistry; Water Law; and Water History, Art, and Culture, edited by Lehr, J. H. and Keeley, J., pp. 200–201, John Wiley & Sons, Hoboken, NJ USA, 2005.

Copernicus: Copernicus Open Access Hub. Dataset, available online: `https://scihub.copernicus.eu/` (accessed on 28 Jun 2019), 2019.

Copernicus Global Land Service: Surface Soil Moisture, available online: `https://land.copernicus.eu/global/products/ssm` (accessed on 21 Jun 2021), 2021.

Copernicus Land Monitoring Service: High Resolution Layer Forest, Dominant Leaf Type 2012 and 2015. Dataset, available online: `https://land.copernicus.eu/pan-european/high-resolution-layers/forests/dominant-leaf-type/status-maps` (accessed on 13 Aug 2019), 2018.

Copernicus Land Monitoring Service: CORINE Land Cover 2012 and 2018. Dataset, available online: `https://land.copernicus.eu/pan-european/corine-land-cover` (accessed on 13 Aug 2019), 2019.

Cosh, M. H., Jackson, T. J., Bindlish, R., Famiglietti, J. S., and Ryu, D.: Calibration of an impedance probe for estimation of surface soil water content over large regions, J. Hydrol., 311, 49–58, doi:10.1016/j.jhydrol.2005.01.003, 2005.

Cosh, M. H., Jackson, T. J., Starks, P., and Heathman, G.: Temporal stability of surface soil moisture in the Little Washita River watershed and its applications in satellite soil moisture product validation, J. Hydrol., 323, 168–177, doi:10.1016/j.jhydrol.2005.08.020, 2006.

Cosh, M. H., Ochsner, T. E., McKee, L., Dong, J., Basara, J. B., Evett, S. R., Hatch, C. E., Small, E. E., Steele-Dunne, S. C., Zreda, M., and Sayde, C.: The Soil Moisture Active Passive Marena, Oklahoma, In Situ Sensor Testbed (SMAP-MOISST): Testbed Design and Evaluation of In Situ Sensors, Vadose Zo. J., 15, 1–11, doi:10.2136/vzj2015.09.0122, 2016.

Crow, W. T.: A Novel Method for Quantifying Value in Spaceborne Soil Moisture Retrievals, J. Hydrometeorol., 8, 56–67, doi:10.1175/JHM553.1, 2007.

Crow, W. T., Wagner, W., and Naeimi, V.: The Impact of Radar Incidence Angle on Soil-Moisture-Retrieval Skill, IEEE Geosci. Remote Sens. Lett., 7, 501–505, doi:10.1109/LGRS.2010.2040134, 2010.

Crow, W. T., Berg, A. A., Cosh, M. H., Loew, A., Mohanty, B. P., Panciera, R., de Rosnay, P., Ryu, D., and Walker, J. P.: Upscaling sparse ground-based soil moisture observations for the validation of coarse-resolution satellite soil moisture products, Rev. Geophys., 50, RG2002, doi:10.1029/2011RG000372, 2012.

Crow, W. T., Chen, F., Reichle, R. H., and Liu, Q.: L band microwave remote sensing and land data assimilation improve the representation of prestorm soil moisture conditions for hydrologic forecasting, Geophys. Res. Lett., 44, 5495–5503, doi:10.1002/2017GL073642, 2017.

Das, K. and Paul, P. K.: Present status of soil moisture estimation by microwave remote sensing, Cogent Geosci., 1, 1084669, doi:10.1080/23312041.2015.1084669, 2015.

Das, N. N. and Mohanty, B. P.: Root Zone Soil Moisture Assessment Using Remote Sensing and Vadose Zone Modeling, Vadose Zo. J., 5, 296–307, doi:10.2136/vzj2005.0033, 2006.

Das, N. N., Entekhabi, D., Njoku, E. G., Shi, J. J. C., Johnson, J. T., and Colliander, A.: Tests of the SMAP Combined Radar and Radiometer Algorithm Using Airborne Field Campaign Observations and Simulated Data, IEEE Trans. Geosci. Remote Sens., 52, 2018–2028, doi:10.1109/TGRS.2013.2257605, 2014.

Das, N. N., Entekhabi, D., Dunbar, R. S., Chaubell, M. J., Colliander, A., Yueh, S., Jagdhuber, T., Chen, F., Crow, W., O'Neill, P. E., Walker, J. P., Berg, A., Bosch, D. D., Caldwell, T., Cosh, M. H., Collins, C. H., Lopez-Baeza, E., and Thibeault, M.: The SMAP and Copernicus Sentinel 1A/B microwave active-passive high resolution surface soil moisture product, Remote Sens. Environ., 233, 111 380, doi:10.1016/j.rse.2019.111380, 2019.

Davidson, M., Gebert, N., and Giulicchi, L.: ROSE-L – the L-band SAR Mission for Copernicus, in: EUSAR21; 13th European Conference on Synthetic Aperture Radar, pp. 236–237, 2021.

Davies, B. E.: Loss-on-Ignition as an Estimate of Soil Organic Matter, Soil Sci. Soc. Am. J., 38, 150–151, doi:10.2136/sssaj1974.03615995003800010046x, 1974.

Davis Instruments: User Manual Rain Collector 7857 and 7857M, Tech. rep., Davis Instruments Corp., Hayward, CA USA, 2015.

De Bruin, H. A. R.: From Penman to Makkink, in: Evaporation and weather, edited by Hooghart, J. C., chap. 2, pp. 5–31, TNO Committee on Hydrological Research, The Hague, NL, 1987.

De Jong, J., Klaassen, W., and Ballast, A.: Rain Storage in Forests Detected with ERS Tandem Mission SAR, Remote Sens. Environ., 72, 170–180, doi:10.1016/S0034-4257(99)00100-5, 2000.

De Lange, W. J., Prinsen, G. F., Hoogewoud, J. C., Veldhuizen, A. A., Verkaik, J., Oude Essink, G. H. P., Van Walsum, P. E. V., Delsman, J. R., Hunink, J. C., Massop, H. T. L., and Kroon, T.: An operational, multi-scale, multi-model system for consensus-based, integrated water management and policy analysis: The Netherlands Hydrological Instrument, Environ. Model. Softw., 59, 98–108, doi:10.1016/j.envsoft.2014.05.009, 2014.

De Lannoy, G. J. M., Reichle, R. H., and Vrugt, J. A.: Uncertainty quantification of GEOS-5 L-band radiative transfer model parameters using Bayesian inference and SMOS observations, Remote Sens. Environ., 148, 146–157, doi:10.1016/j.rse.2014.03.030, 2014.

Decagon Devices: ECH$_2$O-TE/EC-TM - Water content, EC and Temperature Sensors - Operator's Manual, Tech. rep., Decagon Devices, Inc., Pullman, WA USA, available online: `http://manuals.decagon.com/Retired%20and%20Discontinued/Manuals/ECH2O-TEEC-TMv6-Operators-Manual-(discontinued).pdf` (accessed on 8 Sep 2021), 2008.

Delta-T Devices: ThetaProbe soil moisture sensor. Type ML2 User Manual, Tech. rep., Delta-T Devices Ltd, Burwell, UK, available online: `https://delta-t.co.uk/wp-content/uploads/2016/11/ML2-Thetaprobe-UM.pdf` (accessed on 2 Dec 2021), 1998.

Dente, L., Vekerdy, Z., Su, Z., and Wen, J.: Continuous in situ soil moisture measurements at Maqu site, Tech. rep., Strasbourg, France, 2009.

Dente, L., Vekerdy, Z., Su, Z., and Ucer, M.: Twente soil moisture and soil temperature monitoring network, Tech. rep., Faculty of Geo-Information

Science and Earth Observation (ITC), University of Twente, Enschede, NL, available online: https://www.itc.nl/library/papers_2011/scie/dente_twe.pdf (accessed on 27 Sep 2018), 2011.

Dente, L., Su, Z., and Wen, J.: Validation of SMOS Soil Moisture Products over the Maqu and Twente Regions, Sensors, 12, 9965–9986, doi:10.3390/s120809965, 2012.

Dente, L., Ferrazzoli, P., Su, Z., Van der Velde, R., and Guerriero, L.: Combined use of active and passive microwave satellite data to constrain a discrete scattering model, Remote Sens. Environ., 155, 222–238, doi:10.1016/j.rse.2014.08.031, 2014.

Dingman, S. L.: Physical Hydrology, Waveland Press, Long Grove, IL USA, 3 edn., 2015.

Dirmeyer, P. A., Gao, X., Zhao, M., Guo, Z., Oki, T., and Hanasaki, N.: GSWP-2: Multimodel Analysis and Implications for Our Perception of the Land Surface, Bull. Am. Meteorol. Soc., 87, 1381–1397, doi:10.1175/BAMS-87-10-1381, 2006.

Dobriyal, P., Qureshi, A., Badola, R., and Hussain, S. A.: A review of the methods available for estimating soil moisture and its implications for water resource management, J. Hydrol., 458-459, 110–117, doi:10.1016/j.jhydrol.2012.06.021, 2012.

Dobson, M. C., Ulaby, F. T., Hallikainen, M. T., and El-Rayes, M. A.: Microwave Dielectric Behavior of Wet Soil-Part II: Dielectric Mixing Models, IEEE Trans. Geosci. Remote Sens., GE-23, 35–46, doi:10.1109/TGRS.1985.289498, 1985.

Dobson, M. C., Pierce, L., McDonald, K., and Sharik, T.: Seasonal change in radar backscatter from mixed conifer and hardwood forests in northern Michigan, in: IGARSS'91 Remote Sensing: Global Monitoring for Earth Management, pp. 1121–1124, Espoo, Finland, doi:10.1109/igarss.1991.579268, 1991.

Dorigo, W., Himmelbauer, I., Aberer, D., Schremmer, L., Petrakovic, I., Zappa, L., Preimesberger, W., Xaver, A., Annor, F., Ardö, J., Baldocchi, D., Bitelli, M., Blöschl, G., Bogena, H., Brocca, L., Calvet, J.-C., Camarero, J. J., Capello, G., Choi, M., Cosh, M. C., van de Giesen, N., Hajdu, I., Ikonen, J., Jensen, K. H., Kanniah, K. D., de Kat, I., Kirchengast, G., Kumar Rai, P., Kyrouac, J., Larson, K., Liu, S., Loew, A., Moghaddam, M., Martínez Fernández, J., Mattar Bader, C., Morbidelli, R., Musial, J. P., Osenga, E., Palecki, M. A., Pellarin, T., Petropoulos, G. P., Pfeil, I., Powers, J., Robock, A., Rüdiger, C., Rummel, U., Strobel, M., Su, Z., Sullivan, R., Tagesson, T., Varlagin, A., Vreugdenhil, M., Walker, J., Wen, J., Wenger, F., Wigneron, J. P., Woods, M., Yang, K., Zeng, Y., Zhang, X., Zreda, M., Dietrich, S., Gruber, A., van Oevelen, P., Wagner, W., Scipal, K., Drusch, M., and Sabia, R.: The International Soil Moisture Network: serving Earth system science for over a decade, Hydrology and Earth System Sciences, 25, 5749–5804, doi:10.5194/hess-25-5749-2021, 2021.

Dorigo, W. A., Wagner, W., Hohensinn, R., Hahn, S., Paulik, C., Xaver, A., Gruber, A., Drusch, M., Mecklenburg, S., Van Oevelen, P., Robock, A., and Jackson, T.: The International Soil Moisture Network: a data hosting facility for global in situ soil moisture measurements, Hydrol. Earth Syst. Sci., 15, 1675–1698, doi:10.5194/hess-15-1675-2011, 2011.

Doubková, M., Van Dijk, A. I. J. M., Sabel, D., Wagner, W., and Blöschl, G.: Evaluation of the predicted error of the soil moisture retrieval from C-band SAR by comparison against modelled soil moisture estimates over Australia, Remote Sens. Environ., 120, 188–196, doi:10.1016/j.rse.2011.09.031, 2012.

Drusch, M., Wood, E. F., and Gao, H.: Observation operators for the direct assimilation of TRMM microwave imager retrieved soil moisture, Geophys. Res. Lett., 32, L15 403, doi:10.1029/2005GL023623, 2005.

Drusch, M., Del Bello, U., Carlier, S., Colin, O., Fernandez, V., Gascon, F., Hoersch, B., Isola, C., Laberinti, P., Martimort, P., Meygret, A., Spoto, F., Sy, O., Marchese, F., and Bargellini, P.: Sentinel-2: ESA's Optical High-Resolution Mission for GMES Operational Services, Remote Sens. Environ., 120, 25–36, doi:10.1016/j.rse.2011.11.026, 2012.

Dubois, P. C., Van Zyl, J., and Engman, T.: Measuring soil moisture with imaging radars, IEEE Trans. Geosci. Remote Sens., 33, 915–926, doi:10.1109/36.406677, 1995.

El Hajj, M., Baghdadi, N., Zribi, M., and Angelliaume, S.: Analysis of Sentinel-1 Radiometric Stability and Quality for Land Surface Applications, Remote Sens., 8, 406, doi:10.3390/rs8050406, 2016.

El Hajj, M., Baghdadi, N., Zribi, M., and Bazzi, H.: Synergic Use of Sentinel-1 and Sentinel-2 Images for Operational Soil Moisture Mapping at High Spatial Resolution over Agricultural Areas, Remote Sens., 9, 1292, doi:10.3390/rs9121292, 2017.

El Hajj, M., Baghdadi, N., Bazzi, H., and Zribi, M.: Penetration Analysis of SAR Signals in the C and L Bands for Wheat, Maize, and Grasslands, Remote Sens., 11, 31, doi:10.3390/rs11010031, 2019.

Entekhabi, D., Njoku, E. G., Houser, P., Spencer, M., Doiron, T., Kim, Y., Smith, J., Girard, R., Belair, S., Crow, W., Jackson, T. J., Kerr, Y. H., Kimball, J. S., Koster, R., McDonald, K. C., O'Neill, P. E., Pultz, T., Running, S. W., Shi, J., Wood, E., and Van Zyl, J.: The hydrosphere State (hydros) Satellite mission: an Earth system pathfinder for global mapping of soil moisture and land freeze/thaw, IEEE Trans. Geosci. Remote Sens., 42, 2184–2195, doi:10.1109/TGRS.2004.834631, 2004.

Entekhabi, D., Njoku, E. G., O'Neill, P., Kellogg, K. H., Crow, W. T., Edelstein, W. N., Entin, J., Goodman, S. D., Jackson, T. J., Johnson, J. T., Kimball, J. S., Piepmeier, J. R., Koster, R. D., Martin, N., McDonald, K., Moghaddam, M., Moran, M. S., Reichle, R., Shi, J., Spencer, M., Thurman, S. W., Tsang, L., and Van Zyl, J.: The Soil Moisture Active Passive (SMAP) Mission, Proc. IEEE, 98, 704–716, doi:10.1109/JPROC.2010.2043918, 2010a.

Entekhabi, D., Reichle, R. H., Koster, R. D., and Crow, W. T.: Performance Metrics for Soil Moisture Retrievals and Application Requirements, J. Hydrometeorol., 11, 832–840, doi:10.1175/2010JHM1223.1, 2010b.

Entekhabi, D., Yueh, S., O'Neill, P. E., Kellogg, K. H., Allen, A., Bindlish, R., Brown, M., Chan, S., Colliander, A., Crow, W. T., Das, N., De Lannoy, G., Dunbar, R. S., Edelstein, W. N., Entin, J. K., Escobar, V., Goodman, S. D., Jackson, T. J., Jai, B., Johnson, J., Kim, E., Kim, S., Kimball, J., Koster, R. D., Leon, A., McDonald, K. C., Moghaddam, M., Mohammed, P., Moran, S., Njoku, E. G., Piepmeier, J. R., Reichle, R., Rogez, F., Shi, J. C., Spencer, M. W., Thurman, S. W., Tsang, L., Van Zyl, J., Weiss, B., and West, R.: SMAP Handbook-Soil Moisture Active Passive: Mapping Soil Moisture and Freeze/Thaw from Space, Tech. rep., National Aeronautics and Space Administration (NASA) – Jet Propulsion Laboratory, Pasadena, CA USA, available online: `https://smap.jpl.nasa.gov/system/internal_resources/details/original/178_SMAP_Handbook_FINAL_1_JULY_2014_Web.pdf` (accessed on 28 Sep 2021), 2014.

Esch, T., Schenk, A., Ullmann, T., Thiel, M., Roth, A., and Dech, S.: Characterization of Land Cover Types in TerraSAR-X Images by Combined Analysis of Speckle Statistics and Intensity Information, IEEE Trans. Geosci. Remote Sens., 49, 1911–1925, doi:10.1109/TGRS.2010.2091644, 2011.

Escorihuela, M. J., Chanzy, A., Wigneron, J. P., and Kerr, Y. H.: Effective soil moisture sampling depth of L-band radiometry: A case study, Remote Sens. Environ., 114, 995–1001, doi:10.1016/j.rse.2009.12.011, 2010.

European Space Agency: Sentinel Application Platform (SNAP) V6.0, available online: `http://step.esa.int` (accessed on 8 Apr 2019), 2019.

Famiglietti, J. S., Ryu, D., Berg, A. A., Rodell, M., and Jackson, T. J.: Field observations of soil moisture variability across scales, Water Resour. Res., 44, W01 423, doi:10.1029/2006WR005804, 2008.

Fascetti, F., Pierdicca, N., and Pulvirenti, L.: Empirical fitting of forward backscattering models for multitemporal retrieval of soil moisture from radar data at L-band, J. Appl. Remote Sens., 11, 016 002, doi:10.1117/1.jrs.11.016002, 2017.

Feddes, R. A., Kowalik, P., Kolinska-Malinka, K., and Zaradny, H.: Simulation of field water uptake by plants using a soil water dependent root extraction function, J. Hydrol., 31, 13–26, doi:10.1016/0022-1694(76)90017-2, 1976.

Feddes, R. A., Kowalik, P. J., and Zaradny, H.: Simulation of field water use and crop yield, Centre for Agricultural Publishing and Documentation, Wageningen, NL, 1978.

Ferré, P. A. and Topp, G. C.: Methods for Measurement of Soil Water Content: Time Domain Reflectometry, in: Methods of Soil Analysis. Part 4 – Physical Methods, edited by Dane, J. H. and Topp, G. C., chap. 3.1.3.4, pp. 434–446, Soil Science Society of America Book Series, Madison, WI USA, 2002.

Fleming, S. W., Bourdin, D. R., Campbell, D., Stull, R. B., and Gardner, T.: Development and Operational Testing of a Super-Ensemble Artificial Intelligence Flood-Forecast Model for a Pacific Northwest River, J. Am. Water Resour. Assoc., 51, 502–512, doi:10.1111/jawr.12259, 2015.

Flemish Institute for Technological Research (VITO): VITO Product Distribution Portal. Dataset, available online: `https://www.vito-eodata.be/PDF/portal/Application.html` (accessed on 17 Sep 2019), 2019.

Ford, T. W., Harris, E., and Quiring, S. M.: Estimating root zone soil moisture using near-surface observations from SMOS, Hydrol. Earth Syst. Sci., 18, 139–154, doi:10.5194/hess-18-139-2014, 2014.

Frolking, S., Milliman, T., Palace, M., Wisser, D., Lammers, R., and Fahnestock, M.: Tropical forest backscatter anomaly evident in SeaWinds scatterometer morning overpass data during 2005 drought in Amazonia, Remote Sens. Environ., 115, 897–907, doi:10.1016/j.rse.2010.11.017, 2011.

Fung, A. K., Li, Z., and Chen, K. S.: Backscattering from a Randomly Rough Dielectric Surface, IEEE Trans. Geosci. Remote Sens., 30, 356–369, doi:10.1109/36.134085, 1992.

Gao, Q., Zribi, M., Escorihuela, M. J., and Baghdadi, N.: Synergetic Use of Sentinel-1 and Sentinel-2 Data for Soil Moisture Mapping at 100 m Resolution, Sensors, 17, 1966, doi:10.3390/s17091966, 2017.

Gash, J. H. C.: An analytical model of rainfall interception by forests, Q. J. R. Meteorol. Soc., 105, 43–55, doi:10.1002/qj.49710544304, 1979.

Gaskin, G. J. and Miller, J. D.: Measurement of Soil Water Content Using a Simplified Impedance Measuring Technique, J. Agric. Eng. Res., 63, 153–159, doi:10.1006/jaer.1996.0017, 1996.

Geological Survey of the Netherlands (GDN): DINOloket – Ondergrondgegevens. Dataset, available online: https://www.dinoloket.nl/ondergrondgegevens (accessed on 1 Jul 2021), 2021.

Gillespie, T. J., Brisco, B., Brown, R. J., and Sofko, G. J.: Radar Detection of a Dew Event in Wheat, Remote Sens. Environ., 33, 151–156, doi:10.1016/0034-4257(90)90026-I, 1990.

Gleason, M. L., Taylor, S. E., Loughin, T. M., and Koehler, K. J.: Development and Validation of an Empirical Model to Estimate the Duration of Dew Periods, Plant Dis., 78, 1011–1016, doi:10.1094/pd-78-1011, 1994.

Global Climate Observing System: Plan for the Global Climate Observing System (GCOS), Tech. rep., World Meteorological Organization, available online: https://library.wmo.int/doc_num.php?explnum_id=3852 (accessed on 1 Sep 2020), 1995.

Global Climate Observing System: Implementation Plan for the Global Observing System for Climate in support of the UNFCCC, Tech. rep., World Meteorological Organization, Geneva, Zwitzerland, available online: https://library.wmo.int/doc_num.php?explnum_id=3943 (accessed on 1 Sep 2020), 2004.

Global Climate Observing System: Implementation plan for the global observing system for climate in support of the UNFCCC, Tech. rep., World Meteorological Organization, available online: https://library.wmo.int/doc_num.php?explnum_id=3851 (accessed on 1 Sep 2020), 2010.

Global Climate Observing System: The Global Observing System For Climate: Implementation Needs, Tech. rep., World Meteorological Organization, Geneva, Zwitzerland, available online: https://library.wmo.int/doc_num.php?explnum_id=3417 (accessed on 9 Oct 2019), 2016.

Gruber, A., Scanlon, T., Van der Schalie, R., Wagner, W., and Dorigo, W.: Evolution of the ESA CCI Soil Moisture climate data records and their underlying merging methodology, Earth Syst. Sci. Data, 11, 717–739, doi:10.5194/essd-11-717-2019, 2019.

Gruber, A., De Lannoy, G., Albergel, C., Al-Yaari, A., Brocca, L., Calvet, J.-C., Colliander, A., Cosh, M., Crow, W., Dorigo, W., Draper, C., Hirschi, M., Kerr, Y., Konings, A., Lahoz, W., McColl, K., Montzka, C., Muñoz-Sabater, J., Peng, J., Reichle, R., Richaume, P., Rüdiger, C., Scanlon, T., Van der Schalie, R., Wigneron, J. P., and Wagner, W.: Validation practices for satellite soil moisture retrievals: What are (the) errors?, Remote Sens. Environ., 244, 111 806, doi:10.1016/j.rse.2020.111806, 2020.

Guerriero, L., Ferrazzoli, P., Vittucci, C., Rahmoune, R., Aurizzi, M., and Mattioni, A.: L-Band Passive and Active Signatures of Vegetated Soil: Simulations with a Unified Model, IEEE J. Sel. Top. Appl. Earth Obs. Remote Sens., 9, 2520–2531, doi:10.1109/JSTARS.2016.2570424, 2016.

Guo, S., Bai, X., Chen, Y., Zhang, S., Hou, H., Zhu, Q., and Du, P.: An Improved Approach for Soil Moisture Estimation in Gully Fields of the Loess Plateau Using Sentinel-1A Radar Images, Remote Sens., 11, 349, doi:10.3390/rs11030349, 2019.

Haddad, Z. S., Dubois, P., and Van Zyl, J. J.: Bayesian Estimation of Soil Parameters from Radar Backscatter Data, IEEE Trans. Geosci. Remote Sens., 34, 76–82, doi:10.1109/36.481895, 1996.

Hallikainen, M. T., Ulaby, F. T., Dobson, M. C., El-Rayes, M. A., and Wu, L.: Microwave Dielectric Behavior of Wet Soil-Part I: Empirical Models and Experimental Observations, IEEE Trans. Geosci. Remote Sens., GE-23, 25–34, doi:10.1109/TGRS.1985.289497, 1985.

Hamza, M. A. and Anderson, W. K.: Soil compaction in cropping systems: A review of the nature, causes and possible solutions, Soil Tillage Res., 82, 121–145, doi:10.1016/j.still.2004.08.009, 2005.

Hartemink, A. E. and De Bakker, H.: Classification Systems: Netherlands, in: Encyclopedia of Soil Science, edited by Lal, R., pp. 265–268, Taylor & Francis Group, Boca Raton, FL USA, 2 edn., doi:10.1081/E-ESS-120022907, 2006.

Havekes, H., Koster, M., Dekking, W., Uijterlinde, R., Wensink, W., and Walkier, R.: Water governance: The Dutch water authority model, Tech. rep., Dutch Water Authorities, The Hague, NL, available online: https://dutchwaterauthorities.com/wp-content/uploads/2021/05/The-Dutch-water-authority-model.pdf (accessed on 8 Sep 2021), 2017.

Hawkins, R. K., Attema, E., Crapolicchio, R., Lecomte, P., Closa, J., Meadows, P. J., and Srivastava, S. K.: Stability of Amazon Backscatter at C-Band: Spaceborne Results from ERS-1/2 and RADARSAT-1, in: Proceedings SAR Workshop CEOS Committee on Earth Observation Satellites, ESA, Toulouse, France, available online: https://earth.esa.int/eogateway/documents/20142/37627/p103.pdf (accessed on 27 Jun 2019), 1999.

He, L., Chen, J. M., and Chen, K.-S.: Simulation and SMAP Observation of Sun-Glint Over the Land Surface at the L-Band, IEEE Trans. Geosci. Remote Sens., 55, 2589–2604, doi:10.1109/TGRS.2017.2648502, 2017.

He, Y., Wetterhall, F., Cloke, H. L., Pappenberger, F., Wilson, M., Freer, J., and McGregor, G.: Tracking the uncertainty in flood alerts driven by grand ensemble weather predictions, Meteorol. Appl., 16, 91–101, doi:10.1002/met.132, 2009.

Heinen, M., Brouwer, F., Teuling, K., and Walvoort, D.: BOFEK2020 – Bodemfysische schematisatie van Nederland (in Dutch), Tech. rep., Wageningen Environmental Research, Wageningen, NL, doi:10.18174/541544, available online: https://www.wur.nl/nl/show/Bodemfysische-Eenhedenkaart-BOFEK2020.htm (accessed on 17 Jul 2021), 2021.

Henry, J.-B., Chastanet, P., Fellah, K., and Desnos, Y.-L.: Envisat multi-polarized ASAR data for flood mapping, Int. J. Remote Sens., 27, 1921–1929, doi:10.1080/01431160500486724, 2006.

Hoogsteen, M. J. J., Lantinga, E. A., Bakker, E. J., Groot, J. C. J., and Tittonell, P. A.: Estimating soil organic carbon through loss on ignition: effects of ignition conditions and structural water loss, Eur. J. Soil Sci., 66, 320–328, doi:10.1111/ejss.12224, 2015.

Hornacek, M., Wagner, W., Sabel, D., Truong, H.-L., Snoeij, P., Hahmann, T., Diedrich, E., and Doubková, M.: Potential for High Resolution Systematic Global Surface Soil Moisture Retrieval via Change Detection Using Sentinel-1, IEEE J. Sel. Top. Appl. Earth Obs. Remote Sens., 5, 1303–1311, doi:10.1109/JSTARS.2012.2190136, 2012.

Hornbuckle, B., Walker, V., Eichinger, B., Wallace, V., and Yildirim, E.: Soil surface roughness observed during SMAPVEX16-IA and its potential consequences for SMOS and SMAP, in: 2017 IEEE International Geoscience and Remote Sensing Symposium, pp. 2027–2030, Fort Worth, TX USA, doi:10.1109/IGARSS.2017.8127379, 2017.

Houser, P. R., De Lannoy, G. J. M., and Walker, J. P.: Hydrologic Data Assimilation, in: Approaches to Managing Disaster – Assessing Hazards, Emergencies and Disaster Impacts, edited by Tiefenbacher, J. P., chap. 3, pp. 41–64, InTech, doi:10.5772/31246, 2012.

Hoving, I. E., Van den Akker, J. J. H., Massop, H. T. L., Holshof, G. J., and Van Houwelingen, K.: Precisiewatermanagement op veenweidegrond met pompgestuurde onderwaterdrains (in Dutch), Tech. rep., Wageningen Livestock Research, Wageningen, NL, available online: https://edepot.wur.nl/461252 (accessed on 30 Aug 2021), 2018.

Huang, W., De Vries, B., Huang, C., Lang, M. W., Jones, J. W., Creed, I. F., and Carroll, M. L.: Automated Extraction of Surface Water Extent from Sentinel-1 Data, Remote Sens., 10, 797, doi:10.3390/rs10050797, 2018.

IEEE Standards Board: IEEE Standard Definitions of Terms for Radio Wave Propagation, Tech. rep., Institute of Electrical and Electronics Engineers, New York, NY USA, doi:10.1109/IEEESTD.1998.87897, 1997.

IEEE Standards Board: IEEE Standard Definitions of Terms for Radio Wave Propagation, Tech. rep., Institute of Electrical and Electronics Engineers, New York, NY USA, doi:10.1109/IEEESTD.2019.8657413, 2018.

Iida, S., Tanaka, T., and Sugita, M.: Change of interception process due to the succession from Japanese red pine to evergreen oak, J. Hydrol., 315, 154–166, doi:10.1016/j.jhydrol.2005.03.024, 2005.

Iida, S., Levia, D. F., Shimizu, A., Shimizu, T., Tamai, K., Nobuhiro, T., Kabeya, N., Noguchi, S., Sawano, S., and Araki, M.: Intrastorm scale rainfall interception dynamics in a mature coniferous forest stand, J. Hydrol., 548, 770–783, doi:10.1016/j.jhydrol.2017.03.009, 2017.

Ines, A. V. M., Das, N. N., Hansen, J. W., and Njoku, E. G.: Assimilation of remotely sensed soil moisture and vegetation with a crop simulation model for maize yield prediction, Remote Sens. Environ., 138, 149–164, doi:10.1016/j.rse.2013.07.018, 2013.

Jackisch, C., Germer, K., Graeff, T., Andrä, I., Schulz, K., Schiedung, M., Haller-Jans, J., Schneider, J., Jaquemotte, J., Helmer, P., Lotz, L., Bauer, A., Hahn, I., Šanda, M., Kumpan, M., Dorner, J., De Rooij, G., Wessel-Bothe, S., Kottmann, L., Schittenhelm, S., and Durner, W.: Soil moisture and matric potential – an open field comparison of sensor systems, Earth Syst. Sci. Data, 12, 683–697, doi:10.5194/essd-12-683-2020, 2020.

Jackson, T. J. and Moy, L.: Dew Effects on Passive Microwave Observations of Land Surfaces, Remote Sens. Environ., 70, 129–137, doi:10.1016/S0034-4257(99)00021-8, 1999.

Jackson, T. J. and Schmugge, T. J.: Passive microwave remote sensing system for soil moisture: some supporting research, IEEE Trans. Geosci. Remote Sens., 27, 225–235, doi:10.1109/36.20301, 1989.

Jansen, E., Van Schie, A., and Hoving, I. E.: Sturen met water levert veel op; meer dan bodemdaling (in Dutch), Bodem, pp. 26–29, available online: https://www.veenweiden.nl/wp-content/uploads/2015/09/Artikel-Sturen-met-Water-levert-veel-op-meer-dan-bodemdaling.pdf (accessed on 30 Aug 2021), 2017.

Joseph, A. T., Van der Velde, R., O'Neill, P. E., Lang, R. H., and Gish, T.: Soil Moisture Retrieval During a Corn Growth Cycle Using L-Band (1.6 GHz) Radar Observations, IEEE Trans. Geosci. Remote Sens., 46, 2365–2374, doi:10.1109/TGRS.2008.917214, 2008.

Joseph, A. T., Van der Velde, R., O'Neill, P. E., Lang, R., and Gish, T.: Effects of corn on C- and L-band radar backscatter: A correction method for soil moisture retrieval, Remote Sens. Environ., 114, 2417–2430, doi:10.1016/j.rse.2010.05.017, 2010.

Karthikeyan, L., Pan, M., Wanders, N., Kumar, D. N., and Wood, E. F.: Four decades of microwave satellite soil moisture observations: Part 1. A review of retrieval algorithms, Adv. Water Resour., 109, 106–120, doi:10.1016/j.advwatres.2017.09.006, 2017a.

Karthikeyan, L., Pan, M., Wanders, N., Kumar, D. N., and Wood, E. F.: Four decades of microwave satellite soil moisture observations: Part 2. Product validation and inter-satellite comparisons, Adv. Water Resour., 109, 236–252, doi:10.1016/j.advwatres.2017.09.010, 2017b.

Kellogg, K., Hoffman, P., Standley, S., Shaffer, S., Rosen, P., Edelstein, W., Dunn, C., Baker, C., Barela, P., Shen, Y., Guerrero, A. M., Xaypraseuth, P., Sagi, V. R., Sreekantha, C. V., Harinath, N., Kumar, R., Bhan, R., and Sarma, C. V. H. S.: NASA-ISRO Synthetic Aperture Radar (NISAR) Mission, in: 2020 IEEE Aerospace Conference, pp. 1–21, Big Sky, MT USA, doi:10.1109/AERO47225.2020.9172638, 2020.

Kerr, Y. H., Waldteufel, P., Wigneron, J.-P., Martinuzzi, J., Font, J., and Berger, M.: Soil moisture retrieval from space: The Soil Moisture and Ocean Salinity (SMOS) mission, IEEE Trans. Geosci. Remote Sens., 39, 1729–1735, doi:10.1109/36.942551, 2001.

Kerr, Y. H., Waldteufel, P., Wigneron, J.-P., Delwart, S., Cabot, F., Boutin, J., Escorihuela, M. J., Font, J., Reul, N., Gruhier, C., Juglea, S. E., Drinkwater, M. R., Hahne, A., Martín-Neira, M., and Mecklenburg, S.: The SMOS Mission: New Tool for Monitoring Key Elements of the Global Water Cycle, Proc. IEEE, 98, 666–687, doi:10.1109/jproc.2010.2043032, 2010.

Kerr, Y. H., Al-Yaari, A., Rodriguez-Fernandez, N., Parrens, M., Molero, B., Leroux, D., Bircher, S., Mahmoodi, A., Mialon, A., Richaume, P., Delwart, S., Al Bitar, A., Pellarin, T., Bindlish, R., Jackson, T. J., Rüdiger, C., Waldteufel, P., Mecklenburg, S., and Wigneron, J.-P.: Overview of SMOS performance in terms of global soil moisture monitoring after six years in operation, Remote Sens. Environ., 180, 40–63, doi:10.1016/j.rse.2016.02.042, 2016.

Kim, S., Liu, Y. Y., Johnson, F. M., Parinussa, R. M., and Sharma, A.: A global comparison of alternate AMSR2 soil moisture products: Why do they differ?, Remote Sens. Environ., 161, 43–62, doi:10.1016/j.rse.2015.02.002, 2015.

Kim, S.-B., Moghaddam, M., Tsang, L., Burgin, M., Xu, X., and Njoku, E. G.: Models of L-Band Radar Backscattering Coefficients Over Global Terrain for Soil Moisture Retrieval, IEEE Trans. Geosci. Remote Sens., 52, 1381–1396, doi:10.1109/TGRS.2013.2250980, 2014.

Kizito, F., Campbell, C. S., Campbell, G. S., Cobos, D. R., Teare, B. L., Carter, B., and Hopmans, J. W.: Frequency, electrical conductivity and temperature analysis of a low-cost capacitance soil moisture sensor, J. Hydrol., 352, 367–378, doi:10.1016/j.jhydrol.2008.01.021, 2008.

Knyazikhin, Y., Glassy, J., Privette, J. L., Tian, Y., Lotsch, A., Zhang, Y., Wang, Y., Morisette, J. T., Votava, P., Myneni, R. B., Nemani, R. R., and Running, S. W.: MODIS Leaf Area Index (LAI) and Fraction of Photosynthetically Active Radiation Absorbed by Vegetation (FPAR) Product (MOD15) Algorithm Theoretical Basis Document, Tech. rep., available online: `https://modis.gsfc.nasa.gov/data/atbd/atbd_mod15.pdf` (accessed on 9 Oct 2019), 1999.

Kornelsen, K. C. and Coulibaly, P.: Advances in soil moisture retrieval from synthetic aperture radar and hydrological applications, J. Hydrol., 476, 460–489, doi:10.1016/j.jhydrol.2012.10.044, 2013.

Kornelsen, K. C. and Coulibaly, P.: Reducing multiplicative bias of satellite soil moisture retrievals, Remote Sens. Environ., 165, 109–122, doi:10.1016/j.rse.2015.04.031, 2015.

Kosmas, C., Danalatos, N. G., Poesen, J., and Van Wesemael, B.: The effect of water vapour adsorption on soil moisture content under Mediterranean climatic conditions, Agric. Water Manag., 36, 157–168, doi:10.1016/S0378-3774(97)00050-4, 1998.

Kraft, C.: Constitutive Parameter Measurements of Fluids and Soil Between 500 kHz and 5MHz Using a Transmission Line Technique., J. Geophys. Res., 92, 10 650–10 656, doi:10.1029/jb092ib10p10650, 1987.

Lee, J. H. and Walker, J.: Inversion of soil roughness for estimating soil moisture from time-series Sentinel-1 backscatter observations over Yanco sites, Geocarto Int., doi:10.1080/10106049.2020.1805030, 2020.

Lee, J. H., Zhao, C., and Kerr, Y.: Stochastic Bias Correction and Uncertainty Estimation of Satellite-Retrieved Soil Moisture Products, Remote Sens., 9, 847, doi:10.3390/rs9080847, 2017.

Lee, J.-S.: Speckle suppression and analysis for synthetic aperture radar images, Opt. Eng., 25, 636–643, doi:10.1117/12.7973877, 1986.

Lei, F., Crow, W. T., Kustas, W. P., Dong, J., Yang, Y., Knipper, K. R., Anderson, M. C., Gao, F., Notarnicola, C., Greifeneder, F., McKee, L. M., Alfieri, J. G., Hain, C., and Dokoozlian, N.: Data assimilation of high-resolution thermal and radar remote sensing retrievals for soil moisture monitoring in a drip-irrigated vineyard, Remote Sens. Environ., 239, 111 622, doi:10.1016/j.rse.2019.111622, 2020.

LI-COR: LAI-2000 Plant Canopy Analyzer, Tech. rep., LI-COR, Inc., Lincoln, NE USA, available online: `https://www.licor.com/env/support/LAI-2000/home.html` (accessed on 9 Oct 2019), 1992.

LI-COR: FV2000 V1.0. The LAI-2000 Data File Viewer, LI-COR, Inc.. Lincoln, NE USA, 2004.

Lievens, H. and Verhoest, N. E. C.: Spatial and temporal soil moisture estimation from RADARSAT-2 imagery over Flevoland, The Netherlands, J. Hydrol., 456-457, 44–56, doi:10.1016/j.jhydrol.2012.06.013, 2012.

Lievens, H., Verhoest, N. E. C., De Keyser, E., Vernieuwe, H., Matgen, P., Álvarez-Mozos, J., and De Baets, B.: Effective roughness modelling as a tool for soil moisture retrieval from C- and L-band SAR, Hydrol. Earth Syst. Sci., 15, 151–162, doi:10.5194/hess-15-151-2011, 2011.

Link, M., Entekhabi, D., Jagdhuber, T., Ferrazzoli, P., Guerriero, L., Baur, M., and Ludwig, R.: Vegetation Effects on Covariations of L-Band Radiometer and C-Band/L-Band Radar Observations, in: IGARSS 2018 - 2018 IEEE International Geoscience and Remote Sensing Symposium, pp. 357–360, Valencia, Spain, doi:10.1109/igarss.2018.8519395, 2018.

Liu, Z., Li, P., and Yang, J.: Soil Moisture Retrieval and Spatiotemporal Pattern Analysis Using Sentinel-1 Data of Dahra, Senegal, Remote Sens., 9, 1197, doi:10.3390/rs9111197, 2017.

Lu, D., Ricciuto, D., Walker, A., Safta, C., and Munger, W.: Bayesian calibration of terrestrial ecosystem models: a study of advanced Markov chain Monte Carlo methods, Biogeosciences, 14, 4295–4314, doi:10.5194/bg-14-4295-2017, 2017.

Lunn, D., Jackson, C., Best, N., Thomas, A., and Spiegelhalter, D.: The BUGS Book. A Practical Introduction to Bayesian Analysis, CRC Press, Boca Raton, FL USA, 1 edn., 2013.

Lv, S., Zeng, Y., Wen, J., Zhao, H., and Su, Z.: Estimation of Penetration Depth from Soil Effective Temperature in Microwave Radiometry, Remote Sens., 10, 519, doi:10.3390/rs10040519, 2018.

Macdonald, H. C. and Waite, W. P.: Soil Moisture Detection with Imaging Radars, Water Resour. Res., 7, 100–110, doi:10.1029/WR007i001p00100, 1971.

Mahanama, S. P. P., Koster, R. D., Reichle, R. H., and Zubair, L.: The role of soil moisture initialization in subseasonal and seasonal streamflow prediction - A case study in Sri Lanka, Adv. Water Resour., 31, 1333–1343, doi:10.1016/j.advwatres.2008.06.004, 2008.

Maidment, D. R.: Handbook of Hydrology, McGraw-Hill, New York, NY USA, 1 edn., 1993.

Martínez-Fernández, J. and Ceballos, A.: Mean soil moisture estimation using temporal stability analysis, J. Hydrol., 312, 28–38, doi:10.1016/j.jhydrol.2005.02.007, 2005.

Massari, C., Brocca, L., Moramarco, T., Tramblay, Y., and Didon Lescot, J.-F.: Potential of soil moisture observations in flood modelling: Estimating initial conditions and correcting rainfall, Adv. Water Resour., 74, 44–53, doi:10.1016/j.advwatres.2014.08.004, 2014.

Massey, F. J.: The Kolmogorov-Smirnov Test for Goodness of Fit, J. Am. Stat. Assoc., 46, 68–78, doi:10.1080/01621459.1951.10500769, 1951.

Matula, S., Bát'ková, K., and Legese, W. L.: Laboratory Performance of Five Selected Soil Moisture Sensors Applying Factory and Own Calibration Equations for Two Soil Media of Different Bulk Density and Salinity Levels, Sensors, 16, 1912, doi:10.3390/s16111912, 2016.

Mätzler, C.: Applications of the interaction of microwaves with the natural snow cover, Remote Sens. Rev., 2, 259–387, doi:10.1080/02757258709532086, 1987.

McNairn, H., Jackson, T. J., Wiseman, G., Bélair, S., Berg, A., Bullock, P., Colliander, A., Cosh, M. H., Kim, S.-B., Magagi, R., Moghaddam, M., Njoku, E. G., Adams, J. R., Homayouni, S., Ojo, E. R., Rowlandson, T. L., Shang, J., Goïta, K., and Hosseini, M.: The Soil Moisture Active Passive Validation Experiment 2012 (SMAPVEX12): Prelaunch Calibration and Validation of the SMAP Soil Moisture Algorithms, IEEE Trans. Geosci. Remote Sens., 53, 2784–2801, doi:10.1109/TGRS.2014.2364913, 2015.

McNairn, H., Jackson, T. J., Powers, J., Bélair, S., Berg, A., Bullock, P., Colliander, A., Cosh, M. H., Kim, S. B., Magagi, R., Pacheco, A., and Merzouki, A.: SMAPVEX16-MB Experimental Plan, available online: `https://smap.jpl.nasa.gov/internal_resources/390/` (accessed on 27 Sep 2018), 2016.

Mecklenburg, S., Drusch, M., Kaleschke, L., Rodriguez-Fernandez, N., Reul, N., Kerr, Y., Font, J., Martin-Neira, M., Oliva, R., Daganzo-Eusebio, E., Grant, J. P., Sabia, R., Macelloni, G., Rautiainen, K., Fauste, J., de Rosnay, P., Munoz-Sabater, J., Verhoest, N., Lievens, H., Delwart, S., Crapolicchio, R., de la

Fuente, A., and Kornberg, M.: ESA's Soil Moisture and Ocean Salinity mission: From science to operational applications, Remote Sens. Environ., 180, 3–18, doi:10.1016/j.rse.2015.12.025, 2016.

Mengen, D., Montzka, C., Jagdhuber, T., Fluhrer, A., Brogi, C., Baum, S., Schüttemeyer, D., Bayat, B., Bogena, H., Coccia, A., Masalias, G., Trinkel, V., Jakobi, J., Jonard, F., Ma, Y., Mattia, F., Palmisano, D., Rascher, U., Satalino, G., Schumacher, M., Koyama, C., Schmidt, M., and Vereecken, H.: The SARsense Campaign: Air- and Space-Borne C- and L-band SAR for the Analysis of Soil and Plant Parameters in Agriculture, Remote Sens., 13, 825, doi:10.3390/rs13040825, 2021.

METER Group: 5TM, Tech. rep., METER Group, Inc., Pullman, WA USA, available online: `http://publications.metergroup.com/Manuals/20424_5TM_Manual_Web.pdf` (accessed on 8 Sep 2021), 2019.

Minasny, B. and McBratney, A. B.: Limited effect of organic matter on soil available water capacity, Eur. J. Soil Sci., 69, 39–47, doi:10.1111/ejss.12475, 2018.

Ministry of Economic Affairs and Climate Policy: Basisregistratie Gewaspercelen. Dataset, Publieke Dienstverlening Op de Kaart, available online: `https://www.pdok.nl/introductie/-/article/basisregistratie-gewaspercelen-brp-` (accessed on 25 Aug 2021), 2020.

Miralles, D. G., Nieto, R., McDowell, N. G., Dorigo, W. A., Verhoest, N. E. C., Liu, Y. Y., Teuling, A. J., Dolman, A. J., Good, S. P., and Gimeno, L.: Contribution of water-limited ecoregions to their own supply of rainfall, Environ. Res. Lett., 11, 124 007, doi:10.1088/1748-9326/11/12/124007, 2016.

Mironov, V. L., Kosolapova, L. G., and Fomin, S. V.: Physically and Mineralogically Based Spectroscopic Dielectric Model for Moist Soils, IEEE Trans. Geosci. Remote Sens., 47, 2059–2070, doi:10.1109/TGRS.2008.2011631, 2009.

Mironov, V. L., Kosolapova, L. G., Lukin, Y. I., Karavaysky, A. Y., and Molostov, I. P.: Temperature- and texture-dependent dielectric model for frozen and thawed mineral soils at a frequency of 1.4 GHz, Remote Sens. Environ., 200, 240–249, doi:10.1016/j.rse.2017.08.007, 2017.

Molijn, R. A., Iannini, L., Dekker, P. L., Magalhães, P. S. G., and Hanssen, R. F.: Vegetation Characterization through the Use of Precipitation-Affected SAR Signals, Remote Sens., 10, 1647, doi:10.3390/rs10101647, 2018.

Montzka, C., Bogena, H. R., Herbst, M., Cosh, M. H., Jagdhuber, T., and Vereecken, H.: Estimating the Number of Reference Sites Necessary for the Validation of Global Soil Moisture Products, IEEE Geosci. Remote Sens. Lett., 18, 1530–1534, doi:10.1109/lgrs.2020.3005730, 2020.

Moore, D. S., McCabe, G. P., and Craig, B. A.: Introduction to the Practice of Statistics, W.H. Freeman and Company, New York, NY USA, 9 edn., 2017.

Moreira, A., Krieger, G., Hajnsek, I., Papathanassiou, K., Younis, M., Lopez-Dekker, P., Huber, S., Villano, M., Pardini, M., Eineder, M., De Zan, F., and Parizzi, A.: Tandem-L: A Highly Innovative Bistatic SAR Mission for Global Observation of Dynamic Processes on the Earth's Surface, IEEE Geosci. Remote Sens. Mag., 3, 8–23, doi:10.1109/MGRS.2015.2437353, 2015.

Naeimi, V., Paulik, C., Bartsch, A., Wagner, W., Kidd, R., Park, S.-E., Elger, K., and Boike, J.: ASCAT Surface State Flag (SSF): Extracting Information on Surface Freeze/Thaw Conditions From Backscatter Data Using an Empirical Threshold-Analysis Algorithm, IEEE Trans. Geosci. Remote Sens., 50, 2566–2582, doi:10.1109/TGRS.2011.2177667, 2012.

Nagler, T. and Rott, H.: Retrieval of Wet Snow by Means of Multitemporal SAR Data, IEEE Trans. Geosci. Remote Sens., 38, 754–765, doi:10.1109/36.842004, 2000.

Nagler, T., Rott, H., Ripper, E., Bippus, G., and Hetzenecker, M.: Advancements for Snowmelt Monitoring by Means of Sentinel-1 SAR, Remote Sens., 8, 348, doi:10.3390/rs8040348, 2016.

Nguyen, H. H., Cho, S., Jeong, J., and Choi, M.: A D-vine copula quantile regression approach for soil moisture retrieval from dual polarimetric SAR Sentinel-1 over vegetated terrains, Remote Sens. Environ., 255, 112 283, doi:10.1016/j.rse.2021.112283, 2021.

Nieuwe Oogst: Besparen met Beregeningssignaal (in Dutch), available online: https://www.nieuweoogst.nl/nieuws/2015/05/16/besparen-met-beregeningssignaal (accessed on 22 Jul 2021), 2015.

Nolan, M. and Fatland, D. R.: Penetration Depth as a DInSAR Observable and Proxy for Soil Moisture, IEEE Trans. Geosci. Remote Sens., 41, 532–537, doi:10.1109/TGRS.2003.809931, 2003.

Notarnicola, C. and Posa, F.: Bayesian Algorithm for the Estimation of the Dielectric Constant From Active and Passive Remotely Sensed Data, IEEE Geosci. Remote Sens. Lett., 1, 179–183, doi:10.1109/LGRS.2004.827461, 2004.

Notarnicola, C., Angiulli, M., and Posa, F.: Use of Radar and Optical Remotely Sensed Data for Soil Moisture Retrieval Over Vegetated Areas, IEEE Trans. Geosci. Remote Sens., 44, 925–935, doi:10.1109/TGRS.2006.872287, 2006.

Oh, Y., Sarabandi, K., and Ulaby, F. T.: An Empirical Model and an Inversion Technique for Radar Scattering from Bare Soil Surfaces, IEEE Trans. Geosci. Remote Sens., 30, 370–381, doi:10.1109/36.134086, 1992.

Oh, Y., Sarabandi, K., and Ulaby, F. T.: Semi-empirical model of the ensemble-averaged differential Mueller matrix for microwave backscattering from bare soil surfaces, IEEE Trans. Geosci. Remote Sens., 40, 1348–1355, doi:10.1109/TGRS.2002.800232, 2002.

Owe, M., De Jeu, R., and Walker, J.: A methodology for surface soil moisture and vegetation optical depth retrieval using the microwave polarization difference index, IEEE Trans. Geosci. Remote Sens., 39, 1643–1654, doi:10.1109/36.942542, 2001.

Paepen, M. and Wens, D.: VITO Sentinel-2 Products User Manual, Tech. rep., VITO, available online: https://www.vito-eodata.be/PDF/image/VITO%20S2%20-%20Products_User_Manual_v1.0.pdf (accessed on 25 Nov 2021), 2017.

Palmisano, D., Balenzano, A., Satalino, G., Mattia, F., Pierdicca, N., and Monti-Guarnieri, A.: Sentinel-1 Sensitivity to Soil Moisture at High Incidence Angle and its Impact on Retrieval, in: IGARSS 2018 - 2018 IEEE International Geoscience and Remote Sensing Symposium, pp. 1430–1433, Valencia, Spain, doi:10.1109/IGARSS.2018.8518613, 2018.

Paloscia, S., Pettinato, S., Santi, E., Notarnicola, C., Pasolli, L., and Reppucci, A.: Soil moisture mapping using Sentinel-1 images: Algorithm and preliminary validation, Remote Sens. Environ., 134, 234–248, doi:10.1016/j.rse.2013.02.027, 2013.

Pandit, A., Sawant, S., Mohite, J., and Pappula, S.: A data-driven approach for bare surface soil moisture estimation using Sentinel-1 SAR data and ground observations, Geocarto Int., doi:10.1080/10106049.2020.1805028, 2020.

Pathe, C., Wagner, W., Sabel, D., Doubkova, M., and Basara, J. B.: Using ENVISAT ASAR Global Mode Data for Surface Soil Moisture Retrieval Over Oklahoma, USA, IEEE Trans. Geosci. Remote Sens., 47, 468–480, doi:10.1109/TGRS.2008.2004711, 2009.

Pauwels, V. R. N., Hoeben, R., Verhoest, N. E. C., and De Troch, F. P.: The importance of the spatial patterns of remotely sensed soil moisture in the improvement of discharge predictions for small-scale basins through data assimilation, J. Hydrol., 251, 88–102, doi:10.1016/S0022-1694(01)00440-1, 2001.

Pellikaan, F.: Grasseizoen 2017: lang, maar zonder groeispurt (in Dutch), Veeteelt, Oct 2, 46–47, available online: https://edepot.wur.nl/426132 (accessed on 25 Nov 2021), 2017.

Petropoulos, G. P., Ireland, G., and Barrett, B.: Surface soil moisture retrievals from remote sensing: Current status, products & future trends, Phys. Chem. Earth, Parts A/B/C, 83-84, 36–56, doi:10.1016/j.pce.2015.02.009, 2015.

Pezij, M.: Application of soil moisture information for operational water management, Phd, University of Twente, doi:10.3990/1.9789036549486, available online: https://ris.utwente.nl/ws/portalfiles/portal/256553120/Thesis_M_Pezij.pdf (accessed on 24 Aug 2021), 2020.

Pezij, M., Augustijn, D. C. M., Hendriks, D. M. D., and Hulscher, S. J. M. H.: The role of evidence-based information in regional operational water management in the Netherlands, Environ. Sci. Policy, 93, 75–82, doi:10.1016/j.envsci.2018.12.025, 2019a.

Pezij, M., Augustijn, D. C. M., Hendriks, D. M. D., Weerts, A. H., Hummel, S., Van der Velde, R., and Hulscher, S. J. M. H.: State updating of root zone soil moisture estimates of an unsaturated zone metamodel for operational water resources management, J. Hydrol. X, 4, 100 040, doi:10.1016/j.hydroa.2019.100040, 2019b.

Pezij, M., Augustijn, D. C. M., Hendriks, D. M. D., and Hulscher, S. J. M. H.: Applying transfer function-noise modelling to characterize soil moisture dynamics: a data-driven approach using remote sensing data, Environ. Model. Softw., 131, 104 756, doi:10.1016/j.envsoft.2020.104756, 2020.

Piccard, I., Swinnen, E., De Keukelaere, L., Van De Kerchove, R., and Eerens, H.: Terrascope Sentinel-2 Algorithm Theoretical Base Document S2 - NDVI & BIOPAR - V200, Tech. rep., VITO, available online: https://docs.terrascope.be/DataProducts/Sentinel-2/references/VITO_S2_ATBD_S2_NDVI_BIOPAR_V200.pdf (accessed on 25 Nov 2021), 2020.

Pierdicca, N., Pulvirenti, L., and Bignami, C.: Soil moisture estimation over vegetated terrains using multitemporal remote sensing data, Remote Sens. Environ., 114, 440–448, doi:10.1016/j.rse.2009.10.001, 2010.

Pierdicca, N., Pulvirenti, L., and Pace, G.: A Prototype Software Package to Retrieve Soil Moisture From Sentinel-1 Data by Using a Bayesian Multitemporal Algorithm, IEEE J. Sel. Top. Appl. Earth Obs. Remote Sens., 7, 153–166, doi:10.1109/JSTARS.2013.2257698, 2014.

Poe, G.: Remote Sensing Of The Near-Surface Moisture Profile Of Specular Soils With Multi-Frequency Microwave Radiometry, in: Proc. SPIE 0027; Remote Sensing of Earth Resources and the Environment, edited by Katz, Y. H., pp. 135–146, doi:10.1117/12.978140, 1972.

Pulvirenti, L., Squicciarino, G., Cenci, L., Boni, G., Pierdicca, N., Chini, M., Versace, C., and Campanella, P.: A surface soil moisture mapping service at national (Italian) scale based on Sentinel-1 data, Environ. Model. Softw., 102, 13–28, doi:10.1016/j.envsoft.2017.12.022, 2018.

Quets, J., De Lannoy, G. J. M., Al Yaari, A., Chan, S., Cosh, M. H., Gruber, A., Reichle, R. H., Van der Schalie, R., and Wigneron, J.-P.: Uncertainty in soil moisture retrievals: An ensemble approach using SMOS L-band microwave data, Remote Sens. Environ., 229, 133–147, doi:10.1016/j.rse.2019.05.008, 2019.

Rahman, M. M., Moran, M. S., Thoma, D. P., Bryant, R., Holifield Collins, C. D., Jackson, T., Orr, B. J., and Tischler, M.: Mapping surface roughness and soil moisture using multi-angle radar imagery without ancillary data, Remote Sens. Environ., 112, 391–402, doi:10.1016/j.rse.2006.10.026, 2008.

Raj, R., Van der Tol, C., Hamm, N. A. S., and Stein, A.: Bayesian integration of flux tower data into a process-based simulator for quantifying uncertainty in simulated output, Geosci. Model Dev., 11, 83–101, doi:10.5194/gmd-11-83-2018, 2018.

Rao, P. S., Gillespie, T. J., and Schaafsma, A. W.: Estimating wetness duration on maize ears from meteorological observations, Can. J. Soil Sci., 78, 149–154, doi:10.4141/s97-012, 1998.

Reichle, R. H.: Data assimilation methods in the Earth sciences, Adv. Water Resour., 31, 1411–1418, doi:10.1016/j.advwatres.2008.01.001, 2008.

Reichle, R. H. and Koster, R. D.: Bias reduction in short records of satellite soil moisture, Geophys. Res. Lett., 31, L19 501, doi:10.1029/2004GL020938, 2004.

Riedel, T., Pathe, C., Thiel, C., Herold, M., and Schmullius, C.: Systematic investigation on the effect of dew and interception on multifrequency and multipolarimetric radar backscatter signals, in: Proceedings of the Third International Symposium on Retrieval of Bio- and Geophysical Parameters from SAR Data for Land Applications, edited by Wilson, A., pp. 99–104, ESA, Sheffield, UK, 2002.

Robinson, D. A., Campbell, C. S., Hopmans, J. W., Hornbuckle, B. K., Jones, S. B., Knight, R., Ogden, F., Selker, J., and Wendroth, O.: Soil Moisture Measurement for Ecological and Hydrological Watershed-Scale Observatories: A Review, Vadose Zo. J., 7, 358–389, doi:10.2136/vzj2007.0143, 2008.

Robock, A., Vinnikov, K. Y., Srinivasan, G., Entin, J. K., Hollinger, S. E., Speranskaya, N. A., Liu, S., and Namkhai, A.: The Global Soil Moisture Data Bank, Bull. Am. Meteorol. Soc., 81, 1281–1299, doi:10.1175/1520-0477(2000)081<1281:TGSMDB>2.3.CO;2, 2000.

Rondinelli, W. J., Hornbuckle, B. K., Patton, J. C., Cosh, M. H., Walker, V. A., Carr, B. D., and Logsdon, S. D.: Different Rates of Soil Drying After Rainfall are Observed by the SMOS Satellite and the South Fork In Situ Soil Moisture Network, J. Hydrometeorol., 16, 889–903, doi:10.1175/JHM-D-14-0137.1, 2015.

Rosenbaum, U., Huisman, J. A., Weuthen, A., Vereecken, H., and Bogena, H. R.: Sensor-to-Sensor Variability of the ECH_2O EC-5, TE, and 5TE Sensors in Dielectric Liquids, Vadose Zo. J., 9, 181–186, doi:10.2136/vzj2009.0036, 2010.

Rosenbaum, U., Huisman, J. A., Vrba, J., Vereecken, H., and Bogena, H. R.: Correction of Temperature and Electrical Conductivity Effects on Dielectric Permittivity Measurements with ECH_2O Sensors, Vadose Zo. J., 10, 582–593, doi:10.2136/vzj2010.0083, 2011.

Royal Netherlands Meteorological Institute (KNMI): Klimatologie - Metingen en waarnemingen. Dataset, available online: http://www.knmi.nl/nederland-nu/klimatologie-metingen-en-waarnemingen (accessed on 17 May 2017), 2017.

Royal Netherlands Meteorological Institute (KNMI): Klimatologie - Metingen en waarnemingen. Dataset, available online: http://www.knmi.nl/nederland-nu/klimatologie-metingen-en-waarnemingen (accessed on 7 Apr 2019), 2019.

Royal Netherlands Meteorological Institute (KNMI): Klimatologie - Metingen en waarnemingen. Dataset, available online: http://www.knmi.nl/nederland-nu/klimatologie-metingen-en-waarnemingen (accessed on 31 Mar 2021), 2021.

Ryu, D. and Famiglietti, J. S.: Characterization of footprint-scale surface soil moisture variability using Gaussian and beta distribution functions during the Southern Great Plains 1997 (SGP97) hydrology experiment, Water Resour. Res., 41, W12 433, doi:10.1029/2004WR003835, 2005.

Sakaki, T., Limsuwat, A., Smits, K. M., and Illangasekare, T. H.: Empirical two-point α-mixing model for calibrating the ECH_2O EC-5 soil moisture sensor in sands, Water Resour. Res., 44, W00D08, doi:10.1029/2008WR006870, 2008.

Satalino, G., Mattia, F., Davidson, M. W. J., Le Toan, T., Pasquariello, G., and Borgeaud, M.: On Current Limits of Soil Moisture Retrieval From ERS-SAR Data, IEEE Trans. Geosci. Remote Sens., 40, 2438–2447, doi:10.1109/TGRS.2002.803790, 2002.

Scharnagl, B., Vrugt, J. A., Vereecken, H., and Herbst, M.: Inverse modelling of in situ soil water dynamics: investigating the effect of different prior distributions of the soil hydraulic parameters, Hydrol. Earth Syst. Sci., 15, 3043–3059, doi:10.5194/hess-15-3043-2011, 2011.

Schmidt, K., Tous Ramon, N., and Schwerdt, M.: Radiometric accuracy and stability of sentinel-1A determined using point targets, Int. J. Microw. Wirel. Technol., 10, 538–546, doi:10.1017/S1759078718000016, 2018.

Schmugge, T., Gloersen, P., Wilheit, T., and Geiger, F.: Remote Sensing of Soil Moisture With Microwave Radiometers, J. Geophys. Res., 79, 317–323, doi:10.1029/JB079i002p00317, 1974.

Schoups, G. and Vrugt, J. A.: A formal likelihood function for parameter and predictive inference of hydrologic models with correlated, heteroscedastic, and non-Gaussian errors, Water Resour. Res., 46, W10 531, doi:10.1029/2009WR008933, 2010.

Schwerdt, M., Schmidt, K., Tous Ramon, N., Klenk, P., Yague-Martinez, N., Prats-Iraola, P., Zink, M., and Geudtner, D.: Independent System Calibration of Sentinel-1B, Remote Sens., 9, 511, doi:10.3390/rs9060511, 2017.

Schwilch, G., Bernet, L., Fleskens, L., Giannakis, E., Leventon, J., Marañón, T., Mills, J., Short, C., Stolte, J., Van Delden, H., and Verzandvoort, S.: Operationalizing ecosystem services for the mitigation of soil threats: A proposed framework, Ecol. Indic., 67, 568–597, doi:10.1016/j.ecolind.2016.03.016, 2016.

Seneviratne, S. I., Corti, T., Davin, E. L., Hirschi, M., Jaeger, E. B., Lehner, I., Orlowsky, B., and Teuling, A. J.: Investigating soil moisture-climate interactions in a changing climate: A review, Earth-Science Rev., 99, 125–161, doi:10.1016/j.earscirev.2010.02.004, 2010.

Seyfried, M. S. and Murdock, M. D.: Measurement of Soil Water Content with a 50-MHz Soil Dielectric Sensor, Soil Sci. Soc. Am. J., 68, 394–403, doi:10.2136/sssaj2004.0394, 2004.

Shellito, P. J., Small, E. E., Colliander, A., Bindlish, R., Cosh, M. H., Berg, A. A., Bosch, D. D., Caldwell, T. G., Goodrich, D. C., McNairn, H., Prueger, J. H., Starks, P. J., Van der Velde, R., and Walker, J. P.: SMAP soil moisture drying more rapid than observed in situ following rainfall events, Geophys. Res. Lett., 43, 8068–8075, doi:10.1002/2016GL069946, 2016.

Singh, A., Gaurav, K., Meena, G. K., and Kumar, S.: Estimation of Soil Moisture Applying Modified Dubois Model to Sentinel-1; A regional Study from Central India, Remote Sens., 12, 2266, doi:10.3390/rs12142266, 2020.

Smith, A. B., Walker, J. P., Western, A. W., Young, R. I., Ellett, K. M., Pipunic, R. C., Grayson, R. B., Siriwardena, L., Chiew, F. H. S., and Richter, H.: The Murrumbidgee soil moisture monitoring network data set, Water Resour. Res., 48, W07 701, doi:10.1029/2012WR011976, 2012.

Srivastava, P. K.: Satellite Soil Moisture: Review of Theory and Applications in Water Resources, Water Resour. Manag., 31, 3161–3176, doi:10.1007/s11269-017-1722-6, 2017.

Srivastava, P. K., Han, D., Rico-Ramirez, M. A., O'Neill, P., Islam, T., Gupta, M., and Dai, Q.: Performance evaluation of WRF-Noah Land surface model estimated soil moisture for hydrological application: Synergistic evaluation using SMOS retrieved soil moisture, J. Hydrol., 529, 200–212, doi:10.1016/j.jhydrol.2015.07.041, 2015.

Starr, J. L. and Paltineanu, I. C.: Methods for Measurement of Soil Water Content: Capacitance Devices, in: Methods of Soil Analysis. Part 4 – Physical Methods, edited by Dane, J. H. and Topp, G. C., chap. 3.1.3.6, pp. 463–474, Soil Science Society of America Book Series, Madison, WI USA, 2002.

Statistics Netherlands: Bestand bodemgebruik. Dataset, available online: https://www.cbs.nl/nl-nl/dossier/nederland-regionaal/geografische-data/natuur-en-milieu/bestand-bodemgebruik (accessed on 28 Jan 2021), 2015.

Steele-Dunne, S. C., Friesen, J., and Van de Giesen, N.: Using Diurnal Variation in Backscatter to Detect Vegetation Water Stress, IEEE Trans. Geosci. Remote Sens., 50, 2618–2629, doi:10.1109/TGRS.2012.2194156, 2012.

Steele-Dunne, S. C., McNairn, H., Monsivais-Huertero, A., Judge, J., Liu, P.-W., and Papathanassiou, K.: Radar Remote Sensing of Agricultural Canopies: A Review, IEEE J. Sel. Top. Appl. Earth Obs. Remote Sens., 10, 2249–2273, doi:10.1109/JSTARS.2016.2639043, 2017.

Stevens Water Monitoring Systems: HydraProbe (AKA Hydra Probe II) and HydraProbe Analog, Tech. rep., Stevens Water Monitoring Systems, Inc., Portland, OR USA, available online: https://stevenswater.zendesk.com/hc/en-us/articles/360034649013-HydraProbe-AKA-Hydra-Probe-II-and-HydraProbe-Analog (accessed on 17 Nov 2020), 2020.

Stiles, J. M., Sarabandi, K., and Ulaby, F. T.: Electromagnetic Scattering from Grassland — Part II : Measurement and Modeling Results, IEEE Trans. Geosci. Remote Sens., 38, 349–356, doi:10.1109/36.823930, 2000.

Su, C.-H., Ryu, D., Crow, W. T., and Western, A. W.: Beyond triple collocation: Applications to soil moisture monitoring, J. Geophys. Res. Atmos., 119, 6419–6439, doi:10.1002/2013JD021043, 2014.

Su, Z., Troch, P. A., and De Troch, F. P.: Remote sensing of bare surface soil moisture using EMAC/ESAR data, Int. J. Remote Sens., 18, 2105–2124, doi:10.1080/014311697217783, 1997.

Su, Z., Wen, J., Dente, L., Van der Velde, R., Wang, L., Ma, Y., Yang, K., and Hu, Z.: The Tibetan Plateau observatory of plateau scale soil moisture and soil temperature (Tibet-Obs) for quantifying uncertainties in coarse resolution satellite and model products, Hydrol. Earth Syst. Sci., 15, 2303–2316, doi:10.5194/hess-15-2303-2011, 2011.

Sutanudjaja, E. H., De Jong, S. M., Van Geer, F. C., and Bierkens, M. F. P.: Using ERS spaceborne microwave soil moisture observations to predict groundwater head in space and time, Remote Sens. Environ., 138, 172–188, doi:10.1016/j.rse.2013.07.022, 2013.

Tesemma, Z. K., Wei, Y., Western, A. W., and Peel, M. C.: Leaf Area Index Variation for Crop, Pasture, and Tree in Response to Climatic Variation in the Goulburn–Broken Catchment, Australia, J. Hydrometeorol., 15, 1592–1606, doi:10.1175/JHM-D-13-0108.1, 2014.

Tetlock, E., Toth, B., Berg, A., Rowlandson, T., and Ambadan, J. T.: An 11-year (2007-2017) soil moisture and precipitation dataset from the Kenaston Network in the Brightwater Creek basin, Saskatchewan, Canada, Earth Syst. Sci. Data, 11, 787–796, doi:10.5194/essd-11-787-2019, 2019.

Thiel, D. V.: Using the Right Terms [Stand on Standards], IEEE Antennas Propag. Mag., 52, 192–193, doi:10.1109/MAP.2010.5687535, 2010.

Thyer, M., Renard, B., Kavetski, D., Kuczera, G., Franks, S. W., and Srikanthan, S.: Critical evaluation of parameter consistency and predictive uncertainty in hydrological modeling: A case study using Bayesian total error analysis, Water Resour. Res., 45, W00B14, doi:10.1029/2008WR006825, 2009.

Topp, G. C. and Ferré, P. A.: Water Content: General Information, in: Methods of Soil Analysis. Part 4 – Physical Methods, edited by Dane, J. H. and Topp, G. C., chap. 3, pp. 434–446, Soil Science Society of America Book Series, Madison, WI USA, 2002a.

Topp, G. C. and Ferré, P. A.: Methods for Measurement of Soil Water Content: Thermogravimetric Using Convective Oven-Drying, in: Methods of Soil Analysis. Part 4 – Physical Methods, edited by Dane, J. H. and Topp, G. C., chap. 3.1.3.1, pp. 422–424, Soil Science Society of America Book Series, Madison, WI USA, 2002b.

Topp, G. C. and Ferré, P. A.: Methods for Measurement of Soil Water Content: The Basis of Electromagnetic Methods: A Wave Equation Framework, in: Methods of Soil Analysis. Part 4 – Physical Methods, edited by Dane, J. H. and Topp, G. C., chap. 3.1.3.3, pp. 434–446, Soil Science Society of America Book Series, Madison, WI USA, 2002c.

Topp, G. C., Davis, J. L., and Annan, A. P.: Electromagnetic determination of soil water content: Measurements in coaxial transmission lines, Water Resour. Res., 16, 574–582, doi:10.1029/WR016i003p00574, 1980.

Torres, R., Snoeij, P., Geudtner, D., Bibby, D., Davidson, M., Attema, E., Potin, P., Rommen, B., Floury, N., Brown, M., Traver, I. N., Deghaye, P., Duesmann, B., Rosich, B., Miranda, N., Bruno, C., L'Abbate, M., Croci, R., Pietropaolo, A., Huchler, M., and Rostan, F.: GMES Sentinel-1 mission, Remote Sens. Environ., 120, 9–24, doi:10.1016/j.rse.2011.05.028, 2012.

Touzi, R.: A Review of Speckle Filtering in the Context of Estimation Theory, IEEE Trans. Geosci. Remote Sens., 40, 2392–2404, doi:10.1109/TGRS.2002.803727, 2002.

Ulaby, F.: Radar measurement of soil moisture content, IEEE Trans. Antennas Propag., 22, 257–265, doi:10.1109/TAP.1974.1140761, 1974.

Ulaby, F. T. and Long, D. G.: Microwave Radar and Radiometric Remote Sensing, The University of Michigan Press, Ann Arbor, MI USA, 1 edn., 2014.

Ulaby, F. T. and Stiles, W. H.: Microwave response of snow, Adv. Sp. Res., 1, 131–149, doi:10.1016/0273-1177(81)90389-6, 1981.

Ulaby, F. T., Bradley, G. A., and Obson, M. C.: Microwave Backscatter Dependence on Surface Roughness, Soil Moisture, and Soil Texture: Part II–Vegetation-Covered Soil, IEEE Trans. Geosci. Electron., 17, 33–40, doi:10.1109/TGE.1979.294626, 1979.

Ulaby, F. T., Whitt, M. W., and Dobson, M. C.: Measuring the Propagation Properties of a Forest Canopy Using a Polarimetric Scatterometer, IEEE Trans. Antennas Propag., 38, 251–258, doi:10.1109/8.45128, 1990.

Ulaby, F. T., Dubois, P. C., and Van Zyl, J.: Radar mapping of surface soil moisture, J. Hydrol., 184, 57–84, doi:10.1016/0022-1694(95)02968-0, 1996.

U.S. Department of Agriculture: Soil Climate Analysis Network (SCAN), Tech. rep., National Water and Climate Center and Natural Resources Conservation Service, available online: `https://www.wcc.nrcs.usda.gov/scan/scan_brochure.pdf` (accessed on 13 Nov 2017), 2016.

Vachaud, G., Passerat De Silans, A., Balabanis, P., and Vauclin, M.: Temporal Stability of Spatially Measured Soil Water Probability Density Function, Soil Sci. Soc. Am. J., 49, 822–828, doi:10.2136/sssaj1985.03615995004900040006x, 1985.

Van der Velde, R.: Soil moisture remote sensing using active microwaves and land surface modeling, Phd, University of Twente, available online: `http://itc.nl/library/papers_2010/phd/vd_velde.pdf` (accessed on 3 Nov 2015), 2010.

Van der Velde, R. and Benninga, H. F.: Ten years profile soil moisture and temperature measurements in Twente. Dataset, DANS, doi:10.17026/dans-zrn-n8nh, 2020.

Van der Velde, R. and Benninga, H. F.: Twelve years profile soil moisture and temperature measurements in Twente, the Netherlands, in preparation.

Van der Velde, R. and Su, Z.: Dynamics in land-surface conditions on the Tibetan Plateau observed by Advanced Synthetic Aperture Radar (ASAR), Hydrol. Sci. J., 54, 1079–1093, doi:10.1623/hysj.54.6.1079, 2009.

Van der Velde, R., Salama, M. S., Van Helvoirt, M. D., Su, Z., and Ma, Y.: Decomposition of Uncertainties between Coarse MM5-Noah-Simulated and Fine ASAR-Retrieved Soil Moisture over Central Tibet, J. Hydrometeorol., 13, 1925–1938, doi:10.1175/JHM-D-11-0133.1, 2012a.

Van der Velde, R., Su, Z., Van Oevelen, P., Wen, J., Ma, Y., and Salama, M. S.: Soil moisture mapping over the central part of the Tibetan Plateau using a series of ASAR WS images, Remote Sens. Environ., 120, 175–187, doi:10.1016/j.rse.2011.05.029, 2012b.

Van der Velde, R., Salama, M. S., Eweys, O. A., Wen, J., and Wang, Q.: Soil Moisture Mapping Using Combined Active/Passive Microwave Observations Over the East of the Netherlands, IEEE J. Sel. Top. Appl. Earth Obs. Remote Sens., 8, 4355–4372, doi:10.1109/JSTARS.2014.2353692, 2015.

Van der Velde, R., Colliander, A., Pezij, M., Benninga, H. F., Bindlish, R., Chan, S. K., Jackson, T. J., Hendriks, D. M. D., Augustijn, D. C. M., and Su, Z.: Validation of SMAP L2 passive-only soil moisture products using upscaled in situ measurements collected in Twente, the Netherlands, Hydrol. Earth Syst. Sci., 25, 473–495, doi:10.5194/hess-25-473-2021, 2021.

Van Doninck, J., Peters, J., Lievens, H., De Baets, B., and Verhoest, N. E. C.: Accounting for seasonality in a soil moisture change detection algorithm for ASAR Wide Swath time series, Hydrol. Earth Syst. Sci., 16, 773–786, doi:10.5194/hess-16-773-2012, 2012.

Van Emmerik, T., Steele-Dunne, S. C., Judge, J., and Van de Giesen, N.: Impact of Diurnal Variation in Vegetation Water Content on Radar Backscatter from Maize During Water Stress, IEEE Trans. Geosci. Remote Sens., 53, 3855–3869, doi:10.1109/TGRS.2014.2386142, 2015.

Van Emmerik, T., Steele-Dunne, S., Paget, A., Oliveira, R. S., Bittencourt, P. R. L., Barros, F. d. V., and Van de Giesen, N.: Water stress detection in the Amazon using radar, Geophys. Res. Lett., 44, 6841–6849, doi:10.1002/2017GL073747, 2017.

Van Essen Instruments: Product manual – Diver, Tech. rep., Van Essen Instruments B.V., Delft, NL, available online: `https://www.vanessen.com/images/PDFs/Diver-ProductManual-en.pdf` (accessed on 14 Dec 2021), 2016.

Van Genuchten, M. T.: A Closed-form Equation for Predicting the Hydraulic Conductivity of Unsaturated Soils, Soil Sci. Soc. Am. J., 44, 892–898, doi:10.2136/sssaj1980.03615995004400050002x, 1980.

Van Reeuwijk, L. P.: Procedures for soil analysis, Tech. rep., International Soil Reference and Information Centre & Food and Agriculture Organization of the United Nations, Wageningen, NL, available online: `http://www.isric.org/sites/default/files/ISRIC_TechPap09.pdf` (accessed on 13 Nov 2017), 2002.

VanderSat: VanderSat, available online: `www.vandersat.com/` (accessed on 18 Jun 2021), 2021.

Varble, J. L. and Chávez, J. L.: Performance evaluation and calibration of soil water content and potential sensors for agricultural soils in eastern Colorado, Agric. Water Manag., 101, 93–106, doi:10.1016/j.agwat.2011.09.007, 2011.

Vautard, R., Yiou, P., D'Andrea, F., de Noblet, N., Viovy, N., Cassou, C., Polcher, J., Ciais, P., Kageyama, M., and Fan, Y.: Summertime European heat and drought waves induced by wintertime Mediterranean rainfall deficit, Geophys. Res. Lett., 34, L07 711, doi:10.1029/2006GL028001, 2007.

Vaz, C. M. P., Jones, S., Meding, M., and Tuller, M.: Evaluation of Standard Calibration Functions for Eight Electromagnetic Soil Moisture Sensors, Vadose Zo. J., 12, vzj2012.0160, doi:10.2136/vzj2012.0160, 2013.

Veeneman, W., Remmelink, G., Tjoonk, L., Van der Weiden, T., Philipsen, B., Van den Pol van Dasselaar, A., and Stienezen, M.: 2016 was uitstekend graslandjaar (in Dutch), V-focus, Feb, 24–26, available online: `https://edepot.wur.nl/426593` (accessed on 25 Nov 2021), 2017.

Vereecken, H., Huisman, J. A., Bogena, H., Vanderborght, J., Vrugt, J. A., and Hopmans, J. W.: On the value of soil moisture measurements in vadose zone hydrology: A review, Water Resour. Res., 44, W00D06, doi:10.1029/2008WR006829, 2008.

Vereecken, H., Huisman, J. A., Pachepsky, Y., Montzka, C., Van der Kruk, J., Bogena, H., Weihermüller, L., Herbst, M., Martinez, G., and Vanderborght, J.: On the spatio-temporal dynamics of soil moisture at the field scale, J. Hydrol., 516, 76–96, doi:10.1016/j.jhydrol.2013.11.061, 2014.

Verhoef, A., Fernández-Gálvez, J., Diaz-Espejo, A., Main, B. E., and El-Bishti, M.: The diurnal course of soil moisture as measured by various dielectric sensors: Effects of soil temperature and the implications for evaporation estimates, J. Hydrol., 321, 147–162, doi:10.1016/j.jhydrol.2005.07.039, 2006.

Verhoest, N. E. C., De Baets, B., Mattia, F., Satalino, G., Lucau, C., and Defourny, P.: A possibilistic approach to soil moisture retrieval from ERS synthetic aperture radar backscattering under soil roughness uncertainty, Water Resour. Res., 43, W07 435, doi:10.1029/2006WR005295, 2007.

Verhoest, N. E. C., Lievens, H., Wagner, W., Álvarez-Mozos, J., Moran, M. S., and Mattia, F.: On the Soil Roughness Parameterization Problem in Soil Moisture Retrieval of Bare Surfaces from Synthetic Aperture Radar, Sensors, 8, 4213–4248, doi:10.3390/s8074213, 2008.

Vernes, R. W. and Van Doorn, T. H. M.: Van Gidslaag naar Hydrogeologische Eenheid - Toelichting op de totstandkoming van de dataset REGIS II (in Dutch), Tech. rep., TNO - Geological Survey of the Netherlands, Utrecht, NL, available online: `https://www.dinoloket.nl/sites/default/files/file/dinoloket_toelichtingmodellen_20131210_01_rapport_nitg_05_038_b0115_netversie.pdf` (accessed on 13 Nov 2017), 2005.

Vernieuwe, H., Verhoest, N. E. C., Lievens, H., and De Baets, B.: Possibilistic Soil Roughness Identification for Uncertainty Reduction on SAR-Retrieved Soil Moisture, IEEE Trans. Geosci. Remote Sens., 49, 628–638, doi:10.1109/TGRS.2010.2058577, 2011.

Vinnikov, K. Y., Robock, A., Qiu, S., and Entin, J. K.: Optimal design of surface networks for observation of soil moisture, J. Geophys. Res. Atmos., 104, 19 743–19 749, doi:10.1029/1999JD900060, 1999.

Vreugdenhil, M., Wagner, W., Bauer-Marschallinger, B., Pfeil, I., Teubner, I., Rüdiger, C., and Strauss, P.: Sensitivity of Sentinel-1 Backscatter to Vegetation Dynamics: An Austrian Case Study, Remote Sens., 10, 1396, doi:10.3390/rs10091396, 2018.

Vrugt, J. A.: Markov chain Monte Carlo simulation using the DREAM software package: Theory, concepts, and MATLAB implementation, Environ. Model. Softw., 75, 273–316, doi:10.1016/j.envsoft.2015.08.013, 2016.

Wagner, W., Lemoine, G., and Rott, H.: A Method for Estimating Soil Moisture from ERS Scatterometer and Soil Data, Remote Sens. Environ., 70, 191–207, doi:10.1016/S0034-4257(99)00036-X, 1999.

Wagner, W., Sabel, D., Doubkova, M., Bartsch, A., and Pathe, C.: The potential of Sentinel-1 for monitoring soil moisture with a high spatial resolution at global scale, in: Earth Observation and Water Cycle Science, Frascati, Italy, 2009.

Wagner, W., Hahn, S., Kidd, R., Melzer, T., Bartalis, Z., Hasenauer, S., Figa-Saldaña, J., De Rosnay, P., Jann, A., Schneider, S., Komma, J., Kubu, G., Brugger, K., Aubrecht, C., Züger, J., Gangkofner, U., Kienberger, S., Brocca, L., Wang, Y., Blöschl, G., Eitzinger, J., Steinnocher, K., Zeil, P., and Rubel, F.: The ASCAT Soil Moisture Product: A Review of its Specifications, Validation Results, and Emerging Applications, Meteorol. Zeitschrift, 22, 5–33, doi:10.1127/0941-2948/2013/0399, 2013.

Wanders, N., Karssenberg, D., De Roo, A., De Jong, S. M., and Bierkens, M. F. P.: The suitability of remotely sensed soil moisture for improving operational flood forecasting, Hydrol. Earth Syst. Sci., 18, 2343–2357, doi:10.5194/hess-18-2343-2014, 2014.

Wang, H., Li, X., Long, H., Xu, X., and Bao, Y.: Monitoring the effects of land use and cover type changes on soil moisture using remote-sensing data: A case study in China's Yongding River basin, Catena, 82, 135–145, doi:10.1016/j.catena.2010.05.008, 2010.

Wang, J. R. and Schmugge, T. J.: An Empirical Model for the Complex Dielectric Permittivity of Soils as a Function of Water Content, IEEE Trans. Geosci. Remote Sens., GE-18, 288–295, doi:10.1109/TGRS.1980.350304, 1980.

Wang, Q., Van der Velde, R., and Su, Z.: Use of a discrete electromagnetic model for simulating Aquarius L-band active/passive observations and soil moisture retrieval, Remote Sens. Environ., 205, 434–452, doi:10.1016/j.rse.2017.10.044, 2018.

Western, A. W. and Blöschl, G.: On the spatial scaling of soil moisture, J. Hydrol., 217, 203–224, doi:10.1016/S0022-1694(98)00232-7, 1999.

Western, A. W., Grayson, R. B., and Blöschl, G.: Scaling of Soil Moisture: A Hydrologic Perspective, Annu. Rev. Earth Planet. Sci., 30, 149–180, doi:10.1146/annurev.earth.30.091201.140434, 2002.

Wigneron, J.-P., Jackson, T. J., O'Neill, P., De Lannoy, G., de Rosnay, P., Walker, J. P., Ferrazzoli, P., Mironov, V., Bircher, S., Grant, J. P., Kurum, M., Schwank, M., Munoz-Sabater, J., Das, N., Royer, A., Al-Yaari, A., Al Bitar, A., Fernandez-Moran, R., Lawrence, H., Mialon, A., Parrens, M., Richaume, P., Delwart, S., and Kerr, Y.: Modelling the passive microwave signature from land surfaces: A review of recent results and application to the L-band SMOS & SMAP soil moisture retrieval algorithms, Remote Sens. Environ., 192, 238–262, doi:10.1016/j.rse.2017.01.024, 2017.

Wilhite, D. A. and Glantz, M. H.: Understanding: the Drought Phenomenon: The Role of Definitions, Water Int., 10, 111–120, doi:10.1080/02508068508686328, 1985.

Wood, E. F., Roundy, J. K., Troy, T. J., Van Beek, L. P. H., Bierkens, M. F. P., Blyth, E., De Roo, A., Döll, P., Ek, M., Famiglietti, J., Gochis, D., Van de Giesen, N., Houser, P., Jaffé, P. R., Kollet, S., Lehner, B., Lettenmaier, D. P., Peters-Lidard, C., Sivapalan, M., Sheffield, J., Wade, A., and Whitehead, P.: Hyperresolution global land surface modeling: Meeting a grand challenge for monitoring Earth's terrestrial water, Water Resour. Res., 47, W05 301, doi:10.1029/2010WR010090, 2011.

Woodhouse, I. H.: Introduction to Microwave Remote Sensing, CRC Press, Boca Raton, FL USA, 1 edn., 2006.

World Meteorological Organization: Satellite Programme: Sentinel-1, available online: `https://space.oscar.wmo.int/satelliteprogrammes/view/sentinel_1` (accessed on 21 Jun 2021), 2021.

Wösten, J. H. M., Veerman, G. J., De Groot, W. J. M., and Stolte, J.: Waterretentie- en doorlatendheidskarakteristieken van boven- en ondergronden in Nederland: de Staringreeks (in Dutch), Tech. rep., Alterra, Wageningen, NL, available online: `http://edepot.wur.nl/43272` (accessed on 13 Nov 2017), 2001.

Wösten, J. H. M., De Vries, F., Hoogland, T., Massop, H. T. L., Veldhuizen, A. A., Vroon, H. R. J., Wesseling, J. G., Heijkers, J., and Bolman, A.: BOFEK2012, de nieuwe, bodemfysische schematisatie van Nederland (in Dutch), Tech. rep.,

Alterra Wageningen UR, Wageningen, NL, available online: http://edepot.wur.nl/247678 (accessed on 27 Sep 2018), 2013.

Xia, Y., Sheffield, J., Ek, M. B., Dong, J., Chaney, N., Wei, H., Meng, J., and Wood, E. F.: Evaluation of multi-model simulated soil moisture in NLDAS-2, J. Hydrol., 512, 107–125, doi:10.1016/j.jhydrol.2014.02.027, 2014.

Yilmaz, M. T., Crow, W. T., Anderson, M. C., and Hain, C.: An objective methodology for merging satellite- and model-based soil moisture products, Water Resour. Res., 48, W11 502, doi:10.1029/2011WR011682, 2012.

Zacharias, S., Bogena, H., Samaniego, L., Mauder, M., Fuß, R., Pütz, T., Frenzel, M., Schwank, M., Baessler, C., Butterbach-Bahl, K., Bens, O., Borg, E., Brauer, A., Dietrich, P., Hajnsek, I., Helle, G., Kiese, R., Kunstmann, H., Klotz, S., Munch, J. C., Papen, H., Priesack, E., Schmid, H. P., Steinbrecher, R., Rosenbaum, U., Teutsch, G., and Vereecken, H.: A Network of Terrestrial Environmental Observatories in Germany, Vadose Zo. J., 10, 955–973, doi:10.2136/vzj2010.0139, 2011.

Zhang, X., Zhang, T., Zhou, P., Shao, Y., and Gao, S.: Validation Analysis of SMAP and AMSR2 Soil Moisture Products over the United States Using Ground-Based Measurements, Remote Sens., 9, 104, doi:10.3390/rs9020104, 2017.

Zheng, D., Van der Velde, R., Su, Z., Wang, X., Wen, J., Booij, M. J., Hoekstra, A. Y., and Chen, Y.: Augmentations to the Noah Model Physics for Application to the Yellow River Source Area. Part I: Soil Water Flow, J. Hydrometeorol., 16, 2659–2676, doi:10.1175/JHM-D-14-0198.1, 2015.

Zheng, D., Li, X., Wang, X., Wang, Z., Wen, J., Van der Velde, R., Schwank, M., and Su, Z.: Sampling depth of L-band radiometer measurements of soil moisture and freeze-thaw dynamics on the Tibetan Plateau, Remote Sens. Environ., 226, 16–25, doi:10.1016/j.rse.2019.03.029, 2019.

ZLTO: Beregeningssignaal: bespaar! (in Dutch), available online: https://www.zlto.nl/beregeningssignaal (accessed on 22 Jul 2021), n.d.

Zribi, M. and Dechambre, M.: A new empirical model to retrieve soil moisture and roughness from C-band radar data, Remote Sens. Environ., 84, 42–52, doi:10.1016/S0034-4257(02)00069-X, 2002.

Zribi, M., Taconet, O., Le Hégarat-Mascle, S., Vidal-Madjar, D., Emblanch, C., Loumagne, C., and Normand, M.: Backscattering behavior and simulation comparison over bare soils using SIR-C/X-SAR and ERASME 1994 data over Orgeval, Remote Sens. Environ., 59, 256–266, doi:10.1016/S0034-4257(96)00158-7, 1997.

About the author

Harm-Jan Benninga was born on 15 February 1992 in Aalsmeer, the Netherlands. He attended pre-university education (VWO) at the 'Ashram College' in Alphen aan den Rijn from 2004, where he obtained his diploma in 2010. Afterwards, Harm-Jan moved to Twente for a bachelor in Civil Engineering with a minor in Geo Data Processing and Spatial Information at the University of Twente. In 2013 he graduated cum laude with a final project on comparing methods to calculate water levels corresponding to regional surface water flooding norms, carried out at HydroLogic in Amersfoort. After obtaining his bachelor's degree, Harm-Jan started his master in Civil Engineering and Management with a specialization in Water Engineering and Management. He obtained his master's degree cum laude in August 2015. His master's thesis on the performance and limitations of ensemble river flow forecasts was partly conducted at the Institute of Geophysics–Polish Academy of Sciences in Warsaw, Poland. This was awarded with the 'Thesis Prize Civil Engineering 2016' and published as a scientific paper.

During his bachelor's minor he was already introduced to Faculty of Geo-Information Science and Earth Observation (ITC) of the University of Twente, and in October 2015 Harm-Jan joined its department of Water Resources as a PhD candidate on the remote sensing of soil moisture content. This PhD research was part of the project OWAS1S (Optimizing Water Availability with Sentinel-1 Satellites), in which Harm-Jan collaborated with researchers from Wageningen University and from the Water Engineering and Management department of the University of Twente as well as with the project partners from research institutes, consultancy and public authorities. Besides, he was involved in the PhD ITC committee, six master's graduation projects and, since November 2019, as lecturer in four master's courses. Harm-Jan's interests include modelling, remote sensing and data analysis to improve understanding and management of water systems.

List of publications

Journal papers

1. **Benninga, H. F.**, Booij, M. J., Romanowicz, R. J., and Rientjes, T. H. M.: Performance of ensemble streamflow forecasts under varied hydrometeorological conditions, Hydrol. Earth Syst. Sci., 21, 5273–5291, doi:10.5194/hess-21-5273-2017, 2017
2. **Benninga, H. F.**, Carranza, C. D. U., Pezij, M., Van Santen, P., Van der Ploeg, M. J., Augustijn, D. C. M., and Van der Velde, R.: The Raam regional soil moisture monitoring network in the Netherlands, Earth Syst. Sci. Data, 10, 61–79, doi:10.5194/essd-10-61-2018, 2018.
3. **Benninga, H. F.**, Van der Velde, R., and Su, Z.: Impacts of Radiometric Uncertainty and Weather-Related Surface Conditions on Soil Moisture Retrievals with Sentinel-1, Remote Sens., 11, 2025, doi:10.3390/rs11172025, 2019.
4. Carranza, C. D. U., **Benninga, H. F.**, Van der Velde, R., and Van der Ploeg, M. J.: Monitoring agricultural field trafficability using Sentinel-1, Agric. Water Manag., 224, 105698, doi:10.1016/j.agwat.2019.105698, 2019.
5. **Benninga, H. F.**, Van der Velde, R., and Su, Z.: Sentinel-1 soil moisture content and its uncertainty over sparsely vegetated fields, J. Hydrol. X, 9, 100066, doi:10.1016/j.hydroa.2020.100066, 2020.
6. Buitink, J., Swank, A. M., Van der Ploeg, M., Smith, N. E., **Benninga, H. F.**, Van der Bolt, F., Carranza, C. D. U., Koren, G., Van der Velde, R., and Teuling, A. J.: Anatomy of the 2018 agricultural drought in the Netherlands using in situ soil moisture and satellite vegetation indices, Hydrol. Earth Syst. Sci., 24, 6021–6031, doi:10.5194/hess-24-6021-2020, 2020.
7. Van der Velde, R., Colliander, A., Pezij, M., **Benninga, H. F.**, Bindlish, R., Chan, S. K., Jackson, T. J., Hendriks, D. M. D., Augustijn, D. C. M., and Su, Z.: Validation of SMAP L2 passive-only soil moisture products using upscaled in situ measurements collected in Twente, the Netherlands, Hydrol. Earth Syst. Sci., 25, 473–495, doi:10.5194/hess-25-473-2021, 2021.
8. **Benninga, H. F.**, Van der Velde, R., and Su, Z.: Sentinel-1 soil moisture content retrieval over meadows using a physically based scattering model, submitted.
9. Van der Velde, R. and **Benninga, H. F.**: Twelve years profile soil moisture and temperature measurements in Twente, the Netherlands, in preparation.

Datasets

1. **Benninga, H. F.**, Carranza, C. D. U., Pezij, M., Van der Ploeg, M. J., Augustijn, D. C. M., and Van der Velde, R.: Regional soil mois-

ture monitoring network in the Raam catchment in the Netherlands – 2016-04/2017-04 [version 1]. Dataset, 4TU.ResearchData, doi:10.4121/uuid:dc364e97-d44a-403f-82a7-121902deeb56, 2018.

2. **Benninga, H. F.**, Carranza, C. D. U., Pezij, M., Van der Ploeg, M. J., Augustijn, D. C. M., and Van der Velde, R.: Regional soil moisture monitoring network in the Raam catchment in the Netherlands – 2016-04/2017-04 (corrected). Dataset, 4TU.ResearchData, doi:10.4121/uuid:276a8c0e-c9a9-4fdf-916a-75cfe06fa974, 2018.
3. **Benninga, H. F.**, Carranza, C. D. U., Pezij, M., Van der Ploeg, M. J., Augustijn, D. C. M., and Van der Velde, R.: Regional soil moisture monitoring network in the Raam catchment in the Netherlands – 2017-04/2018-04. Dataset, 4TU.ResearchData, doi:10.4121/uuid:afb36ac8-e266-4968-8f76-0d1f6988e23d, 2018.
4. **Benninga, H. F.**, Carranza, C. D. U., Pezij, M., Van der Ploeg, M. J., Augustijn, D. C. M., and Van der Velde, R.: Regional soil moisture monitoring network in the Raam catchment in the Netherlands – 2018-04/2019-04. Dataset, 4TU.ResearchData, doi:10.4121/uuid:b68e3971-c73e-4d7f-b52f-9ef7d7fe1ed2, 2020.
5. Van der Velde, R. and **Benninga, H. F.**: Ten years profile soil moisture and temperature measurements in Twente. Dataset, DANS, doi:10.17026/dans-zrn-n8nh, 2020.
6. **Benninga, H. F.**, Van der Velde, R., and Su, Z.: Supplementary data of 'Sentinel-1 soil moisture content and its uncertainty over sparsely vegetated fields'. Dataset, DANS, doi:10.17026/dans-xfs-3anu, 2020.
7. **Benninga, H. F.**, Van der Velde, R., and Su, Z.: Leaf area index field measurements. Dataset, DANS, doi:10.17026/dans-xxv-sdez, 2021.
8. **Benninga, H. F.**, Van der Velde, R., and Su, Z.: Supplementary data of 'Sentinel-1 soil moisture content retrieval over meadows using a physically based scattering model'. Dataset, DANS, doi:10.17026/dans-z9z-t36z, 2021.

Conference contributions

1. **Benninga, H. F.**, Van der Velde, R., and Su, Z.: Soil moisture retrieval from Sentinel-1 satellite data, in: EGU General Assembly 2016, EGU2016–8427, Vienna, Austria, available online: `https://meetingorganizer.copernicus.org/EGU2016/EGU2016-8427.pdf` (accessed on 22 November 2021), 2016.
2. Agten, D., **Benninga, H. F.**, Diaz-Schümmer, C., Donnerer, J., Fischer, G., Henriksen, M., Hippert Ferrer, A., Jamali, M., Marinaci, S., Mould, T. J. D., Phelan, L., Rosker, S., Schrenker, C., Schulze, K., and Monteiro, J. E. T. B.: SWEAT: Snow Water Equivalent with AlTimetry, in: EGU General Assembly 2017, EGU2017–16487, Vienna, Austria, available online: `https://meetingorganizer.copernicus.org/EGU2017/EGU2017-16487.pdf` (accessed on 22 Nov 2021), 2017

3. **Benninga, H. F.**, Van der Velde, R., and Su, Z.: Uncertainty of Effective Roughness Parameters Calibrated on Bare Agricultural Land Using Sentinel-1 SAR, in: IGARSS 2018 - 2018 IEEE International Geoscience and Remote Sensing Symposium, pp. 108–111, Valencia, Spain, doi:10.1109/IGARSS.2018.8518371, 2018.

Professional articles

1. Pezij, M., **Benninga, H. F.**, Carranza, C. D. U., Augustijn, D. C. M., Van der Velde, R., and Van der Ploeg, M. J.: Bodemvocht uit satellietdata voor optimalisatie waterbeheer (in Dutch), Land + Water, 56, 26–27, 2016.
2. Van der Velde, R., **Benninga, H. F.**, Pezij, M., Augustijn, D. C. M., Carranza, C. D. U., Van der Ploeg, M. J., and Hendriks, D. M. D.: Bodemvocht uit satellietdata: wat kan de Nederlandse waterbeheerder ermee? (in Dutch), H2O, pp. 1–11, available online: `https://www.h2owaternetwerk.nl/vakartikelen/bodemvocht-uit-satellietdata-wat-kan-de-nederlandse-waterbeheerder-ermee` (accessed 22 November 2021), 2018.